PO-AK80

1561

FINAL REPORT
Contract 03-5-022-67 to 13
Research Unit #519

METEOROLOGY OF THE ALASKAN ARCTIC COAST

Thomas L. Kozo
Polar Science Center
Division of Marine Resources
University of Washington
Seattle, Washington 98195

1 April 1980

FINAL REPORT

Contract: 03-5-022-67 to 13
Research Unit: 519
Reporting Period: 1 Apr 79 - 31 Mar 80
Number of Pages: 137

METEOROLOGY OF THE ALASKAN ARCTIC COAST

Thomas L. Kozo
Research Scientist

Polar Science Center
Division of Marine Resources
University of Washington
Seattle, Washington 98195

1 April 1980

CONTENTS

		Page
I.	Summary	1
II.	Introduction	1
III.	Current State of Knowledge	3
IV.	Study Area	3
V.	Sources, Methods and Rationale of Data Collection	4
VI.	Results	4
VII.	Discussion	5
VIII.	Conclusions	7
IX.	Needs for Further Study	8
	References	9
	Figures	11

Appendix A: Sea Breezes on the Alaskan Arctic Coast, Ph.D. Dissertation by Thomas L. Kozo

Appendix B: Evidence for Sea Breezes on the Alaskan Beaufort Sea Coast; in Geophysical Research Letters, by Thomas L. Kozo

Appendix C: Mountain Barrier Baroclinicity Effects on Surface Winds Along the Alaskan Arctic Coast; submitted to Geophysical Research Letters, by Thomas L. Kozo

I. Summary of objectives, conclusions, and implications with respect to OCS oil and gas development

The objectives of this program were to measure and analyze surface winds, temperature and atmospheric pressures along the Alaskan arctic coast for the purpose of deriving the wind field responsible for nearshore (water depths to 20 meters) surface water movement.

Results of this study have shown that the surface wind field in spring and summer is strongly correlated at measuring stations separated by distances Up to 100 km. This strong mesoscale correlation implies that a minimum of surface wind measurement points could provide a reasonable data set for coastal current trajectory studies.

Two mesoscale phenomena investigated were sea breeze forcing and mountain barrier baroclinicity. The breeze forcing is an important factor in the summer months while the mountain barrier effect appears to be most significant in the winter months.

The effect of coastal winds on the summer nearshore circulation has relevance to transport of detritus, biota, spilled oil, and small ice floes. The sea breeze promoted barrier island lagoon flushing, and upwelling by maintaining persistent NE to E surface winds.

Use of data from three atmospheric pressure and position relaying buoys within the arctic ice pack, and two land pressure stations has shown a strong correlation between computed geostrophic winds and ice edge movement during the first week in August 1979. This period was chosen because reasonable ice edge data was available.

II. Introduction

A. General_ Nature of the Study

This study was designed to measure surface winds and surface atmosphere pressures in the Simpson Lagoon-Prudhoe Bay area. These surface winds were to be compared with predicted winds from National Weather Service (NWS) pressure charts. Causes of gross departures from NWS chart predictions were to be investigated and those attributed to mesoscale phenomena were to be examined and possibly modeled.

Measurements made during the 1977, 1978, and 1979 field seasons served as input for studies by Mathews (RU 526), Mungall (RU 531) and Naidu (RU 529).

B. Specific Objectives

This study has specific objectives of:

1. Measurement of surface winds and atmospheric pressures in the Simpson Lagoon-Prudhoe Bay area during seasons of interest.

2. Development of a sea breeze model tested with data from the 1976 and 1977 field seasons, to determine the degree and extent of breeze influence seaward from the coastline (see Appendices A and B).

3. Documentation of hydrometeorological extremes such as storm surges (see Kozo, 1979).

4. Determination of the degree of influence orographic baroclinicity exerts on coastal surface winds (see Appendix C).

5. Relate the summer ice edge position to the large scale wind field.

C. Relevance to Problems of Petroleum Development

Winds are the principle driving force for summer surface currents in the nearshore waters of the Alaskan arctic coast. Therefore any attempt to predict current trajectories must include a prediction of the surface wind field. The summer main ice pack edge (offshore several 100 km) serves as a source for small ice floes (roughly 30,000 kg) which are driven into the nearshore region by surface wind and resultant currents. The floes will exhibit movement in the nearshore region influenced by the combined effect of the large scale gradient wind and the sea breeze. Uncovered sea bed pipelines in trenches running from the offshore islands to the coast will be susceptible to ice damage when floes move into shallow water with a northerly velocity component. Oil slicks that may result from the above accident or other types of accidents will also' be strongly influenced by the wind regime. Clean-up and containment operations will be made more difficult since local coastal winds will be hard to predict and sea breeze influence will diminish with distance from the coast leading to surface current divergence or convergence effects as a function of large scale winds.

In winter a relevant mesoscale phenomenon which affects the surface wind direction and speed and therefore the wind stress on the nearshore ice is mountain barrier baroclinicity (see Appendix C). This effect diminishes with distance from the Brooks Range (Kozo, 1979). Recent data show that a 180° surface wind reversal occurs between Pt. Barrow and Barter Island while National Weather Service (NWS) synoptic charts cannot account for it. The lateral extent of the reversal reaches from Prudhoe Bay to Barter Island.

III. Current State of Knowledge

The Alaskan arctic coast in contact with the Beaufort Sea has five year-round weather reporting sites but only two are official NWS stations (Class A). These are Pt. Barrow and Barter Island, approximately 540 km apart. Located between Pt. Barrow and Barter Island are two Distant Early Warning (DEW) stations, Lonely and Oliktok and one airport at Deadhorse routinely reporting supplementary" data to the NWS but this information is mainly for post analysis and is not incorporated into twice-daily NWS pressure charts. The traditional method of approximating the surface wind from surface pressure field derived geostrophic winds is of limited use since the only surface input data comes from the above two Class A stations. No inland pressure data exists near the Beaufort Coast until south of the Brooks Range and none has been routinely collected in the Beaufort Sea. Kozo (1977) illustrated the increased detail in the pressure field when data from offshore buoys and additional land pressure measuring sites were added to the NWS data set.

Estimation of the surface winds from the synoptic pressure field is further complicated by the existence of an intermittent sea breeze circulation (Kozo, 1977; Moritz, 1977) during the summer months and mountain barrier effects

(Schwerdtfeger, 1974) during the winter months. The summer sea breeze circulation is generated by a time. varying but always positive land-sea temperature gradient (land temperature greater than the water temperature, Moritz, 1977). This results in a tendency to set up an along-shore component of the surface wind at the coast (a wind from 90"T ± 200). previous work (Kozo, 1977) from analysis of historical data suggests that the sea breeze occurs approximately 25% of the time in the summer months. The extent of offshore influence is less than 60 km (Hufford, 1979).

Mountain barrier baroclinicity, as explained by Schwerdtfeger (1974), results from a piling up of cold air against the Brooks Range when the atmospheric boundary layer is statically stable. The resultant mesoscale pressure gradient is favorable to westerly winds. The increased frequency of winter west winds recorded at Barter Island (near the Brooks Range) over that recorded simultaneously at Lonely or Pt. Barrow (both several 100 km from the Brooks Range) and Barter Island rawinsonde data are circumstantial evidence of this effect (see Appendix C).

Recent developments are:

1. The Polar Science Center has established (February 1979) the Arctic Basin Buoy network (TIROS satellite) of surface pressure stations which marked the beginning of continuous pressure data from the Beaufort Sea at two locations 300 km north of the Alaskan arctic coast. This data is being analyzed to determine the extent and duration of mesoscale influences on the synoptic wind field.

2. Two buoys purchased by OCS were implanted July 13, 1979 (NIMBUS satellite). One is permanently fixed at Franklin Bluffs and the one placed in the ice pack near shore lasted from July 13 to August 17, 1979. As a result, a permanent surface pressure triangle exists when Pt. Barrow and Barter Island data are used yielding a geostrophic wind with a solution center over Simpson Lagoon.

IV. Study Area

The study area for the past four years was contained within the latitudes 69"N - 74°N and longitudes 143°W - 157°W. In this way, buoy (1976 and 1979 only) installations within the ice pack, NWS stations at Barrow and Barter Island, DEW sites at Oliktok and Lonely (1976 and 1979 only), and camps at Umiat and Happy Valley (1976 only) could be used as surface pressure data sources to model the gradient wind fields.

Figure 1 shows the relative positions of the pressure stations (P) within the land-based grid for August 1979. The W's indicate the locations of portable weather stations (MRI's).

Data collection periods for 1976 were spring (April 27 to June 1) and summer (August 11 to September 6); for 1977 were spring (April 25 to June 1) and summer (July 20 to September 1); for 1978 were summer only (July 20 to September 1); and for 1979 were (July 15 to August 29).

V. Sources, Methods and Rationale of Data Collection

The previous years of 1976, 1977, and 1978 are discussed in Carsey (1977), Leavitt (1978) and Kozo (1979) respectively.

Data was collected in 1979 in the summer only, from July 15 through September 1. Meteorology Research, Inc. (MRI) mechanical weather stations recorded wind speed, wind direction, and temperature at Cross Island, Cottle Island, and Narwhal Island. A mesoscale surface pressure triangle was maintained using Weather Measure and Belfort microbarographs at Lonely, Narwhal, Franklin Bluffs and Oliktok. These microbarographs were services weekly and calibrated with two Negretti and Zambra precision digital barometers. In addition, a drifting pressure and position buoy was placed 100 km north of Barter Island in the sea ice, and one in a fixed position at Franklin Bluffs.

Weekly transportation to the surface pressure stations was provided by Cessna 206's belonging to Jim Helmrich and transportation to the MRI stations was provided by ERA (Deadhorse helicopters.

VI. Results

A. 1979 - Pressure Data and MRI Data

The MRI weather stations recorded average direction, wind run (converted to speed), and temperature on a strip chart. One hour averages of these variables were selected for three-hourly intervals at 00, 03, 06, 09, 12, 15, 18 and 21 hours GMT. Pressure was also reported at three-hourly intervals (from continuous microbarograph output). The pressures were calibrated using Negretti and Zambra precision barometers as transfer standards and then were reduced to sea level pressure using the hypsometric equation, station altitude and mean air temperature. The data has been submitted to the OCS data bank in card form and on magnetic tape. Time series plots of wind. and temperature, along with histograms are presented below in Section VII. Pressure data from the CANRAMS buoys relies on NASA output and is reported randomly averaging one pressure and position per day.

B. 1979 - Pilot Balloon Data and NWS Data

The following data in this subsection are presented and discussed in Section VII:

1. Pilot balloon launch data from Arco causeway for 8 August 1979 showing sea breeze influence on the large scale wind.

2. Scattergrams and histograms of February and March 1979 surface wind data from Barter Island and Pt. Barrow.

3. Histograms of surface wind data from Barter Island and Pt. Barrow for August 1979.

4. Data from 4 rawinsonde launches in March 1979 showing changes in wind direction of 180° from the surface to 250 meters.

5. NWS charts for selected days in March 1979 with surface wind arrows from Prudhoe Bay and surface pressure data from the Arctic Basin Buoy net added.

C. Sea Breeze

(See Appendix A and B)

D. Ice edge position in response to the large scale wind field.

Buoy data (offshore pressure and position) from two units of the previously mentioned Arctic Basin Buoy Array plus one offshore OCS buoy have been coupled to land station data from Pt. Barrow and Barter Island. This data was used to compute the 3-hourly geostrophic wind for a solution center near 72"N and 151°W. The buoy movement and ice edge movement in response to this large scale wind are shown for July 31 to August 7, 1979 in Section VII.

VII. Discussion

A. 1979 - MRI Data

Wind speeds (Figure 2) , wind directions (Figure 3), and temperature (Figure 4) are shown for Cross Island (July 15 - August 17, 1979), Cottle Island (August 8 - August 29, 1979) and Narwhal Island (August 8 - August 29, 1979). The horizontal notches are three days apart. There is an expected close agreement in wind speed and direction between stations since their total separation is less than 70 km and both Cross Island and Narwhal Island are only 20 km seaward (within the zone of sea breeze influence). The temperature data from these stations also show close correlation. The data presented in the previous 1977, 1978, and 1979 annual reports show similar results.

Histograms of surface wind speed, direction, and temperature for Cottle Island (Figure 5), Narwhal Island (Figure 6), and Cross Island (Figure 7) show similar results to data seen in the previous reports with the usual persistence of east winds. The wind speed is 6 m/s or less 60% of the time and is from the NE-E 50% of the time. These data compare favorably with the historical August data collected at Oliktok (west end of Simpson Lagoon) and recorded in the OCS Climatic Atlas (Brewer et al., 1977). The temperature histograms show a typical value between O and 4°C at 10 meters elevation.

B. Pilot Balloon Launch Data

Pilot balloon launch data from Arco Causeway (August 1979) (Figure 8), shows approximately 160° of turning from the upper (above 800 m) geostrophic wind level to the surface and is another example of the mesoscale effect of the summer thermal contrast between the water and land along the arctic coastline (see Appendix B for Cottle Island profiles).

C. Mountain Barrier Baroclinicity

Scattergrams showing simultaneous wind directions for Barter Island and Pt. Barrow in the months of February 1979 (Figure 9) and March 1979 (Figure 10) have a curious extra cluster of points. The clusters in the lower left and

and upper right are evidence of usual synoptic wind field effects covering the entire north coast of Alaska. The third cluster (enclosed in the rectangle) is evidence of mountain barrier baroclinicity as postulated by Schwerdtfeger (1974). Comparing histograms for February 1979 (Figure 11) and March 1979 (Figure 12) shows an increase in the percent of westerlies at Barter Island (which is close to the Brooks Range) over that of Pt. Barrow which is 300 km from the Brooks Range. This phenomenon which is also a function of atmospheric stability virtually disappears in the summer months as seen in histograms of the August 1979 data (Figure 13). The data from four rawinsonde launches (Figures 14-15) in March 1979 at Barter Island are ample evidence that the geostrophic wind direction (free stream flow) cannot be used to approximate the surface wind direction since 180° wind shifts have occurred.

The sections of NWS synoptic charts (Figures' 16-17) have surface wind arrows from Prudhoe Bay and surface pressure data from the Arctic Basin Buoy Net added. The large scale wind field as depicted by the isobars does not explain the surface wind directions and buoy 1914 shows that the isobars (from the NWS analysis) are misplaced while the surface wind at Prudhoe Bay indicates 100 km influence (Schwerdtfeger, 1979). See Appendix C for more explanation.

D. Summer Ice Edge Position

A unique data set has been obtained through the implementation of the University of Washington, Polar Science Center's Arctic Basin Buoy (ABB) array (sponsored by the National Science Foundation) by mid-February 1979. These buoys (within the polar ice pack) transmit pressure and position data to the TIROS-N satellite and use the ARGOS data collection and location system. Use of data from two of these offshore buoys with concomitant onshore station data has allowed the calculation of 3-hourly geostrophic winds through a two-dimensional least squares fit numerical fit technique (see Appendix A) for the north coast of Alaska. This data was coupled (July 31 to August 7) to simultaneous position data from the two ABB buoys (//1913 and #1914) plus position data from one OCS buoy (0063) implanted 100 km north of Barter Island on July 13, 1979. The buoy movement corresponded closely to the calculated geostrophic winds and the ice edge movement taken from the Navy-NOAA Joint Ice Center analyses of 29-31 July 1979 and 5-7 August 1979 showed an average 40 km coastward movement of the ice boundary (5 oktas concentration for this analysis) as seen in Figure 18.

It should be noted that Rogers (1978) concluded that the lack of a relationship between geostrophic wind direction and the distance to the ice margin (Sater et al., 1974) was that either the geostrophic wind was not a useful parameter or geostrophic wind data are unreliable in the arctic. In addition Rogers (1978) indicates that surface wind directions are significantly correlated to ice edge movement. Figure 18 coupled with Figure 19 show that the geostrophic wind is certainly a useful parameter since the buoy motion and ice edge movement agree quite well with the geostrophic direction during the study period. In fairness to Rogers, however, the geostrophic wind data before February 1979 was certainly unreliable in the arctic. Figure 19 also shows that due to the constant thermal contrast between the coast and the arctic ocean water (see Appendix A and B), surface winds (Cross Island data) at coastal stations are not good indicators of ice edge position.

It must be also noted that in contrast to winter ice studies where Agerton and Kreider (1979) concluded that a threshold wind velocity of 13 m/s was necessary to induce ice movement in the nearshore areas, a wind velocity of 6 m/s can cause considerable movement in the loosely consolidated summer ice with considerable onshore or offshore motion. Figures 20 and 21 show that the NWS analysis would do little to predict ice edge shoreward movement since a very weak large scale wind field is depicted for the August 2 to 5, 1979 period.

VIII. Conclusions

There is a strong correlation between surface winds (10 m) measured at remote station separations of 200 km or less along the Alaskan arctic coast from Lonely to Barter Island (obtained from data presented in this study and Leavitt, 1978). Presently available geostrophic wind calculations from NWS charts are of limited use in estimating the surface wind since simultaneous boundary layer stratification data usually doesn't exist. The charts are of no use during dominance by mesoscale influences such as the sea breeze in the summer dominates after snow leaves the arctic tundra and mountain barrier baroclinicity in the winter (see Appendix C). The NWS charts themselves (in absence of mesoscale effects) are marginally useful due to lack of data reporting stations north and south of the Beaufort Sea coast resulting in poor resolution and coastal biasing of geostrophic calculations. Therefore for nearshore use (less than 30 km from the coast), a few (6) wind velocity sensors between Barrow and Barter Island could provide the wind data for predicting coastal current velocities and trajectories.

Beyond 30 km at sea, geostrophic wind will be a better estimator of surface winds since the sea breeze influence will be minimal and orographic effects will be diminished. For this part of the shelf, pressure sensor equipped data buoys can be deployed on the main ice pack (200 km from shore) and inland 100 km to maintain a pressure grid with the correct geometry. A combination of coastal wind measurements and pressure measurements in a higher resolution grid could provide a proper data base for studies of oil spill trajectories, upwelling, lagoon flushing, and ice edge motion.

The major implications of sea breeze forcing along the coast are:

1. Maintenance of along-shore and offshore surface currents in the nearshore zone which promote lagoon flushing during low synoptic conditions.

2. Weakening of adverse synoptic wind conditions (those that prevent lagoon flushing) and may eventually offset or neutralize them during the afternoon hours.

3. Increasing the persistence of upwelling conditions.

4. Production of wind driven current shears beyond 30 km offshore where synoptic conditions are not influenced by thermal contrasts.

Theoretical evidence for the last effect (surface wind direction) has been demonstrated in model output and data from Hufford (1979) has shown that surface winds at 60 km from the coast are not influenced by the sea breeze. The sea breeze model (running at the University of Washington) can be used

to predict surface wind vector rotation from the coast to 50 km at sea under varying synoptic conditions and land-sea thermal contrasts. It has reproduced the pilot balloon measurements for both 270° and 220° synoptic winds. The gross asymmetry in histograms of summer surface wind direction (biased toward E-NE directions) from the study area can be explained by normal synoptic effects augmented by sea breeze forcing.

Major implications of the mountain barrier baroclinicity are:

1. 180degree surface wind shifts between Pt. Barrow and Barter Island.

2. Inability to predict wind stress and ice motion near shore.

3. Inability to predict ice movement farther off the coast since the surface pressure at Barter Island may be as much as 4 mb too high (Schwerdtfeger, 1979) resulting in an incorrect computation of geostrophic wind speed and direction.

Note: Complete evidence for the last effect is still being collected from surface pressure buoys and DEW line station data.

IX. Needs for Further Study

As mentioned in the conclusion, surface wind prediction from geostrophic winds requires a surface pressure grid with reasonable geometry. This has only existed sporadically in the Alaskan arctic. A study of pressure data from the two new pressure buoys (ABB) should be the beginning of a larger coastal buoy program this summer.

The past four years of field work did not include the 'winter months. In view of the large changes in the histograms of monthly wind directions for Barter Island, Oliktok and Lonely throughout the year, a simultaneous investigation of surface winds and geostrophic winds should be undertaken for December, January and February 1981, along with pressure measurements near the base of the Brooks Range. This should aid in producing a predictive model for this effect.

A study of sea breeze seaward extent should be made to tie in nearshore current data with outer-shelf current data and to determine its influence on summer nearshore small ice floe trajectories.

A combined inversion height-atmospheric boundary layer study should be initiated at Oliktok DEW site instrumenting their 100 meter tower and using an acoustic sounder to determine atmospheric diffusion parameters and wind profiles under very stable boundary layer conditions near the coast.

A study of sea ice edge position vs. large scale winds with the new ABB network should be established based on the encouraging results seen in this. report.

References

Agerton, D. J. and J. R. Kreider, 1979. Correlation of storms and major ice movements in the nears'here Alaskan Beaufort Sea. Fifth International Conference on Port and Ocean Engineering Under Arctic Conditions. Norwegian Institute of Technology, Vol. 1," 810 pp.

Berry, F. A., E. Bollay, and N. R. Beers, 1973. Handbook of Meteorology, McGraw-Hill, New York, 1068 pp.

Brewer, W. A., H. F. Diaz, A. S. Prechtel, H. W. Searby and J. L. Wise, 1977. Climatic Atlas of the Outer Continental Shelf Waters and Coastal Regions of Alaska, NOAA, NCC, EDS, Asheville, North Carolina, 409 pp.

Businger, J. A., J. C. Wyngaard, Y. Izumi, and E. F. Bradley, 1971. Flux - profile relationships in the atmospheric surface layer. J. Atmos. Sci., 28, 181-189.

Carsey, F. D., 1977. C astal meteorology of the Alaskan Arctic Coast. OC S Contrast 03-5-022-671011.

Defant, F., 1951. Local winds. Compendium of Meteorology. Boston, Massachusetts, Amer. Meteor. Sot., 655-662.

Estoque, M. A., 1961. A theoretical investigation of the sea breeze. Quart. J. R. Meteor. Sot., 87, 136-146.

Gonella, J., 1972. A rotary-component method for analysing meteorological and oceanographic vector time series. Deep-Sea Res., 19, 833-846.

Haurwitz, B., 1947. Comments on the sea-breeze circulation. J. Meteor. , 4, 1-8.

Hufford, G. L., 1979. Personal communication, OCS Office, Anchorage, Alaska.

Kozo, T. L., 1977. Coastal meteorology of the Alaskan Arctic Coast. P.I., F. Carsey; OCS Contract 03-5-022-671011.

Kozo, T. L., 1978. Coastal meteorology of the Alaskan Arctic Coast, Appendix, P.I., E. Leavitt. OCS Contract 03-5-022-67 to 13.

Kozo, T. L., 1979. Meteorology of the Alaskan Arctic Coast. P.I., T. Kozo; OCS Contract 03-5-022-67 to 13.

Kuo, H. L., 1968. The thermal interaction between the atmosphere and the earth and propagation of diurnal temperature waves. J. Atmos. Sci., 25, 682-706.

Leavitt, E., 1978. Coastal meteorology of the Alaskan Arctic Coast. Ocs Contract 03-5-022-67 to 13.

Moritz, R. E., 1977. On a possible sea breeze circulation near Barrow, Alaska. Arctic Alp. Res., 9, 427-431.

Neumann, J., 1977. On the rotation rate of the direction of sea and land breezes. J. Atmos. Sci., 34, 1913-1917.

Neumann, J. and Y. Mahrer, 1975. A theoretical study of the lake and land breezes of circular lakes. Mon. Wea. Rev., 103, 474-485.

O'Brien, J. J. and R. D. Pillsbury, 1974. Rotary wind spectra in a sea breeze regime. J. of App. Meteor. , 13, 820-825.

Physick, W., 1976. A numerical model of the sea-breeze phenomenon over a lake or gulf. J. Atmos. Sci., 33, 2107-2135

Rogers, J. C., 1978. Meteorological factors affecting inter-annual variability of summertime ice extent in theBeaufort Sea. Mon. Wea. Rev., 106, 890-897.

Sater, J. E., J. E. Walsh and W. I. Wittmann, 1974. Impingement of sea ice on the north coast of Alaska. The Coast and Shelf of the Beaufort Sea, J. C. Reed and J. E. Sater, Eds., Arctic Inst. of North America, 85-105.

Schwerdtfeger, W., 1974. Mountain barrier effect on the flow of stable air north of the Brooks Range. Climate of the Arctic, Conference Publication of the Geophysical Institute, University of Alaska, Fairbanks, 204-208.

Schwerdtfeger, W., 1979. Meteorological aspects of the drift of ice from the Weddell Sea toward the mid-latitude westerlies. J. Geophys. Res., 84, 6321-6328.

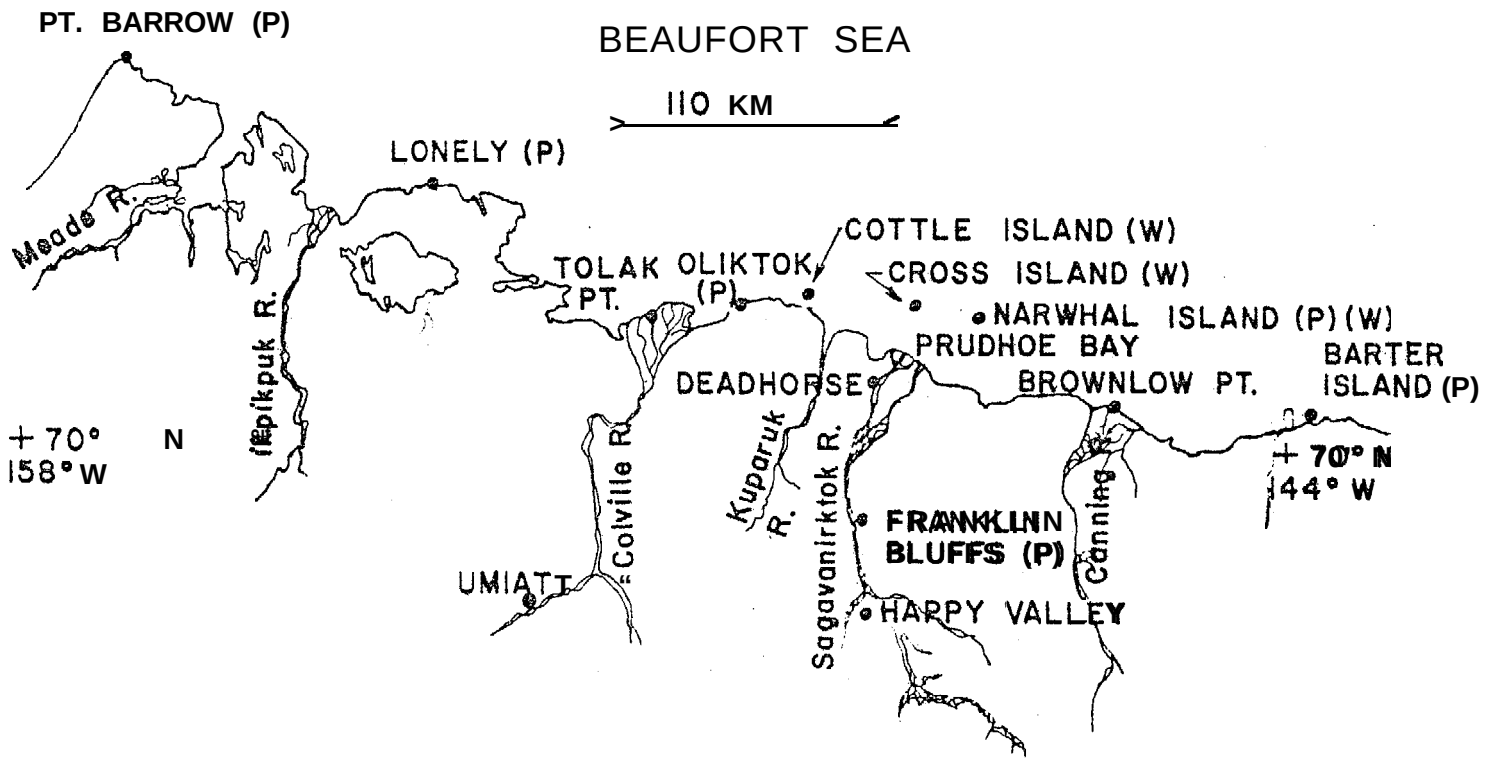

Fig. 1 Relative positions of the pressure stations (P) within the land-based grid for August 1979. The W's indicate the locations of portable weather stations (MRI's).

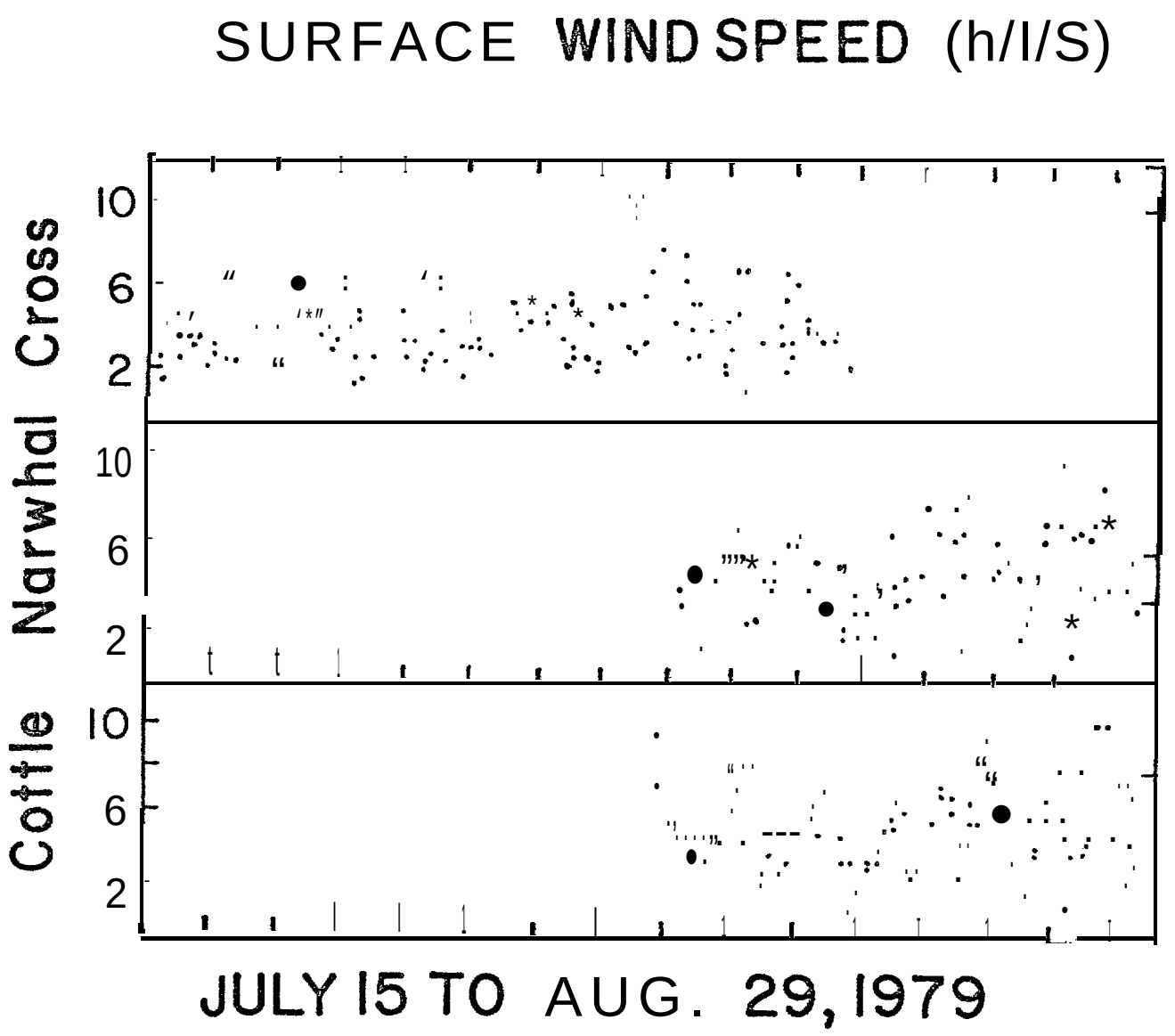

Fig. 2 Time series of surface wind speeds for Cross Island (July 15 - August 17, 1979), Cottle Island and Narwhal Island (both August 8 - August 29, 1979). The notches on the horizontal axes are 3-day intervals beginning July 15.

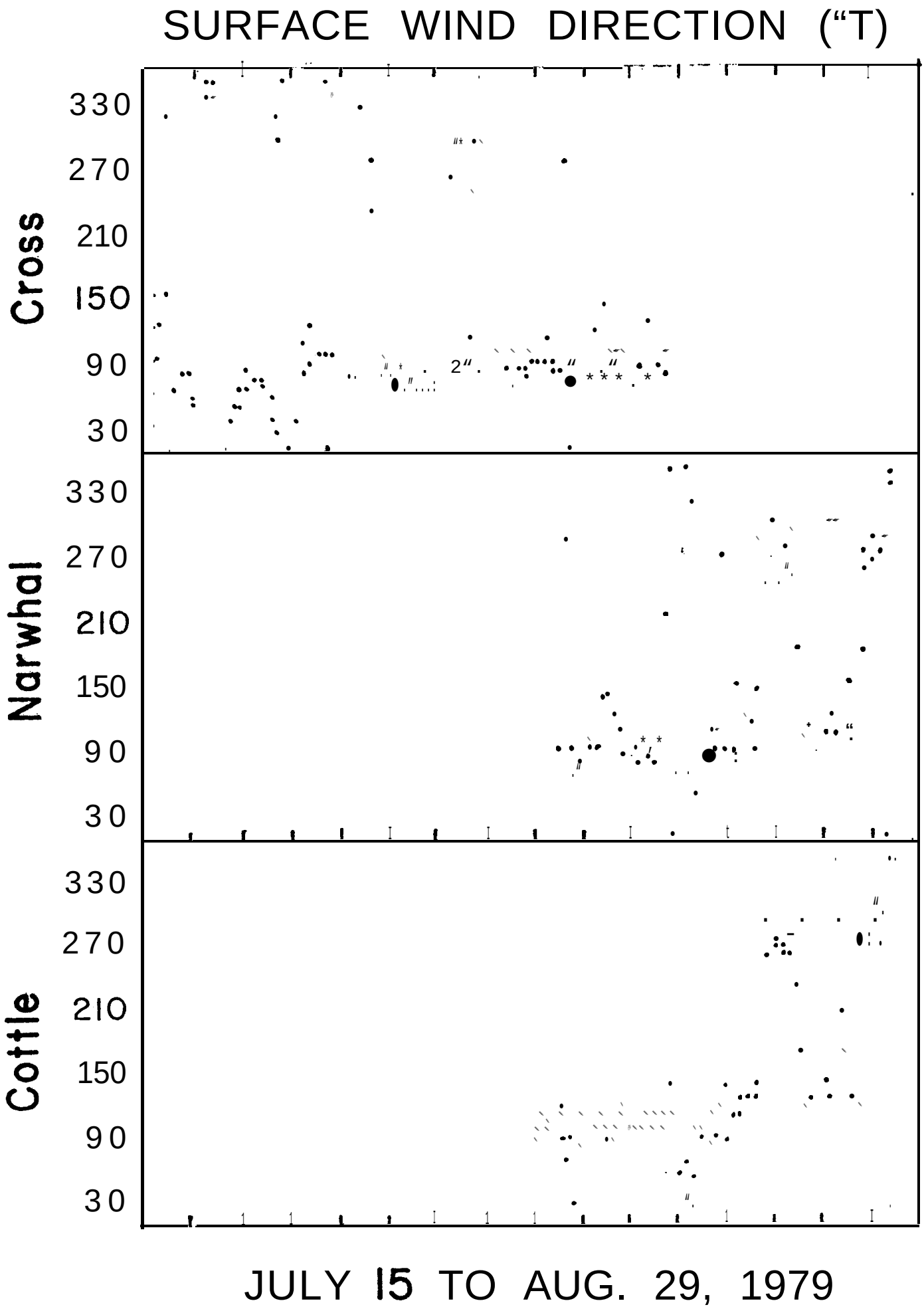

Fig. 3 Time series of surface wind directions - Same as Fig. 2.

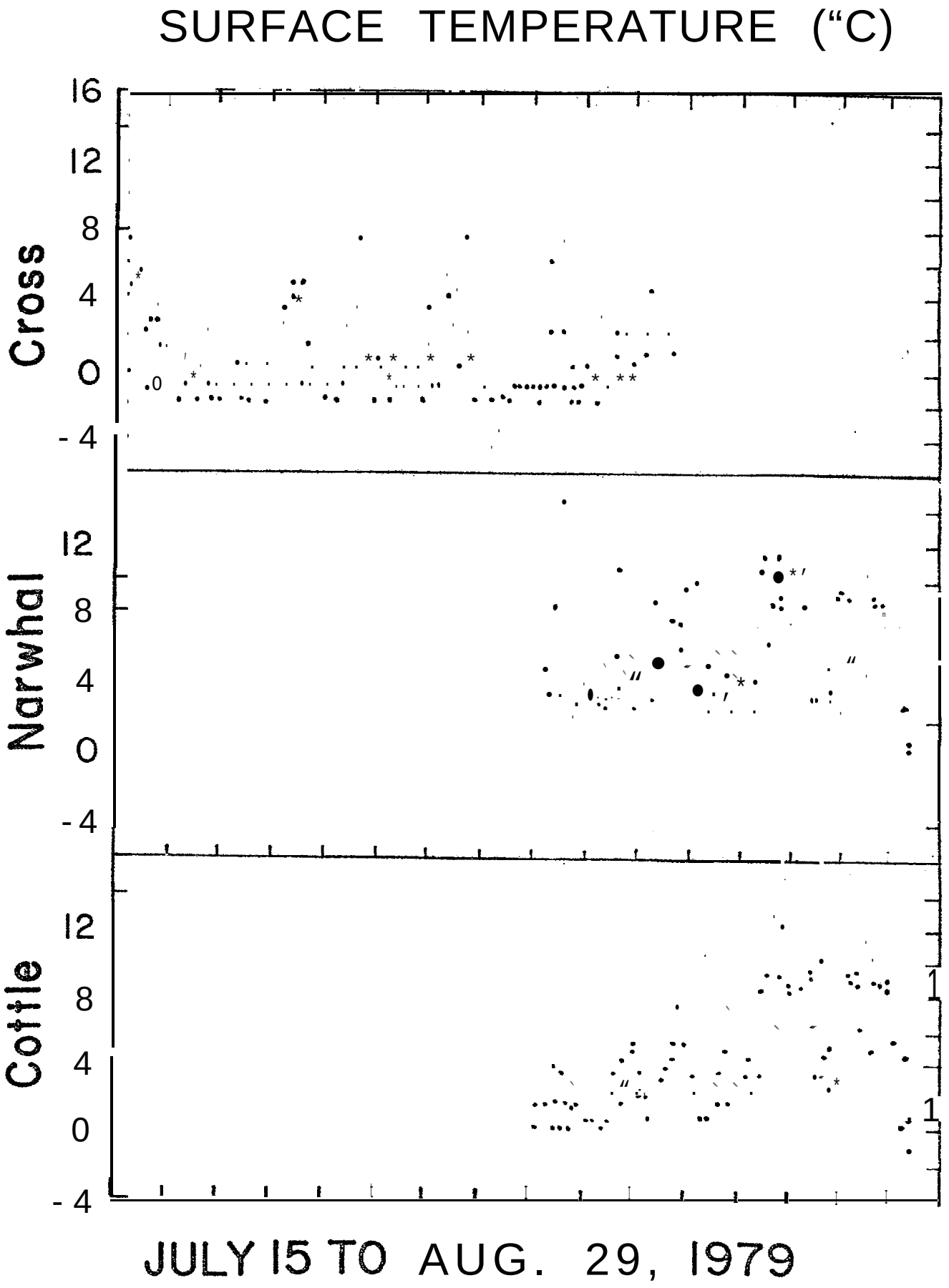

Fig. 4 Time series of surface temperature for Cross Island (July 15 - August 17, 1979), Cottle Island and Narwhal Island (both August 8 - August 29, 1979). The notches on the horizontal axes are 3-day intervals beginning July 15..

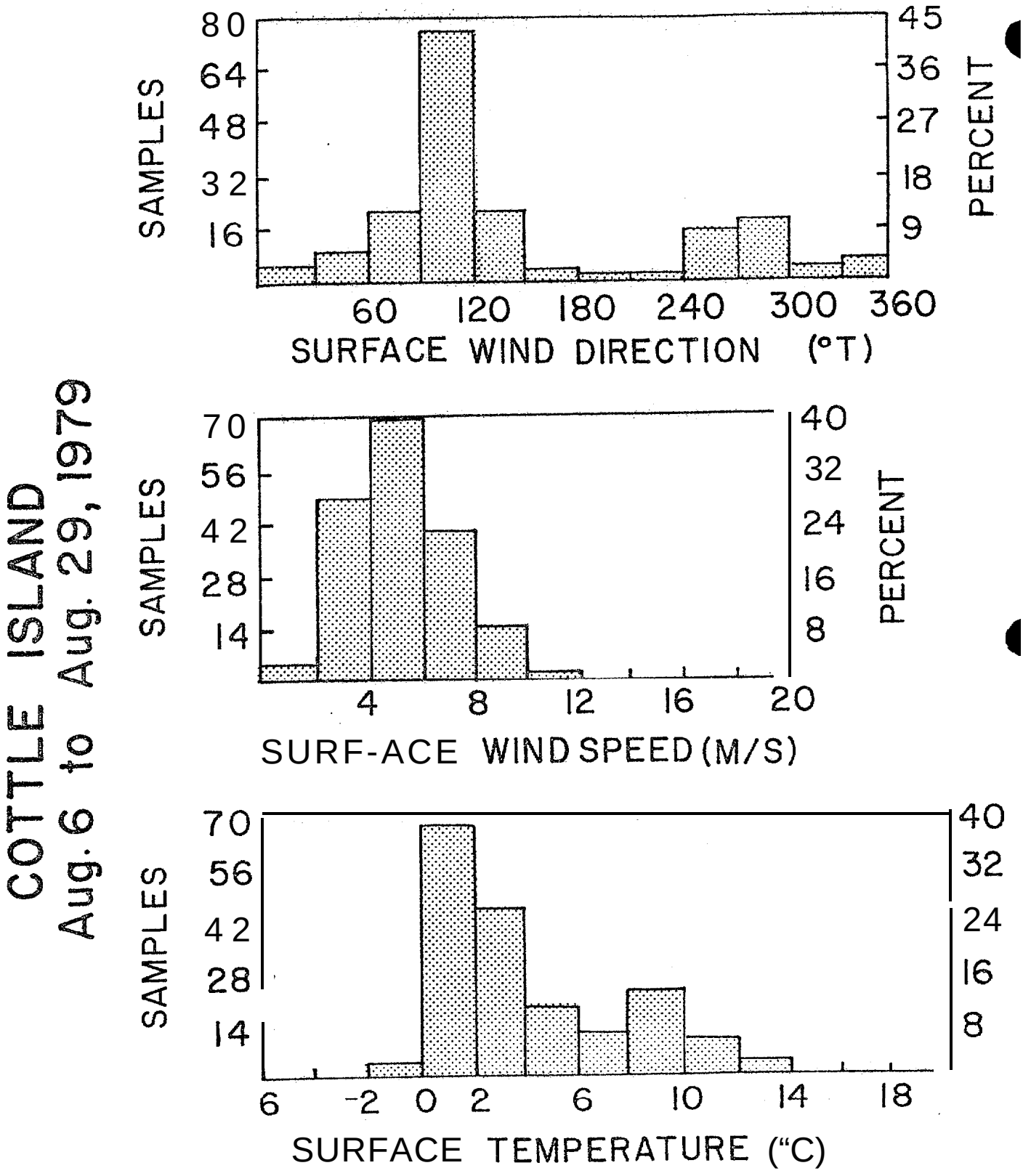

Fig. 5 Histograms of surface wind speed, direction, and temperature for Cottle Island (August 8 - August 29, 1979).

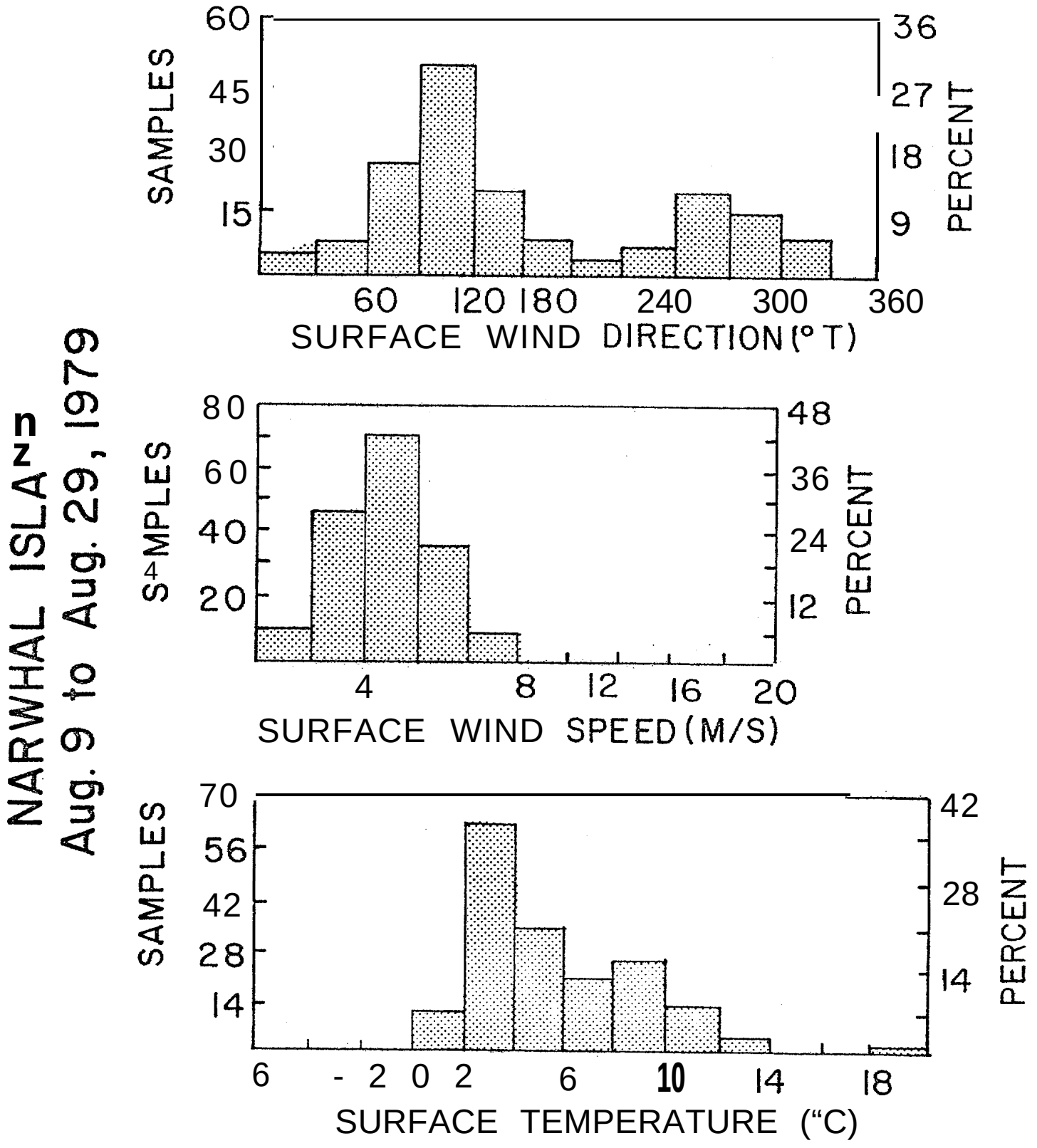

Fig. 6 Histograms of surface wind speed, direction, and temperature for Narwhal Island (August 8 - August 29, 1979) .

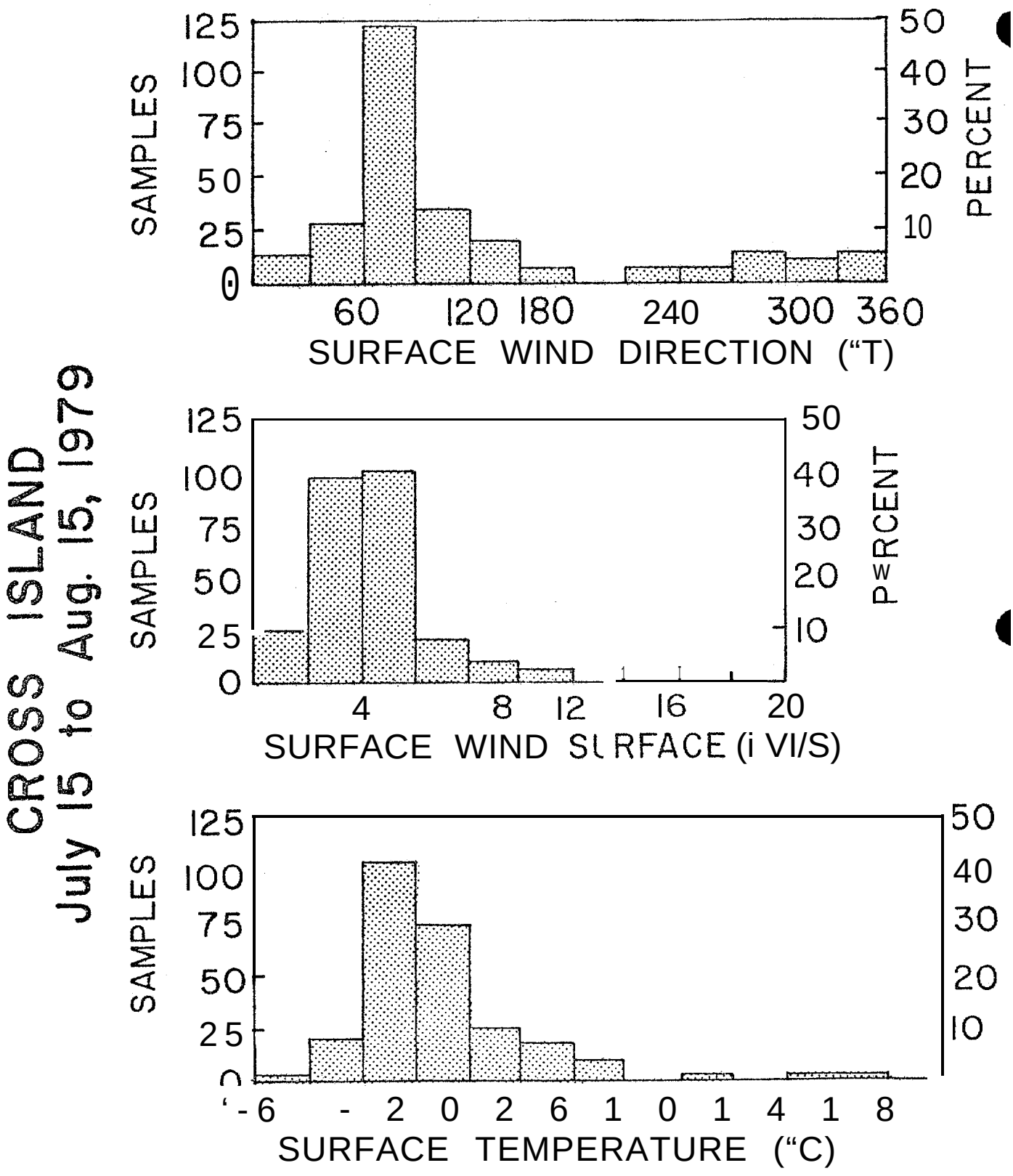

Fig. 7 Histograms of surface wind speed, direction, and temperature for Cross Island (July 15- August 17, 1979) .

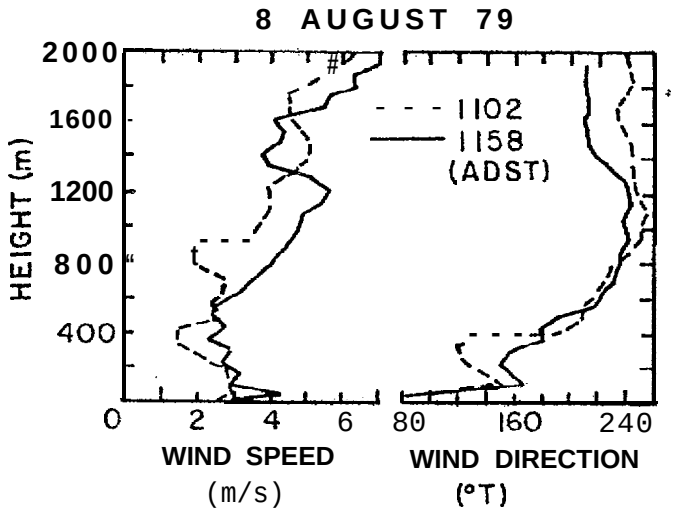

Fig. 8 Pilot balloon launch data from Arco Causeway in Prudhoe Bay (August 1979).

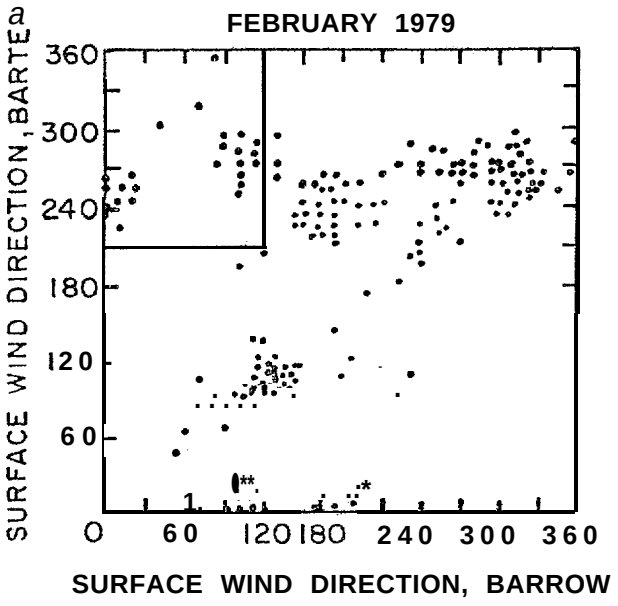

Fig. 9 A scattergram showing simultaneous wind directions for Barter Island and Pt. Barrow for February 1979. The mountain effect data points are enclosed within the rectangle (upper left).

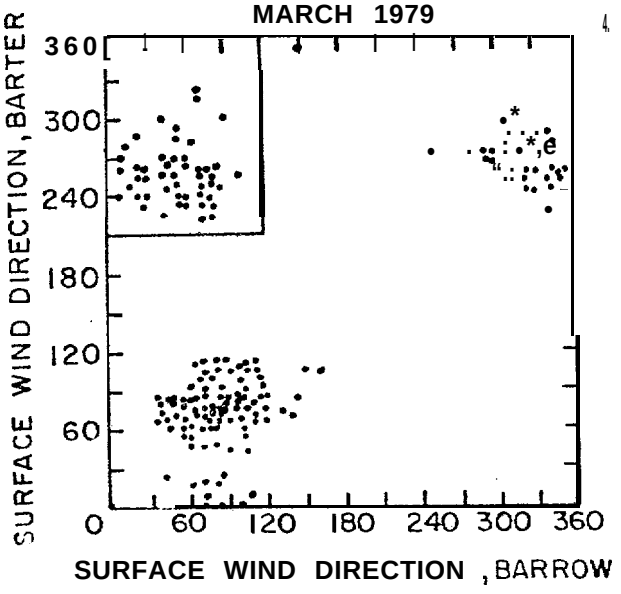

Fig. 10 A scattergram showing simultaneous wind directions for Barter Island and Pt. Barrow for March 1979. The mountain effect data points are enclosed within the rectangle (upper left).

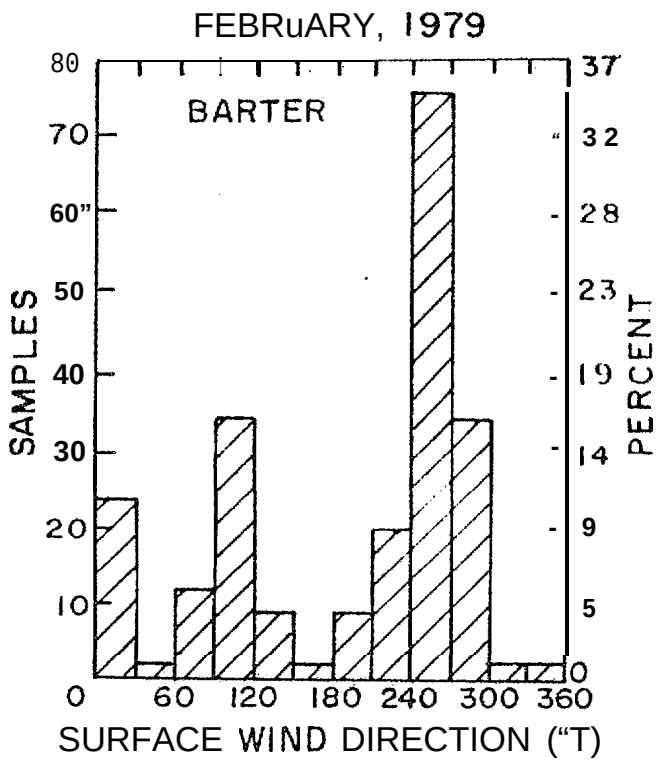

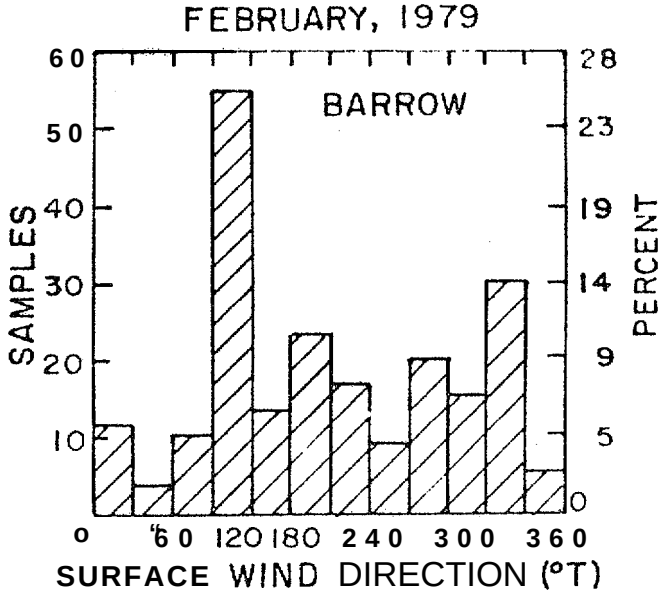

Fig. 11 Histograms comparing wind directions at Barter Island and Pt. Barrow, Alaska in February 1979.

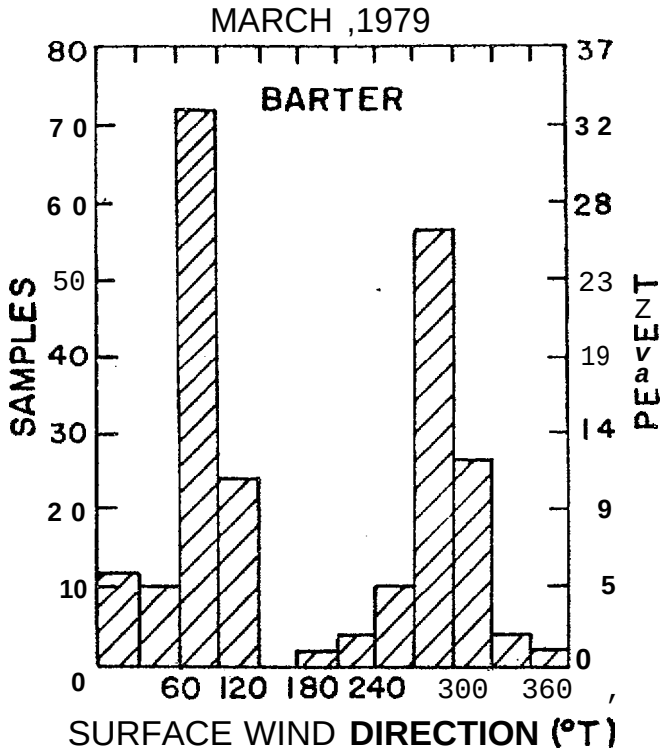

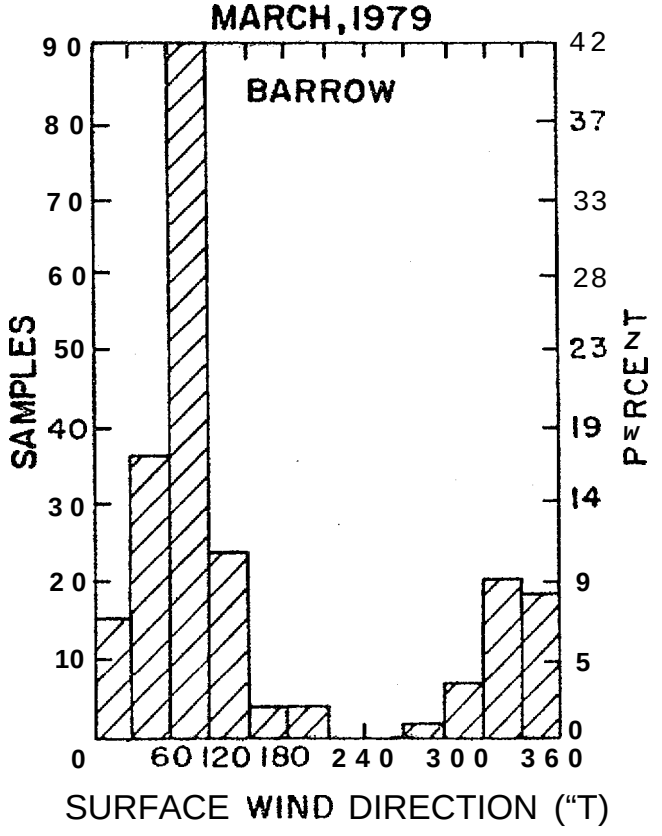

Fig. 12 Histograms comparing wind directions at Barter Island and Pt. Barrow, Alaska in March 1979.

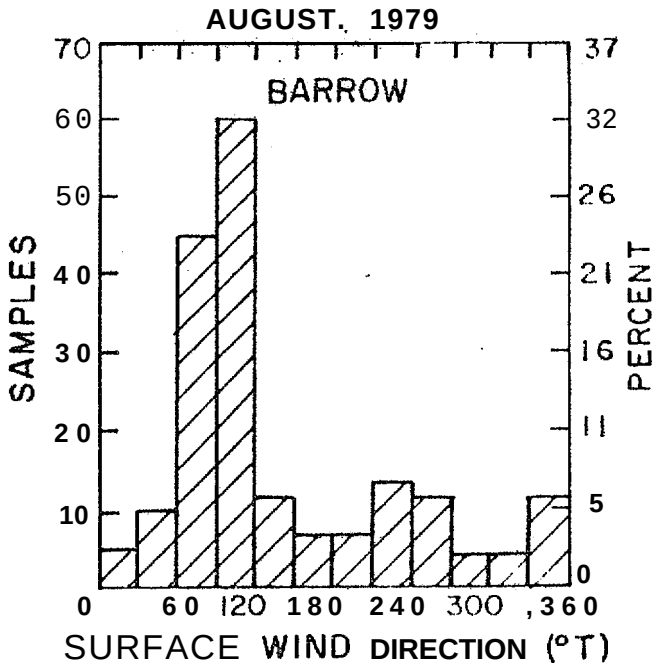

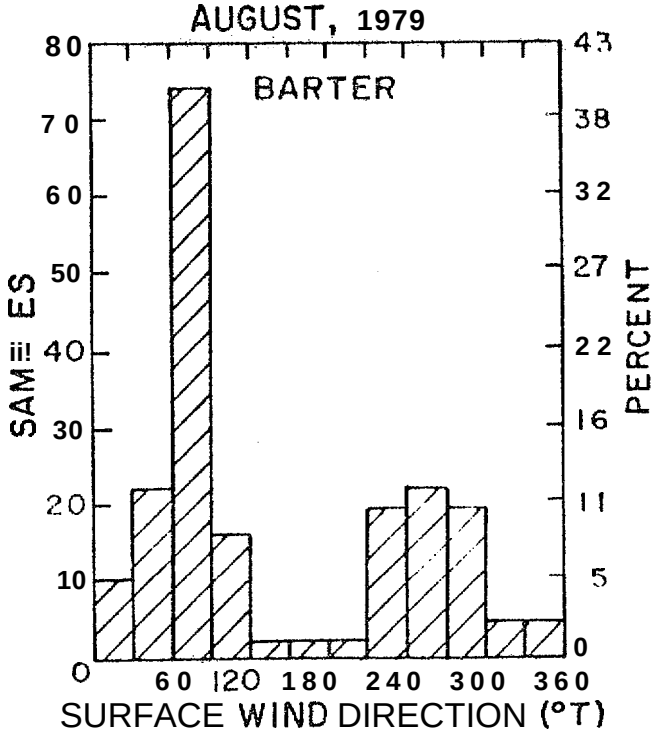

Fig. 13 Histograms comparing wind directions at Barter Island and Pt. Barrow, Alaska in August 1979.

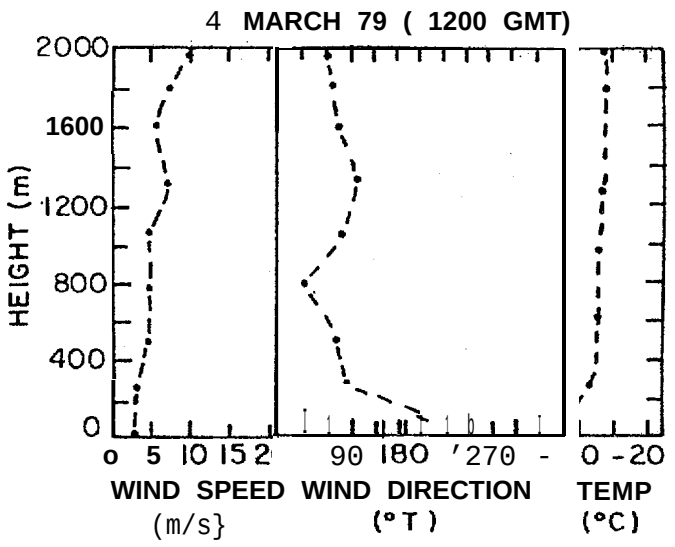

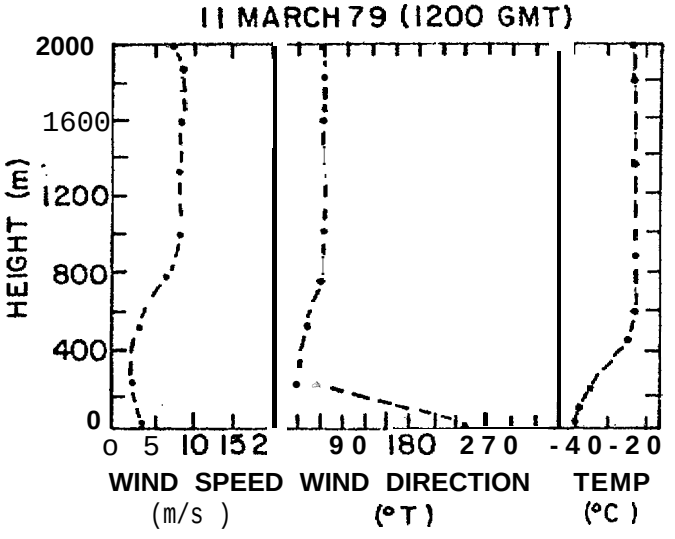

Fig. 14 Vertical profiles of wind speed, wind direction and temperature from rawinsonde data taken at Barter Island for 4 March and 11 March 1979.

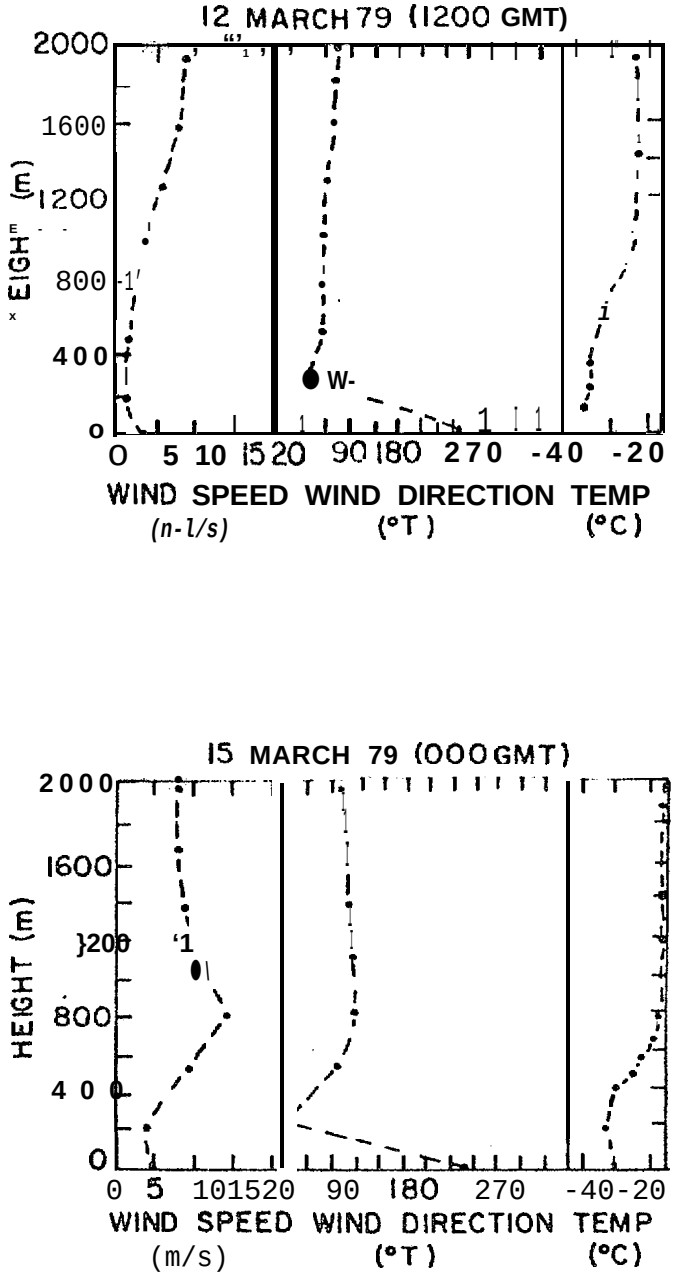

Fig. 15 Vertical profiles of wind speed, wind direction and temperature from rawinsonde data taken at Barter Island for 12 March and 15 March 1979.

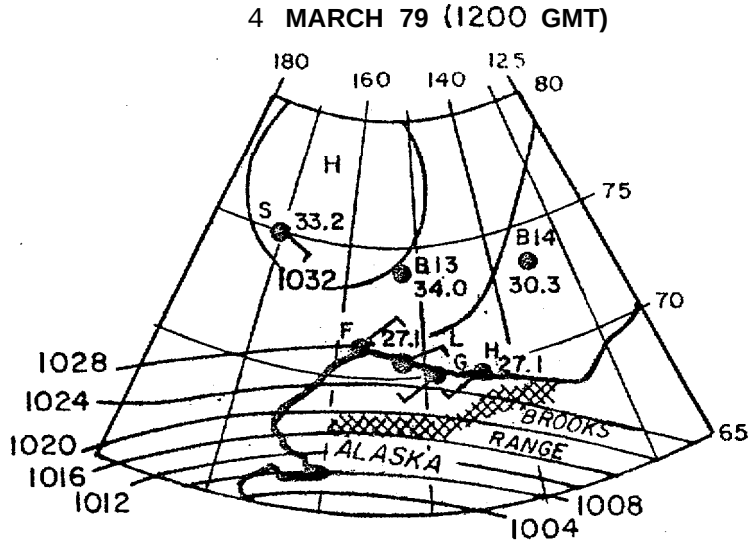

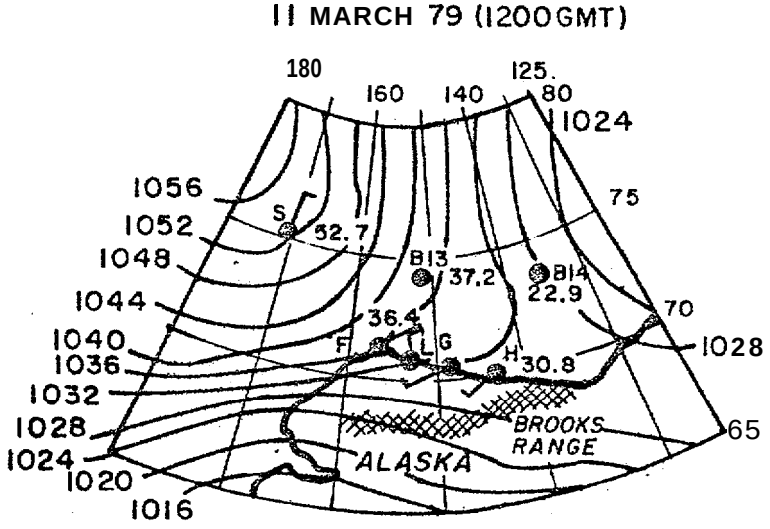

Fig. 16 Sections of NWS synoptic charts for 4 March and ,11 March 1979. B13 and B14 are part of the ABB array. S ≡ Russian Ice Station, F ≡ Pt. Barrow, L ≡ Lonely Dew Site, G ❑Prudhoe Bay, H ≡ Barter Island. The numbers adjacent to S, B13, B14, F and-H represent surface pressure – 1000 mb.

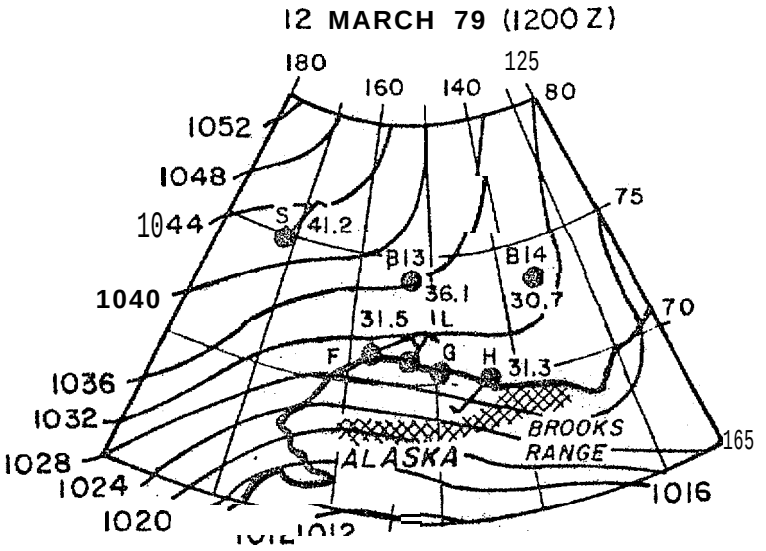

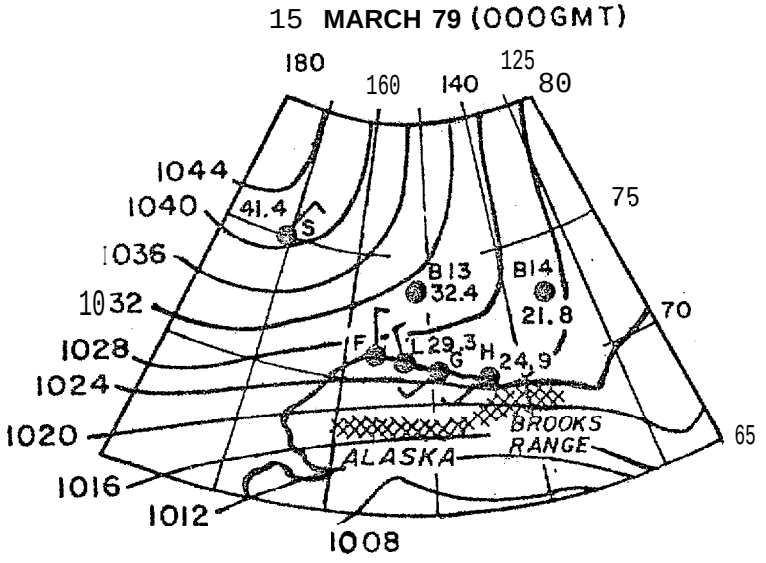

Fig. 17 Sections of NWS synoptic charts for 12 March and 15 March 1979. B13 and B14 are part of the ABB array. S ≡ Russian Ice Station, F ≡ Pt. Barrow, L ≡ Lonely Dew Site, G ≡ Prudhoe Bay, H ≡ Barter Island. The numbers adjacent to S, B13, B14, F and H represent surface pressure - 1000 mb.

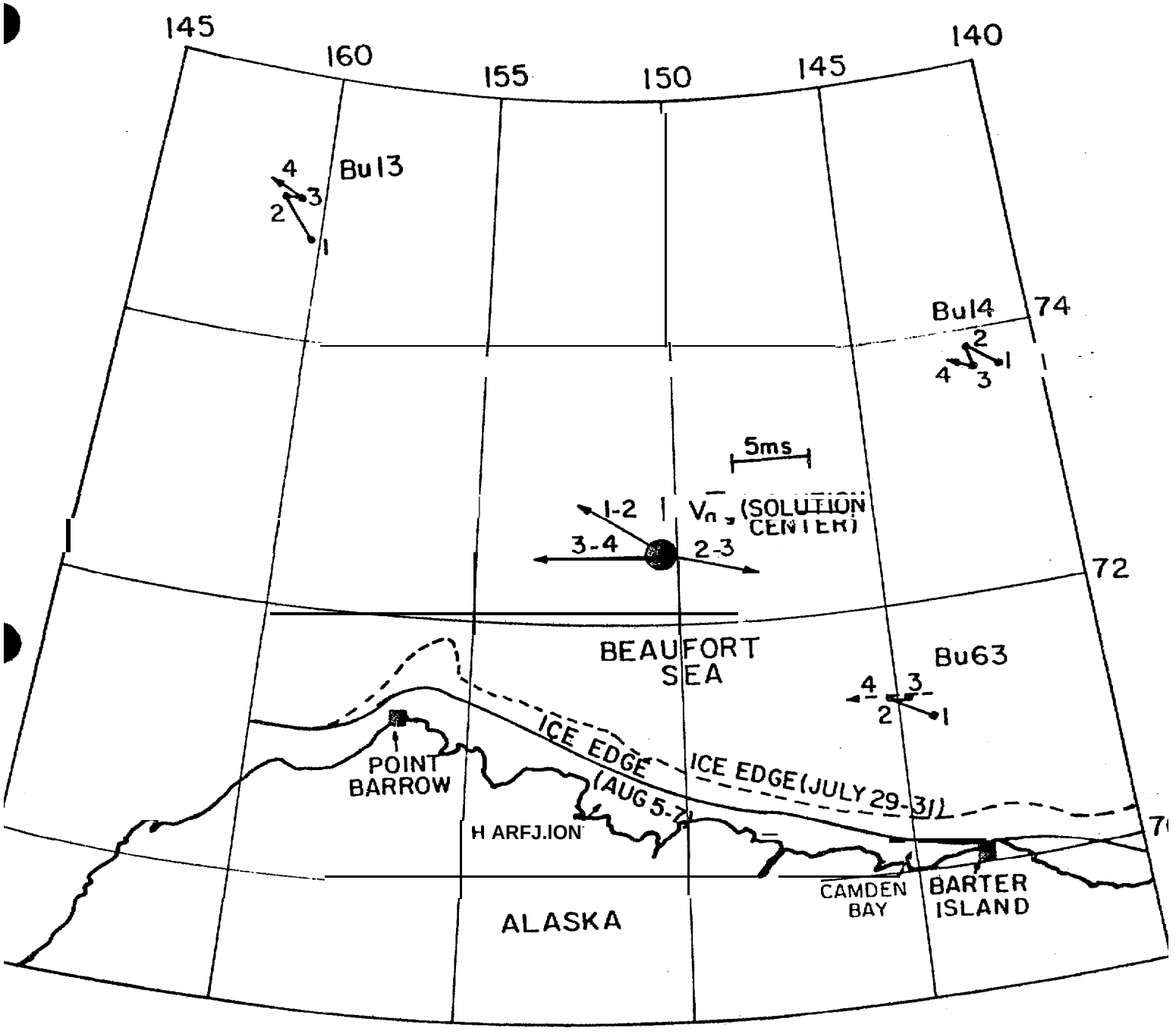

Figure 18. The ice edge position on days 29-31 July 79 compared to the position on 5–7 August 79. Buoy movements for Bu 13, Bu 14 (ABB array) and Bu 63 (OCS) are shown. The solution center for the calculated geostrophic winds is plotted. The arrows indicated the average geostrophic wind velocity for 27 July - 2 August (1-2), 2-5 August (2-3) and 5-7 August (3-4). The dashed line for Bu 63 means that the buoy position was known 3 August and 7 August but not between these dates.

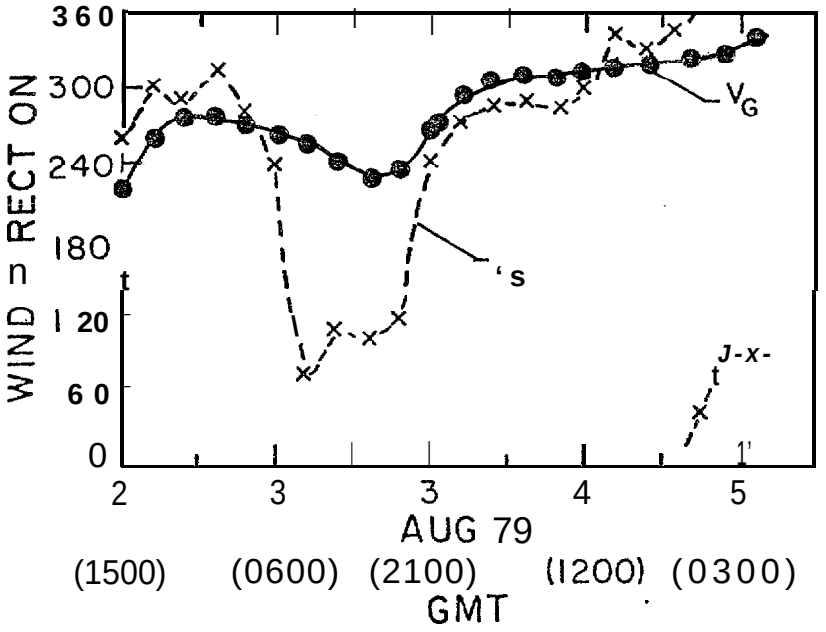

Figure 19. A simultaneous comparison of the calculated geostrophic wind (V_G) direction with the surface wind (V_S) direction on Cross Island from 2 August to 5 August 1979. This was the time period designated period 2-3 in Fig. 18.

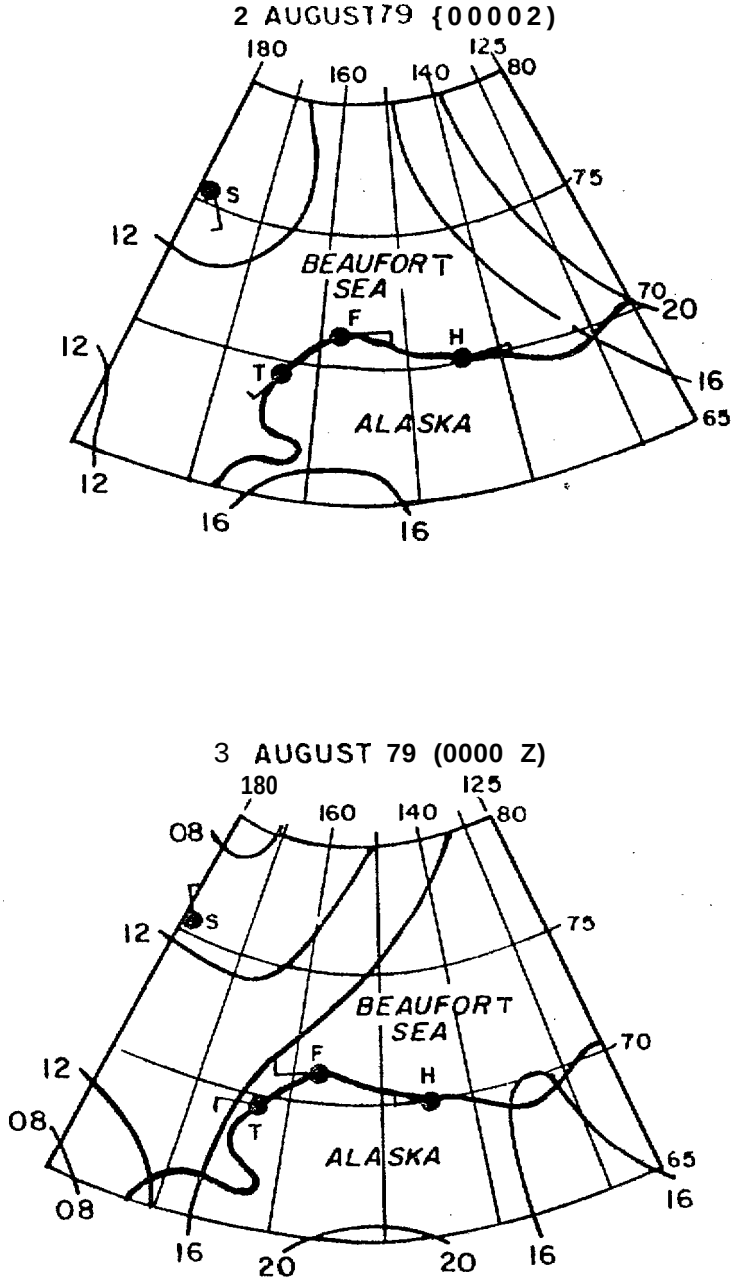

Figure **20.** Sections of NWS synoptic charts for 2 August and 3 August 1979. S ≡ Russian Ice Station, F ≡ Pt. Barrow, H ≡ Barter Island, T ≡ Pt. Lay. The numbers attached to the isobars represent surface pressure -1000 mb. The time designated z refers to Greenwich Mean Time.

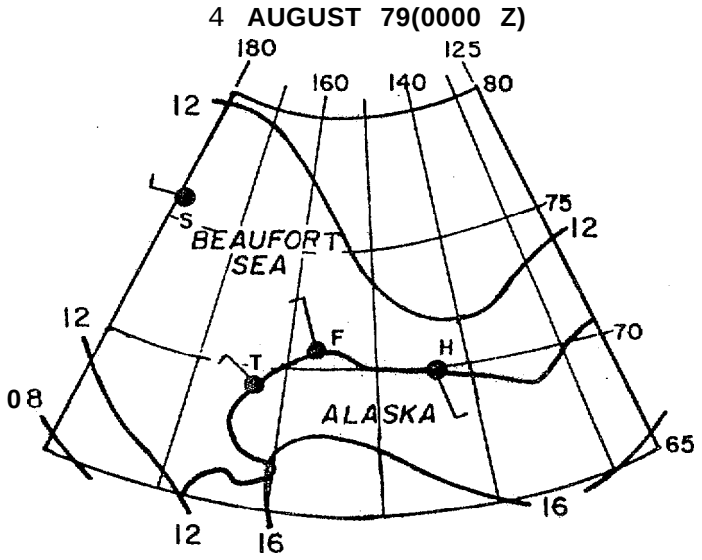

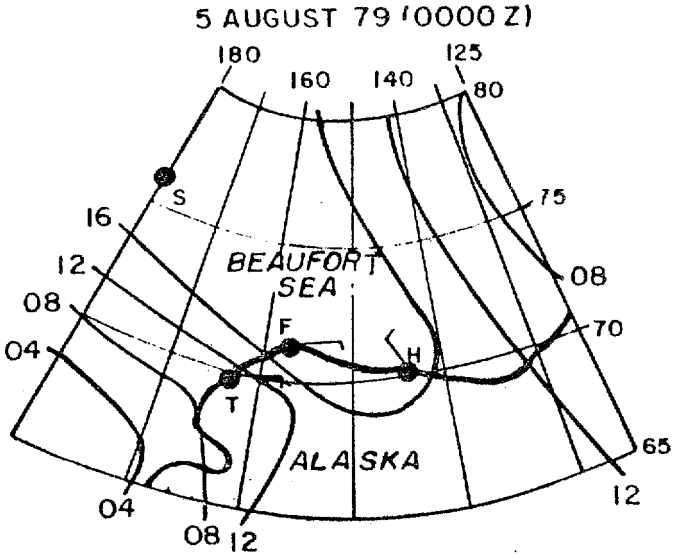

Figure 21. Sections of NWS synoptic charts for 4 August and 5 August 1979. S ≡ Russian Ice Station, F ≡ Pt. Barrow, H ≡ Barter Island, T ≡ Pt. Lay. The numbers attached to the isobars represent surface pressure, -1000 mb. The time designated z refers to Greenwich Mean Time.

Appendix A

Sea Breezes on the Alaskan Arctic Coast

University of Washington

Abstract

SEA BREEZES ON THE ALASKAN ARCTIC COAST

By Thomas Leslie Kozo

Chairperson of the Supervisory Committee: Professor Franklin I. Badgley
Atmospheric Sciences

Though sea breezes are not often associated with the arctic, this combined experimental and theoretical study offers proof, not only that they exist but that they can become the overriding meteorological feature.

Atmospheric environmental data collected in August 1976 and 1977 (when nearshore waters are relatively ice free) along the Beaufort Sea Coast of Alaska are examined for circumstantial and direct evidence of the existence of sea breezes at 70°N latitude. As one estimate of total atmospheric boundary layer wind velocity vector turning with height, a two-dimensional least squares technique is used to reproduce a three-hourly gradient wind field with data acquired from irregularly distributed surface pressure stations for simultaneous comparison to surface wind data. Rotary spectra from time series data of surface winds measured at offshore and inshore sites are examined to determine the horizontal extent of sea breeze influence.

A numerical, nonlinear, time-dependent, two-dimensional sea breeze model was formulated using typical measured conditions as input to uncover and simulate the dominant physical factors responsible for the

atmospheric boundary layer turning of the wind with height as seen in pilot balloon data. The sea breeze influence on boundary layer turning with height is largely responsible for the increased persistence of surface onshore (northeasterly and easterly) winds documented in August historical data for the Alaskan arctic coast. The model closely reproduced the pilot balloon wind velocity data, surface wind vector turning (with time) data and inversion height data, while giving evidence that sea breeze circulation could be strengthened by weak offshore (southwesterly and westerly winds) opposing synoptic winds. The model and data also showed reduced inland penetration of sea breezes with offsetting synoptic winds.

© copyright by

THOMAS LESLIE KOZO

1979

Sea Breezes on the Alaskan Arctic Coast

by

Thomas Leslie Kozo

A dissertation submitted in partial fulfillment
of the requirements for the degree of

Doctor of Philosophy

University of Washington

1979

Approved by _____
(Chairperson of Supervisory Committee)

Pro"gram Authorized
to Offer Degree Geophysics

Date June 8, 1979

Doctoral Dissertation

In presenting this dissertation in partial fulfillment of the require-. ments for the Doctoral degree at the University of Washington, I agree that the Library shall make its copies freely available for inspection. I further agree that extensive copying of this dissertation is allowable only for scholarly purposes. Requests for copying or reproduction of this dissertation may be referred to University Microfilms, 300 North Zeeb Road, Ann Arbor, Michigan 48106, "to whom the author has granted "the right to reproduce and sell (a) copies of the manuscript in micro-form and/or (b) printed copies of the manuscript made from microform."

Signature Thomas Leslie Kozo

Date June 8, 1979

TABLE OF CONTENTS

LIST OF FIGURES iv

LIST OF SYMBOLS ix

I. INTRODUCTION 1

1.1 Background 1
1.2 previous Work 4
1.3 Study Area 7
1.4 Goals and Motivation 9
1.5 Synopsis of Chapter I 11

II. ENVIRONMENTAL DATA 13

2.1 Continuously Recording Equipment 13
2.2 Atmospheric Sounding and Wind Profiling Equipment . . 15
2.3 Geostrophic Wind Data 18
2.4 PilotBalloonData 34
2.5 SurfaceWindData 52
2.6 Acoustic Sounder Data 74
2.7 Synopsis of Chapter II 76

111. THE THEORETICAL SEA BREEZE MODEL 78

3.1 Sea Breeze Properties Included in the Model 78
3.2 Coordinate System and Domain of Coverage 79
3.3 Surface Layer Equations 79
3.4 Upper Sublayer Equations 84
3.5 Initial and Boundary Conditions 87
3.6 The Numerical Integration Procedure 89
3.7 Input to the Model 90
3.8 Additional Numerical Techniques 92
3.9 Synopsis of Chapter III 94

IV. MODEL RESULTS. 96

4.1 Zero geostrophic wind (Case 1), Velocity and Temperature Contours 96
4.2 Geostrophic Wind 270°T, at 3 m/s and 5 m/s (Case 2a and 2b), Velocity and Temperature Contours 101
4.3 Geostrophic Wind 220°T, at 3 m/s and 5 m/s (Case 3a and 3b), Velocity and Temperature Contours 113

4.4 Geostrophic Wind 090°T, at 3 m/s and 5 m/s (Case 4a and 4b), Velocity and Temperature Contours 125
4.5 Geostrophic Wind 040°T, at 3 m/s and 5 m/s (case 5a and 5b), Velocity and Temperature Contours 132
4.6 Surface Wind Vectors for Cases 2-5 139
4.7 Simulated Pilot Balloon Data for Cases 2-5 152
4.8 Synopsis ofChapterIV. 159

V. THE PHYSICAL FACTORS WHICH CHARACTERIZE THE ARCTIC SEA BREEZE 162

5.1 Zero (0) Geostrophic Wind 162
5.2 Intensity, Fronts and Frontal Advancement 163
5.3 Rotation and Rotation Rates 167
5.4 Synopsis of ChapterV 172

VI. CONCLUSIONS AND RECOMMENDATIONS 174

REFERENCES 176

APPENDIX A: THE PREDICTION EQUATIONS IN FINITE-DIFFERENCE FORM. . . . . , ... 181

APPENDIX B: DERIVATIONS OF THE U, θ, u_*, θ_* AND $K(h)$ EQUATIONS FOR THE SURFACE LAYER 185

LIST OF FIGURES

1. Geometry for application of the circulation theorem to the sea breeze problem 3

2. Locations of atmospheric pressure stations (P) within the land-based grid for 1976, 1977 and 1978 and primary study area(A) 8

3. Primary study area with (W) and (WA) representing mechanical weather stations and airport weather stations, respectively. 10

4. National Weather Service (NWS) surface pressure chart for. August 16, 1976 (000 GMT) . . . . . *..*...*. . 24

5. Two-dimensional least squares fit (TDLSF) to surface pressure network on August 16, 1976 (.000 GMT) 25

6. NWS surface pressure chart for August 18, 1976 (000 GMT) . . . 26

7. TDLSF to surface pressure network on August 18, 1976 (000 GMT) 27

8. NWS surface pressure chart for August 21, 1976 (000 GMT) . . . 28

9. TDLSF to surface pressure network on August 21, 1976 (000 GMT) . . . . . ● .o.9000. soD29

10. Comparison of surface (lO-meter) winds on Cottle Island with geostrophic winds in August 1976 35

11. Geostrophic wind direction (D_G) as a function of surface wind direction (S_{10}) using data from the same time period as in Figure 10 36

12. Analog uncalibrated pyrheliograph data illustrating relatively high or low radiation day readings from August 1–21, 1977 . . . . . ••. ••. . . . ••••38

13. Pilot balloon derived profiles of wind speed and wind direction from Pingok Island on August 7, 1977 39

14. NWS surface pressure chart for August 8, 1977 (000 GMT) 41

15. Pilot balloon derived profiles of wind speed and wind direction from Pingok Island on August 14, 1977 42

33. Three hourly local surface wind vectors for designated stations (as in Figure 30) on August 17, 1977 69

34. Three hourly local surface wind vectors for designated stations (as in Figure 30) on August 19, 1977 . . . . . , . . . 70

35. Facsimile record of acoustic soundings from 0700 ADST on August 20, 1976 to 0200 ADST on August 21, 1976 (a sea breeze day) recorded 15 km inland at a site between ARCO and Deadhorse Airports 75

36. Sea breeze model coordinate system and x, y, z and domains of coverage. 80

37. Model output of isotachs (m/s) of $U(U_L + U')$ for 0 geostrophic wind ($U_L = 0$) . . . . . .*. 97

38. Model output of isotachs (m/s) (cross-section) of $V(V_L + V')$ for 0 geostrophic wind ($V_L = 0$) 98

39. Model output of isotachs of w' (cm/s) for a 0 geostrophic wind. 99

40. Model output of temperature contours (°C) for a 0 geostrophic wind. . . . . , ... 100

41. Model output of total u-W plane velocity vectors for geostropic wind from 270°T 103

42. Model output of isotachs (m/s) of $U(U_L + U')$ for geostrophic windfrom270°T 105

43. Model output of isotachs (m/s) (cross-section) of $V(V_L + V')$ for geostrophic wind from 270°T , ... 107

44. Model output of isotachs of w' (cm/s) for geostrophic wind from270°T. 1 0 9

45. Model output of temperature contours (°C) for a goestrophic wind from 270°T 111

46. Model output of total u-w plane velocity vectors for a geostrophic wind from 220°T 114

47. Model output of isotachs (m/s) of $(U_L + U')$ for a geostrophic windfrom220°T . . . . . , ... 116

48. Model output of isotachs (m/s) of V(VL + V') for a geostropic wind from 220°T 118

49. Model output of isotachs of w' (cm/s) for a geostrophic wind from 220″T . . . .** .**.. 120

50. Model output of temperature contours (°C) for a geostrophic wind from 220°T 122

51. Model output of total u-w plane velocity vectors for a geostrophic wind from 090°T 126

52. Model output of isotachs (m/s) of $U(U_L + U')$ for a geostrophic wind from 090°T 128

53. Model output of isotachs (m/s) of $V(V_L + V')$ for a geostrophic wind from 090°T 130

54. Model output of isotachs of w' (cm/s) for a geostrophic wind from 090°T 133

55. Model output of temperature contours (Co) for a geostrophic wind from 090°T 135

56. Model output of total u-w plane velocity vectors for a geostrophic wind from 040°T 137

57. Model output of isotachs (m/s) of $U(U_L + U')$ for a geostrophic windfrom040°T 140

58. Model output of isotachs (m/s) of $V(V_L + V')$ for a geostrophic wind from 040°T 142

59. Model output of isotachs of w' (cm/s) for a geostrophic wind from 040°T 144

60. Model output of temperature contours (°C) for a geostrophic wind from 040°T 146

61. Model output of surface wind vectors for 1500, 1700 and 1900 with V_g (geostrophic wind) from 270°T 149

62. Model output of surface wind vectors for 1500, 1700 and 1900 with V_g from 220°T. 150

63. Model output of surface wind vectors for 1500, 1700 and 1900 with V_g from 090°T. 151

64. Model output of surface wind vectors for 1500, 1700 and 1900 with V_g from 040°T 152

65. Model output of wind speed and wind direction profiles, 5 km seaward from the coast, for 1500, 1700 and 1900 with V_g's of 3 m/s and 5 m/s (as shown) from 270°T 154

66. Model output of wind speed and wind direction profiles, 5 km seaward from the coast, for 1500, 1700 and 1900 with V_g's of 3 m/s and 5 m/s (as shown) from 220°T 155

67. Model output of wind speed and wind direction profiles, 5 km seaward from the coast, for 1500, 1700 and 1900 with V_g's of 3 m/s and 5 m/s (as shown) from 090°T 156

68. Model output of wind speed and wind direction profiles, 5 km seaward from the coast, for 1500, 1700 and 1900 with V_g's of 3 m/s and 5 m/s (as shown) from 040°T 157

LIST OF SYMBOLS

C_p	specific heat at constant pressure
f	Coriolis parameter
g	acceleration due to gravity
h	surface layer height
K	eddy coefficient
%	eddy thermal diffusivity
K_m	eddy viscosity
k	von Karman's constant
L	Obukhov length
P	atmospheric pressure
R	gas constant for air
Ri	Richardson number [$\equiv (g/\overline{\theta})(\partial\overline{\theta}/\partial z)\,\vert\,(\partial\overline{U}/\partial z)^2$]
T	temperature
u, v, w	wind components; primed quantities refer to sea breeze disturbance components
U	$= (u^2 + v^2)^{1/2}$
u_*	friction velocity [$\equiv (\tau/\rho)^{1/2}$]
z_0	roughness length
Δz	distance from surface layer to first upper level grid point of the model
α	angle between positive x-axis (north) and the wind direction
ζ	dimensionless height [$\equiv z/L$]
θ	potential temperature

ACKNOWLEDGMENTS

I wish to express my sincere gratitude to my advisor, Professor. Franklin 1. Badgley, for his generous gift of time and insight. In addition, I want to thank the other reading committee members, Joost A. Businger and Conway B. Leovy, for their careful perusal of the original draft and helpful suggestions for its improvement. The other members of the advisory committee, Robert S. Crosson and Robert E. Street, were instrumental in acquainting me with techniques of spectral analysis and numerical analysis which were necessary tools in this study. .

I wish to thank Roger Colony of the Polar Science Center for his expert advice on mathematical modeling techniques. I also want to thank Miles McPhee and Rich Hall, both of the Polar Science Center, for valuable advice and for just listening.

I also want to express my appreciation to Mike Reynolds, Al Macklin and Bob Charnell of the Pacific Marine Environmental Lab for their instructions on using and the loan of equipment. A special thanks is in order to Gunter Weller of the University"of Alaska for his aid in procuring equipment and grant money for this study..

The funding for data collection and computer modeling was made possible through the Outer Continental Shelf Project Office (part of the U.S. Department of the Interior) in Fairbanks, Alaska, under contract #03-5-022-671013.

Peggy Dent and Carolynn Padgett deserve mention for their fine cooperation and careful work in typing the first and final drafts of

this dissertation.

My deepest gratitude goes to my wife Carolyn, who stuck with me through almost five years of emotional troughs and financial hardship, to make me feel that this work was worthwhile-

Finally, I want to thank Victor "Scotty" Roxburgh for saving my Pingok Island experiment,

I. INTRODUCTION

1.1 Background

Sea breezes are common mesoscale features in coastal areas around the world. The intensity, duration, and extent of the sea breeze circulation are mainly determined by horizontal gradients in the amount of heat supplied by the earth's surface to the atmosphere (e.g., Defant, 1951 and Estoque, 1961) and by the large-scale synoptic conditions (Estoque, 1962). The horizontal gradient in surface heating is caused by a difference in the response of land and water to solar radiation. For equal amounts of incoming radiation the surface temperature of the water will be less than land because more energy is used for evaporation and the rest of the energy reaches greater depths due to water turbulence and water transparency. Surprisingly, though the heat capacity of water (1 cal g^{-1} $°C^{-1}$) is greater than land (usually .6 cal g^{-1} $°C^{-1}$ or less), the thermal conductivity of water ($1,3 \times 10^{-3}$ cal cm^{-1} sec^{-1} $°C^{-1}$) is less than land (5×10^{-3} cal cm^{-1} see-l $°C^{-1}$ for wet soil), therefore without the earlier-mentioned factors, the water surface and land surface would not exhibit a significant horizontal thermal gradient (Yoshino, 1975).

Coastal lands warming in the morning cause an increased thickness of isobaric layers over land and a downward sloping upper pressure surface from land to sea. The resultant horizontal pressure gradient force accelerates air from land to sea aloft. This air movement causes an increase in sea level pressure offshore (mass excess) and a decrease onshore (mass defect). The result is a sea level pressure gradient force that accelerates

air from sea to land. This circulation is reversed at night in temperate and tropical latitudes when the land-sea temperature differential reverses and the land becomes cooler than the ocean.

Using Kelvinrs circulation theorem to consider a simplified version of the problem, Holton (1972) shows there is an acceleration in surface wind at a land-sea interface

$$\frac{d\bar{v}}{dt} = \frac{R \ln\left(\frac{P_0}{P_1}\right)(\bar{T}_2-\bar{T}_1)}{2(h+L)} \tag{1.01}$$

where R is the gas constant, T_1 and T_2 are air temperatures over land and sea, respectively, L is the sea breeze cell dimension normal to the coast, h is the cell height, P. is the surface atmospheric pressure, and P_1 is the atmospheric pressure at the cell top (see Figure 1). For more temperate latitudes P_1 is usually 100 mb less than in the arctic. However, the AT value is often one-half that of the arctic regions, resulting in comparable magnitudes for the acceleration term for both regions, demonstrating the feasibility of an arctic sea breeze. Typical values for the arctic coast can be P_1 = 900 mb, P_0 = 1000 mb, $2'_2 - T_1$ = 20°C, h = 1000 m and L = 40 km.

The sea breeze cell is usually contained in the planetary boundary layer and is therefore strongly influenced by eddy viscosity, surface roughness, and conduction processes. Yet its horizontal extent is large enough that the earth's rotation and the synoptic (large-scale) pressure gradient cannot be ignored (Walsh, 1974).

Previous investigators (Cotton, et al., 1976) have found that the synoptic environment' is altered by the sea breeze through

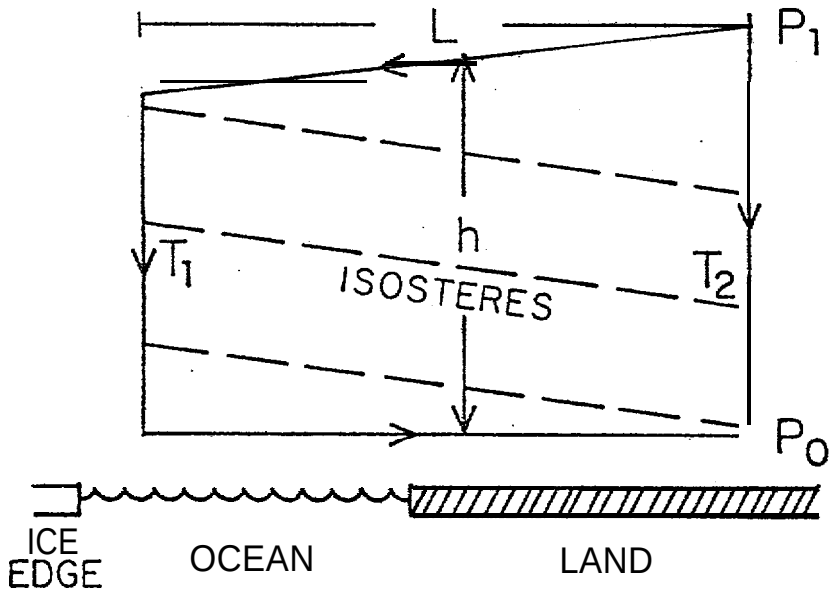

Circulation Theorem in a Plane
⊥ to Coast

Fig. 1. Geometry for application of the circulation theorem to the sea breeze problem.

(1) perturbing the vertical thermodynamic profile, (2) increasing the depth of the planetary boundary layer, (3) inducing greater surface fluxes of momentum, heat, and moisture, (4) changing the vertical shear of the horizontal wind in the lower levels of the atmosphere, and (5) developing intense, horizontal convergence regions of heat, moisture and momentum.

Two papers that give insight into sea breeze and synoptic wind field interactions in mid-latitudes are those of Schroeder, et al. (1967, with a literature review), and Hawkins (1977).

1.2 Previous Work

While sea breeze work in the tropics and mid-latitudes has been extensive and of both a theoretical and experimental nature, studies in the arctic have been limited by scarcity of data, expensive logistics, and lack of interest. The discovery and development of the Prudhoe oil fields (mid-sixties) has led to increased shipping and increased probability of permanent man-made and natural offshore drilling platforms in the Beaufort Sea. Since the nearshore ocean current flow along the Alaskan Arctic Coast is primarily wind driven, an interest in caostal meteorology with direct application to oil spill trajectories in lagoons and embayments has grown from the necessity to provide comprehensive environmental impact statements to the U.S. Department of the Interior. "

Inherent in higher latitude studies are temperature inversions which promote a stably stratified atmosphere. Shaposhnikova, et al. (.1968) discussed the problem of a non-stationary, nonlinear breeze in a stable atmospher. They criticized Estoque's model (1961) for violation of mass conservation because he modified the incompressible form of the continuity

equation. They also noted the generally weak reverse (land to sea) flow aloft depicted in previous theoretical models (including Estoque's). Their paper was not an improvement, however, since they omitted a synoptic wind field, used a constant eddy viscosity, neglected the Coriolis force, used a lapse rate greater than Estoque (1962) and. utilized an awkward temperature equation by not writing it in potential temperature form. Their results were similar to Estoque's case #6 (1962) (with no synopitc wind and isothermal layer from 0 to 1 km) in that both had a significant reverse flow aloft.

The farthest north experimental sea breeze study found in the literature was done by Rossi (1957) near Ilmala, Finland, on the shores of the Baltic Sea (60°N). Nordlund (1971) did a theoretical study using Rossi's data to compare with his numerical model. The model was identical to Estoque's (1961) , except for use of a linear grid in the x-direction. Nordlund used measured local conditions to simulate his heating function, lapse rate, and land-sea temperature difference. The model became unstable after 12 hours due to computational difficulties probably related to time step size and lack of parameterization of subgrid-scale diffusion.

Moritz (1977), after investigating historical data in January and July from Pt. Barrow, Alaska, discovered two significant facts. The first was that calculated geostrophic wind speeds in January were 40% greater on the average than those calculated for July, but the observed surface wind speeds from both months were approximately the same. The second was that calculated geostrophic wind speeds and direction frequencies for July were similar for winds with east and west components, but

measured surface east winds had greater magnitudes and frequency than west winds. He suggests (without proof) that the surface temperature contrasts across the boundary along Alaska's north coast produce an added pressure gradient component that is not recorded by the existing synoptic observation network. Moritz thought the pressure gradient produced a sea breeze circulation with a larger alongshore component (from the east in this case) than mid-latitude breezes because of almost continuous solar irradience, 33% greater Coriolis force (70°N), and the great horizontal extent of the coastline. The last reason seems questionable since it cannot be a condition solely confined to the Arctic and coastline irregularities exist of mesoscale proportion.

Walsh (1977) examined data from three summertime flights of the NCAR (National Center for Atmospheric Research) Electra across the Alaskan north slope. The land-sea temperature contrast was investigated as a source of local thermal circulation. Unfortunately, the three flights were chosen on days with synoptic winds unfavorable to sea breeze formation. However, useful data on the coastal temperature contrast and inland temperatures were collected and served as both input and a check on the model in this study.

Walsh mentioned a linearized sea breeze occurrence criterion of the form:

$$V_g^2 < \beta(\Delta T)_{MAX}$$

where V_g is the offshore component of. the gradient wind, $(\Delta T)_{MAX}$ is the maximum land-sea temperature difference observed during the day, and β is an empirical constant (Walsh, 1974) $\simeq 1.5\ m^2s^{-2}C^{-1}$. New data, and

model results examined in this study indicate that the criterion may underestimate the value of V_g needed to preclude sea breeze occurrence on shore. Also, the data and model show that the surface wind direction 0 to 5 km at sea may still be dominated by the sea breeze though limited effects are seen on land.

The summertime land-sea temperature difference has a synoptic scale effect which is important since the sea breeze is a function of the prevailing synoptic situation. A semi-permanent arctic front (distinct from the year-round polar front) caused solely by the thermal contrast along the northern shores of Alaska, Siberia, and Canada has been described by Dzerdzeeskii (1945). Reed and Kunkel (1960), however, feel that interaction of orographic features and the general circulation play equally important roles in the existence and position of the front.

1.3 Study Area

The study area is contained within the latitudes 69°N-74°N and longitudes 143°W-157°W. In this way, buoy installations (1976 only) within the ice pack, NWS (National Weather Service) stations at Barrow and Barter Island, DEW (Distant Early Warning) sites at Oliktok and Lonely (1976 only) and camps at Umiat and Happy Valley (1976 only) could be used as surface pressure data sources to model the synoptic wind field. The degree of influence exerted on surface atmospheric pressure measurements by the sea breeze mesoscale pressure perturbation is discussed in Chapter II, Section 2.3 for the above-mentioned stations.

Figure 2 shows the relative positions of the pressure stations (P)

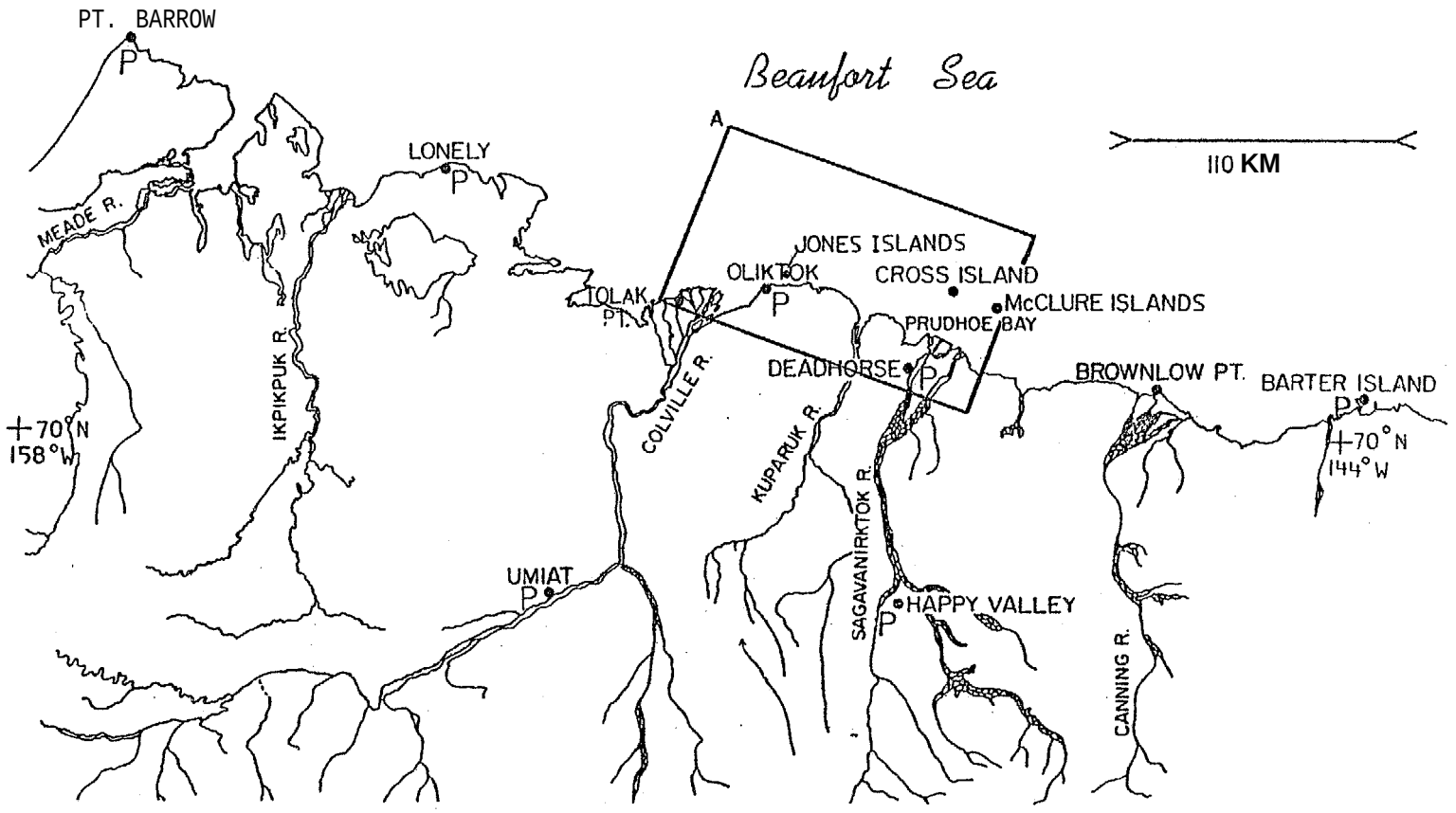

Fig. 2. Locations of atmospheric pressure stations (P) within the land-based grid for 1976, 1977 and 1978 and primary study area (A). Stations at Lonely and Happy Valley were used in 1976 only.

within the land-based grid for August 1976 and 1977. The primary study area is contained within the rectangle A and shown in more detail in Figure 3. The W's and WA's indicate the locations of portable weather stations and small airport weather stations, respectively.

The experimental work for this project was conducted at two main field locations, Prudhoe Bay, Alaska (acoustic sounder data) in August 1976 and Pingok Island, Alaska (radiosondes, and pilot balloon data) in August 1977 (see Figure 3). These coastal locations exist in an area where the summer tundra-ocean thermal contrast remains positive (land always warmer than water) despite 15°C drops in land temperature over the short arctic summer nights (Kozo, 1978 and Moritz, 1977). This unique feature of the Alaskan Arctic Coast means that a summer sea breeze will not be followed by a land breeze.

1.4 Goals and Motivation

The primary goal of this study is to model the interaction of the arctic sea breeze with the prevailing synoptic wind field and to assess the degree of influence that this mesoscale thermally induced feature exhibits on surface winds in the Beaufort Sea coastal zone. This study proceeded at its inception to document a phenomenon, previously considered rare at extreme northern latitudes. (Defant, 1951). With increased experimental evidence, the novelty aspect diminished and emphasis changed to consideration of the utility of the findings. Study data, recently compiled historical data, and supplemental model predictions indicate that the breeze can dominate the surface wind direction at least 25% of the time during the arctic summer. This is true of a zone at least 20

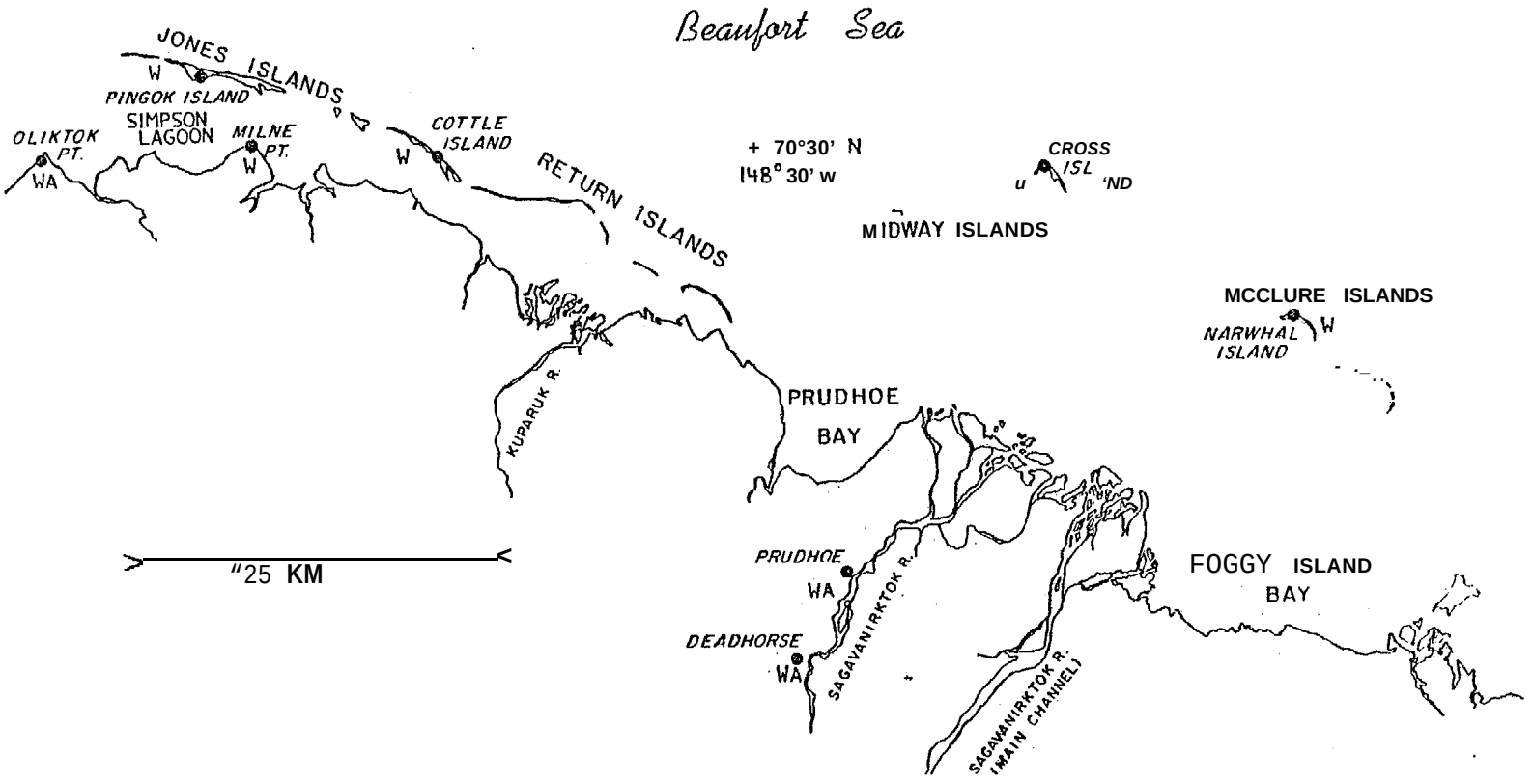

Fig. 3. Primary study area with (W) and (WA) representing mechanical weather stations and airport weather stations, respectively.

km landward and 20 km seaward of the coast.

The numerical model used in this study can, by variation of input parameters, be used to investigate the degree of influence exerted by the land-sea thermal gradient, the planetary boundary layer inversion strength, the eddy flux (heat and momentum) magnitude and vertical variation, and the large-scale wind field velocity. These physical influences determine the resultant surface wind which can be used to" estimate the wind-driven ocean current velocities in the coastal zone. In turn, the intensity of upwelling, and lagoon flushing can be predicted for major biologically active areas.

1.5 Synopsis

Chapter 2 contains environmental data which was used as input to the theoretical model and as the physical evidence both circumstantial and direct for the existence of an arctic sea breeze. Data were collected in August 1976 and 1977 when coastal watters were essentially ice free (except for small floes).

Chapter 3 is a description of the theoretical model for the sea breeze with emphasis on the planetary boundary layer equations, relevant departures from earlier models such as Estoque's original model (1961, the basis for many subsequent studies, e.g., Moroz, 1967; Krishna, 1968; Delage and Taylor, 1970; Neumann and Mahrer, 1971; Nordlund, 1971; and Sheih and Moroz, 1975) and techniques for incorporation of arctic environmental input parameters.

In Chapter 4, model output is compared to the measured wind data from days when a thermally induced non-stationary mesoscale effect is apparent.

Chapter 5 discusses the main physical factors which determine the existence, the relative strength, the degree of interaction with prevailing synoptic winds, the rotation rate, and the frontal advancement of the arctic sea breeze'.

Conclusions and recommendations are presented in Chapter 6.

II. ENVIRONMENTAL DATA

2.1 Continuously Recording Equipment

To supplement our land-based large-scale pressure grid data (1976), inputs from two ocean buoys in the polar ice pack remaining from the AIDJEX (Arctic Ice Dynamics Joint Experiment--University of Washington) grid were utilized. These pressure and position data buoys depended on the Nimbus 6 satellite RAMS (Random Access Measurement System) for tracking and data relay. Accuracy of positioning was ± 2 km (Martin and Gillespie, 1978) and pressure was ± .25 mb (Martin and Clarke, 1978) with sampling intervals of three hours (8 satellite orbits/day).

The land-based pressure grid used temperature compensated Weathermeasure B211 microbarographs which recorded continuously on charts with a seven-day drum rotation and had spring wound drives. They operated between surface pressures of 945 mb to 1045 mb with an accuracy of ± .15% of range. The stations using these microbarographs were serviced and calibrated weekly with two Negretti and Zambra precision digital barometers. Comparisons with the digital barometers have shown the experimental accuracy in our data range to be ± .25 mb.

The 10 meter wind velocity at the main experimental site (Pingok Island) in August 1977 was obtained by a generator-powered Climet Cl-25 wind measurement system with an accuracy of 1% for wind speed (threshold .27 m/s) and ± 3° for wind direction (threshold .34 m/s), recording one-minute averages of the measured data in ten-minute intervals.

The 10 meter wind velocity and temperature were recorded at other

sites by MRI (Meteorology Research, Inc.) Mechanical Weather Stations (Model 1071). They were battery wound systems set for 30-day operations with a clock accuracy of ± 60 seconds per 24 hours. The wind direction (damped aluminum vane) has an accuracy of ± 1% of full scale (3600). Wind run (fast response aluminum cups with a threshold of .34 m/s) which is converted to hourly wind speed is ± 2% of the measured value. The temperature is a shielded bimetal coil sensor with an accuracy of ± 1.7°C.

Solar radiation was measured with a Belfort Pyrheliograph Model 5-3850. The instrument chart drive is spring-wound and set for 7-day drum rotation. The accuracy is ± 5% over a total range. of .21 Wcm^{-2}. The pyrheliograph dome has a 90% transmission coefficient for all wavelengths from .36 to 2.0 microns.

A less conventional continuous recording meteorological instrument used in August 1976 near Prudhoe Bay (20 km inland from the coast) was the generator-powered acoustic sounder (also known as sodar and acoustic radar) . It is an active ranging sensor using sound as the propagating energy wave.

This sounder was the NOAA (National Oceanic and Atmospheric Administration) Mark VII portable Acoustic Echo Sounder and consisted of a central control unit, power amplifier, facsimile recorder, and 4-foot parabolic reflector antenna. It theoretically can receive echoes from atmospheric layers up to a height of 1360 m, and was operated in the monostatic mode, with receiving and transmitting antennas collocated. The monostatic mode records backscatter due to small-scale atmospheric fluctuations. Investigators such as Reynolds (1970), Wyckoff, et al.

(1973) and Holmgren, et al. (1974) have used the fixed, vertically pointing sounder to monitor inversion height and planetary boundary layer structure. The sounder can also observe the roots of convection near the earth's surface (Hall et al., 1975). The 1976 data on inversion height and convective plumes serves as an output check on the sea breeze model by indicating height fluctuations in the planetary boundary layer (capped by the inversion), and by indicating the type of transition of the boundary layer from one of static stability at sunrise to one approaching free convection by noon. Since the data from the sounder had no coincident radiosonde or pilot balloon (both discussed below) information, accuracy limits are not quoted on actual inversion heights. A comparison of the sounder inversion heights to those derived from more conventional noncontinuous atmospheric sounding systems can be found in Wyckoff, et al. (1973) and Carsey (1975).

Sources of supplementary continuous data were airfield weather stations near Deadhorse, Arco Camp (Prudhoe), Oliktok, Lonely, Umiat, Happy Valley, Barter Island, and Barrow. These data were of varying quality but valuable extensions to the unavoidably small area experimental network. The last two sources are used as direct input to NWS {National Weather Service) daily synoptic charts.

2.2 Atmospheric Sounding and Wind Profiling Equipment

At Pingok Island, the main experimental *site* for August 1977, radiosonde information was collected daily (except during a six-day storm) to monitor the vertical temperature and humidity structure of the atmosphere. The radiosonde is a battery-powered expendable scientific instrument

that transmits radio signals during balloon-borne ascent, which when properly interpreted give a continuous record of pressure, temperature, and humidity of the atmosphere through which it passes. The sensing elements have ranges as follows: barometric pressure from 1060 mb to 5 rob., temperature from 50"C to 90"C and relative humidity from 15% to 90%. The frequency of the transmitter may be adjusted from 400 to 406 megahertz. The receiver (403 megahertz) was made by Borders Electronics and the recorder was made by Leeds and Northrup. Both were standard portable U.S. Weather Service units, The radiosondes were made by Bendix Corporation (older models) and VIZ Corporation (newer weather service models).

The launch balloons (100 g) were underinflated to decrease their rise rate and thereby increase the informational detail in the atmosphere's lowest 1000 meters during the radiosonde ascent. It was discovered that radiosonde ascents could also be made by substituting two smaller capacity (30 g) standard pilot balloons (see below) for one 100 g balloon with interesting results. If one pilot balloon was underinflated and one slightly overinflated, rupture of the latter balloon would occur on ascent at approximately 3000 meters. The underinflated balloon would act as a braking mechanism on descent and two atmospheric soundings could be obtained with one launch, well within the two-hour battery life limits of the radiosonde transmitter system.

The atmospheric soundings were used as input to the computer model to establish the large-scale vertical temperature structure and as a check on the model output at various time periods during the sea breeze evolution. Accuracy limits on temperature are ± .5°C with a lag

coefficient of 2.7 seconds for a balloon rise rate of ,3 m/s (Hart et al., 1977) . Typical rise rates for this study were 1.5 m/s. Assuming the temperature sensor's (thermistor) lag coefficient to be dependent on ventilations the following relationship applies:

$$\lambda(\text{lag coefficient}) = Kv^{-1/2}$$

where K is the sensor constant and v is the velocity in meters/second (Middleton and Spilhaus, 1953). The new λ increased to 3.9 seconds. However, for a maximum temperature change of 10°C in 200 m (typical of the surface-based inversion data measured on Pingok Island) the temperature is still within the previously mentioned accuracy limits. The accuracy limits on pressure were ± 3 mb of the actual pressure (Middleton and Spilhaus, 1953). These pressure limits are considered adequate for this study and corresponding altitudes have been checked by simultaneous theodolite tracking when possible (fog conditions were often present).

Two theodolites were used to track standard meteorological pilot balloons (August 1977, Pingok Island) and thus determine their position at prescribed time periods (20- to 30-second intervals). In this way no assumptions had to be made about ascent rates or vertical currents. Each of two theodolite readings consisted of an elevation and azimuth angle which together defined a ray from the theodolite to the balloon. The method for calculating the balloon position using all four of the theodolite angles to make an optimum estimate is that of Thyer (1961}. It also does not fail when the balloon is near or over the base line between the two theodolites. The balloon position data are converted to horizontal

wind velocity versus height, which results in a fair determination of the wind vector turning induced in the planetary boundary layer when compared to inversion heights measured by the radiosonde system. This technique is considered more accurate than earlier double theodolite methods which claim a maximum 10% error (Singer, 1953) on the horizontal wind velocities. Middleton and Spilhaus (1953) list accuracies of ± 2° in true wind direction and ± 1 m/s in speed for altitudes less than 5 km. This tracking was performed daily when visibility permitted and periodically during the day if sea breeze conditions seemed probable.

A source of twice daily atmospheric soundings which included temperature, humidity, and wind velocity versus height data was the Barter Island weather station. These data were used to supplement our own and as a check on conditions along the coast.

2.3 Geostrophic Wind Data

Surface atmospheric pressure gradients can be used to determine the geostrophic wind which approximates the free stream flow immediately above the planetary boundary layer (Brown, et al., 1974).

The equation for atmospheric flow (synoptic scale) is:

$$\frac{\partial \underset{\sim}{V}}{\partial t} + \underset{\sim}{V} \cdot \nabla \underset{\sim}{V} + f(k \times V) + \frac{\nabla P}{\rho} = 0 \qquad (2.01)$$

The last two terms are generally much larger than the first two terms and yield the geostrophic velocity with flow parallel to the isobars.

Several complicating factors can occur to invalidate the geostrophic approximation. One of these, the thermal wind, results when the pressure

gradient at the surface differs significantly from that at the free stream level due to strong horizontal gradients in temperature. Another factor is represented by the first term above and becomes important in synoptically short time scales during accelerating conditions such as frontal passages (isallobaric effect) when large wind changes occur in less than five hours. A last factor which may be significant is the second term above. It becomes large when strong curvature of flow exists (radius of curvature of isobars less than 300 km, in cases where isobars can be used to estimate air parcel trajectories) and appears as a centrifugal term (Holton, 1972) added to the geostrophic terms resulting in the gradient wind approximation. The curvature calculation approximates air trajectories by isobars which should only be done if the large-scale system is not moving (steady state). In the examples to follow, this approximation is made in all cases. Therefore, the gradient wind approximation may be no better than the geostrophic approximation. Since the curvature effect is a correction to the speed rather than direction at a specific time, sea breeze existence is still established for the examples shown.

All or any of the above three considerations may be important during sea breeze conditions in the arctic and the data were examined with these in mind.

The first approximation to the geostrophic wind field was obtained from NWS U.S. National Weather Service twice-daily (0000 and 1200 GMT) surface pressure maps for the northern hemisphere. Surface "pressure data from Barrow and Barter Island (520 km apart) are the only inputs for the Alaskan Arctic Coast. There were usually no pressure data inputs from

the Beaufort Sea (except summer 1976 with remnant buoys from AIDJEX) to the north and no pressure data inputs to the south until below the Brooks Range. Therefore, geostrophic wind velocities determined from isobaric direction and spacing on the maps are questionable for intermediate points such as Oliktok or Pingok Island.

To increase the resolution of the existing NWS pressure grid (1976) a system of microbarograph pressure stations at DEW (Distant Early Warning) sites Lonely and Oliktok, and at the air control towers of Umiat, Happy Valley and Deadhorse was created. Coupled to these were the already existing surface pressure inputs from the Barter Island and Barrow NWS stations, and pressure data from two AIDJEX buoys (mentioned above). These nine data points provided the basic input to a TDLSF (two-dimensional least squares fit) numerical tecnique which produced a higher resolution pressure map for the study area.

Though direct evidence is limited, it can be stated that the mesoscale pressure perturbation caused by the sea breeze had limited effect on the surface pressure data from the two AIDJEX buoy stations (more than 100 km offshore, 1976) and the inland stations of Umiat and Happy Valley (both approximately 100 km inland). Surface wind direction data from Hufford (1977) show that sea breeze influence does not reach 64 km offshore. Rotational spectra (see Chapter II, Section 2.5) show that sea breeze influence has diminished in a horizontal distance of 20 km offshore. O'Brien and Pillsbury (1974) state that sea breeze circulation is limited to 30 km off the Oregon Coast. Simpson, et al. (1977) from 900 total days of sea breeze observations over 12 years on the south coast of England indicates that less than 1% reached 85 km inland.

Rossi's (1957) experimental study of sea breezes on the south coast of Finland indicated a landward extent of 24 km. Finally, model output (see Chapter IV) indicates that sea breeze effects are minimal beyond 50 km to either side of the coastline.

The pressure data collected at the coastal stations of Barter Island, Pt. Barrow, Oliktok, Lonely and Deadhorse are certainly within the zone of sea breeze influence. Data from Defant (1951, Baltic Sea) indicate that coastal stations may exhibit a maximum reduction in surface pressure relative to a seaward station of 1 mb for the hours from 1300 to 2100 LST on sea breeze days. Limited data from this study (Kozo, 1978) indicate a maximum .5 mb pressure reduction at Oliktok on days when sea breezes occurred.

The TDLSF (cubic) technique was used for cases with 0 mb, .5 mb and 1 mb addedto the surface pressures (to simulate removal of the sea breeze induced pressure effect) from the five above-mentioned coastal stations at 1500 ADST. The maximum change (over the 0 pressure perturbation case) in computed geostrophic wind direction was 17° and the maximum change in wind speed was 20% for the three sea breeze days in 1976 that are discussed in this section. Since this study is concerned with establishing sea breeze existence and ability to influence the surface wind direction, the computed geostrophic winds in all cases were still from the southwest quadrant and therefore sea breeze induced pressure perturbations do not detract from the arguments to follow.

The basic technique which is used when observations are limited in number and are irregularly distributed over a mapping area is explained in Krumbein (1959). In least squares techniques for one-dimensional

cases, deviations (residuals) from

$$y = a + bx \quad \text{(straight line)}$$
$$y = a + bx + cx^2 \quad \text{(parabola)} \qquad (2.02)$$
$$y = a + bx + cx^2 + dx^3 \quad \text{(cubic)}$$

and similar higher order curves are minimized to produce a best fit by varying a, b, c, and d, which are constants. Pressure is a function of latitude and longitude, requiring extension of the least squares method to two dimensions. Since the study area size usually precludes the simultaneous existence of more than one high and one low, a two-dimensional cubic fit is the maximum degree of variation used to resolve the pressure field. An exception to this occurs when sharp frontal zones exhibiting discontinuities exist. The two-dimensional cubic polynomial to be solved is

$$\text{Pressure} \equiv Z(x,y) = a + bx + cy + dx^2 + exy + fy^2 + gx^3 + hx^2y + jxy^2 + ky^3 \qquad (2.03)$$

Constants a through k can be computed from a 10×10 matrix, where x and y are the longitdue and latitude, respectively. For the TDLSF the above nine real data inputs were blended with eight weighted (5%) boundary inputs obtained from existing NWS isobaric charts. At prescribed latitude and longitude points on a uniform grid a pressure value can be calculated using the derived constants a through k. The resultant pressure field can be contoured and geostrophic velocities (partial derivatives of the above polynomial with respect to x and y are used to calculate them) can be obtained at field data sites where 10-meter winds were measured. The

resultant simultaneous comparisons can be used as an estimate of the total boundary layer turning during sea breeze and non-sea breeze influenced periods.

Figures 4, 6, and 8 are portions of NWS surface pressure maps for days (August 1976) that exhibit definite evidence that surface winds are influenced by sea breeze forcing. The inset in each of these figures shows the orientation of the study area to the Alaskan coastline, with both drawn to the map scale. The bounds of the higher resolution TDLSF plots are indicated by the dash-lined study area (on the map) with an "arrowhead" indicating the Oliktok-Pingok Island-Cottle Island position. Figures 5, 7, and 9 are the actual TDLSF plots. The 000 GMT (Greenwich Mean Time) corresponds to 1500 ADST (Alaska Daylight Savings Time) on the previous day. The surface winds at the five indicated stations are shown using standard NWS notation for the wind velocity: arrows (—┤, short slash ≡ 3 to 7 knots; —┤, long slash ≡ 8 to 12 knots). Knots multiplied by .5 are roughly equal to meters/second.

The calculated geostrophic wind for Cottle Island on August 16, 1976 (000 GMT) was .93 m/s from 188.5°T with a measured surface wind (10 m) of 5.28 m/s from 90°T. Figures 4 and 5 chow a weak pressure gradient in the Cottle Island area. The surface wind data did not indicate large speed changes 12 hours prior' to the above time and none occurred until six hours later. The NWS chart 12 hours earlier (not shown) did not indicate rapid changes, but the 1200 GMT August 16, 1976 chart showed a stationary front along the coast. However, the isallobaric effect was considered negligible for the time period around 000 GMT. The atmospheric sounding data from Barter Island (250 km to the

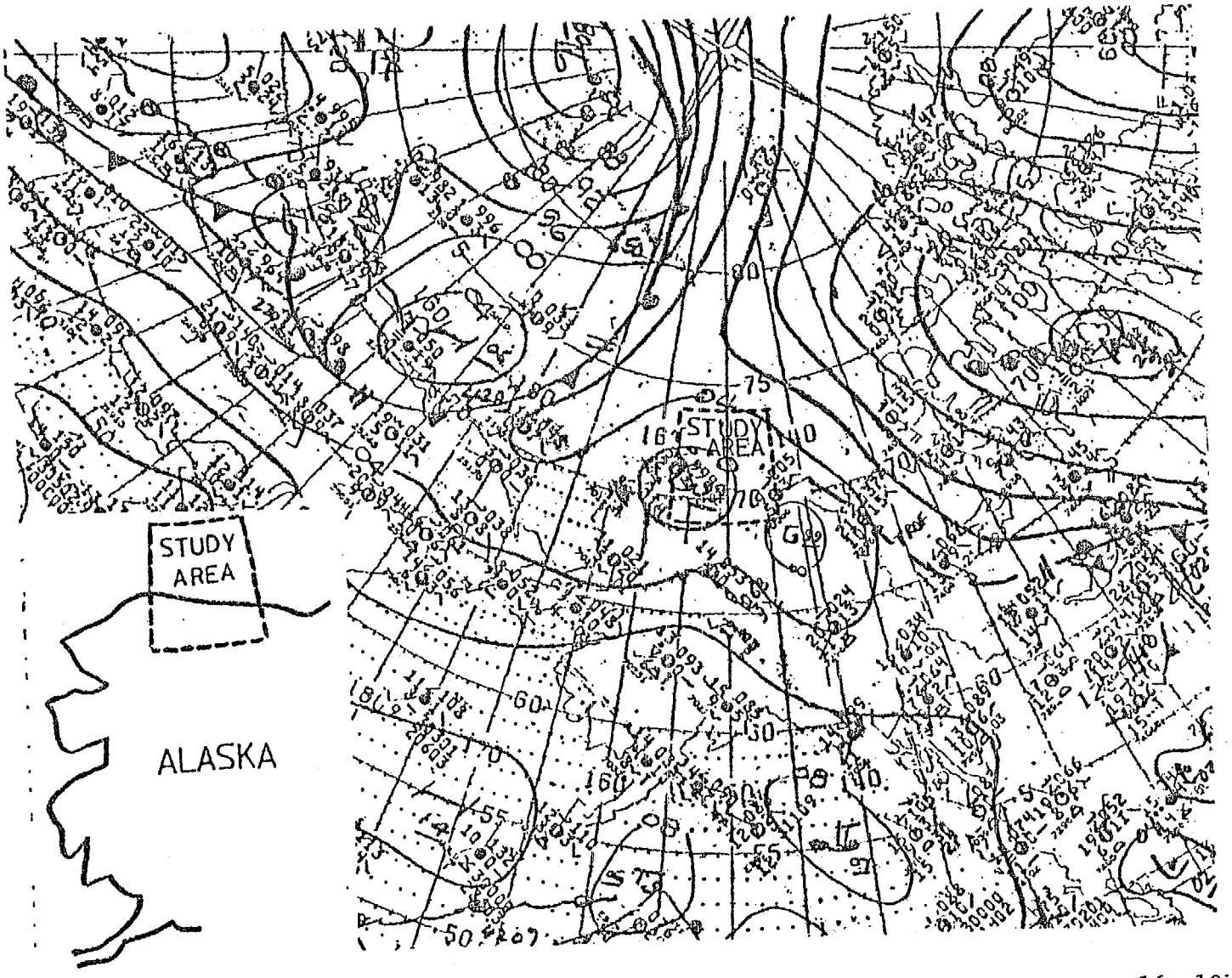

Fig. 4. National Weather Service (NWS) surface pressure chart for August 16, 19:6 (000 GMT). The inset shows the orientation of the study area to the Alaskan coastline.

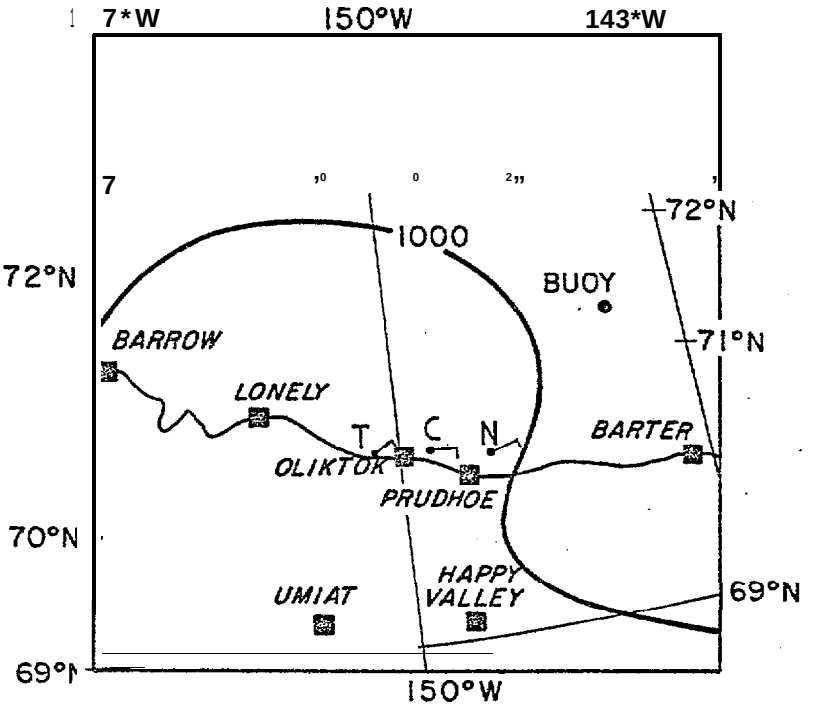

Fig. 5. Two-dimensional least squares fit (TDLSF) to surface pressure network on August 16, 1976 (000 GMT). C, N, T represent actual surface wind measurements from Cottle Island, Narwhal Island and Tolaktovut Point, respectively. (Pressure contours - ME)

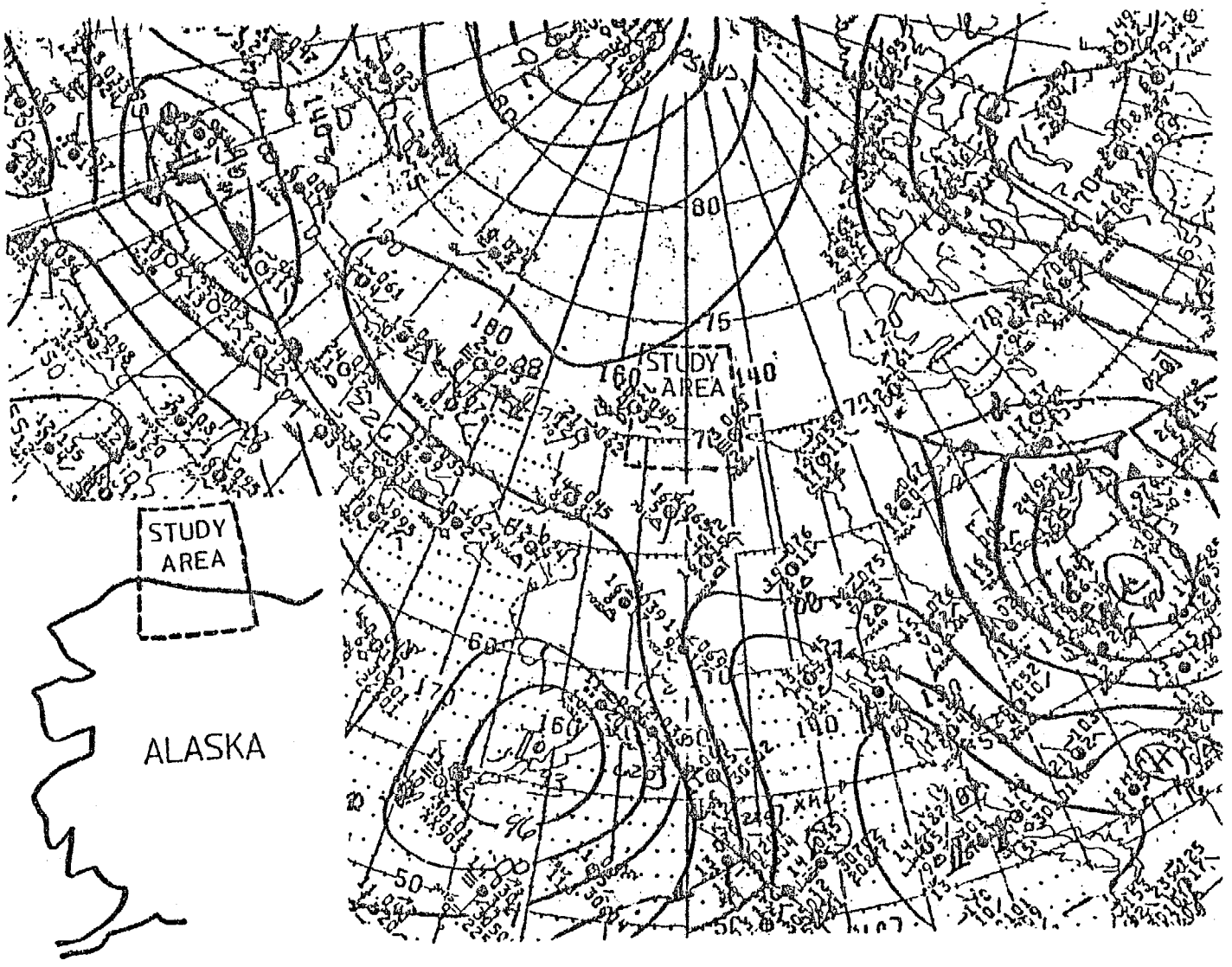

Fig. 6. Two-dimensional least squares fit (TDLSF) to surface pressure network on August 16, 1976 (000 GMT). The inset shows the orientation of the study area to the Alaskan coastline.

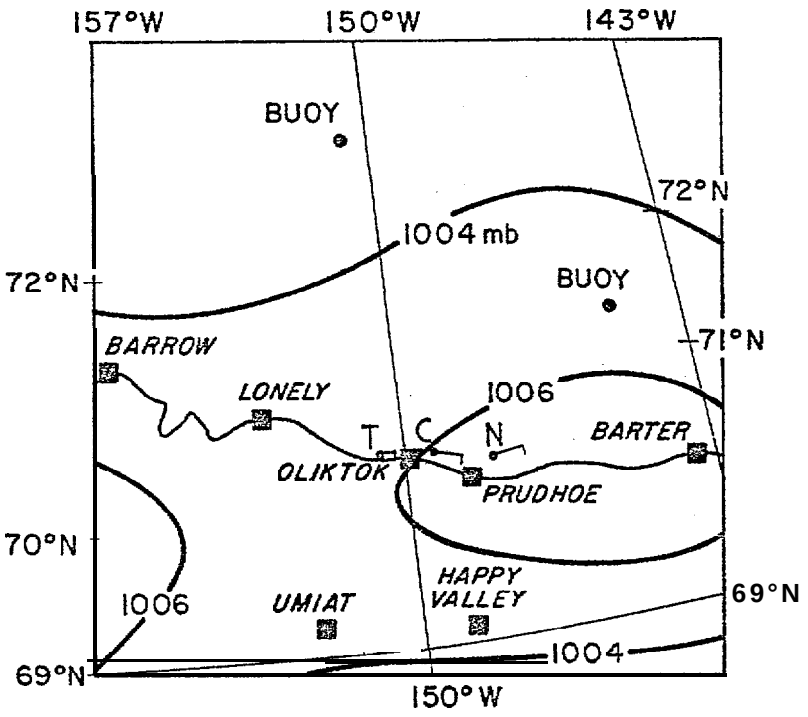

Fig. 7. TDLSF to surface pressure network on August 18, 1976 (000 GMT). Designations and scale are the same as in Figure 5. (Pressure contours - MB)

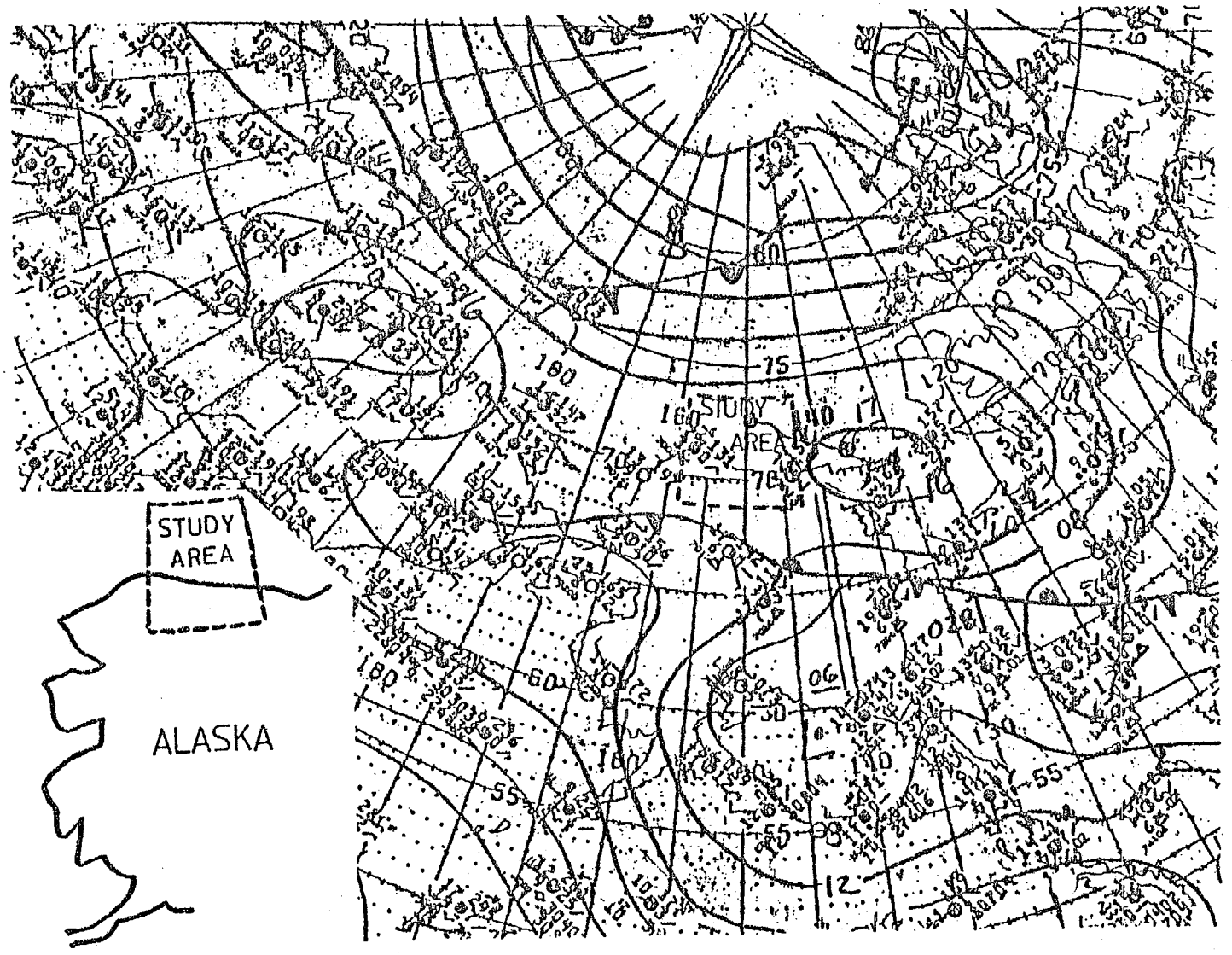

Fig. 8. NWS surface pressure chart for August 21, 1976 (000 GMT). The inset shows the orientation of the study area to the Alaskan coastline.

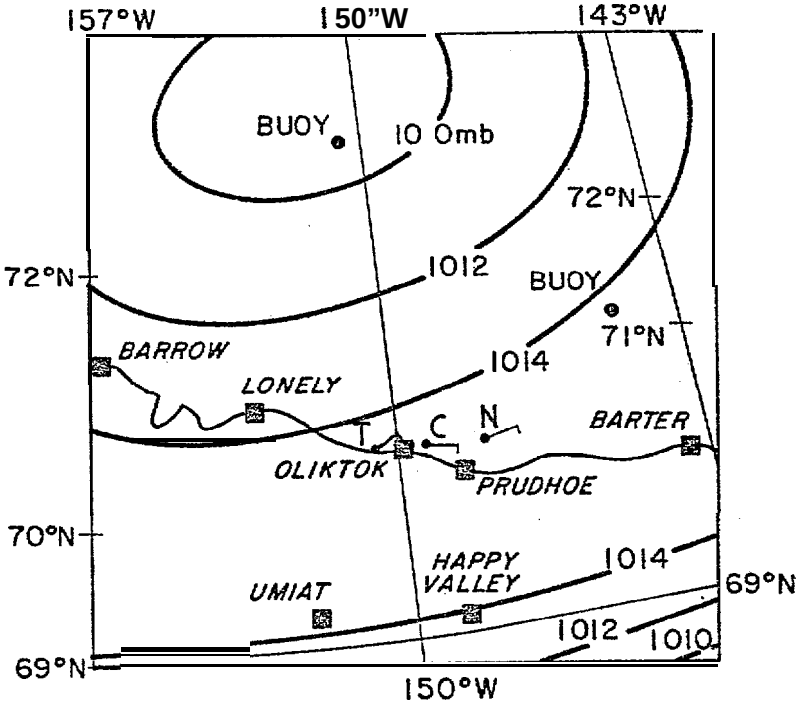

Fig. 9. TDLSF to surface pressure network on August 21, 1976 {000 GMT). Designations and scale are the same as in Figure 5. (Pressure contours - MB)

east) showed a wind of 3 m/s from 147°T between altitudes of 438 m and 899 m. The vertical shear of the wind above the inversion in the free stream (thermal wind) was negligible. The isobaric radius of curvature (south of Cottle Island) as seen in Figure 5 is approximately equal to +155 km (approximates the radius of trajectory) for cyclonic flow. Form Holton (1972) the gradient wind velocity can be calculated by solving

$$\frac{V^2}{R} + fV - V_g = 0 \tag{2.04}$$

for Vwith R ≡ radius of curvature and V_g ≡ geostrophic velocity. The solution by using the quadratic equation requires the -i- root and results in $|V|$ = .89 m/s. The geostrophic wind speed was an overestimate of the gradient wind by 4% in the area near the curved isobar. The V above the boundary layer is small and should allow a sea breeze to develop. The land-sea temperature difference from Prudhoe Airport to the coast (15 km) was 15.5°C.

The calculated geostrophic wind for Cottle Island on August 18, 1976 (000 GMT) was 2.14 m/s from 219.2°T with a measured surface wind (10 m) of 3.10 m/s from 105"T. Both Figures 6 and 7 show a weak synoptic wind field. The surface wind data did not show large wind speed changes occurring during the time period in question and the NWS charts ± 12 hours from 000 GMT did not indicate rapidly changing conditions. Therefore, despite a stationary front appearing on the charts near the study area, the isallobaric effect (mentioned above) is not significant. Atmospheric sounding data from Barter Island (250 km to the east) showed a wind of 2.0 m/s from 240°T between 470 m and 900 m, which agrees

closely with the above calculated value. This is evidence that the thermal wind on this scale is also negligible. The isobaric curvature (approximates the trajectory curvature) as seen in Figure 7 results in a radius of curvature equal to roughly -74 km for anticyclonic flow. The solution of equation 2.04 requires the negative root for a normal high and results in $|V|$ = 3.06 m/s. The geostrophic wind speed underestimated the gradient wind speed by 43% in the area near the curved isobar (less error near Cottle Island). In this case the V above the boundary layer is still small and the sea breeze should be able to override the large-scale wind. The land-sea temperature difference over 15 km (Prudhoe Airport to the coast) was 7.8°C. .

On August 21, 1976 (000 GMT) the geostrophic wind for Cottle Island was 4.48 m/s from 252.1°T while the measured surface wind was 5.30 m/s from 110"T. The NWS map (Figure 8) indicates a col (region" of relatively flat pressure gradient between two highs and two lows which generally results in a low synoptic wind). The synoptic wind field is stronger (see Figure 9) than the previous case but appears to weaken from Oliktok to Barter Island. The gradient wind velocity is similar to the geostrophic because the radius of curvature of the isobars near the study area is greater than 300 km.

Atmospheric sounding data from Batter Island showed a weak wind of 1 m/s from variable directions between the altitudes of 542 m and 981 m. The vertical shear of the wind above the inversion in the free stream (thermal wind) appeared to be insignificant. Though a stationary front appears near the study area, prior surface wind data do not show large velocity changes and the NWS chart 12 hours before 000 GMT did not show

rapidly changing conditions. Wind data (10 m) taken 12 hours later did show an abrupt increase in wind speed (5 m/s to 10 m/s) and change in wind direction (210°F to 300°T) which coincided with a frontal passage near the Cottle Island data site and documented on the next NWS chart. This frontal passage had no influence at the time of the TDLSF plot and the isallobaric effect can still be considered negligible. The land-sea temperature difference from Prudhoe Airport to the coast (15 km) was 6.7°C.

The TDLSF technique applied for a cubic surface was used twice daily for comparison with NWS surface pressure maps and atmospheric sounding data from Barter Island, both of which are produced for 000 GMT and 1200 GMT. To compare surface winds with the geostrophic winds on a 3-hourly basis, the least squares technique was used to fit a linear surface (plane) to pressure data from Prudhoe, Lonely, Umiat and one AIDJEX buoy (closest to coast). These data sites surrounded the experimental area. In this case the two-dimensional polynomial to be solved which gives the best fit *to* four data points is

$$\text{Pressure} \equiv Z(x,y) = a + bx + cy \tag{2.05}$$

The constants a through c are computed from a 3x3 matrix with x the longitude and y the latitude of the respective data site locations. Partial derivatives (with respect to x and y) of the linear pressure POIYnomial were used to calculate geostrophic velocities. These velocities were first compared to those from the previously mentioned cubic fit (twice daily) and were found to agree (± 30°) 75% of the observed times. The linear surface can only approximate a mesoscale pressure higher low,

therefore local perturbations appearing in the cubic fit would be missed by the plane fit resulting in substantially different geostrophic winds calculated from respective pressure gradients. The computed geostrophic winds from the three sea breeze days (discussed above) were compared (for 000 GMT) using the linear and cubic fits. The linear fit for August 16, 1976 was 1.37 m/s from 142.4°T to .93 m/s from 188.5°T for the cubic fit. On August 18, 1976 the linear fit was 2.39 m/s from 232.4°T to 3,19 m/s from 226.7°T for the cubic fit. The last day, August 21, 1976, produced a linear fit of 3.76 m/s from 231.7°T while the cubic fit showed 4.48 m/s from 245.1°T. The geostrophic winds all had a southerly component and were weaker than 5 m/s.

The linear fit did provide the only continuous comparison (3-hourly) of the geostrphic wind (near Cottle Island) with the 10-meter wind measured at Cottle Island over a two week period in August 1976. Figure 10 shows a histogram both of the 10-meter surface wind (solid line) and the computed geostrophic wind (dashed line) for a time segment from August 13 to 23 and August 30 to September 3, 1976. The wind direction is divided into 15° increments with the y-axis indicating the number of samples. Planetary boundary layer turning, usually the result of a three-way balance between the Coriolis force, the large-scale pressure gradient force and the viscous force, would show winds shifted approximately 20°CCW (counterclockwise) from their free stream direction to their 10-meter direction. In Figure 10, the lined-in area under the geostrophic wind direction (above the boundary layer) curve with an average direction of 225°T occurs simultaneous to the lined-in area under the 10-meter wind direction (surface wind) curve with an average direction

of 105°T. The sea breeze has offset weak geostrophic winds in the boundary layer to produce" an average "turning" of 120° counterclockwise from the free stream level to the surface. The frequency of surface winds from the east has been almost doubled.

Another way of presenting the data in Figure 10 is shown in Figure 11. The geostrophic wind direction (D_G, ordinate) is plotted as a function of the surface wind direction (S_{10}, abscissa). The sea breeze influenced data points. (*SB*) are contained within the dashed lines. The geostrophic winds within a 60° band from 195° - 255° (SW quadrant) corresponding to surface winds in a 60° band from 90° - 150° (SE quadrant) exhibit an average turning of 120° from the free stream level to the surface.

As discussed earlier, the pressure data from the coastal stations of Prudhoe and Lonely are subject to sea breeze influence. The TDLSF (plane fit) technique was run for cases where .5 mb and 1 mb were added in turn to each of the coastal station readings *from 1200* to 2100 ADST. The greatest directional change (over the 0 pressure perturbation case) was 44°, while the maximum wind speed change was 1.5 m/s. The shape of the 3-hourly geostrophic wind histograms for the + .5 mb and + 1 mb coastal cases was not changed significantly from that exhibited in Figure 10. Again, the essential arguments presented in this thesis are not weakened by sea breeze mesoscale pressure gradient effects on coastal station pressure data.

2,4 Pilot Balloon Data

These data were collected in August 1977 on Pingok Island (see Figure 3), the primary experimental site. Early morning and late evening

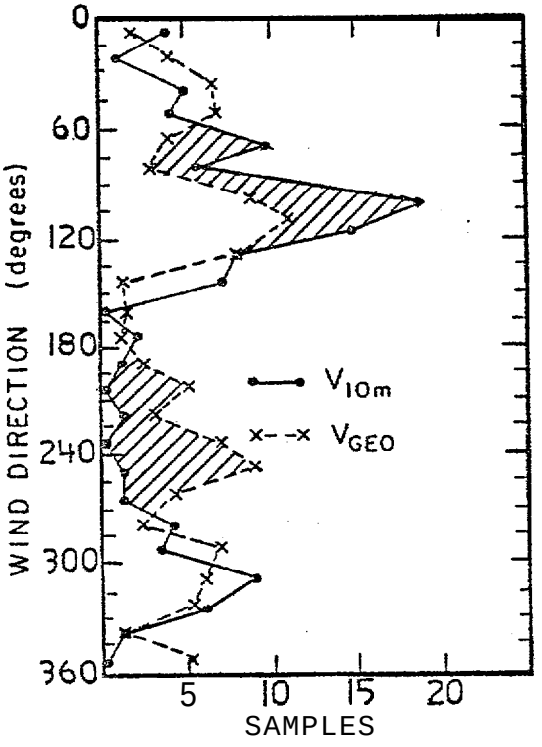

Fig. 10. Comparison of surface (10 meter) winds on Cottle Island with geostrophic winds in August 1976. The wind directions are in 15 degree increments. The actual time period is for August 13 to August 23 and August 30 to September 3, 1976.

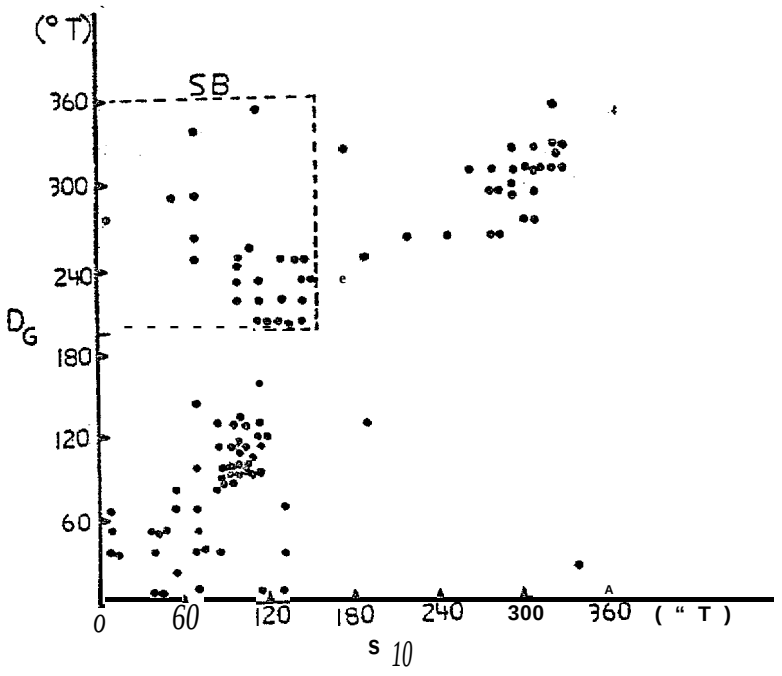

Fig. 11. Geostrophic wind direction (D_G) as a function of surface wind direction (S_{10}) using data from the same time period as in Figure 10.

tracking was precluded by fog conditions. Figure 12 consists of analog uncalibrated pyrheliograph data to illustrate relatively high or low radiation day readings from August 1-21, 1977,

August 7, 1977 data are presented in Figure 13. The vertical axis is height (m) with the horizontal axes indicated as either wind speed (m/s) or wind direction (°T). The times are in Alaskan Daylight Saving Time (ADST) with 1500 ADST corresponding to 000 GMT the following day, for example. The surface temperature was 6.8°C and temperature at the top of the inversion layer (ILT) was 14.5°C at 400 m for 1500 ADST (from radiosonde data).

Figure 13a shows wind speed and direction vs. height data at 1043 and 1235 ADST. The 1043 profile of the wind direction from 100 m to 500 m is similar to the 1235 profile. The 1235 profile shows approximately 20° of clockwise surface turning since 1043 and 20° of counterclockwise turning (backing) from the surface to 400 m. This backing with height is not typical and certainly not predicted by the classical steady state Ekman layer solution.

The 1518 and 1710 profiles (Figure 13b) show the surface wind direction to be turning clockwise with time and show the free stream wind direction above the inversion layer top to be turning counterclockwise with time. The 1518 wind backs from the surface to the top of the inversion layer, a total of 80°, while the 1710 wind veers 190° from the surface to the inversion layer top. Abnormally large boundary layer turning with height has occurred. The temperature difference (1500 ADST) between Prudhoe Airport and the coast (13 km) was 8.3°C. The pyrheliograph output (Figure 12) shows that August 7 was relatively clear '.

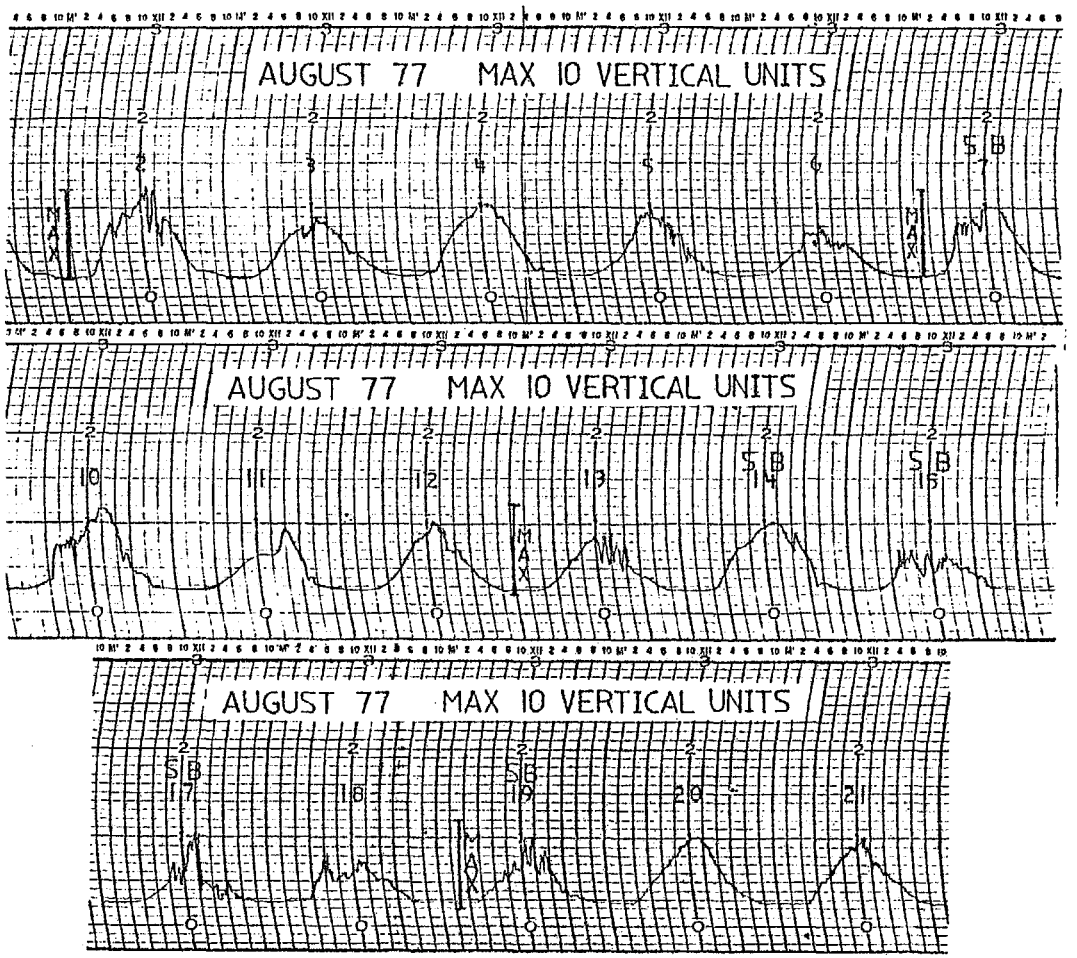

Fig. 12. Analog uncalibrated pyrheliograph data illustrating relatively high or low radiation day readings from August 1–21, 1977.

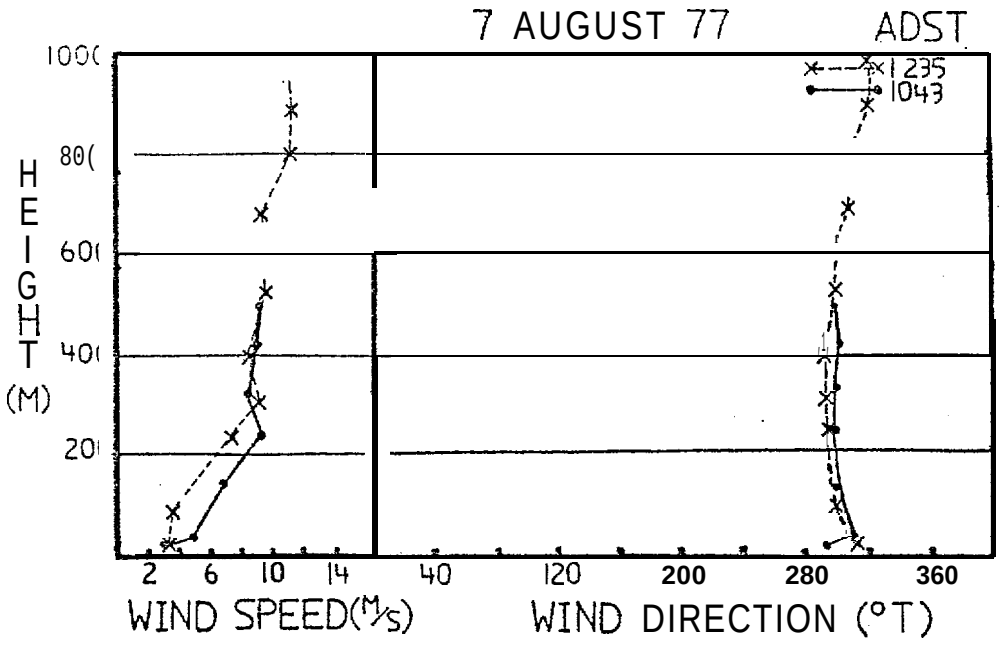

(a)

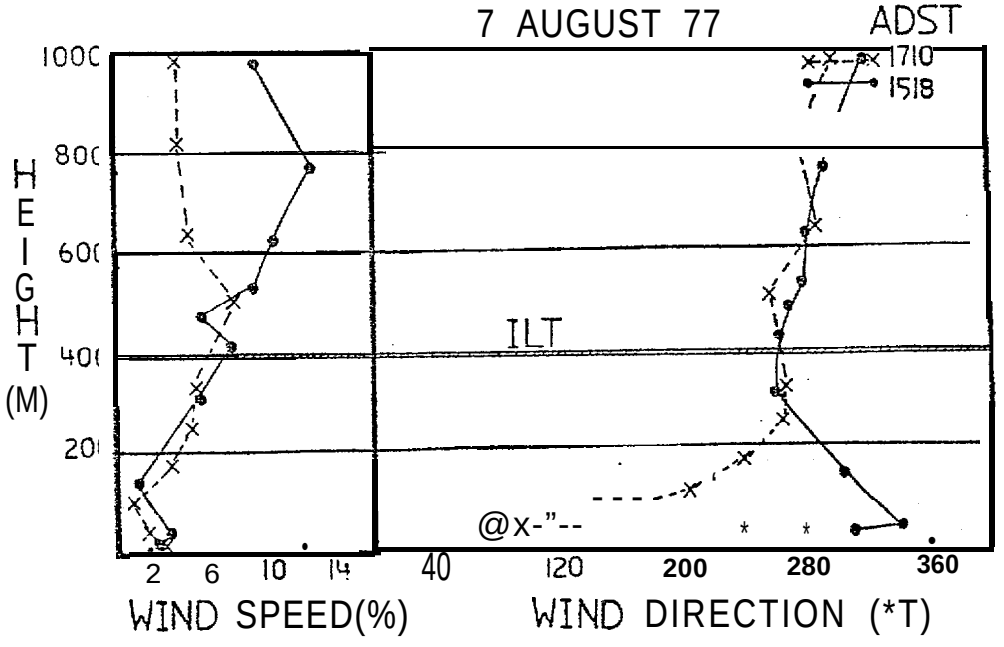

(b)

Fig. 13. Pilot balloon derived profiles of wind speed and wind direction from Pingok Island on August 7, 1977 for ADST times of (a) 1043 and 1235 and (b) 1518 and 1710.

(extremely clear days were reported prior to sounding equipment setup, with peaks of 10 chart intervals above the base level).

The NWS surface pressure map for August 8, 1977 (000 GMT) shown in Figure 14 plus the atmospheric soundings from Barter Island (250 km east) do not indicate a geostrophic wind from the northwest quadrant. The August 7, 1977 (1200 GMT) map (not shown) has evidence of isobaric curvature which could produce northwest winds, while the corresponding Barter Island soundings indicate a negligible wind above the inversion. Surface wind data from Pingok Island, Cottle Island and Cross Island all show an abrupt wind direction change at 1200 GMT (August 7, 1977) to the northwest quadrant. This example appears to be a case where the NWS chart does not provide the resolution to estimate the proper gradient winds for the area of the Beaufort Coast between Barter Island and Pt. Barrow. Other examples of limited resolution are noted by Kozo (1977).

August 14, 1977 data are presented in Figure 15 with the axes, time, and inset designations the same as in Figure 13. Radiosonde data from two launches (1427, 1815 ADST) indicated the top of the inversion layer (ILT--200 meters) temperature was 17.5*C with a 5.0°C surface temperature. Figure 15a shows wind speed and direction versus height data at 1017 and 1107. Both profiles have low wind speeds above the 200 m and exhibit veering from the surface to 200 m of approximately 110°.

The 1427 profile (Figure 15b), again with weak upper level winds, veers 100° and shows a surface wind speed larger than the free stream wind. Normal boundary layer surface wind speeds should be 50% to 60% less than the geostrophic wind speeds. The 1815 and 2253 profiles

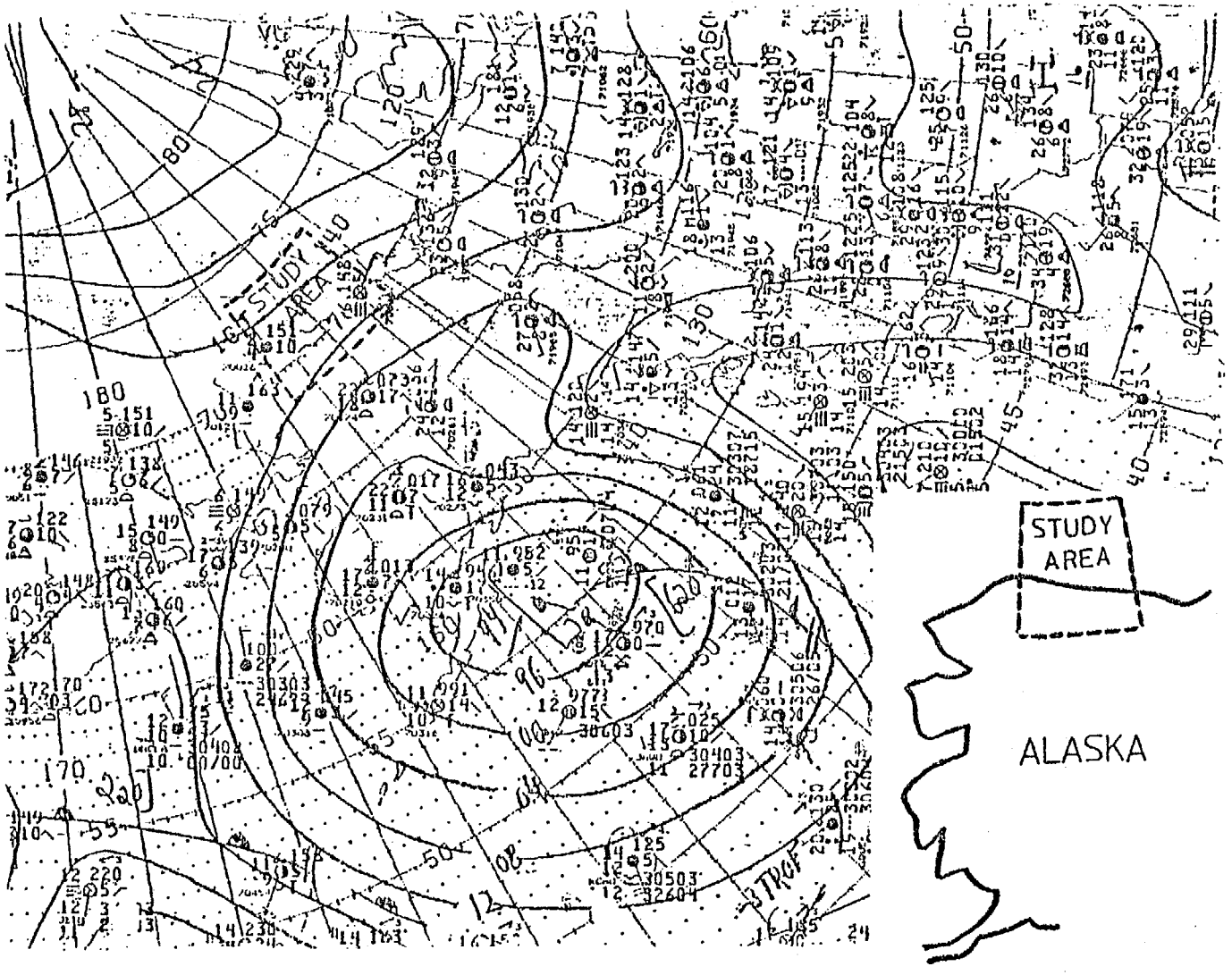

Fig, 14. NWS surface pressure chart for August 8, 1977 (000 GMT). The inset shows the orientation of the study area to the Alaskan coastline.

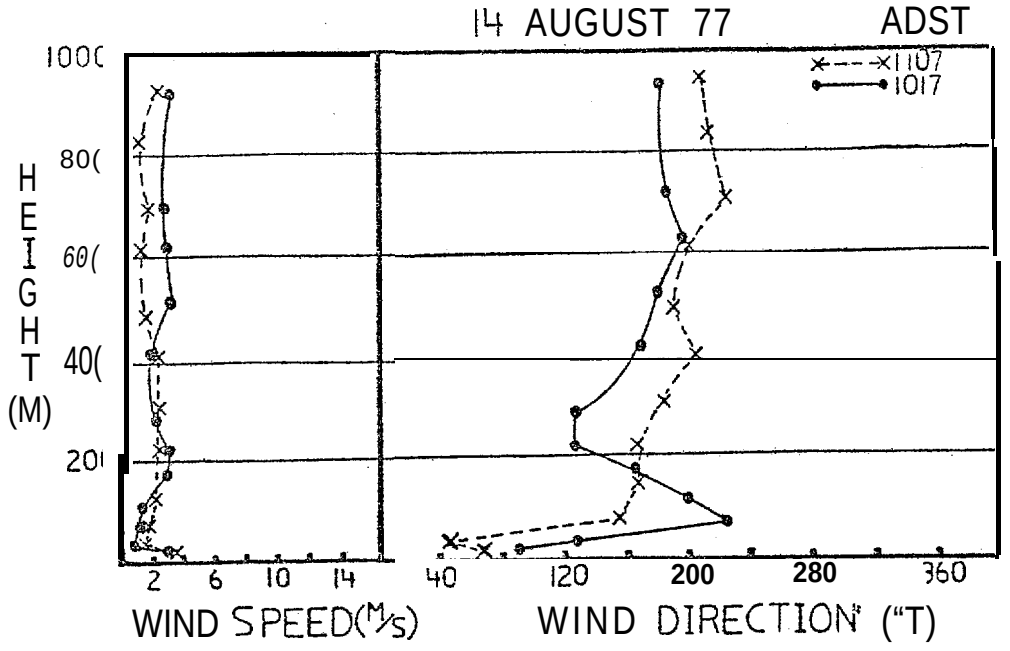

(a)

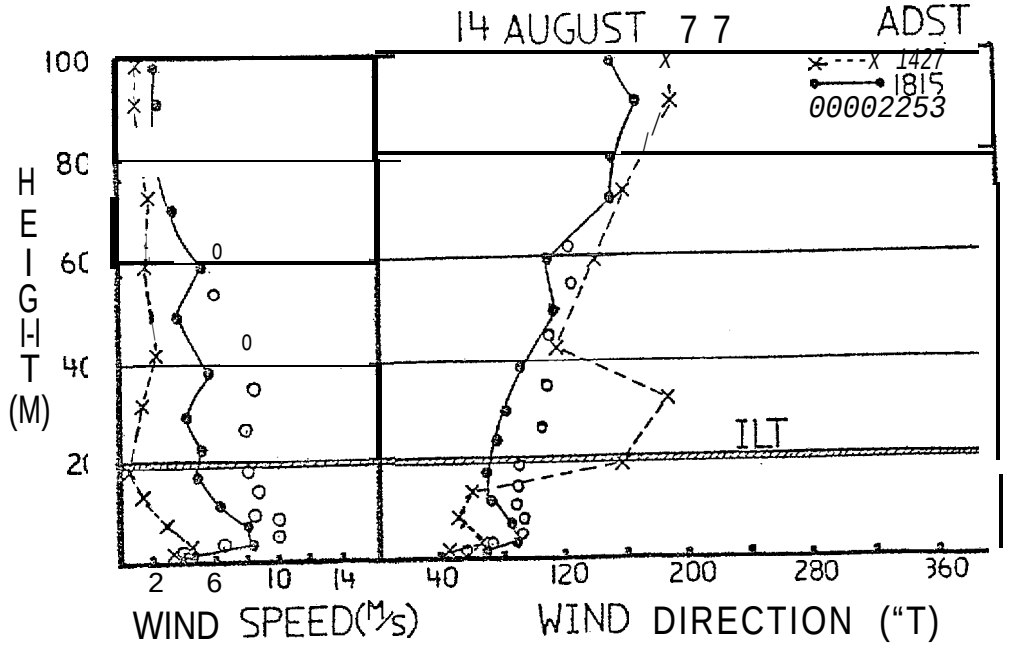

(b)

Fig. 15. Pilot balloon derived profiles of wind speed and wind direction from Pingok Island on August 14, 1977 for ADST times of (a) 1017 and 1107 and (b) 1427, 1815 and 2253.

exhibit normal boundary layer veering up to the inversion layer top but both show a wind speed increase within the boundary layer resulting in a speed greater than the apparent geostrophic wind. The temperature difference (1500 ADST) from Prudhoe Airport to the coast was + 13.3°C. The pyrheliograph output (Figure 8) indicates that August 14 was clear.

A U.S. Coast Guard icebreaker (Glacier WAGB-4) was positioned approximately 64 km north of Pingok Island from 1050 to 1850 ADST on August 14, 1977, remaining stationary while deploying two helicopters for ocean current measurements (Hufford, 1977). While surface winds at Pingok Island were averaging 64°T and 4 m/s from 1200 to 1400 ADST, the icebreaker was recording surface winds averaging 170°T and 2.5 m/s. The pilot balloon sounding (Figure 15b) at 1427 ADST showed weak winds of less than 2 m/s and wind directions above the surface-based inversion layer from 180°T to 150°T. The upper level wind directions prior to 1200 ADST were from 180°T (Figure 15a). This difference in surface wind direction from Pingok Island to the icebreaker shows the limit of the sea breeze influence to be certainly less than 69 km from the coast.

The NWS surface pressure map for August 15, 1977 (000 GMT) shown in Figure 16 is in fair agreement with the 1427 profile (above) and shows a geostrophic wind from 120°T at 3 m/s. The Barter Island soundings are not similar and for the same time (000 GMT) show 60° of backing from the surface to the inversion layer top (200 m), with free stream winds averaging 340°T and 2 m/s. These types of variations over 250 km for weak wind conditions are not unusual.

August 15, 1977 data are presented in Figure 17 with similar axes, time, and inset designations as Figure 13. Radiosonde data from two

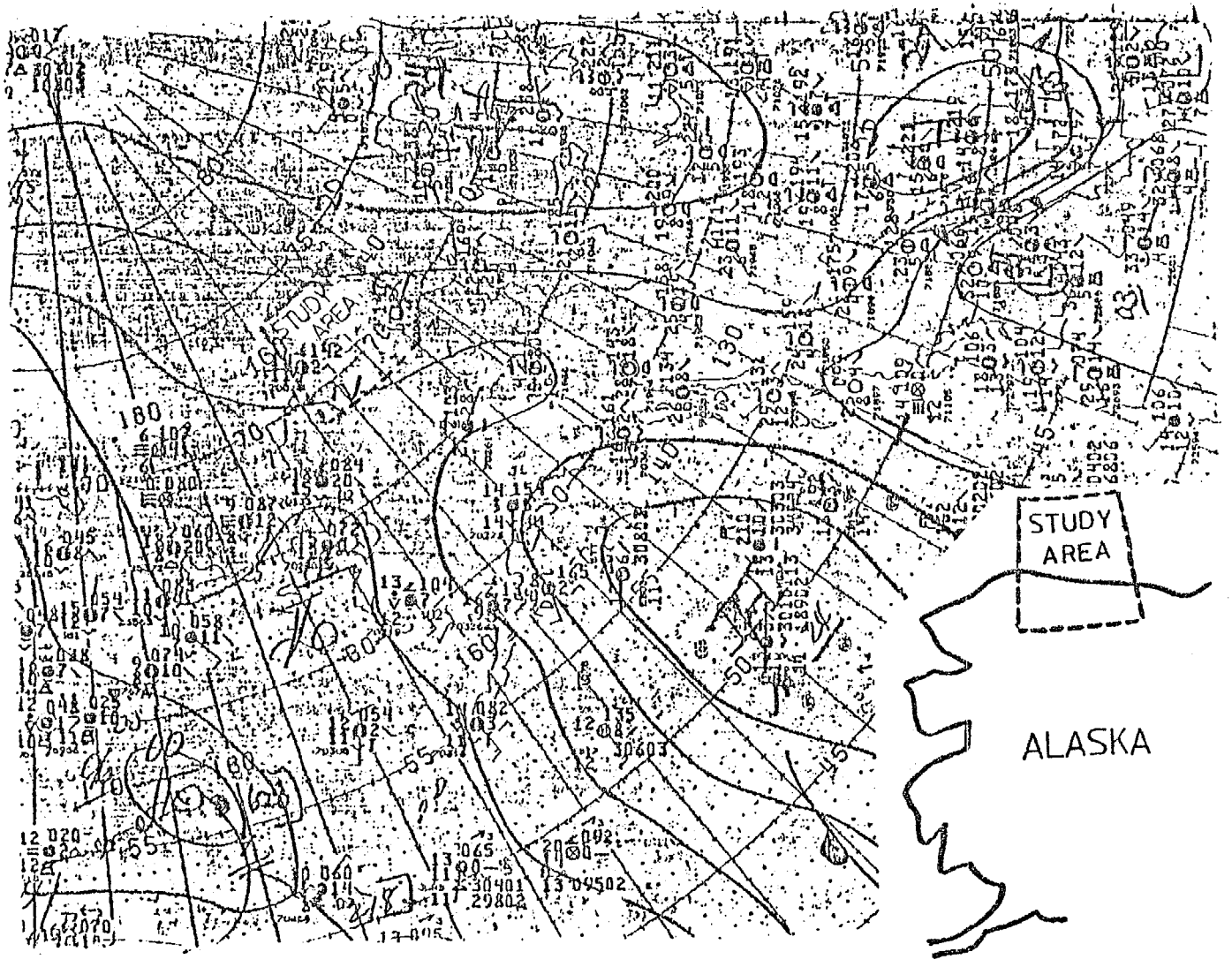

Fig. 16. NWS surface pressure chart for August 15, 1977 (000 GMT). The inset shows the orientation of the study area to the Alaskan coastline.

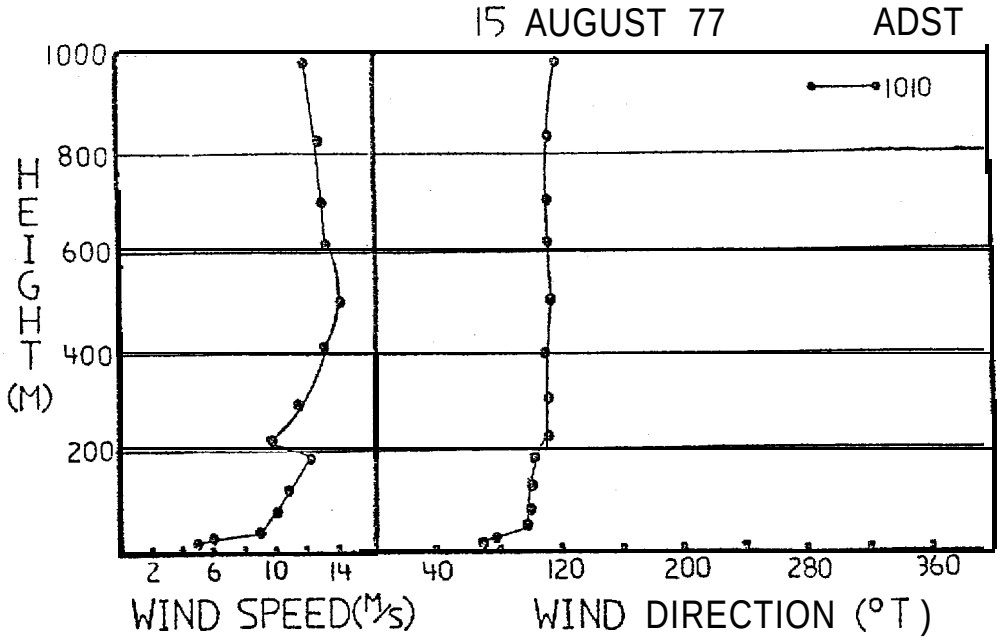

(a)

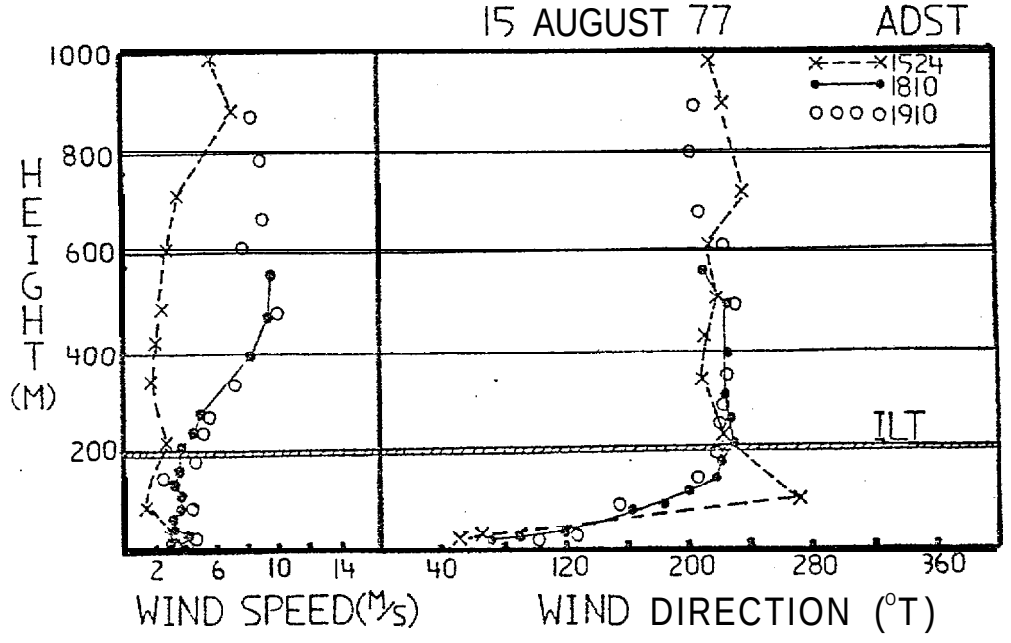

(b)

Fig. 17. Pilot balloon derived profiles of wind speed and wind direction from Pingok Island on August 15, 1977 for ADST times of (a) 1010 and (b) 1524, 1810 and 1910.

launches (1526 and 1810 ADST) indicated the top of the inversion layer (ILT--200 meters) temperature was 17.5°C with a 5.0°C surface temperature. Figure 17a shows wind speed and direction data at 1010 ADST. This rpofile with wind speeds of 12 m/s above 200 m and veering of 30° is close to a normal barotropic boundary layer profile. Figure 17b shows that the free stream wind direction had changed 110° by 1524 ADST but remained constant at approximately 220°T for the next four hours of balloon tracking. The 1524, 1810, and 1910 profiles show temporal veering of the surface wind vector as expected during times of sea breeze influence and all show abnormal veering of the wind vector with height" (greater than 100° to the inversion layer top). The upper level winds at 1524 during the sea breeze' maximum were weak (averaging 3 m/s) and" should have allowed for its development. The Prudhoe-coast temperature difference (1500 ADST) was 12.8°C while the pyrheliograph output (Figure 8) indicates that August 15 was overcast (at least at Pingok Island).

The NWS pressure map for August 16, 1977 (000 GMT) shown in Figure 18 indicates a weak gradient wind in the area while the Barter Island sounding has a surface wind of 340°T at 2 m/s (almost perpendicular to the local coastline orientation) with 0 m/s as upper level wind speed (above the inversion to 955 m). There is ample evidence that the sea breeze is the controlling influence at this time.

August 17, 1977 data are presented in Figure 19 with similar axes, time, and inset designations as Figure 13. Radiosonde data (2144 ADST) indicated the top of the inversion layer (ILT--200 meters] temperature was 15.4°C while the surface temperature was 3.0°C. Figure 19a shows the morning profiles for times 0901 and 1050. The upper level (free stream)

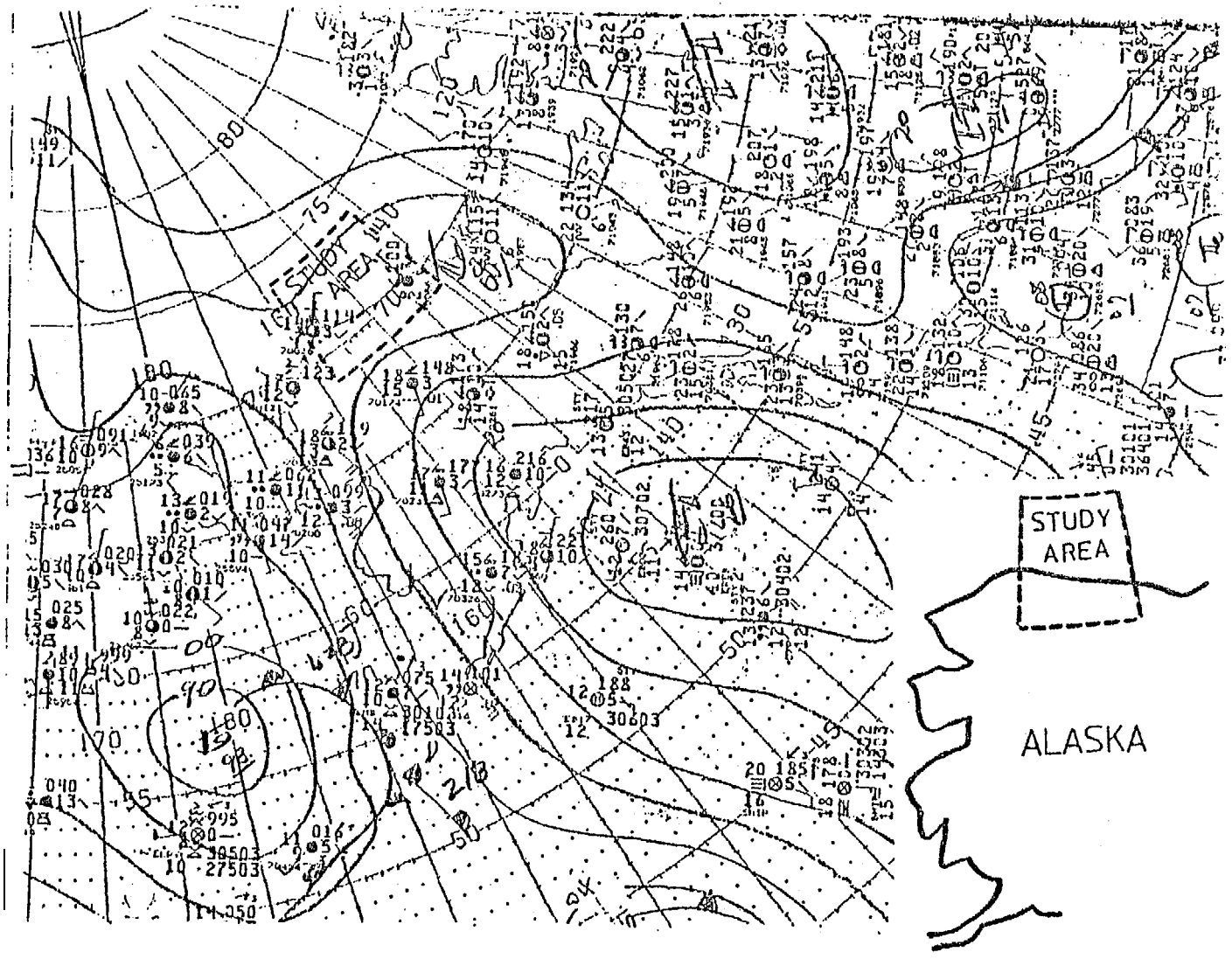

Fig. 18. NWS surface pressure chart for August 16, 1977 (00⊙ GMT). The inset shows the orientation of the study area to the Alaskan coastline.

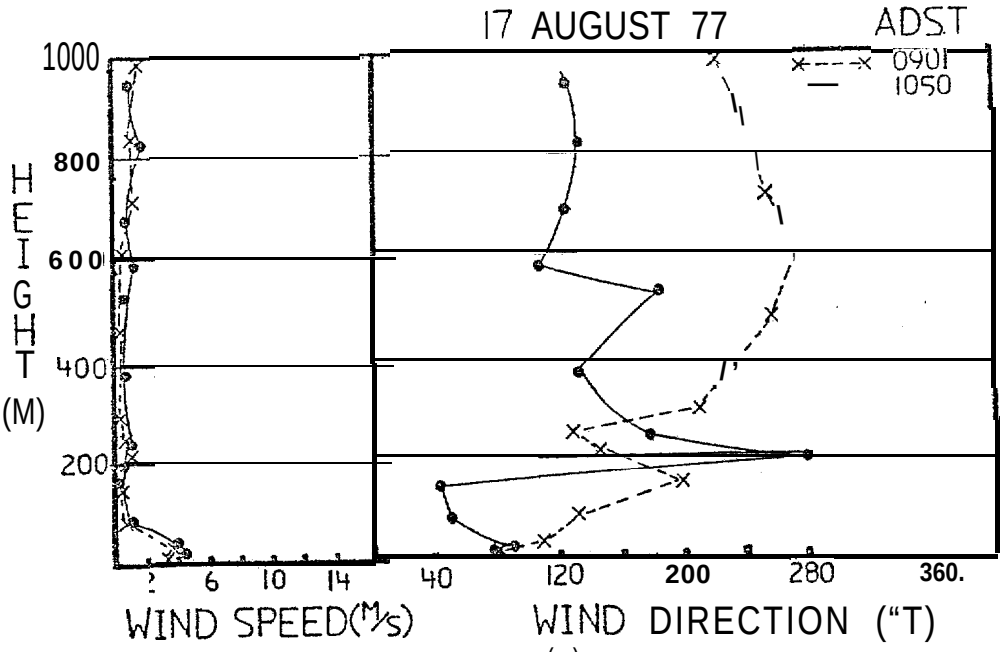

(a)

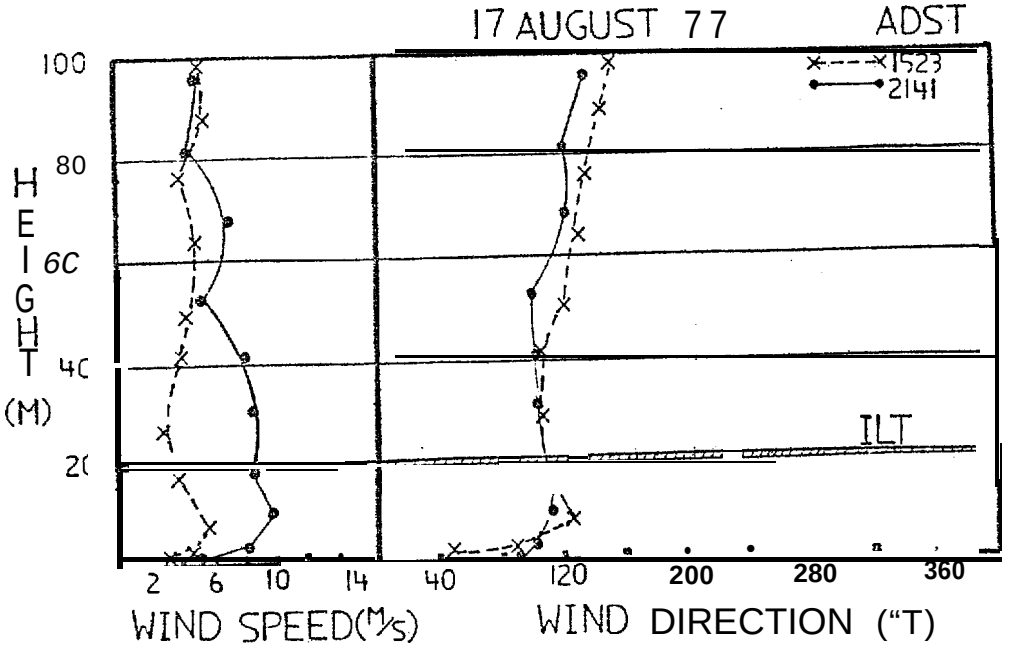

(b)

Fig. 19. Pilot balloon derived profiles of wind speed and wind direction from Pingok Island for August 17, 1977 for ADST times of (a) 0901 and 1050 and (b) 1523 and 2141.

wind speeds were less than 2 m/s and surface wind directions were controlled by the sea breeze (note: sunrise was at 0300 ADST) several hours before reaching its theoretical maximum. Figure 16b shows the afternoon profiles which exhibit more normal surface to inversion height veering as the geostrophic wind speed increases. The 1523 profile has a larger turning of 70° clockwise (from the surface) with a wind speed increase below the inversion layer top which indicates sea breeze influence by interaction of the geostrophic and sea bteeze wind components. The P-C (Prudhoe-coast) temperature difference (1500 ADST) was 7.8°C while the pyrheliograph output (Figure 12) shows that sky conditions went from scattered to overcast cloud cover.

The NWS surface pressure map for August 18, 1977 (000 GMT) indicates a weak gradient wind of less than 3 m/s from the southeast quadrant near pingok Island (Figure 20). Barter Island soundings indicate a weak above-inversion wind speed (less than 3 m/s) from the northeast quadrant. The Barter Island surface wind is 5 m/s from 70″ which indicates an increase in wind speed beneath the inversion (sea breeze influence).

Figure 21 has August 19, 1977 data labeled as in Figure 13 above. Radiosonde plots (1702 and 2212 ADST) showed an average top of the inversion layer (ILT--150 meters) temperature of 13°C and surface temperature of 8°C. The inversion steepness increased slightly from 1702 to 2212 as the surface temperature decreased. Figure 21 shows the 1024 and 1205 profiles with wind veering up to the inversion height while the 140.0 and 1500 (Figure 21b) wind profiles exhibit counterclockwise turning (backing) up to the inversion height. Also, a local surface veering can be noted from 1200 to 1500. The wind speed above the inversion by 1400 is less

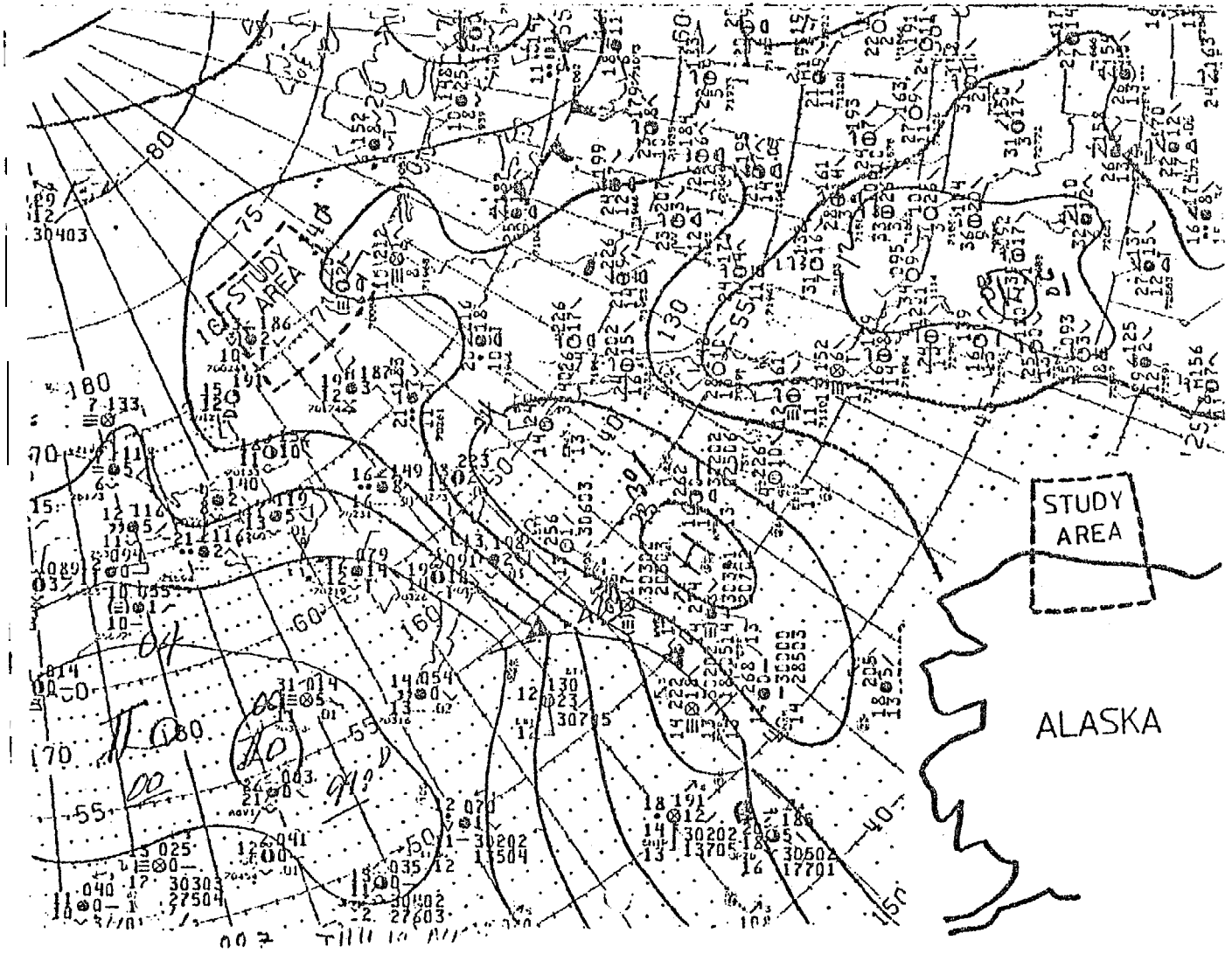

Fig. 20. NWS surface pressure chart for August 18, 1977 (000 GMT). The inset shows the orientation of the study area to the Alaskan coastline.

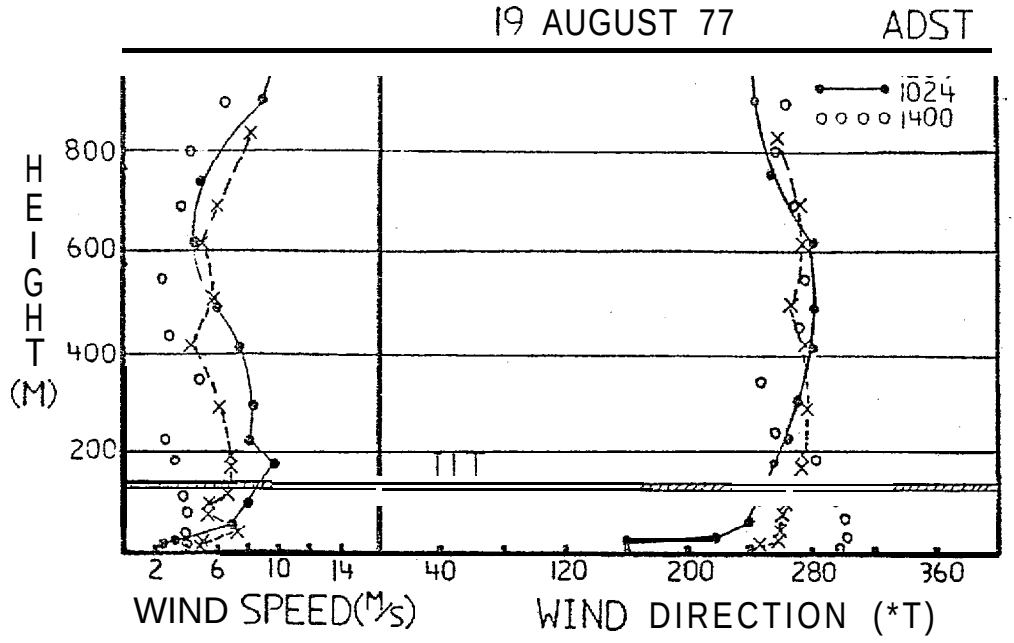

(a)

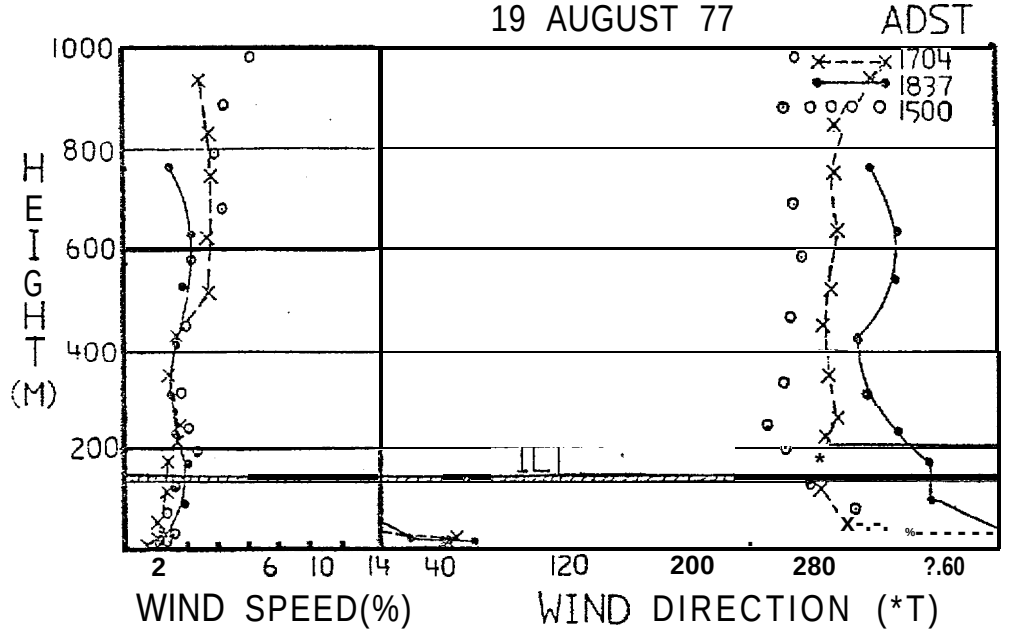

(b)

Fig. 21. Pilot balloon derived profiles of wind speed and wind direction from Pingok Island on August 19, 1977 for ADST times of (a) 1024, 1205, and 1400 and (b) 1500, 1704 and 1837.

than 5 m/s and is considered moderately weak. The 1704 and 1$37 profiles (Figure 21b) exhibit backing of greater than 90° through the inversion height with the free stream wind direction changing 25° in 1.5 hours. The wind speed above the inversion is weak and again the sea breeze influence is dominant. The P-C temperature difference (.1500 ADST) was 8.9°C and the pyrheliograph output (Figure 12) shows that sky conditions were scattered cloud cover.

The NWS surface pressure map for Aguust 20, 1977 (000 GMT) depicts a weak gradient wind (col situation} for the Pingok Island area (Figure 22). Barter Island soundings for the same time indicate a free stream wind averaging 7 m/s from 280°T. The Barter surface wind is 4 m/s from 90°T which is abnormal boundary layer turning not unlike that at Pingok Island. There is evidence at both sites of sea breeze influence.

2.5 Surface Wind Data

Figure 23 was obtained from monthly summaries of surface wind directions for Oliktok (15 km from Cottle Island) in the OCS (Outer Continental Shelf) Climatic Atlas (Brewer et al., 1977) for the months of January (limited thermal contrast across the coastline) and August (thermal contrast across the coast and maximum open water). These are histograms of wind speed and direction with the top scales representing direction (from) frequencies and indicated by The bars. bottom scales represent speed frequency and are indicated by printed numbers. It can be seen that 67% of the measured surface wind speeds in August were below 6 m/s. There is a bimodality in wind direction which is attributed to the large-scale wind field. The asymmetry that appears in the August data can be

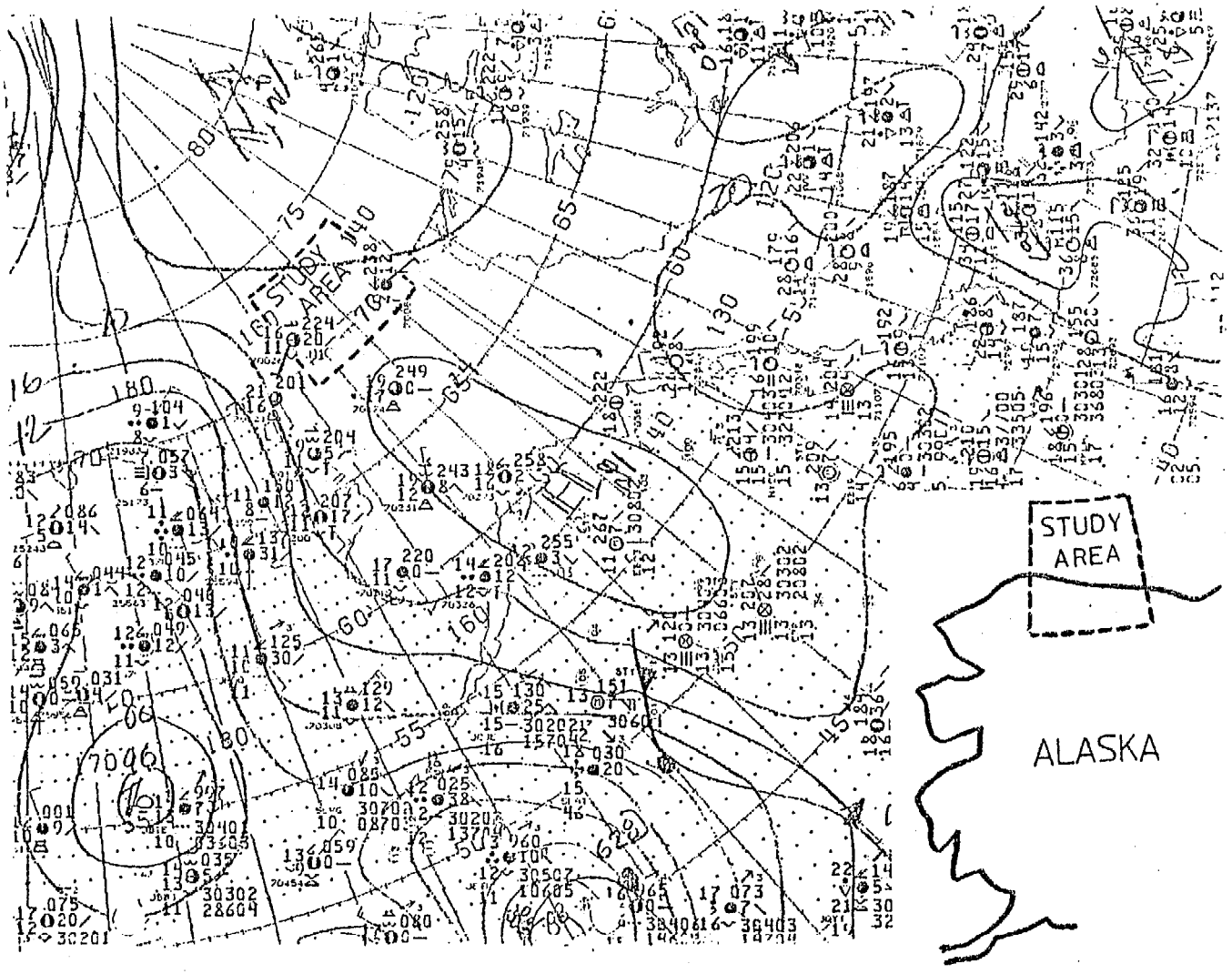

Fig. 22. NWS surface pressure chart for August 20, 1977 (000 GMT). The inset shows the orientation of the study area to the Alaskan coastline.

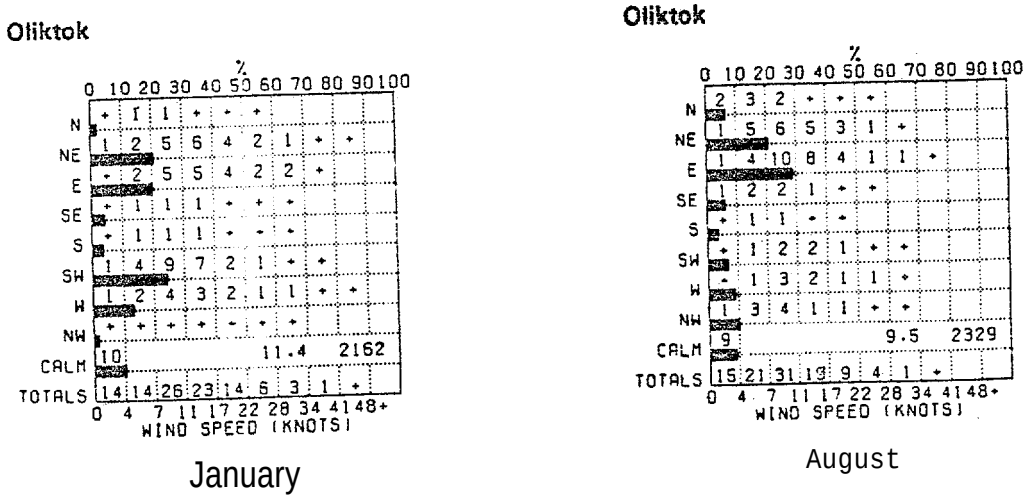

WIND SPEED/DIRECTION

Fig. 23. January and August monthly summaries of surface wind directions for Oliktok (15 km from Cottle Island) from the Outer Continental Shelf (OCS) Climatic Atlas (Brewer, et al. 1977).

partly explained by the latitudes 70°N to 75°N (north of Alaska) becoming a region of anti-cyclonic flow during arctic summers (Reed and Kunkel, '1960). This is a synoptic effect; however, Figure 10 above shows that some of this asymmetry must also be a thermally induced mesoscale effect (sea breeze). The Oliktok histogram for August compiled from historical data is remarkably similar to the Cottle Island (10-meter wind) histogram compiled during three Augusts from 1976 to 1978 (Figure 24). The left scale is the direction percentage frequency with bars representing winds from each direction. The right scale is the speed frequency with printed numbers representing the percentage frequency of wind speed observed from each direction. Here 62.5% of the measured surface wind speeds during the times of observation were below 6 m/s. This similarity in the histograms from Oliktok and Cottle Island implies that the wind velocity data taken during this experiment were representative of previous Augusts for this part of the Alaskan arctic coast.

Time series of surface wind data from coastal stations and islands were examined with a less conventional technique of spectral analysis than that used for typical speed (scalar) spectra. The technique computes a rotary spectrum as output and is described in detail by Gonella (1972) and utilized to determine the existence of sea breezes by O'Brien and Pillsbury (1974).

The rotary spectrum is a representation in frequency space of the variance spectrum of a two-dimensional (vector) time series. The variance for each frequency band is divided into clockwise rotating variance (at negative frequency) and counterclockwise rotating variance (at positive frequency). For a single frequency band, the horizontal velocity

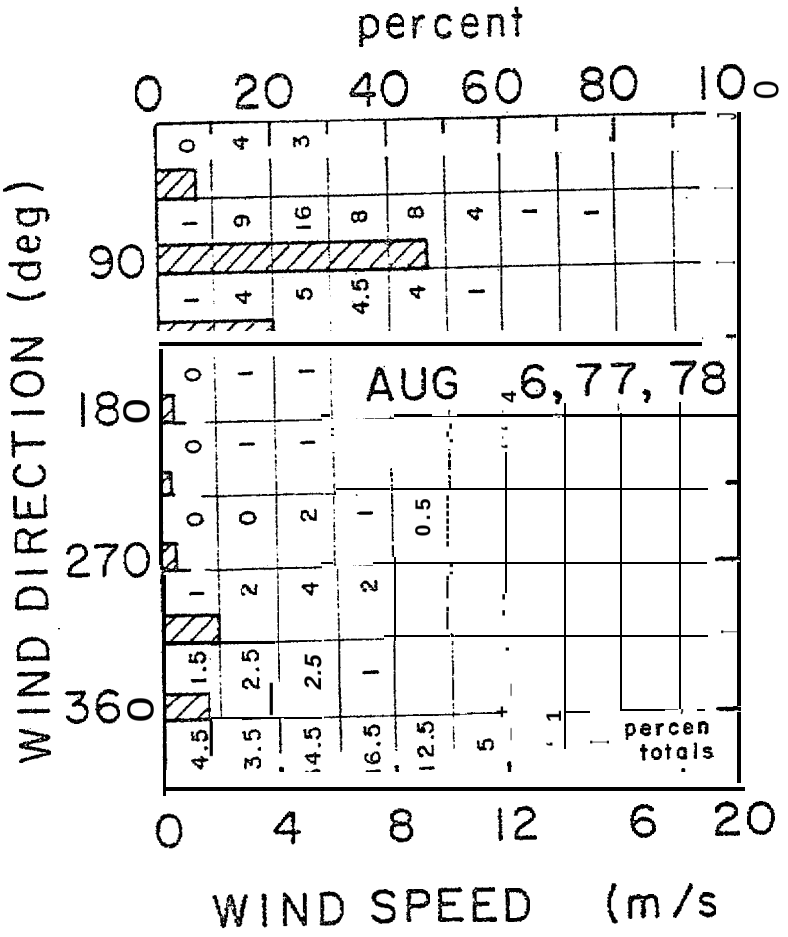

Fig. 24. Histogram of surface wind speed and direction for August 1976, 1977, and 1978 combined (from Cottle Island). Note: Direction Frequency-Top Scale-Bars represent percentage frequency of winds from each direction. Speed Frequency-Bottom Scale-Printed numbers are percentage frequency of wind speeds observed from each direction.

$w = u + iv$ can be written with the u and v components as arbitrary sinusoids (O'Brien and Pillsbury, 1974):

$$u(t) = a_1(f) \cos(2\pi ft) + b_1(f) \sin(2\pi ft)$$
$$v(t) = a_2(f) \cos(2\pi ft) + b_2(f) \sin(2\pi ft) \qquad (2.06)$$

If the cosine and sine terms are replaced by complex exponentials, then rearranging results in

$$w = \left[\frac{a_1 + b_2}{2}\right] e^{i2\pi ft} + i\left[\frac{a_2 - b_1}{2}\right] e^{i2\pi ft}$$
$$+ \left[\frac{a_1 - b_2}{2}\right] e^{-i2\pi ft} + i\left[\frac{a_2 + b_1}{2}\right] e^{-i2\pi ft} \qquad (2.07)$$

w can now be written, on appropriate coordinate transformation involving rotation of axes., as

$$w = Ae^{in} e^{i2\pi ft} + Ce^{-i\zeta} e^{-2\pi ft} \qquad (2.08)$$

where:

$$A = \tfrac{1}{2}[(b_2 + a_1)^2 + (a_2 - a_1)^2]^{1/2}$$

$$C = \tfrac{1}{2}[(b_2 - a_1)^2 + (b_2 + a_1)^2]^{1/2}$$

and

$$\tan n = \frac{a_2 - b_1}{a_1 + b_2}, \quad \tan \zeta = \frac{a_2 + b_1}{a_2 - a_1}$$

The amplitude A corresponds to the counterclockwise component while C corresponds to the clockwise component of the motion. Comparison of Eq. (2.08) with Eq. (2.07) indicates that A is the amplitude of w at positive frequency and C the amplitude of w at negative frequency. The variance

of w is $2(A^2 + C^2)$ and is partitioned as a function of frequency into counterclockwise and clockwise portions. The rotary spectrum is a plot of $2\Delta TA^2$ (units of energy density) versus frequency at positive frequency and $2\Delta TC^2$ versus frequency at negative frequency (where AT is the minimum data interval in seconds). The squared modulus of w is proportional to the rotary spectrum. The rotary spectrum can be shown to be the sum of the kinetic energy (speed) spectrum plus twice the quadrature (out-of-phase) spectrum between u and v. The shape of the rotary spectrum is determined by the quadrature spectrum, since the speed spectrum is symmetric with respect to frequency. O'Brien and Pillsbury (1974) state that the rotary spectrum from time series of horizontal winds collected at station's (offshore and land) near the Oregon coast show the sea breeze to be a predominantly clockwise (veering) wind oscillation. Also, the absence of significant peaks at the 24-hour period in the clockwise part of the spectrum (buoys 30 km offshore) indicate that the sea breeze ocean surface circulation is limited to 30 km offshore.

Figures 25 and 26 are plots of rotary spectra for August 1976 and 1977 from time series data of surface wind velocities at various stations both inland and offshore. They are semi-log plots with 95% confidence limits (C) and bandwidths (B) indicated, The spectral peaks occurring near -1 cycle/day (24-hour period) are "the clockwise-rotating contributions from the sea breeze. The vertical axes are spectral densities ($[m^2/s^2]/[c/3h]$) with the horizontal axes in frequency units of cycles/day.

Figure 25 represents spectra for data (1976) collected at (a) Narwhal Island (18 km offshore), (b) Cottle Island (5 km offshore), (c)

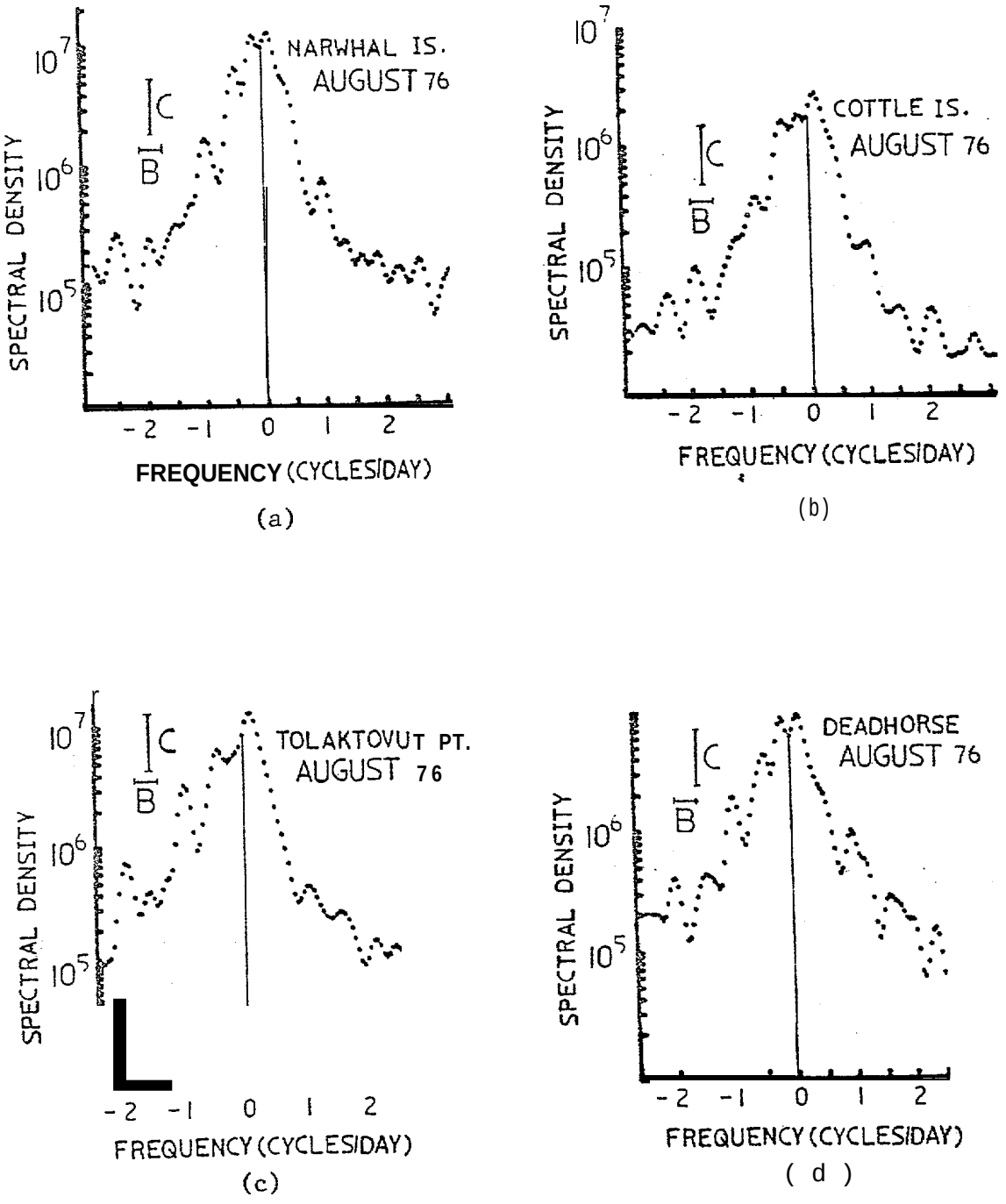

Fig. 25. Time series rotary spectra of surface wind velocity data for August 1976 collected from Narwhal Island (a), Cottle 'Island (b), Tolaktovut Point (c) and Deadhorse (d).

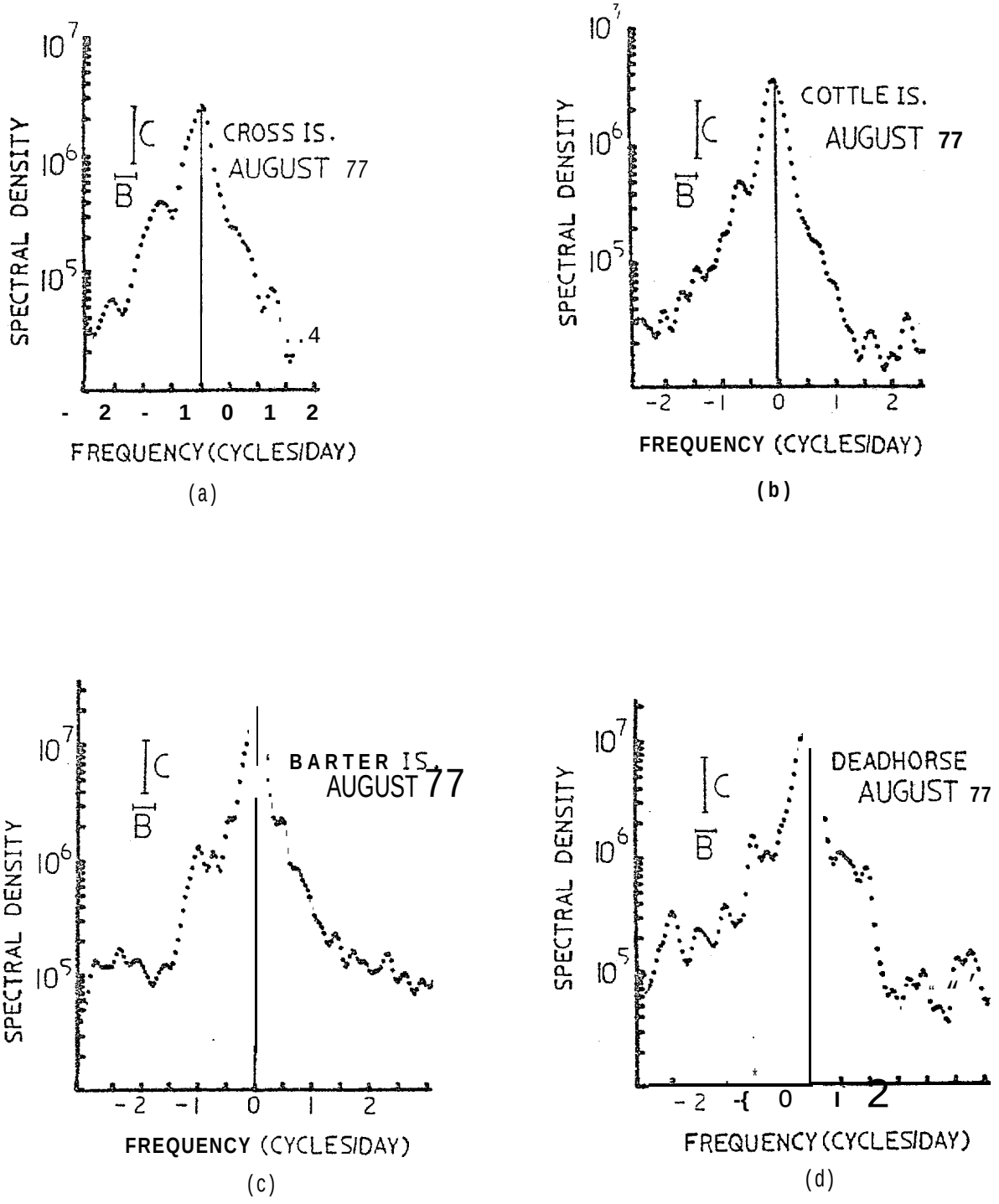

Fig. 26. Time series rotary spectra of surface wind velocity data for August 1976 collected from Cross Island (a), Cottle Island (b), Barter Island (c), and Deadhorse (d).

Tolaktovut (coastal station), and (d) Deadhorse Airport (19 km inland), respectively (see Figures 2 and 3). There is a marked asymmetry around the 0 frequency line and all have significant peaks corresponding to the 24-hour period on the negative frequency axis. The peaks related to clockwise rotation in the Deadhorse (Figure 25d) and Narwhal (Figure 25a) spectra are evidence (O'Brien and Pillsbury, 1974) of sea breeze influence in at least a 37 km band centered on the coastline.

Figure 26 has spectra from data (1977) collected at (a) Cross Island (19 km offshore), (b) Cottle Island (5 km offshore), (c) Barter Island (coastal station), and (d) Deadhorse Airport (19 km inland). Again, asymmetry and significant peaks near the -1 cycle/day frequency (24-hour period) can be seen. Cross Island (instead of Narwhal Island) and Deadhorse spectra show sea breeze existence in a 38 km coastal zone.

Both sets of spectra sometimes show peaks on the positive frequency axis near 1 cycle/day. The sea breeze induces clockwise rotation of local wind vectors with time under conditions of weak synoptic flow (Schmidt, 1947; Defant, 1951; and Haurwitz, 1947). It has been shown by Haurwitz (1947) that prevailing synoptic conditions may interact with the sea breeze to cause counterclockwise rotation of the local wind vector. These spectral peaks near the 24-hour period for this data and on O'Brien and Pillsbury's (1974) spectra (though not specifically mentioned by them) are thought to be caused by the sea breeze in combination with the large-scale wind field. In the case of the Beaufort Sea coast, a moderate southwest synoptic wind (220°T) existing in the morning hours could be "rotated" to 70"T (counterclockwise) as the sea breeze became dominant. A quantitative way to look at the turning of the local wind

vector has been developed by Neumann (1977) and will be discussed in Chapter V.

Examples of time variation of the local surface wind vector (direction versus true north, coastal orientation 25° to east-west line) with distance seaward and landward from the coast are presented to illustrate the clockwise and counterclockwise -rotation (Figures 27-34). They have been chosen for the days (mentioned above) in August 1976 and August 1977 (see above) which exhibited sea breeze characteristics. For August 1976 Narwhal Island was the most seaward site (18 km) while Deadhorse Airport was the most inland site (19 km). August 1977 had Cross Island (19 km) and Deadhorse Airport as the most seaward and most inland sites, respectively (see Figures 2 and 3). The data sites are designated by letters with E ≡ Narwhal Island, C ≡ Tolaktovut Pt. for 1976; E ≡ Cross Island, C ≡ Oliktok for 1977; and D ≡ Cottle Island, A ≡ Deadhorse, B ≡ ARCO Airport for both years.

August 15, 1976 (calculated geostrophic wind--188°T and 1 m/s 1500 ADST) is seen in Figure 27 with local wind vectors at the times (ADST) and distances from the coast (km) for the indicated data sites. The wind vector at Tolaktovut (coastline site) rotated from 090°T at 0600 to 255° at midnight in a counterclockwise direction with a wind direction of 045°T and 3.6 m/s for the time of maximum sea breeze influence (1500). All five of the sites had wind directions 270° ± 20°T (surface) by midnight (near minimum influence of the coastal thermal contrast) while the computed geostrophic wind was 265°T and 10 m/s. The five sites exhibited general counterclockwise rotation of the surface wind vector while the geostrophic wind vector rotated clockwise approximately

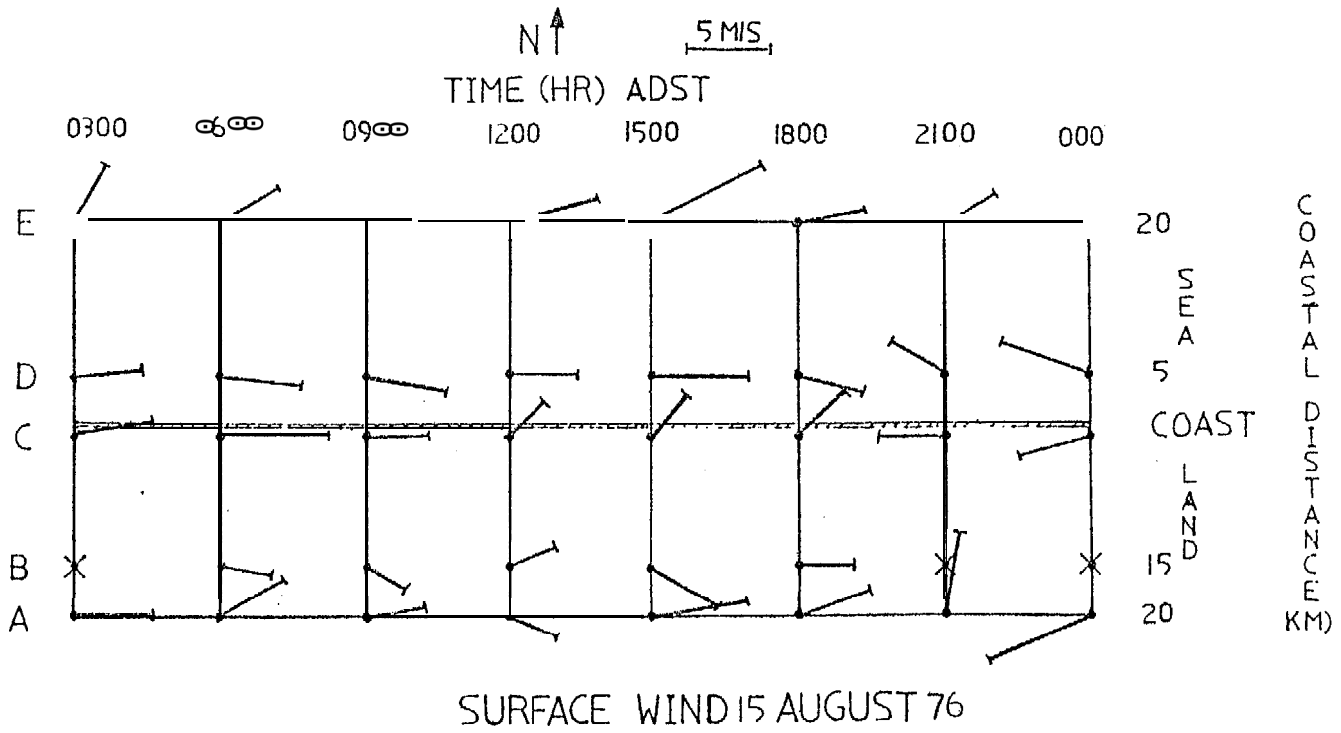

Fig. 27. Three hourly local surface wind vectors for stations at Narwhal Island (E), Cottle Island (D), Tolaktovut Point (C), ARCO Airport (B), and Deadhorse Airport (A) from 0300 to 2400 LDST on August 15, 1976. The calculated goestrophic wind was from 188°T at 1 m/s for 1500 ADST.

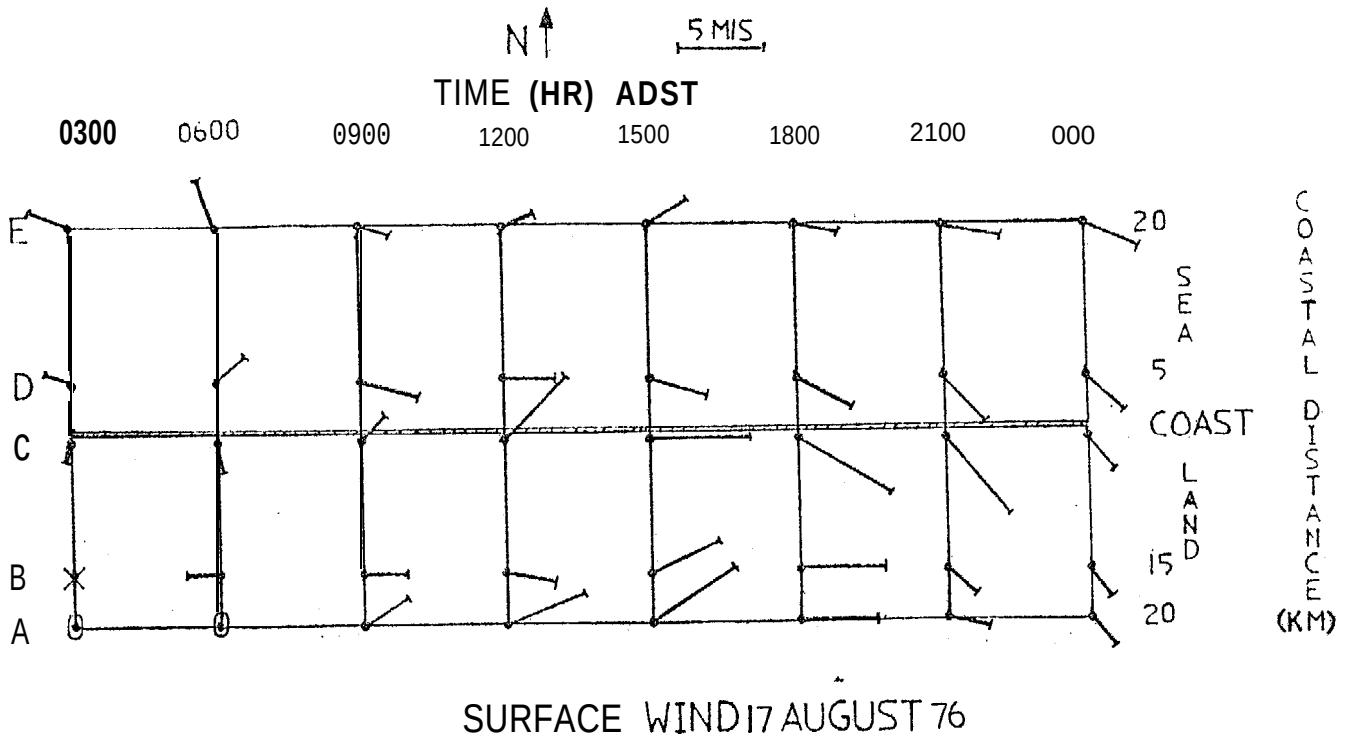

Fig. 28. Three hourly local surface wind vectors for designated stations (as in Figure 27) on August 17, 1976. The calculated geostrophic wind was from 227°T at 3.2 m/s for 1500 ADST.

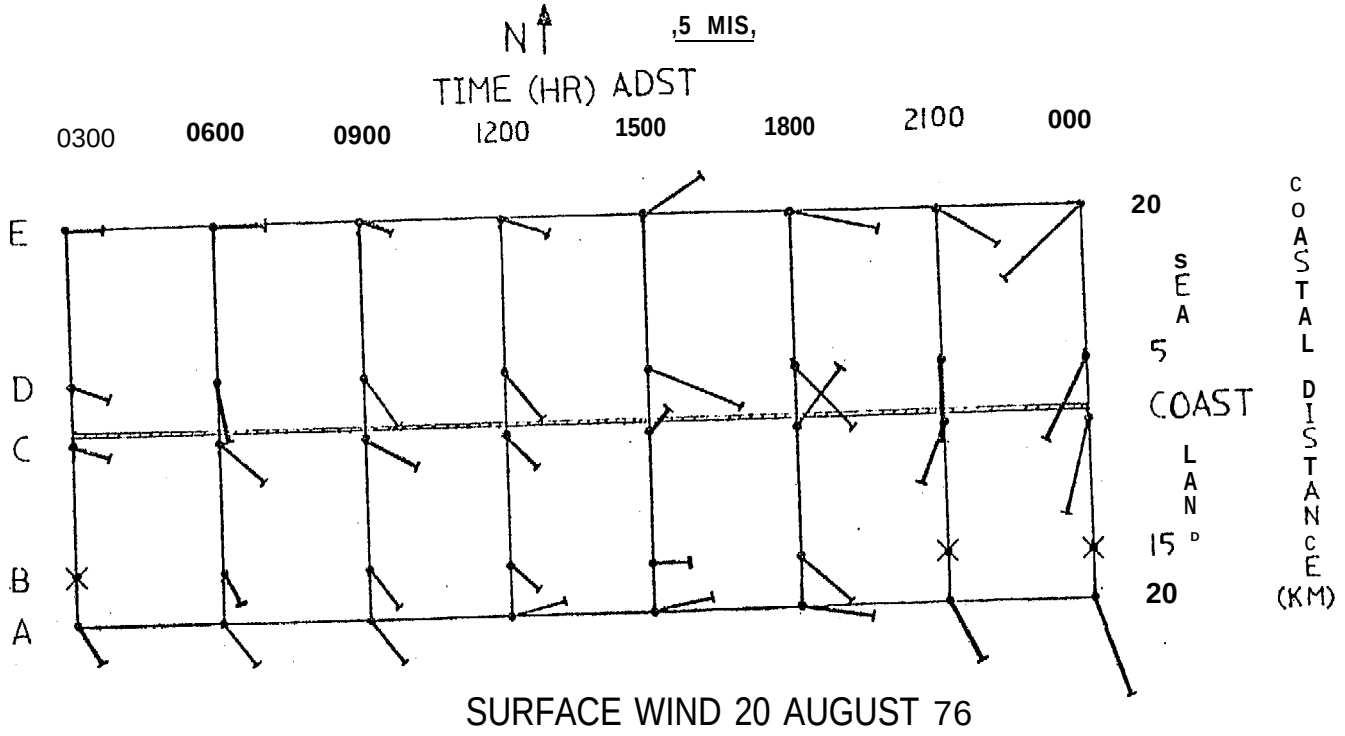

Fig. 29. Three hourly local surface wind vectors for designated stations (as in Figure 27) on August 20, 1976. The calculated geostrophic wind was from 245°T at 4.5 m/s for 1500 ADST.

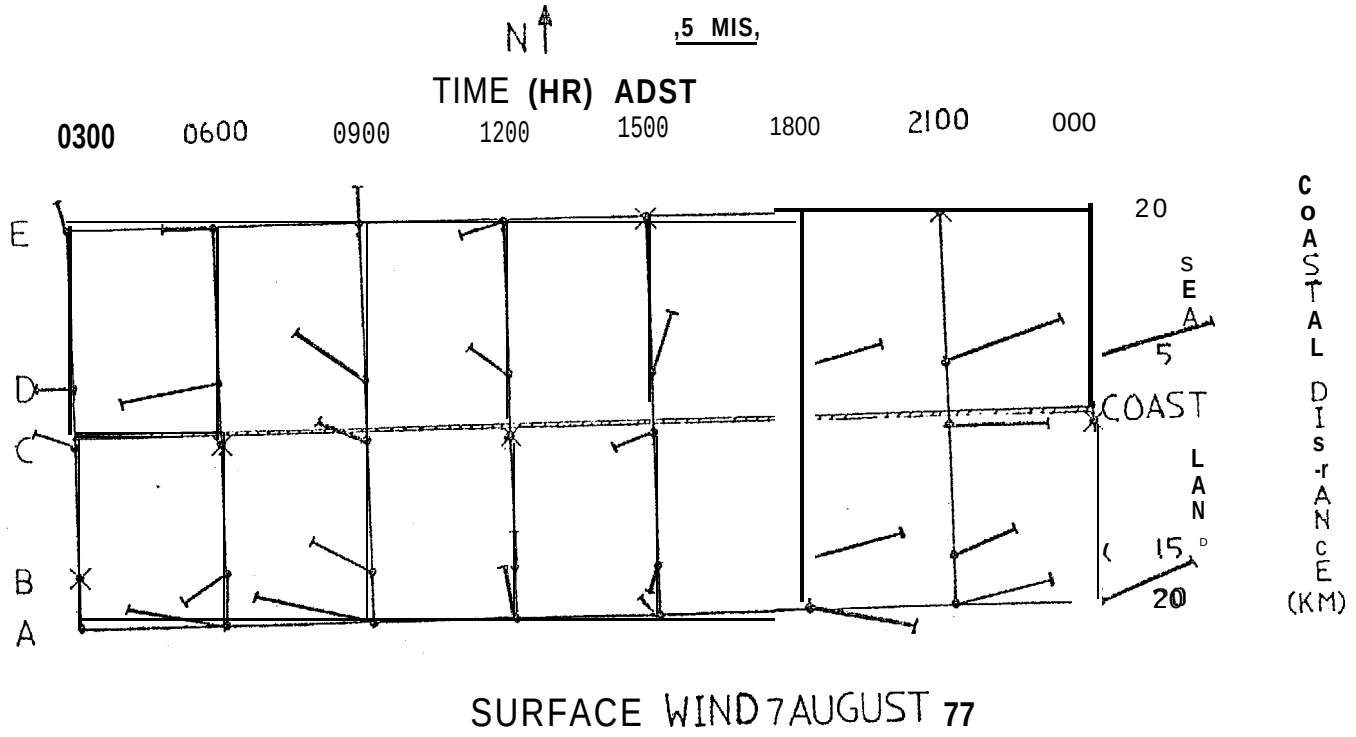

Fig. 30. Three hourly local surface wind vectors for stations at Cross Island (A) (E), Cottle Island (D), Oliktok (C), ARCO Airport (B), and Deadhorse Airport from 0300 to 0400 LDST on August 7, 1977. The geostrophic wind was 280°T at 2 m/s for 1500 ADST.

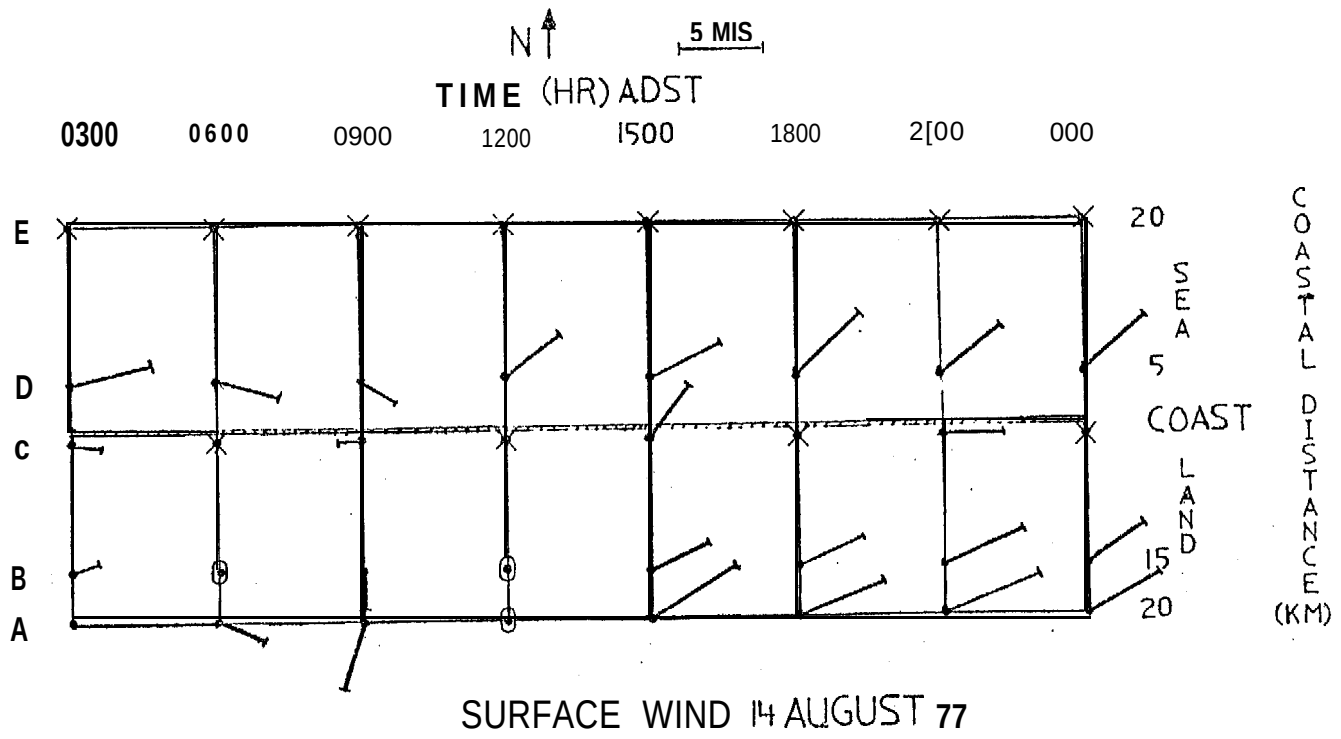

Fig. 31. Three hourly local surface wind vectors for designated stations (as in Figure 30) on August 14, 1977. The geostrophic wind was 280°T at 2 m/s for 1500 ADST.

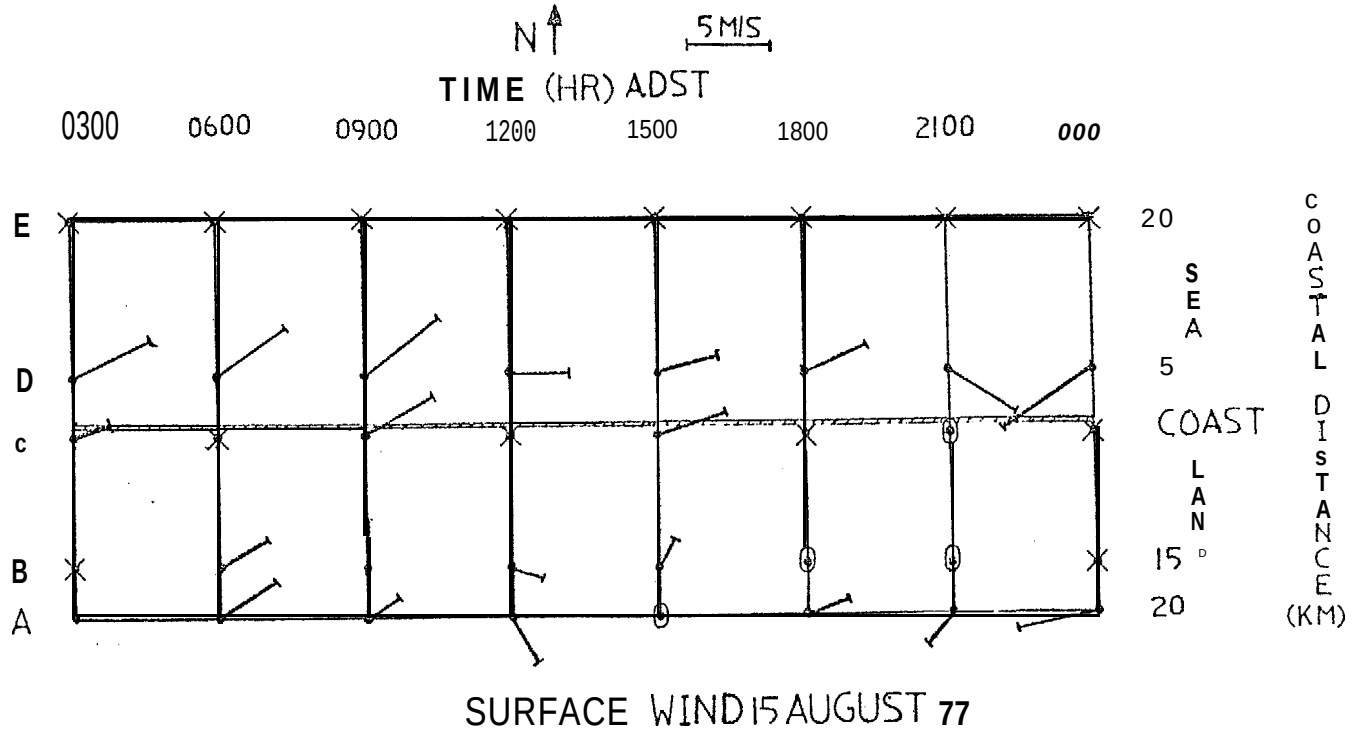

Fig. 32. Three hourly local *surface* wind vectors for designated stations (as in Figure 30) on August 15, 1977. The geostrophic wind was 220°T at 3 m/s for 1500 ADST.

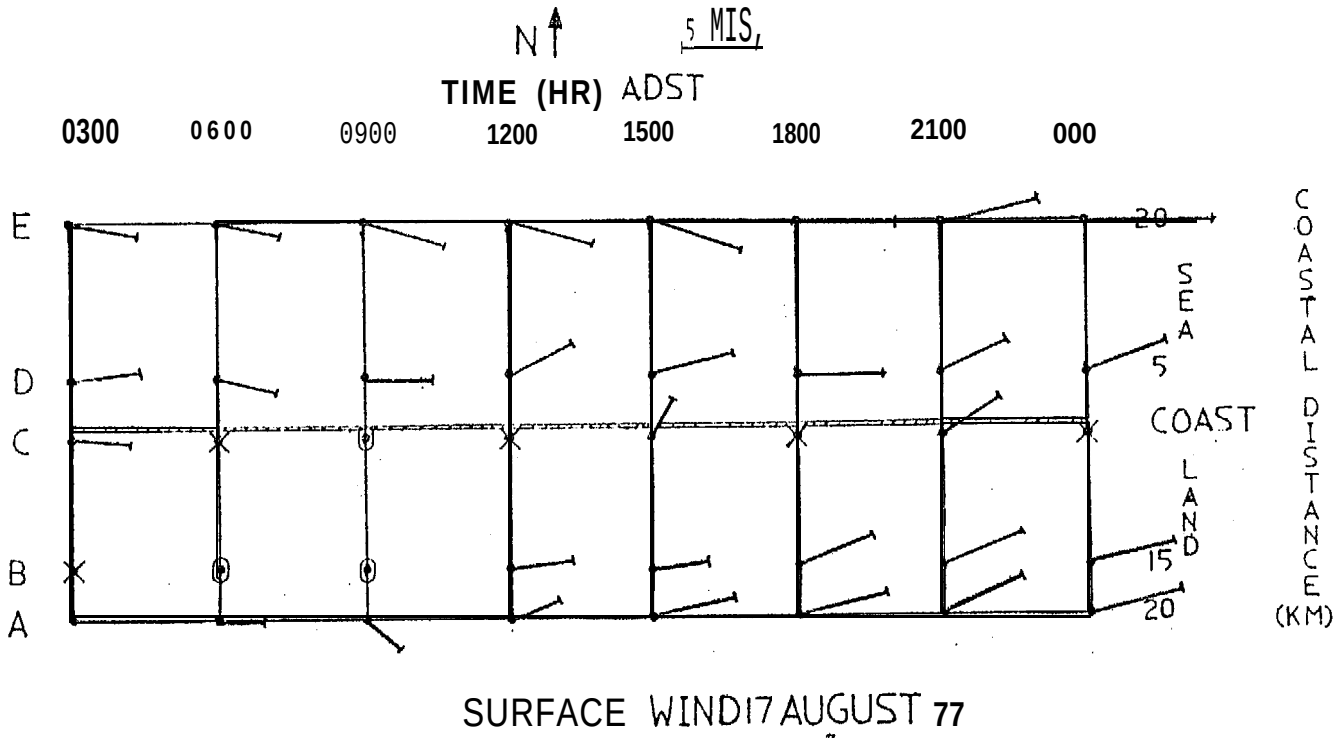

Fig. 33. Three hourly local surface wind vectors for designated stations (as in Figure 30) on August 17, 1977. The geostrophic wind was 110°T at 4 m/s for 1500 ADST .

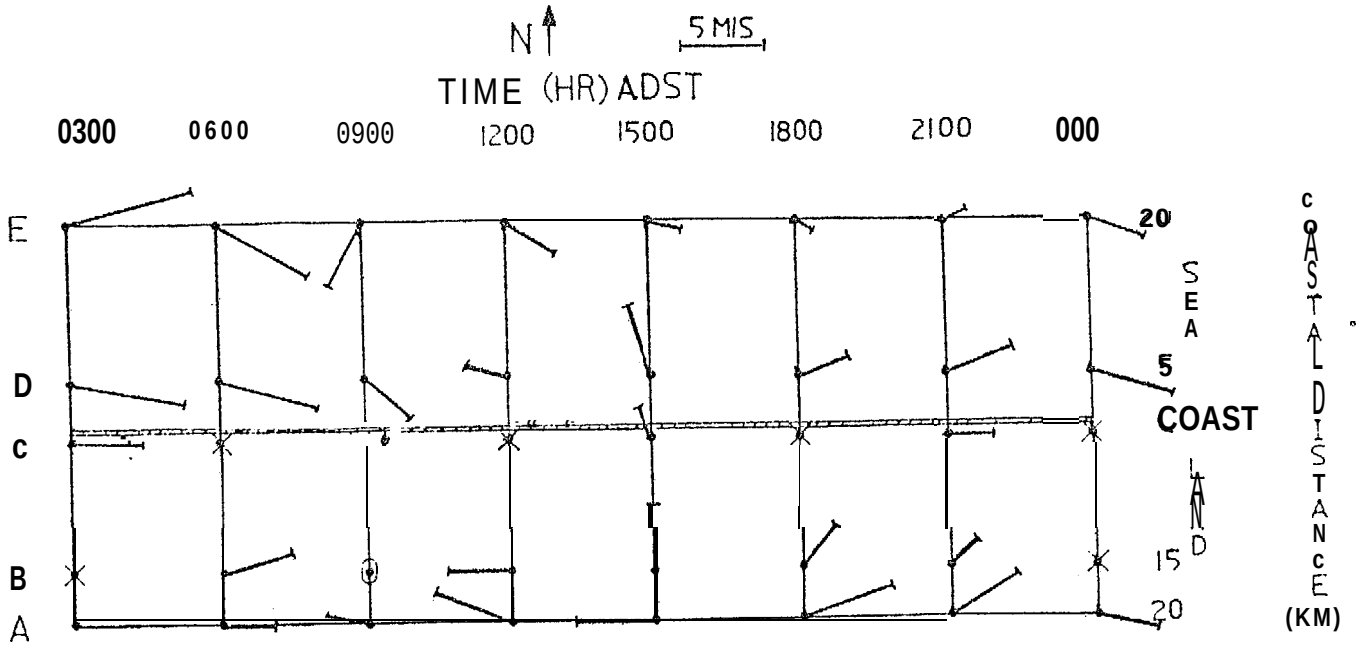

SURFACE WIND 19 AUGUST 77

Fig. 34. Three hourly local surface wind vectors for designated stations (as in Figure 30) on August 19, 1977. The geostrophic wind was 260°T at 4 m/s for 1500 ADST .

70°. The sea breeze influence appeared to reach the stations most distant from the coast later and diminished later. ARCO Airport experienced a 3° drop in temperature from 1500 to 1700 after the wind changed to the east from the southeast.

August 17, 1976 (calculated geostrophic wind, 226.7°T and 3.2 m/s; 1500 AllST) is seen in Figure 28 with local wind vectors, positions and times as indicated. All five of the sites had wind vectors that exhibited a clockwise rotation from 1500 (maximum sea breeze influence) to midnight while the 0900 to 1500 time period had generally counterclockwise surface wind rotation, The computed geostrophic wind direction for midnight was 137°T and 2.2 m/s. The rotation of the computed geostrophic wind was counterclockwise 110° from 1500 to midnight. In this case the geostrophic winds (free stream) were very weak and should have had limited influence on the sea breeze rotation.

August 20, 1976 (calculated geostrophic wind, 245.1°T and 4.48 m/s, 1500 ADST) is seen in Figure 29 with local wind vectors, positions, and times as indicated, The wind vectors from five sites exhibited counterclockwise rotation until 1500 and clockwise rotation thereafter until midnight. The computed geostrophic wind direction was 246°T and 9 m/s by midnight, indicated a steady geostrophic direction with a doubling of speed. This is a definite example of the sea breeze causing both clockwise and counterclockwise rotation and maintaining an easterly wind component when a westerly component should have prevailed. ARCO Airport data showed a temperature that peaked at 1300 and did not increase until 1900 when the wind began to assume its normal gradient direction.

August 7, 1977 (Figure 30) is labeled as the previous figure and

has a geostrophic wind (pilot balloon data) from 280°T and 2 m/s (1500 ADST). The data from all stations show a general clockwise rotation from early morning until midnight as the sea breeze influence forced the northwesterly wind to a more northerly direction and finally, to the northeast quadrant. The free stream wind velocity was 5.5 m/s from 265°T at 1710 ADST (pilot balloon data) to maintain a steady direction with a speed increase, while the surface winds showed at least 60° of clockwise rotation, The surface temperature dropped 4.5°C by 1700 at ARCO Airport as the wind approached a northwesterly direction.

August 14, 1977 (Figure 31) had a weak geostrophic wind shown on PBD (pilot balloon data, Figure 15) of less than 2 m/s from 180°T in the morning until 1427, which changed to a moderate wind of 5 m/s and 90°T by 1815 in the later afternoon. This was 90° clockwise rotation of the free stream wind vector in a time period of four hours. The data from land-based stations show that the sea breeze did not dominate the local wind vector until 1300 (not shown in Figure 31) while the seaward station at Cottle Island was already influenced by 0900. ARGO Airport data showed a 3.5°C drop in temperature from 1300 to 1600 ADST as the wind went from null to 3 m/s from the northeast, This is an example of a weak offshore gradient wind "stalling" the advancement of the sea breeze front, but nevertheless allowing the sea breeze to build. After 1800, the sea breeze and the geostrophic wind were aligned in the same direction which inhibited further rotation of the local wind vectors (see Chapter V).

August 15, 1977 (Figure 32) has a geostrophic wind shown on PBD (Figure 13) of 3 m/s from 220°T at 1527 ADST. The local surface wind

vector at Deadhorse (14 km inland) was just showing evidence of sea breeze arrival by 1500, while the stations closer to the coastline (usual area of sea breeze genesis) had surface wind vectors already controlled by the breeze. Later in the evening as the sea breeze strength diminished and the gradient wind increased in speed, the surface wind vectors went back to synoptically controlled directions. The ARCO Airport temperature had no evidence of sea breeze frontal approach.

August 17, 1977 (Figure 33) had very weak gradient winds (PBD, Figure 15) of less than 2 m/s in the morning, which changed to 4 m/s from 110°T by 1523. The surface winds on the seaward side of the coast showed a speed increase over the gradient wind aloft which must be attributed to the sea breeze' dominating in the morning and aligning itself with the gradient wind in mid-afternoon. The afternoon alignment accounts for lack of rotation of the local wind vectors (see Chapter V). A wind speed increase from 3 m/s to 5 m/s in four minutes with a 2°C temperature drop in two hours at ARGO Airport signaled the sea breeze arrival.

August 19, 1977 (Figure 34) had weak gradient winds (PBD, Figure 17) of 4 m/s with a relatively constant direction of 260°T from 1205 to 1500. During this time the Cottle Island and Oliktok surface winds rotated clockwise to become more northerly under the sea breeze influence. Cross Island appears to be under different synoptic situation (located in the northeast corner of the data grid) in a col situation which would account for the morning surface wind (see Figure 22) direction. By 1837 the geostrophic wind has changed to 320°T in a clockwise rotation while the surface wind vectors for all stations (except Cross

Island) have rotated 100° clockwise, In this case Deadhorse, the most inland, "felt" the sea breeze effects last. ARCO Airport temperatures did not. show any abrupt changes which would signify frontal arrival.

2.6 Acoustic Sounder Data

Figure 35 is a facsimile record of acoustic soundings from 0700 ADST on August 20, 1976 to 0200 ADST on August 21, 1976 (sea breeze day) recorded 15 km inland at a site between ARCO and Deadhorse airports. The vertical scale is in meters while the horizontal scale is time (hours). The geometry of real atmospheric waves may differ markedly from the wave shapes on the facsimile records. since the horizontal scale is a time scale. Intermittent dark vertical bands seen extending into the upper parts of the records are due to noise from road and airplane traffic.

During stable conditions, backscatter appears as multi-layered, quasi-horizontal bands. In the case of a ground-based inversion during early morning and late evening hours on clear days (Figure 35, August 26, 1976, from 0100 to 0200) there is one horizontal band from the base of the scale to approximately 100 meters,

Stun (1975) states that when turbulence diminishes in the late evening, subsidence and infrared radiation lower and smooth out the old passive inversion while a new ground-based inversion could be created simultaneously.

During unstable conditions echo patterns can become vertically oriented. The spacing of these echoes may indicate that the convection is organized into thermal plumes. The upper limit of the echoes usually

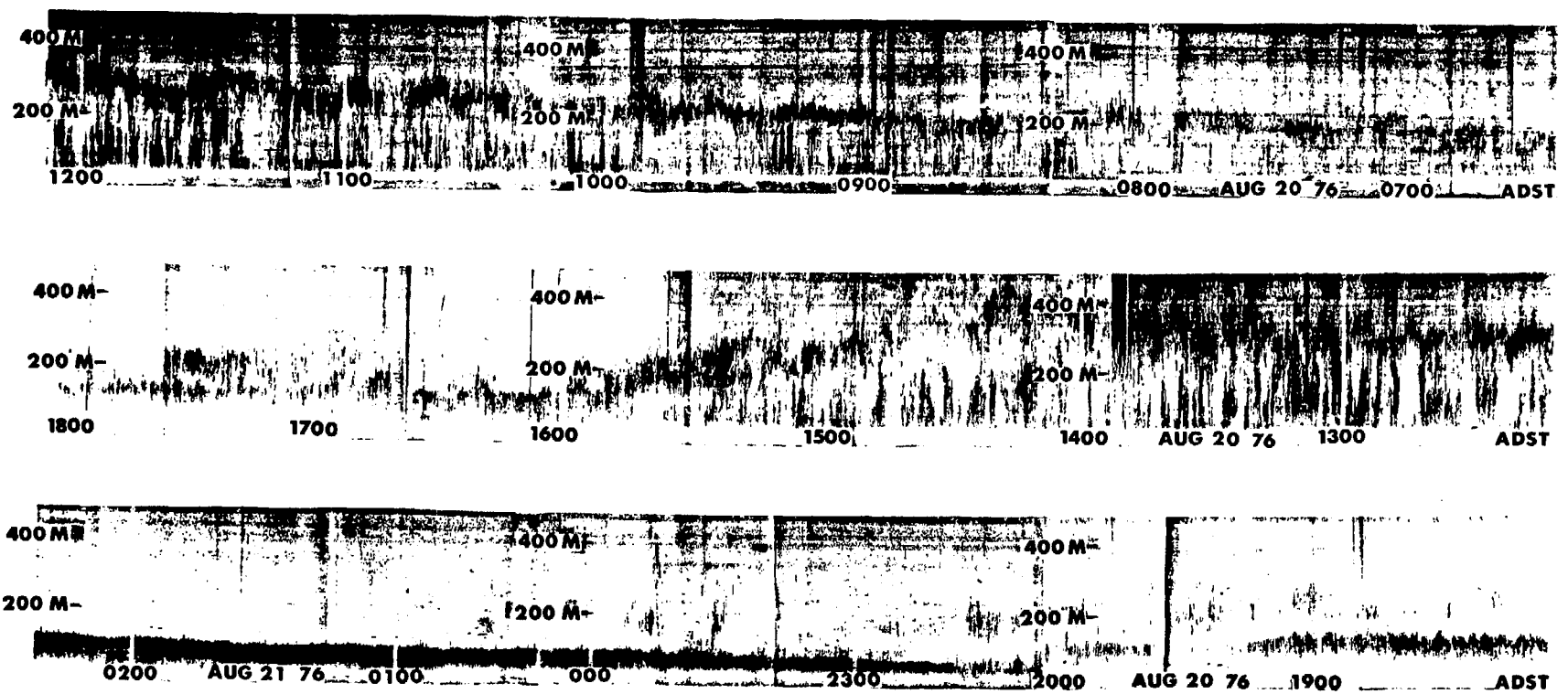
400 M
200 M
1200
1100
1000
0900
0800
AUG 20 76
0700
ADST
400 M
200 M
1800
1700
1600
1500
1400
AUG 20 76
1300
ADST
400 M
200 M
0200
AUG 21 76
0100
000
2300
2000
AUG 20 76
1900
ADST

Fig. 35. Facsimile record of acoustic soundings from 0700 ADST on August 20, 1976 to 0200 ADST on August 21, 1976 (a sea breeze day) recorded 15 km inland at a site between ARCO and Deadhorse Airports.

does not correspond to the maximum range of the convective plumes (unless capped by an inversion). The echoes indicate that the small-tale temperature fluctuations are more marked in the lower part of the plumes and in the superadiabatic surface layer on which the plumes feed (Holmgren, et al., 1974), In Figure 35 the times 1200-1400 ADST show an inversion layer capping thermal. plume activity with an apparent interaction between waves in the inversion and the underlying thermal plumes. It is not known whether the waves are generated by penetrative convection or whether the waves control the thermal convection. This day's data are merely included to show that the boundary layer height (assumed to be contained beneath the inversion) has risen from 100 m in the morning hours to 450 m by1500 ADST (15 km inland), the time of typical sea breeze maxima. The model output will be compared to this data (Chapter IV) for an inland check and Pingok Island soundings for an offshore check on typical inversion heights planetary boundary layer height) during daily sea breeze evolution.

2.7 Synopsis of Chapter II

This chapter has covered the data gathering techniques, the types of equipment, the mathematical tools used to extract additional knowledge by changing the data to a more usable form, and the data themselves, which present both circumstantial and direct evidence of effects due to sea breezes.

The data have shown the maximum time of sea breeze influence to be from 0900 to 2100 LDST, and the landward-seaward influence to cover a zone of at least 38 km. The sea breeze (with no land breeze) has been

shown to increase the persistence of easterly surface winds and to account for part of the asymmetry in the typically bimodal histograms of wind direction for the month of August. Evidence has been presented for advancement or stalling both of the sea breeze front and the local surface wind vector rotation as a result of the prevailing wind field. Data from atmospheric soundings have shown wind speed increases below the inversion layer when the gradient wind and sea breeze were aligned and cases of abnormal boundary layer turning both clockwise and counter-clockwise when the gradient wind and sea breeze were not aligned. Finally, as seen in the acoustic sounder data, the depth of the inversion layer (planetary boundary layer) was altered during a sea breeze day.

While most of these characteristics also apply to a mid-latitude sea breeze, they represent documentation of events at 70°N latitude with a *frequency* of occurrence that makes them a meteorological feature of importance in the Beaufort Sea coastal zone.

III. THE THEORETICAL SEA BREEZE MODEL

3.1 *Sea* Breeze Properties Included in the Mode-l

The sea breeze is air moving inland from the sea in response to differential heating across the coastline. The zone that separates the marine air from the land air often is narrow enough to be considered a sea breeze front. The return flow is weak but over a deep layer above the sea breeze, the circulation is closed by subsidence in the region behind the frontal zone, The differential thermal structure which drives the sea breeze circulation is created by heat input at the ground and distributed aloft by turbulent diffusion. This circulation which develops in response to thermal contrast is thoroughly nonlinear (Geisler and Bretherton, 1969). The landward advected sea air modifies the thermal pattern which initiated it. The range of altitude over which the heat is diffused before the breeze begins, and later ahead of the sea breeze front, is a result of continuing evolution of the circulation. The rate of growth of the circulation is slowed or stopped by surface drag. The sea breeze is usually imbedded in the synoptic scale motion of the atmosphere which alters the differential heating pattern and advects momentum to modify the circulation. Similarly, synoptic scale features of stable stratification limit the altitude range over which heat is diffused and effect the circulation dynamics.

The above properties have been included in a time dependent, nonlinear, two-dimensional numerical model which allows turbulent diffusion of heat and momentum to depend on the *local* velocity and temperature

fields. T-he unique properties of the arctic sea breeze can be studied by the following model which can be conveniently adjusted to simulate experimental data or other possible relevant meteorological circumstances.

3.2 Coordinate System and Domain of Coverage

Figure 36 represents a right-handed coordinate system and the domain of coverage used in the model. The shoreline is straight and parallel to the y-axis (+ y-axis points west) with no variation in the sea breeze along this direction. The x-axis is normal to the shoreline with the (+) axis pointing north. The z-axis is + upward. This vertical cross-section of the atmosphere is bounded at the bottom by the earth's surface and at the top by $z = H$. A variable horizontal grid has values of x = 0, ± 5 km, ± 10 km, ± 20 km, ± 30 km, ± 40 km, ± 50 km, ± 70 km, ± 90 km, ± 120 km and ± 150 km. The lateral boundaries (running north and south) are $x = \pm D$. The magnitudes of H and D have been chosen so that velocity and temperature changes there are negligible. The vertical distance is subdivided into the surface layer, $0 < z \leq h$ = 25 m and the transition layer, $h \leq z \leq H = 1$ km, where the eddy fluxes decrease with elevation.

3.3 Surface Layer Equations

The wind velocity and temperature profiles in the surface layer can be expressed for stable conditions as [see Appendix B for derivations of equations used in this section, and Estoque's (1961) sea breeze paper for greater detail on the procedure that matches the surface layer conditions at $z = h$ to those of the transition layer at $z = h + \Delta z$]:

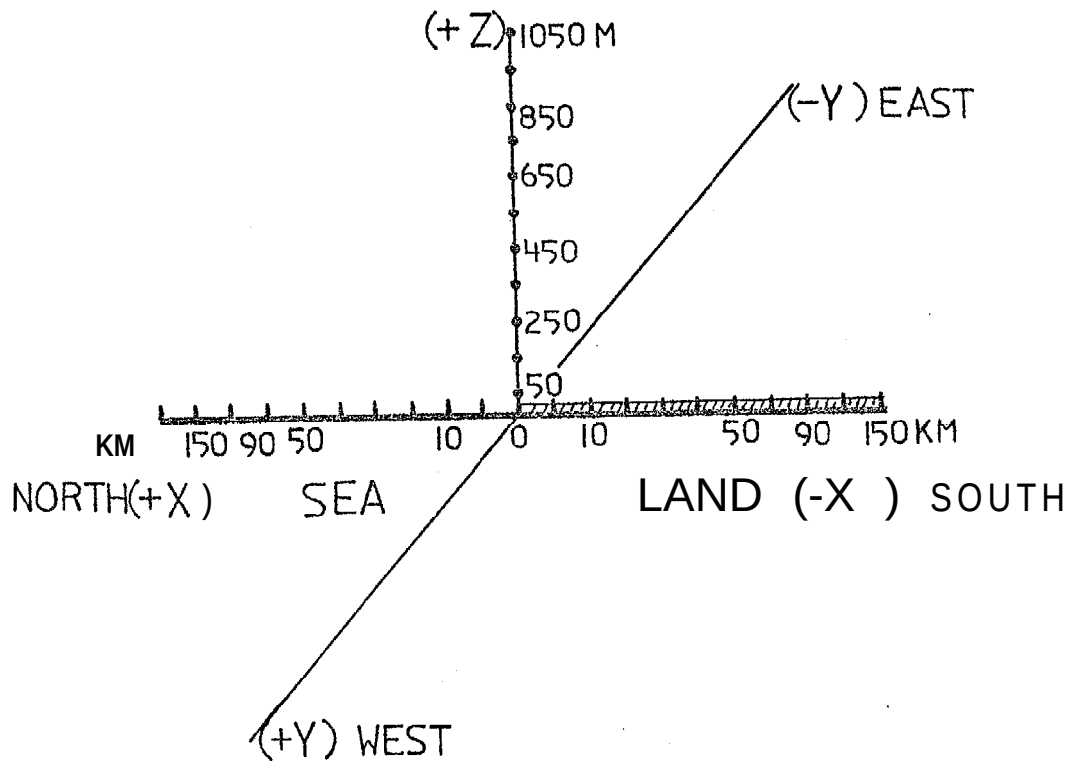

Fig. **36.** Sea breeze model coordinate system and x, y, z domains of coverage.

$$U = \frac{u_*}{k}\left(\ln\frac{z + z_0}{z_0} + 4.7\zeta\right) \tag{3.01}$$

$$\theta = \theta_0 + \frac{\theta_*}{k_0}\left[\ln\frac{z + z_0}{z_0} + 4.7\zeta\right] \quad \text{(see Appendix B)} \tag{3.02}$$

where $U = (u^2 + v^2)^{1/2}$

$\theta \equiv$ potential temperature

The mixing coefficients are defined as

$$K_m \equiv \text{eddy viscosity} = \frac{u_* k z}{1 + 4.7\zeta} \tag{3.03}$$

$K_h \equiv$ eddy thermal diffusion $\approx K_m$

$L \equiv$ Obhukov Length (see Appendix 3)

$\zeta \equiv$ stability parameter $= \frac{z}{L}$

The friction velocity $u_* \equiv \left(\frac{\tau}{\rho}\right)^{1/2}$ can be written

$$u_* = \frac{k\,U(h+\Delta z)(h+z_0)}{\Delta z+(h+z_0)\ \ln\left[\frac{h+z_0}{z_0}\right]}\left\{1 - \frac{4.7g(h+z)[\theta(h+\Delta z) - \theta_0]}{\bar{\theta}\,U(h+\Delta z)^2}\right\} \tag{3.04}$$

The scaling temperature $\theta_* \equiv \frac{\overline{w'\theta'}}{ku_*}$ can be written

$$\theta_* = \frac{u_*[\theta(h + \Delta z) - \theta_0]}{u(h + \Delta z)} \quad (h + \Delta z \equiv \text{first level above surface layer}) \tag{3.05}$$

The momentum flux for the surface" layer at h is u_*^2, while the sensible heat flux is $u_*\theta_*$.

$K(h)$ where $Km(h) \approx K_h(h) = K(h)$, on application of $Km\left[\frac{\partial u}{\partial z}\right]_h = u_*^2$ can be written

$$K(h) = u_* \, k(h+z_0) \left\{1 + \frac{4.7(h+z_0)}{L}\right\}^{-1} \tag{3.06}$$

The profiles for unstable conditions in the surface layer are:

$$U = \frac{u_*}{k}\left(\ln \frac{z+z_0}{z_0} - \psi_1\right) \tag{3.07}$$

where $\psi_1 = 2\ \ln[(1+x)/2] + \ln[(1+x^2)/2] - 2\ \tan^{-1}(x) + \frac{\pi}{2}$

and $x = \left(1 - 15\ \frac{z}{L}\right)^{1/4}$

$$\theta = .74\ \frac{\theta_*}{k}\left\{\ln \frac{z+z_0}{z_0} - \psi_2\right\} + \theta_0 \tag{3.08}$$

where $\psi_2 = \ln[(1+y)/2]$, $y = .74(1 - 9\ \frac{z}{L})^{1/2}$

and θ_0 is the temperature at $z = 0$ (after Paulson, 1970).

The missing coefficients are defined as:

$$K_m = u_* \, k \, z \left\{ 1 - 15\ \mathrm{Ri} \right\}^{1/4} \tag{3.09}$$

$$K_h = \frac{u_* \, k \, z}{.74} \left\{ 1 - 9\ \mathrm{Ri} \right\}^{1/2} \tag{3.10}$$

Here Ri = Richardson number $\equiv \frac{g}{\left[\frac{\partial u}{\partial z}\right]^2} \frac{\frac{\partial \theta}{\partial z}}{}$ and $k \equiv$ Von Karman's constant.

The form of the K's has been taken from Businger, et al. (1971), with Ri $\approx \frac{z}{L}$ for unstable conditions.

The friction velocity u_* is written as

$$u_* = \frac{u_* = k(h+\Delta z)\ U(h+\Delta z)}{\ln \frac{h+\Delta z}{z_0}\left\{\Delta z(1-15\ \mathrm{Ri})^{-1/4} + \left(-\frac{4}{45}\ \frac{h}{\mathrm{Ri}}\right)\left[(1-15\ \mathrm{Ri})^{3/4}-1\right]\right.} \tag{3.11}$$

and the scaling temperature as

$$\theta_* = \frac{k\,(h+\Delta z)\,[\theta(h+\Delta z) - \theta_0]}{\ln\left(\frac{h+\Delta z}{z_0}\right)\left\{\Delta z\left[.74(1-9\ \mathrm{Ri})^{-1/2}\right]+\left(.74\,\frac{-2h}{9\mathrm{Ri}}\right)\left[(1-9\ \mathrm{Ri})^{1/2}-1\right]\right\}} \tag{3.12}$$

Again, the momentum flux for the surface "layer at h is u_*^2 while the sensible heat flux is $U_*\theta_*$.

The momentum flux yields an expression for the eddy viscosity at h:

$$K_m(h) = \frac{u_*^2}{\left(\frac{\partial u}{\partial z}\right)_h} = k\,u_*(h+z_0)\left\{1 - 15\,\frac{h}{L}\right\}^{1/4} \tag{3.13}$$

The sensible heat flux yields an expression for the eddy thermal diffusion coefficient at h:

$$K_h(h) = \frac{u_*\theta_*}{\left(\frac{\partial\theta}{\partial z}\right)_h} = k\,u_*(h+z_0)(.74)\left\{1 - 9\,\frac{h}{L}\right\}^{1/2} \tag{3.14}$$

These fluxes at h for the stable and unstable conditions are set equal to the fluxes in the $h \leq z \leq h + \Delta z$ layer by the following approximation after Estoque **(1963)**:

$$\left[\frac{K(h)+K(h+\Delta z)}{2}\right]\left[\frac{U(h+\Delta z)-U(h)}{\Delta z}\right] = \left(K\,\frac{\partial u}{\partial z}\right)_h = u_*^2 \tag{3.15}$$

$$\left[\frac{K(h)+K(h+\Delta z)}{2}\right]\left[\frac{\theta(h+\Delta z)-\theta(h)}{\Delta z}\right] = \left(K\,\frac{\partial\theta}{\partial z}\right)_h = \theta_* u_* \tag{3.16}$$

Equations (3.06) for the stable case and (3.13) and (3.14) for the unstable case are combined with (3.15) and (3.16) plus known values of $K_h(h+\Delta z)$, $K_m(h+\Delta z)$ (given by a linear decrease with height from $z = h$ to

z = the boundary layer height), $\theta(h+\Delta z)$ and $U(h+\Delta z)$, (model input). With these we can solve for $\theta(h)$ and $U(h)$. To obtain the wind components a constant direction from $z = h$ to $z = h+\Delta z$ is assumed, resulting in

$$u(h) = \frac{U(h)}{U(h+\Delta z)}\, u(h+\Delta z) \tag{3.17}$$

$$v(h) = \frac{U(h)}{U(h+\Delta z)}\, v(h+\Delta z) \qquad \text{(Estoque, 1963)} \tag{3.18}$$

3.4 Upper Sublayer Equations (transition layer)

The equations for the upper layer $h \leq z \leq H$ can be derived using the following equations where each dependent variable is the sum of a given large scale synoptic component (subscript L) and a disturbance (primed quantity, due to sea breeze). Therefore, $u = u_L + u'$, $v = v_L + v'$, $\theta = \theta_L + \theta'$ etc.

$$\frac{\partial(u_L+u')}{\partial t} + (u_L+u')\frac{\partial(u_L+u')}{\partial x} + (w_L+w')\frac{\partial(u_L+u')}{\partial z} = - \frac{R(T_L+T')}{(P_L+P')}\frac{\partial(P_L+P')}{\partial x} + f(v_L+v') + \frac{\partial}{\partial z}\left[K_m \frac{\partial(u_L+u')}{\partial z}\right] \tag{3.19}$$

$$\frac{\partial(v_L+v')}{\partial t} + (u_L+u')\frac{(v_L+v')}{\partial x} + (w_L+w')\frac{(v_L+v')}{\partial z} = - \frac{R(T_L+T')}{(P_L+P')}\frac{\partial(P_L+P')}{\partial y} - f(u_L+u') + \frac{\partial}{\partial z}\left[K_m \frac{\partial(v_L+v')}{\partial z}\right] \tag{3.20}$$

$$\frac{(P_L+P')}{\partial z} = \frac{-(P_L+P')g}{R(T_L+T')} \tag{3.21}$$

$$(P_L+P') = (\rho_L+\rho')\, R(T_L+T') \tag{3.22}$$

$$\frac{\partial(\theta_L+\theta')}{\partial t} + (u_L+u')\frac{\partial(\theta_L+\theta')}{\partial x} + (w_L+w')\frac{\partial(\theta_L+\theta')}{\partial z} = \frac{\partial}{\partial z}\left(K_h \frac{\partial(\theta_L+\theta')}{\partial z}\right) \tag{3.23}$$

$$\theta = T\left(\frac{P_0}{P}\right)^{R/c_p} \tag{3.24}$$

$$\frac{\partial(u_L+u')}{\partial x} + \frac{\partial(w_L+w')}{\partial z} = 0 \tag{3.25}$$

t is time, x, y and z are spatial coordinates, and u, v and w are the corresponding velocity components in these directions. θ, P, p, T, P_0, g, f, R and C_p are potential temperature, pressure, density, Kelvin temperature, reference pressure, gravitational acceleration> Coriolis parameter, gas constant, and specific heat at constant pressure. All variables are assumed constant in the y-direction, except that a large-scale pressure gradient may exist in the y-direction above the surface layer. The eddy diffusivity terms start at a value equal to that at the top of the lower layer, $z = h$, and decrease to zero at the boundary layer top. The full vertical momentum equation is replaced by the hydrostatic approximation (Eq. 3.21) which is reasonable when the ratio of horizontal to vertical grid lengths is $\geq$ 3 (Physick, 1976; Neumann and Mahrer, 1975). The ratio in the model is greater than 50 for all" levels.

The continuity equation (3.25) is in the incompressible form which is acceptable when the atmospheric motion (sea breeze rarely exceeds 2 km depth) are confined to a depth which is much less than the scale of

density variation in the vertical (scale height . 8 km). These assumptions, although valid, cause a problem when the vertical velocity component is computed from Eq. 3.12. This is a first order partial differential equation in z. Therefore, no unique solution can be obtained since there are two boundary conditions, i.e., w = 0 for z = 0 and $z = H$, available for the vertical motion (Sheih and Moroz, 1975). Since in *sea* breeze studies (particularly the arctic) the flow field near the ground is the important one; the integration will be performed from the ground upward and only the lower boundary condition used.

For

$$w_L = 0 , \quad \frac{\partial u_L}{\partial x} \quad \frac{\partial v_L}{\partial x} = \frac{\partial \theta_L}{\partial x} = \frac{\partial u_L}{\partial y} = \frac{\partial v_L}{\partial y} = \frac{\partial \theta_L}{\partial y} = 0 ,$$

$$\frac{\partial P_L}{\partial z} = - \frac{P_L g}{RT_L} , \quad \frac{\partial u_L}{\partial x} + \frac{\partial w_L}{\partial z} = 0$$

$$+ \frac{RT_L}{P_L} \frac{P_L}{\partial x} = f v_L , \quad \frac{RT_L}{P_L} \frac{P_L}{\partial y} = -f u_L \text{ (geostrophic approximation)}$$

and

$$\frac{\partial u_L}{\text{at}} \quad \frac{\partial v_L}{\text{at}} = \frac{\partial \theta_L}{\text{at}} = 0 \text{ (mesoscale < 24 hrs.)}$$

the prediction equations for the sea breeze can be written: (note: $u = u_L + u'$, $v = v_L + v'$, $\theta = \theta_L + \theta'$, etc., and $(RT_L/P_L)\,\nabla P_L \simeq (RT/P)\,\nabla P_L$

$$\frac{\partial u'}{\text{at}} = f v' - \frac{RT}{P} \frac{\partial P'}{\partial x} + \frac{\partial}{\partial z} \left[K_m \frac{\partial u}{\partial z} \right] - u \frac{\partial u'}{\partial x} - w' \frac{\partial u}{\partial z} \tag{3.26}$$

$$\frac{\partial v'}{\text{at}} = - f u' + \frac{\partial}{\partial z} \left(K_m \frac{\partial v}{\partial z} \right) - u \frac{\partial v'}{\partial x} - w' \frac{\partial v}{\partial z} \tag{3.27}$$

(the mesoscale disturbance is assumed to have no y dependence)

$$\frac{P'}{z} = \frac{-qP}{RT} + \frac{qP_L}{RT_L} \tag{3.28}$$

$$\frac{\partial \theta'}{\partial t} = -u\frac{\partial \theta'}{\partial x} - w'\frac{\partial \theta}{\partial z} + \frac{\partial}{\partial z}\left(K_h \frac{\partial \theta}{\partial z}\right) \tag{3.29}$$

$$\frac{\partial w'}{\partial z} = -\frac{\partial u'}{\partial x} \tag{3.30}$$

The Eqs. (3.26) to (3.30) are a set of equations which can be integrated numerically if the synoptic scale wind and temperature fields are given. They are essentially the same as those used by Estoque (1962) except that the expressions for X_m and K_h differ and the equation of continuity is not differentiated with respect to z a second time.

The eddy diffusivity terms of Estoque were defined for a stable boundary layer and for a free convective boundary layer with no intermediate transition expressions for unstable conditions. Also, Estoque's twice-differentiated incompressible form of the continuity equation does not satisfy the law of conservation of mass (Peterson, 1970; Neumann and Mahrer, 1971).

The prediction equations in finite-difference form are derived in Appendix A.

3.5 Initial and Boundary Conditions

The external boundary conditions at the lateral extremities, $x = \pm D$, are:

$$\frac{\partial}{\partial x}(u', v', p', \theta') = W' = 0 \quad \text{(where } D = 150 \text{ km)}$$

at the top, z = H, are:

$$p' = u' = v' = T' = \theta' = 0 \quad \text{(excluding } w') \quad \text{(where } H = 1050 \text{ km)}$$

with vertical gradients and horizontal gradients of all variables except pressure = 0

and at the earth's surface, z = 0, are:

$u = v = w = 0$ (Note: to be more precise, the conditions $u=v=0$ apply at $z=z_0$, the surface roughness length, and are implicit in development of the surface layer equations)

with all horizontal gradients except for pressure = 0 and

$$\theta = \theta(x,t) .$$

The initial conditions are $u' = v' = T' = 0$ at $t = 0300$ while the large-scale velocity, temperature, and pressure fields are specified (see below) and held constant during the integration period.

The internal boundary conditions at $z = h$ require continuity of the wind velocity and temperature and their respective fluxes. To insure that fluxes in the surface layer are applied at $z = h + \Delta z$ (upper sub-level), the fluxes in the layer from $z = h$ to $z = h + \Delta z$ are set equal to those in the surface layer (Δz = 25 m). This method of matching fluxes was seen in Eqs. (3.15) and (3.16) above.

3.6 The Numerical Integration Procedure

The integration is performed in the upper layer ($h \leq z < H$) only, with the following steps depending on surface layer conditions:

a. Using given initial values for T', u' and v' at the lowest gridpoint ($z = h + \Delta z$) and the boundary value for temperature at the ground, the values of u', v', θ', and K at $z = h$ are computed from equations in section 3.3. Note: primes are the disturbance values.

b. Compute the pressure distribution (p') by integrating Eq. (3.28) downward from $z = H$ where $p' = 0$ using given values of T', T_L and P_L.

c. Compute the w' distribution using Eq. (3.30) and the given initial u' distribution.

d. Compute $\frac{u'}{\partial t}$, $\frac{v'}{\partial t}$ and $\frac{\partial \theta'}{\partial t}$ using Eqs. (3.26), (3.27) and (3.29), respectively.

e. These result in a new u', v', and θ' (canbe converted to T'), depending on the time interval of integration (2 to 5 minutes).

f. Repeat steps a to e until the desired time period *is* reached.

As mentioned above, the finite difference methods are shown in Appendix A and are used in normal fashion except for bridging the $z = h$ to $z = h + \Delta z$ layer. The following finite-difference analog (for the vertical temperature diffusion term) has been suggested by Estoque (1973)

$$\frac{\partial}{\partial z}\left(K \frac{\partial \theta}{\partial z}\right) = \frac{\bar{K}\left(\frac{\theta_{h+\Delta z} - \theta_h}{\Delta z}\right) - \left(K_h \frac{\partial \theta}{\partial z}\right)_h}{\Delta z/2} \tag{3.31}$$

where

$$\bar{K} = \frac{\left(K_{h+\Delta z} + K_h\right)}{2} \text{ and } \left(K_h \frac{\partial \theta}{\partial z}\right)_h$$

is the flux in the surface layer. The same type analog applies for the u and v equations.

3.7 Input to the Model

The model starts at zero disturbance wind velocity at 0300 (August arctic sunrise) and is driven by differential heating of the earth's surface. Therefore, attention must be given to the surface heating function. Haurwitz (1947) mentions that the diurnal surface temperature curve follows a simple harmonic function in daytime, but not at night when nocturnal cooling precedes at a different rate. As a result of this characteristic, a simple harmonic heating function is not satisfactory over a 24-hour period. The forms of the diurnal temperature functions at various elevations in the air and various depths in the ground have been delineated by Kuo *(1968).*

Air temperature records from coastal stations have limited use in sea breeze work when used to obtain land-sea temperature differences since advection of cold marine air by the breeze will alter the diurnal temperature wave. Temperatures obtained from Prudhoe (15 km inland) and Umiat (100 km inland) air fields (Stevenson screen temperature - 1.3 meters above the ground) were utilized to obtain more representative land-sea differences. Helicopter flights inland indicated minimal temperature increases from 30 km inland to Umiat (100 km inland). This factor was used to shape the model temperature function (see below) from 30 km to 150 km inland. Walsh (1977) reported radiometric surface

temperatures near Pt. Barrow from the coast to 50 km "inland for three days in July 1975 (at 1500 ADST). He found the land-sea temperature difference at the coast to average 12°C and inland surface temperature maxima from 16°C to 24°C. This information coupled with Kuo's (1968) 25°C maximum to minimum range of surface temperature was used to shape the temperature function from the coast to 30 km inland.

The surface heating function for the above-mentioned arctic conditions with $+x$ (northward) from the coast over the sea for 150 km and $-x$ (southward) from the coast over land for 150 km can be written as

(temperatures in Kelvin degrees)

$$\text{at } z = 0 \begin{cases} T = 273 & \text{water } x > 0 \\ T = 273 + .5\ (25)\ (\text{ARG}) & \text{coastline } x = 0 \\ T = 273. + 18\ \{\text{ARG}\} & x' \text{ -5 km} \\ T = 273. + 20\ \{\text{ARG}\} & \text{land } x = \text{-10 km} \\ T = 273. + 24\ \{\text{ARG}\} & x = -20 \text{ km} \\ T = 273. + 25\ \{\text{ARG}\} & x \leq -30 \text{ km} \end{cases} \tag{3.32}$$

where

$$\text{ARG} = .47 \sin (15\, t + 265) + .15 \sin (30\, t + 102) + \\ + .08 \sin (45\, t + 306) + .36 \tag{3.33}$$

This is a tri-harmonic fit to Kuo's (1968) surface temperature plot modified for the arctic by keeping the temperature over land > 273°K (greater than the ocean temperature) for the entire 24-hour period. The maximum temperature contrast (between the sea and land) at the coast is 12.5 C at 1500 ADST and reaches 25°C at 30 km inland.

The large-scale temperature field (from radiosonde data), held constant during the integration. is represented by a linear increase in temperature from the surface (273°K) to 150 m (283°K) where it is isothermal to 550 m. From 550 m on, the temperature has a lapse rate of .6°K/100 m. These values are the same for each horizontal level in the model from +150 km to -150 km.

The large-scale pressure field on O synoptic wind days is taken from tables of the U.S. Standard Atmosphere (Berry, et al., 1945) to level $H = 1050$ m. On model runs with a geostrophic wind, a pressure distribution is imposed at each vertical grid level which just balances the given prevailing wind.

The surface roughness z_0 is approximated by .001 m and .01 m for water and land, respectively.

3.8 Additional Numerical Techiques

A two-step dampening spatial filter is applied twice every 10 time steps of the form

$$\bar{\alpha}_x = \alpha_x + 1/4 \left(\alpha_{x-\Delta x} - 2\alpha_x + \alpha_{x+\Delta x}\right)$$

$$\bar{\bar{\alpha}}_x = \bar{\alpha}_x - 1/4 \left[\bar{\alpha}_{x-\Delta x} + 2\bar{\alpha}_x + \bar{\alpha}_{x+\Delta x}\right] \qquad (3.34)$$

This method used by Physick (1976) simulates the energy cascade from the shortest wavelength ($2\Delta x$) able to be resolved by the grid to subgrid scale waves where dissipation eventually occurs in the real atmosphere. Physick states that application of this filter ensures that the energy of the shortwaves never becomes great enough to cause numerical instabilities in the model while simultaneously ensuring that longer

wave amplitudes are not reduced significantly. Work by Shapiro (1971) has shown that this filter type can be used to act in place of an explicit horizontal diffusion term in numerical model equations and essentially leaves waves of four grid-lengths or larger unaffected. The top equation in (3.34) will act to damp out waves of two grid-lengths, but will reduce the amplitude of four grid-length waves by .5. Since this is not satisfactory, the bottom equation in (3.34) is used, which restores amplitude to the waves greater than two grid-lengths (Francis, 1975) .

Two time step restrictions (Deardorff, 1973) are checked as the model runs. The first in the linear advective instability criterion:

$$\Delta t < \text{minimum } \{\Delta x/u_{max}, \Delta y/v_{max}, \Delta z/w_{max}\}$$

which is easily satisfied by Δt = 4 minutes since the model has a minimum x of 5 km and a minimum z of 100 meters while u never exceeds 10 m/s and w never exceeds 10 cm/s. The second is the diffusive criterion

$$\Delta t \leq 1/4 \frac{\Delta z^2}{K} \qquad \text{(where } K \text{ is an eddy diffusivity)}$$

For the range of K's encountered At must be 120 seconds or less from 1200 to 1800 ADST, while changing to 300 seconds. for other times when is small. The latter criterion is the most sensitive for this model and has resulted in the use of a variable Δt for the model runs.

An additional feature of this model is that a boundary layer height is determined over land and water after each integration at an appropriate horizontal grid point. When parameters from any two vertical grid points at a given horizontal distance from the coast 'nave a computed Richardson

number greater than 1, that level is considered the height of the planetary boundary layer. The criterion in the case of this model is more restrictive than the one proposed by Anthes (1978), where he defines the height of the planetary boundary layer as the first level above the ground at which the vertical gradient of potential temperature exceeds $1°C\ km^{-1}$. Physick {1976) defines Ri number = 1 as the height limit on convective depth in his model for unstable conditions. It is more realistic than Estoque's (1961) model where he allows his boundary layer to reach 2000 meters regardless of the stability at upper grid levels, and certainly a more reasonable method in the arctic.

In the case of this model the eddy diffusivities are reduced by two orders of magnitude and held constant from the top of the boundary layer to 1050 meters (H). For stable levels from h (25 meters) upward (at given horizontal distances from the coast). the diffusivities are linearly reduced from $h+\Delta z$ to the corresponding variable boundary layer height, while for unstable levels, the diffusivities are held constant until the first stable level is reached and then are linearly reduced from that level to the boundary layer top. In this way the K_h and Km are specified as functions of wind shear and stability at all the model levels within the planetary boundary layer.

3.9 Synopsis of Chapter 111

This chapter has covered the non-linear numerical model setup, imposition of large-scale wind fields, techniques used to maintain numerical stability and formulations of the eddy diffusivity terms within the surface layer under dynamically stable and unstable

atmospheric conditions. Though the model is an offshoot of Estoque's (1961) original sea breeze work, there are some fundamental differences.

Some of these differences have been necessitated by imposing environmental peculiarities of the arctic on the model, such as the initial large-scale temperature field with a strong inversion. This inversion is synonymous with atmospheric stability and internal waves. These waves, if subgrid scale, could be a source of numerical instability, so application of a spatial filter was required. Also, the fact that the land temperatures never fell below the ocean temperature in August led to modification of the heating function.

Other differences were required to reproduce the basic physics more accurately, The transition from a stable boundary layer to one of free convection was replaced by a transition to an unstable boundary layer instead, with a more accurate expression for K_h and K_m. Estoque's (1961) doubly differentiated incompressible continuity equation was replaced by the normal form of the incompressible continuity equation.

Still other modifications were made to simulate environmental conditions more accurately, These were a tri-harmonic heating function with a gradual increase in temperature from the coast to 30 km inland, variable roughness lengths (z_0) for land (.01 m) and water (.001 m) and variable boundary layer heights (computed after each model time step).

The variable time step was used to promote numerical stability (shortened to 2 minutes) during maximum surface heating and for reasons of economy during more stable periods (increased to 5 minutes) in the early morning.

IV. MODEL RESULTS

4.1 Zero Geostrophic Wind (Case 1), Velocity and Temperature Contours

The results of the model integration are first presented for the ideal case of zero geostrophic wind (Figures 37–40) to show some of the basic characteristics of the sea breeze model output for the arctic environment. Prior to 1500, the disturbance winds were very weak, so the model output was not put in graphical form. Note: All model output is shown with a variable linear horizontal distance scale.

Figure 37 represents isotachs (contours of constant velocity) for u, the wind component normal to the shoreline (- represents shoreward flow) . The maximum u component (greater than 3 m/s) occurs by 1800 at 20-25 km inland near the isotach core. There is weak return flow of .5 m/s above 350 m level existing to 1050 meters. Figure 38 shows (cross-section) isotachs of V, the parallel to the coast velocity component with + values representing easterly winds and - values westerly winds. Again, a maximum isoline core (greater than 2 m/s) is seen to exist 20-25 km inland at 1800 hours. The core strength diminishes for both u and v components by 2200 and the winds die down by midnight (0000), the start of the next day. Positive values of v in regions of -u and vice versa, show the extent of clockwise rotation exhibited by the wind vector with time. The rotation rate from 1200 to 2200 was 4°/hr (see Chapter V for discussion of rotation rates).

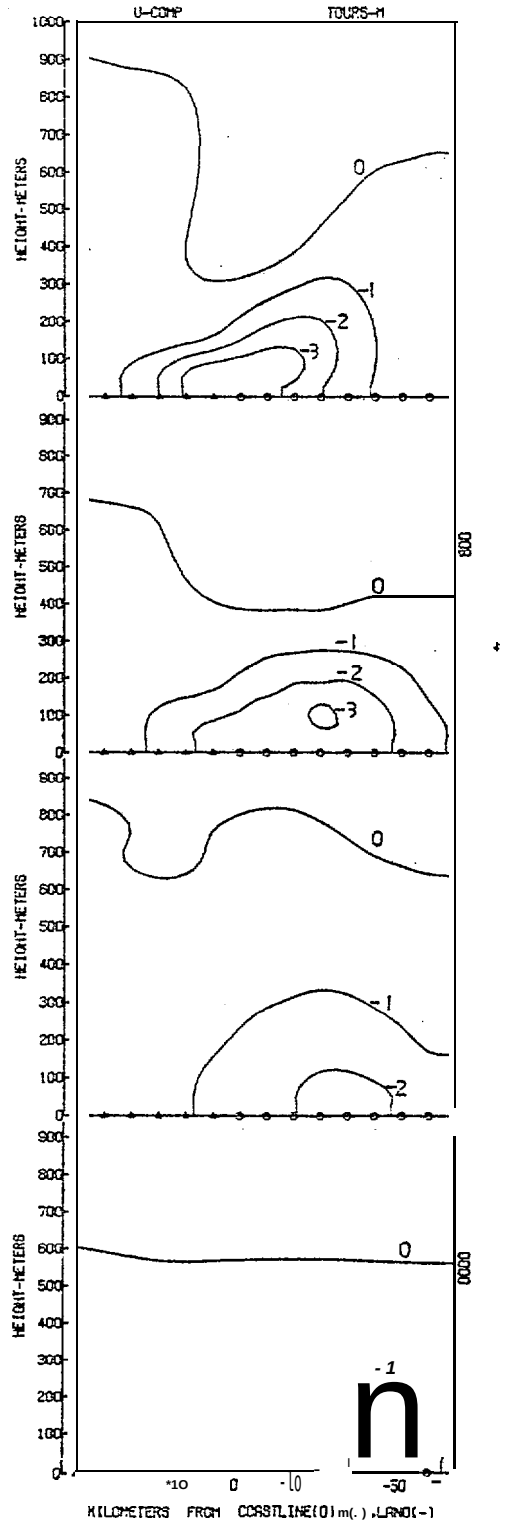

Fig. 37. Model output of isotachs (m/s) Of $U(U_L + U')$ fOr 0 geostrophic wind (U_L = 0). The U component is perpendicular to the coast with (-) values representing shoreward flow (north winds). (Variable horizontal scale.)

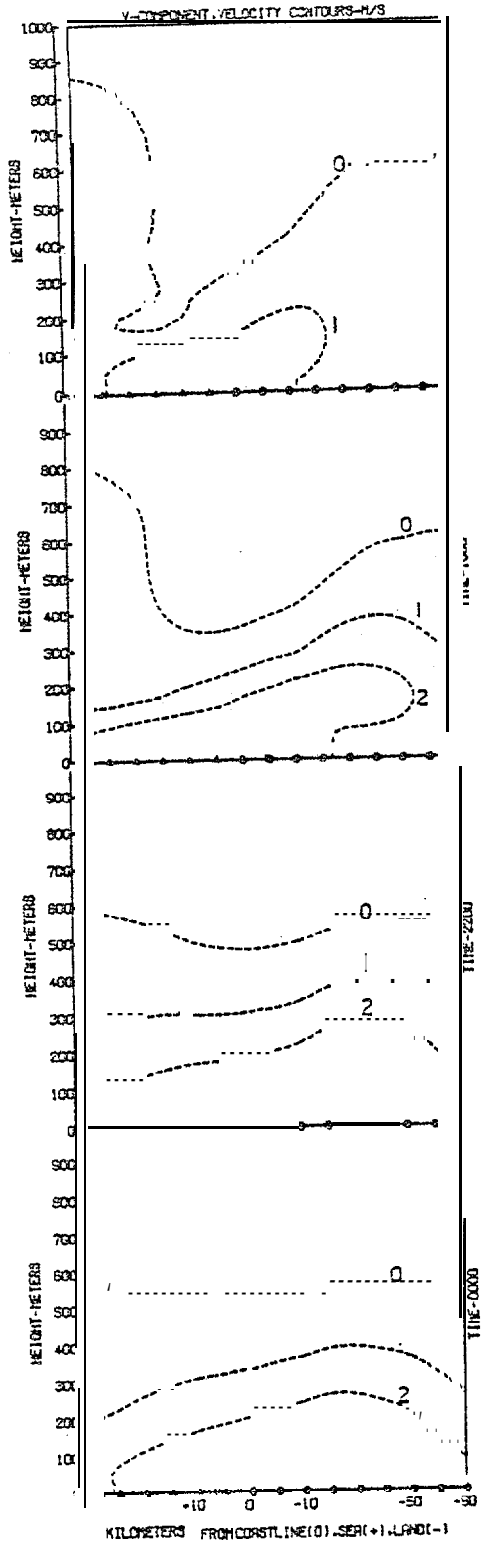

Fig. 38. Model output of isotachs (m/s) (cross section of $(V_L + V')$ for 0 geostrophic wind $(U_L = 0)$. The V component is parallel to the coast with (-) values representing flow into the figure (west winds). (Variable horizontal scale.)

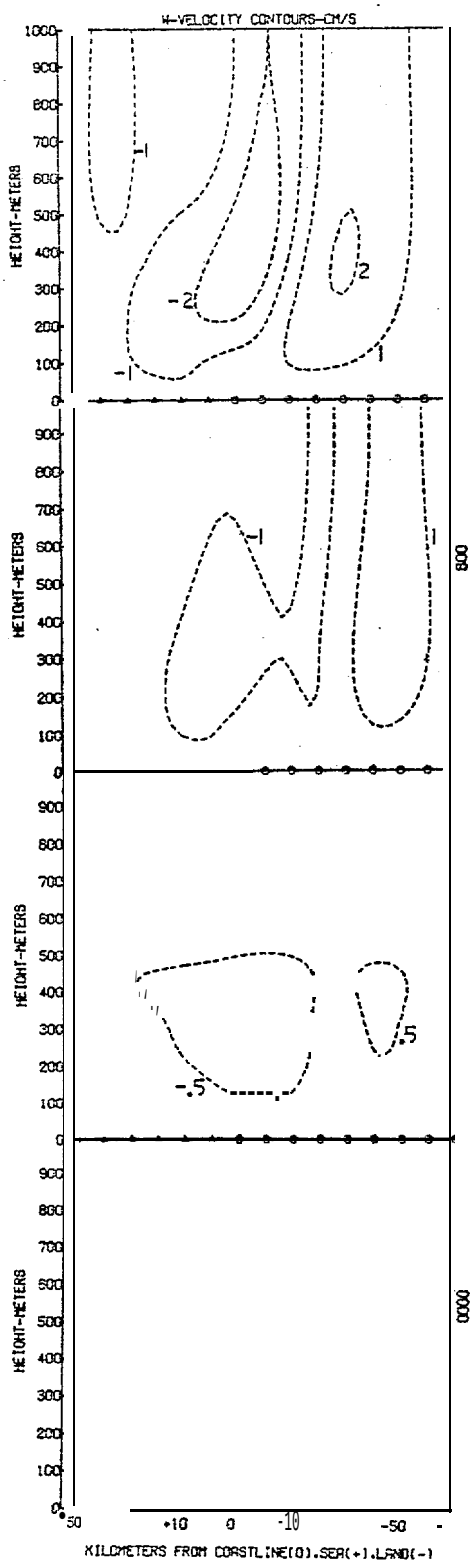

Fig. *39.* Model output of isotachs of w′ (cm/s) for a 0 geostrophic wind. Note: W_L = 0 for all model runs. The W′ component is (+) for upward flow. (Variable horizontal scale.)

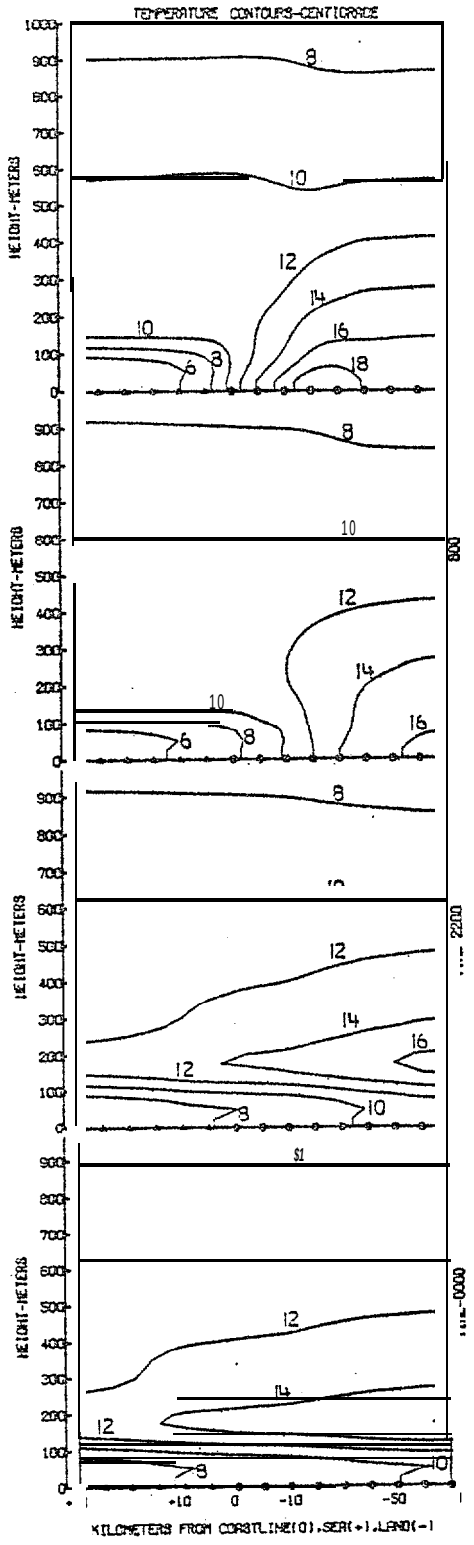

Fig. 40. Model output. of temperature contours (°C) for a 0 geostrophic wind. (Variable horizontal scale.)

The w velocity is a parameter which has not been measured in the field but is shown in the model results to give a qualitative picture of the strength of the vertical circulation and to indicate the existence of a sea breeze front (usually located by the position of the upward maximum w contour). Figure 39 shows the upward flow maximum at 1500 to be *25 km* inland while at 1800 it is 50 km inland. For this case it is also the *2* m/s countour location for the u and v components. Using the upward flow maximum as an indicator of a possible front position, the rate of frontal advance under these 0 synoptic wind conditions is apprxoimately 8 km/hr. This compares favorably with that of Simpson (1964) who measured a frontal advance of 7.2 km/hr on the coastline of the English Channel and Rossi (1957) who measured a frontal advance of. 6 km/hr in the Gulf of Finland (60°N).

The temperature (*C) contours (Figure 40) show a surface-based inversion layer existing over the water throughout the integration period of the model (as radiosonde data show). The above land temperature contours indicate a change from slight static instability at 1500, through neutral by 1800 to establishment of the inversion over both land and water by midnight (0000).

4.2 Geostrophic Wind 270°T, at 3 m/s and 5 m/s (Case 2a and 2b), Velocity and Temperature Contours

Typical gradient wind directions are from the east. or west, thus the model used 3 m/s and 5 m/s large-scale winds from these directions as new input with all other initial conditions the same. The coastline orientation from Oliktok to Prudhoe Bay, which subtends an angle of 115°

clockwise from the north instead of a true east-west orientation of 90°, was incorporated into the model. The 3 m/s cases were chosen to look at breeze development in moderately weak synoptic wind conditions while the 5 m/s cases were chosen to determine if sea breeze circulation could progress when the large-scale winds were of comparable magnitude.

Figures 41-45 were for the cases of geostrophic winds from 270°T at (a) 3 m/s and (b) 5 m/s, respectively. The total velocity vectors ($u^2 + u'$ etc.) in the u ($\perp$ coast flow, 111/s) - w (vertical flow, cm/s) plane are depicted in Figures 4ia and 41b. The circulation pattern in both figures can be seen to progress inland from the coast and decay with time (slower decay in the 5 m/s case). The u component flow is shoreward below 200 m in the sea breeze area while seaward above. The return flow is mainly due to the existence of a u component (southerly) of the geostrophic wind relative to the coastline orientation. The figures 42a and 42b represent isotachs of u for 3 m/s and 5 m/s geostrophic winds, respectively. The planetary boundary layer (PBL) height (determinedly a procedure described in Section 3.4 above) reaches 750 meters over land by 1700 hours while falling within the surface-based inversion layer over water in both figures. The maximum u component (greater than 3 m/s) occurs at the coast for the higher speed synoptic case. The lower speed synoptic case results in a slightly lower u maximum developing 5 km onshore. The maximum velocity core doesn't move inland at the speed shown in Case 1 (above), while the u component near the surface becomes negligible due to interaction of the breeze and the synoptic wind.

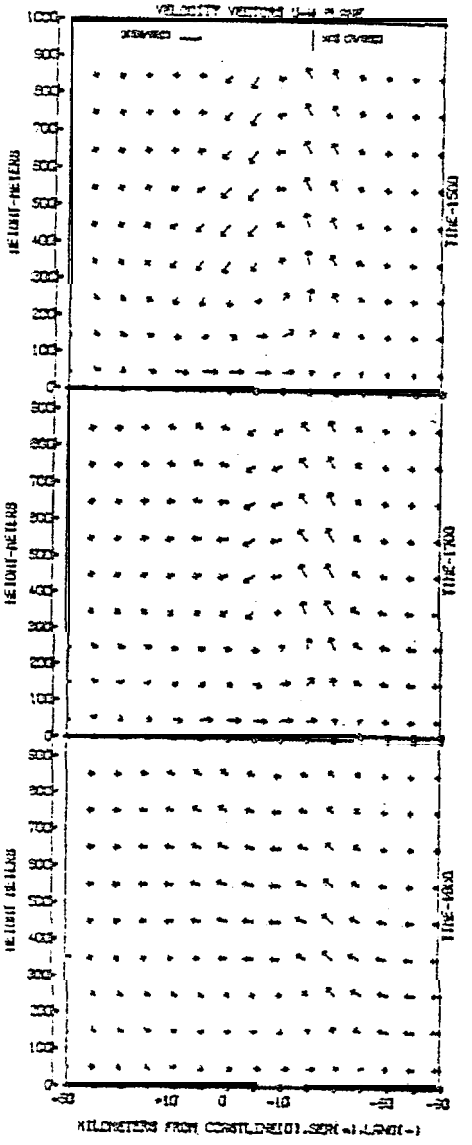

Fig. 41a. Model output of total u-w plane velocity vectors for a 3 m/s geostrophic wind from 270°T. The u component is perpendicular to the coast and the w is the vertical velocity component.(Variable horizontal scale.)

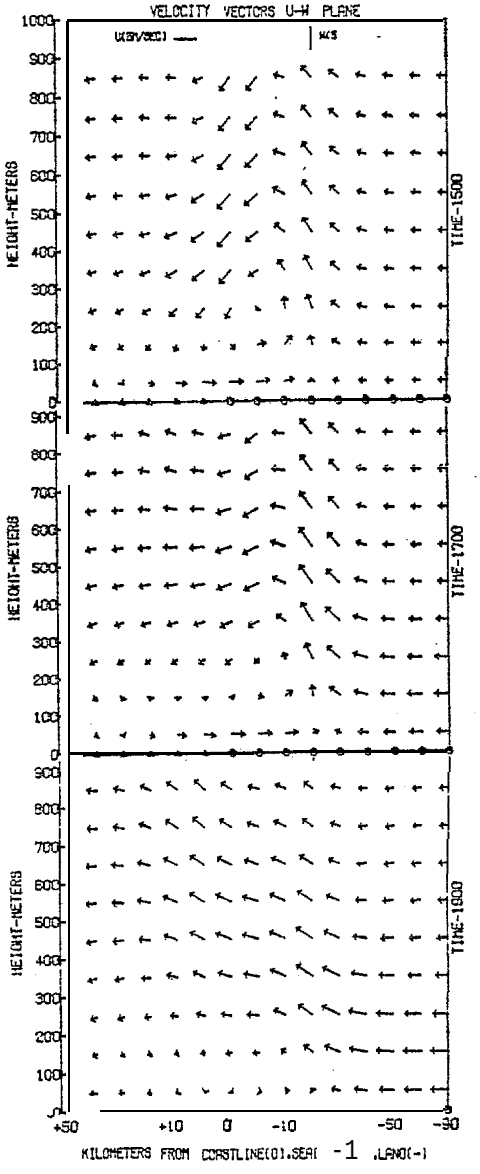

Fig. 41b. Model output of total u-w plane velocity vectors for a 5 m/s geostrophic wind from 270°T. The u component is perpendicular to the coast and the w is the vertical velocity component. (Variable horizontal scale.)

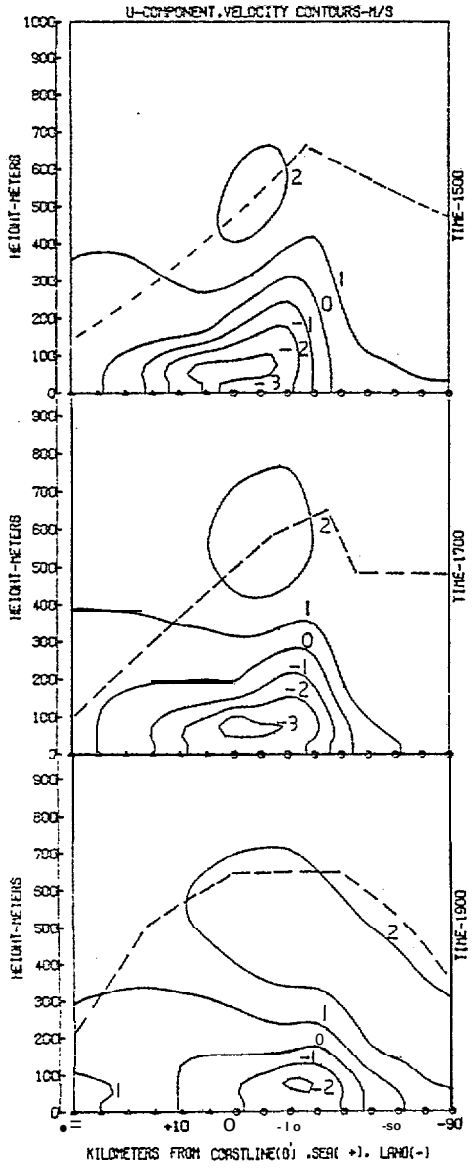

Fig. 42a. Model output of isotachs (m/s) of $U(U_L + U')$ for 3 m/s geostrophic wind from 270°T. The u component is perpendicular to the coast with (-) values representing shoreward flow (north winds). The boundary layer height (PBL) is shown as a dashed line. (Variable horizontal scale.)

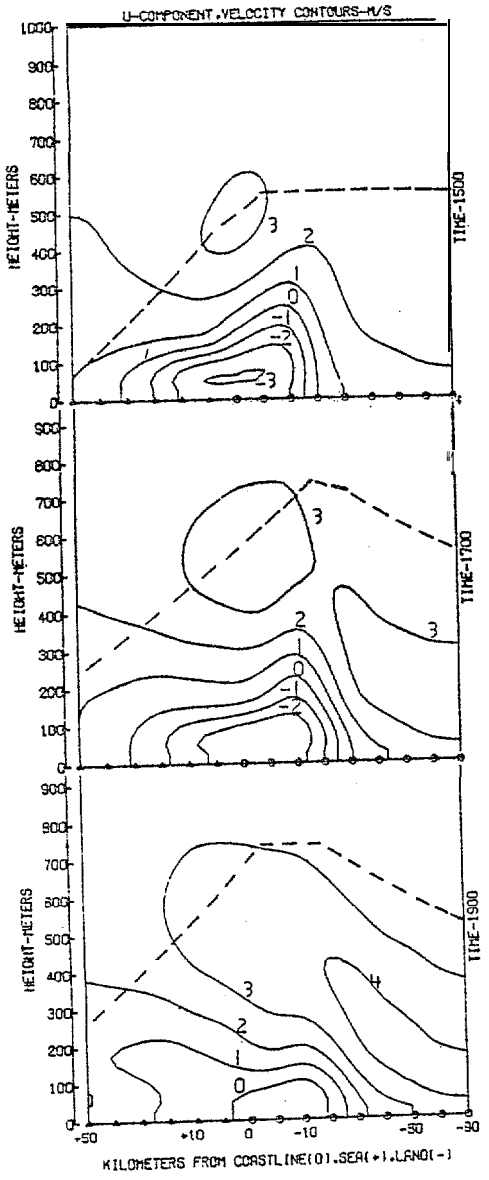

Fig. 42b. Model output of isotachs (m/S) of $U(U + U')$ for 5 m/s geostrophic wind from 270°T. The u component is perpendicular to the coast with (-) values representing shoreward flow (north winds). The boundary layer height (PBL) is shown as a dashed line. (Variable horizontal scale.)

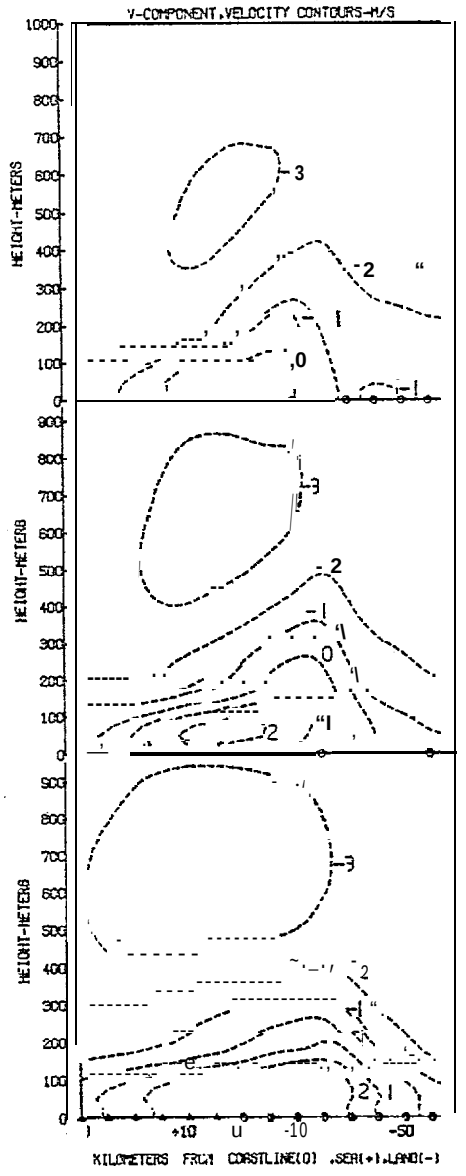

Fig. 43a. Model output of isotachs (m/s) (cross section) of $V(V_L + V')$ for 3 m/s geostrophic wind from 270° T. Designations are the same as Figure 38. (Variable horizontal scale.)

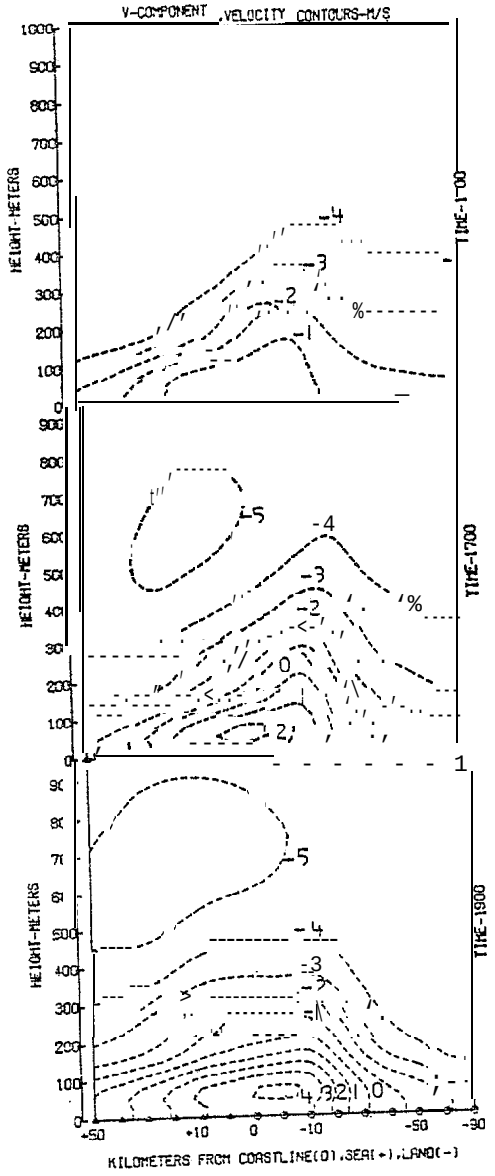

Fig. 43b. Model output of isotachs (m/s) (cross sections) of V(VL + V') for 5 m/s geostrophic wind from 270°T. Designations are the same as Figure 38. (Variable horizontal scale.)

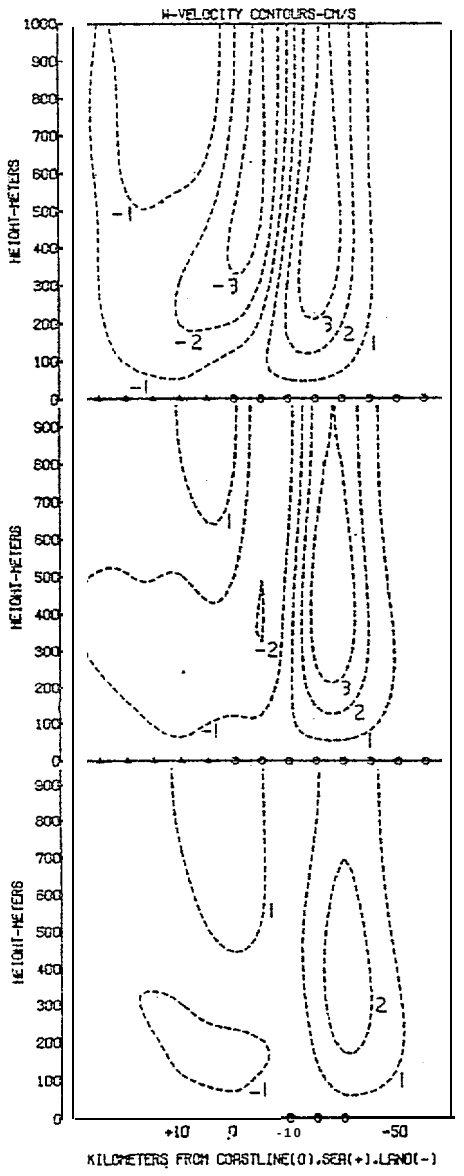

Fig. 44a. Model output of isotachs of w' (cm/s) for a 3 m/s geostrophic wind from 270°T. Designations are the same as Figure 39. (Variable horizontal scale.)

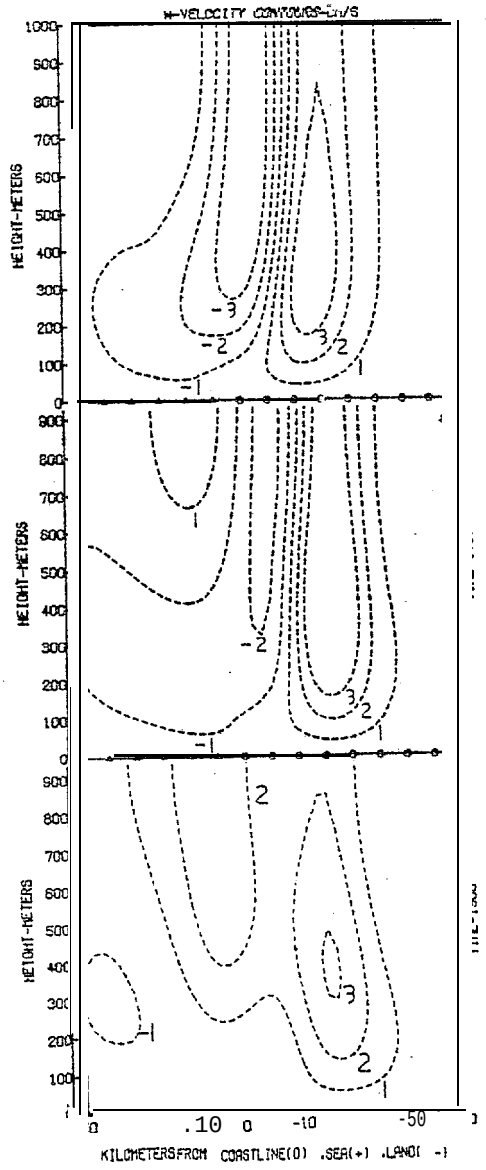

Fig. 44b. Model output of isotachs of w' (cm/s) for a 5 m/s geostrophic wind from 270°T. Designations are the same as Figure 39. (Variable horizontal scale.)

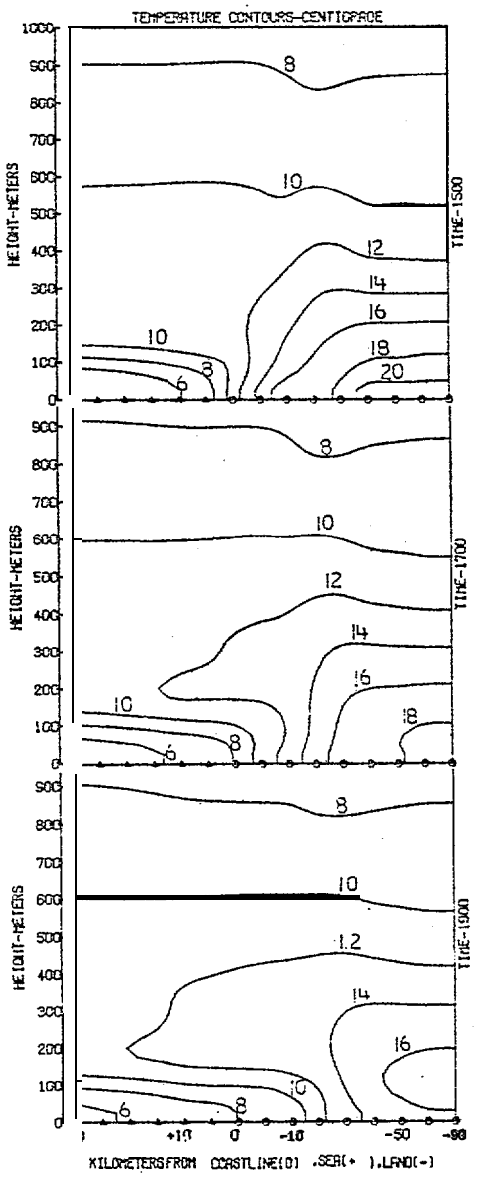

Fig, 45a, Model output of temperature contours (“C) for a 3 m/s geostrophic wind from 270°T. (Variable horizontal scale.)

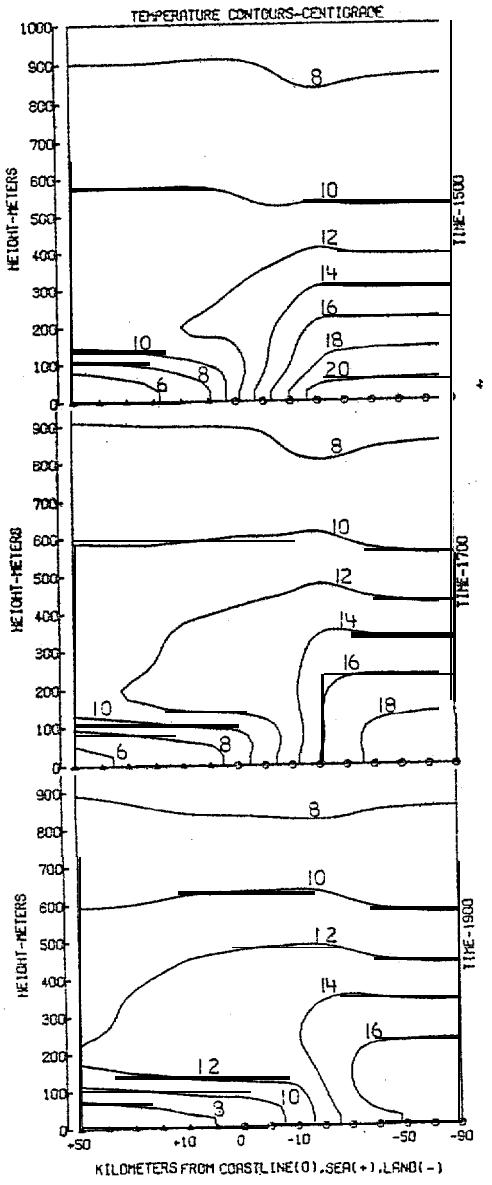

Fig. 45b. Model output of temperature contours (°C) for a 5 m/s geostrophic wind from 270°T. (variable horizontal scale.)"

Figures 43a and 43b depict isotachs of v. In these cases the maximum isotach core doesn't progress inland as far or as fast as in Case 1. The increased core strength (higher geostrophic wind - Figure 35c) represents augmented clockwise turning of the total wind vector at the surface.

The w velocity contours (44a and 44b) show an increased vertical circulation over land (5 m/s geostrophic wind) and 20 km less inland penetration of the upward flow maximum when compared to Case 1.

The temperature contours (°C) shown in Figures 45a and 45b show a surface-based inversion layer existing over water from 1500 to 1900 but *stronger* vertical circulation (sinking) and offshore advection ,(5 m/s geostrophic wind has a larger $+u$ component than the *3* m/s geostrophic wind) produce a stronger inversion in 45b.

The disturbance velocity (at 1500), $V' = (u'^2 + v'^2)^{1/2}$ is greater than Case 1 by 15% and 40% for the 3 m/s and 5 m/s geostrophic velocities, respectively.

4.3 Geostrophic Wind 220°T, at 3 m/s and 5 m/s (Case 3a and 3b), Velocity and Temperature Contours

The interesting aspect of Case 2 was the offshore component of the geostrophic wind relative to the actual coastline orientation. The following cases shown in Figures 46-50 were chosen to be representative of large-scale wind directions and velocities measured during pilot balloon ascents and inferred from calculated geostrophic winds.. This particular direction is one that almost directly opposes sea breeze surface wind direction,

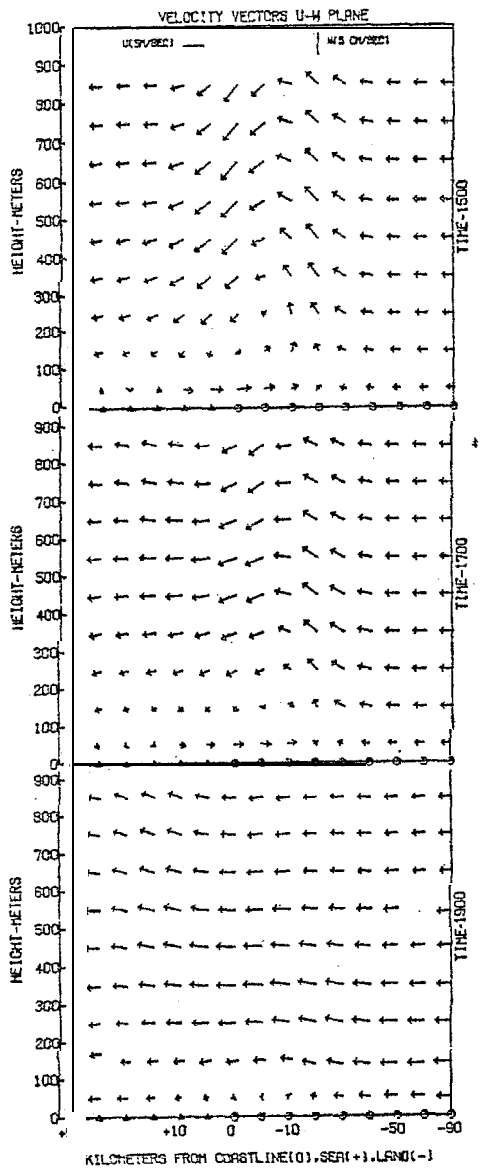

Fig. 46a. Model output of total u-w plane velocity vectors for a 3 m/s geostrophic wind from 220°T. Designationsare the same as Figure 41. (Variable horizontal scale.)

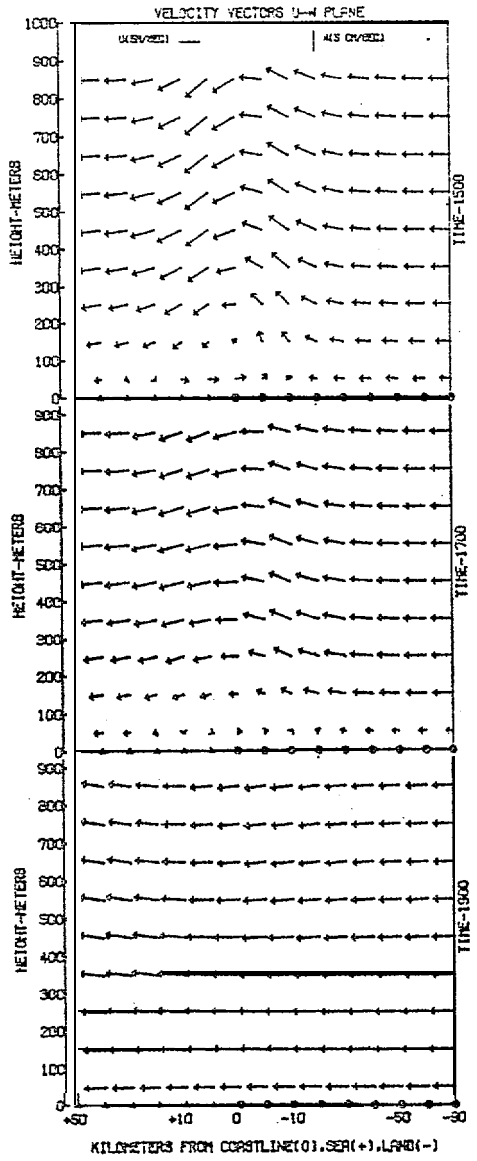

Fig. 46b. Model output of total u-w plane velocity vectors for a 5 m/s geostrophic wind from 220°T. Designations are the same as Figure 41. (Variable horizontal scale.)

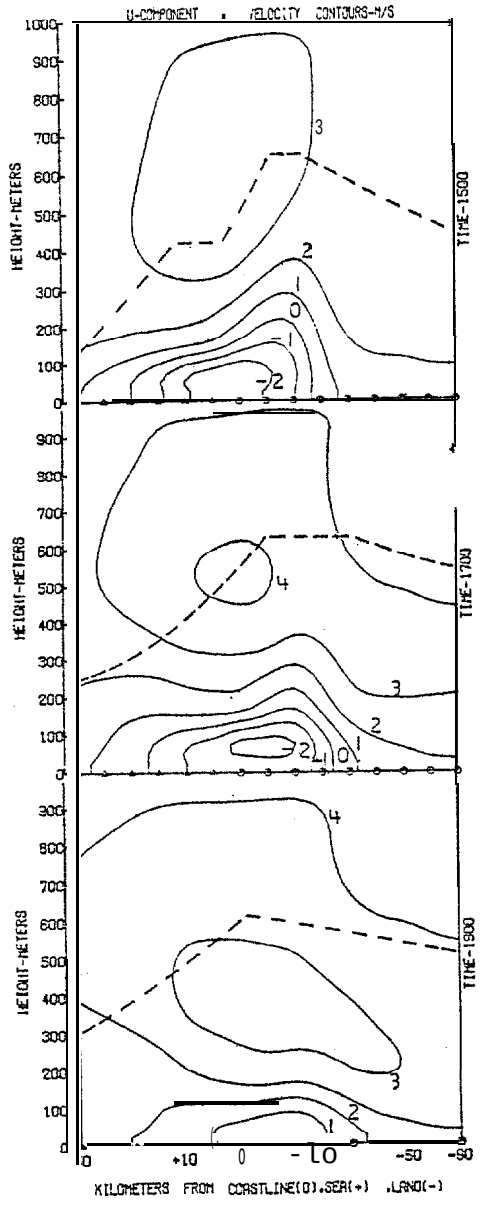

Fig. 47a. Model output of isotachs (m/s) of $U(U_L + U')$ for a 3 m/s geostrophic wind from 220°T. Designations are the same as Figure 42. (variable horizontal scale.)

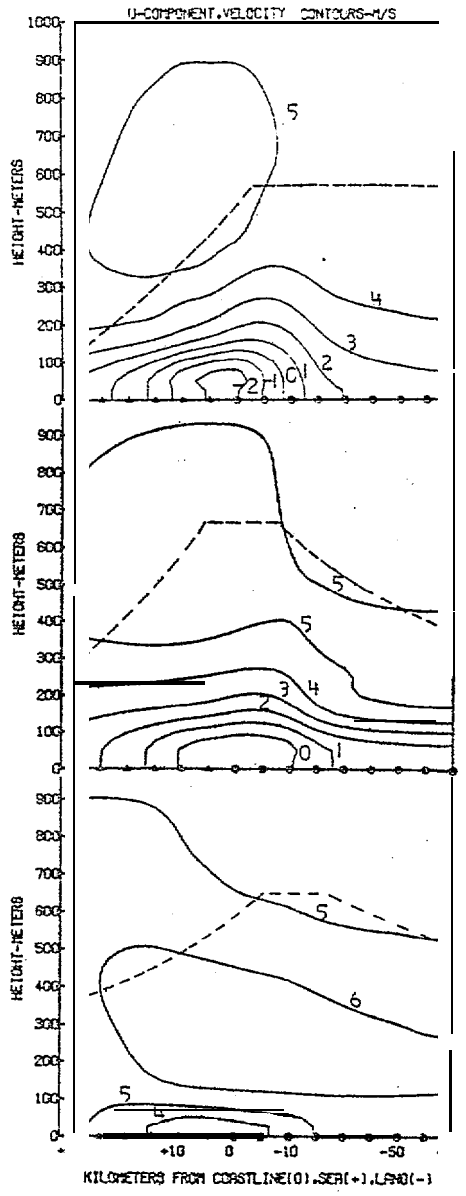

Fig. 47b. Model ouput of isotachs (m/s) of $U(U_L + U')$ for a 5 m/s geostrophic wind from 220°T. Designations are the same as Figure 42. (Variable horizontal scale.)

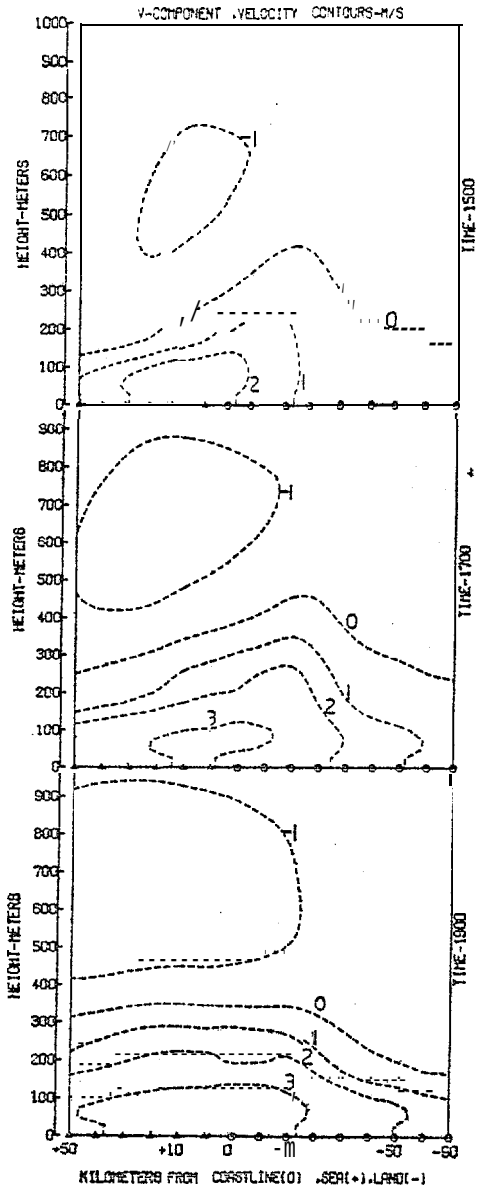

Fig. 48a. Model output of isotachs (m/s) of $V(V_L + V')$ for a 3 m/s geostrophic wind from 220°T. Designations are the same as Figure 44. (Variable horizontal scale.)

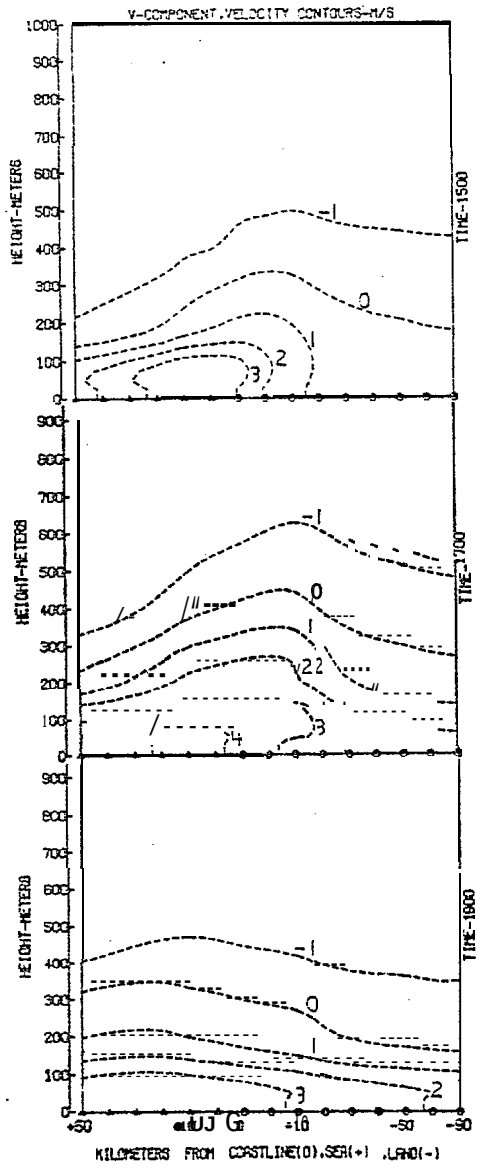

Fig. 48b. Model output of isotachs (m/s) of $V(V_L + V')$ for a 5 m/s geostrophic wind from 220°T. Designations are the same as Figure 43. (Variable horizontal scale.)

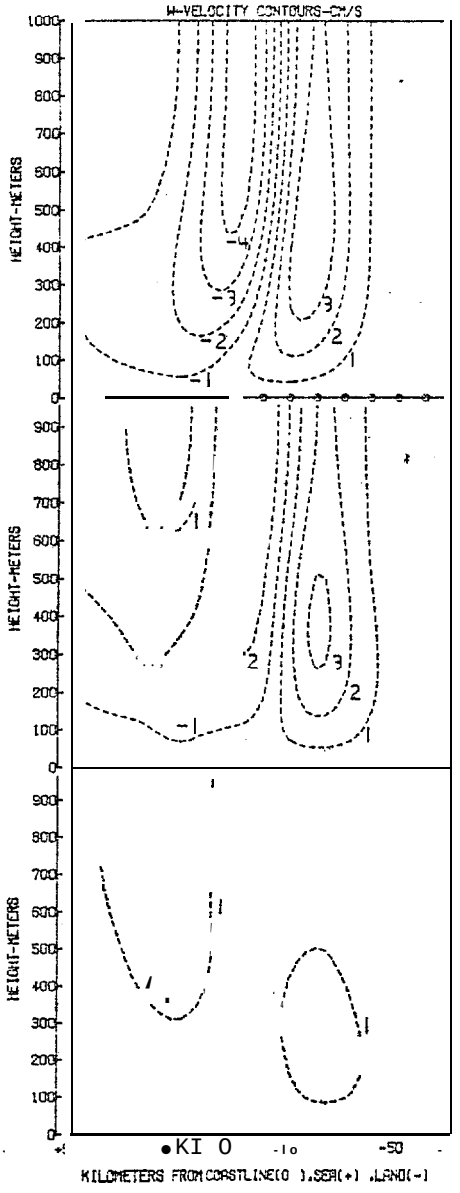

Fig. 49a. Model output of isotachs of w' (cm/s) for a 3 m/s geostrophic wind from 220° T. Designations are the same as in Figure 44. (Variable horizontal scale.)

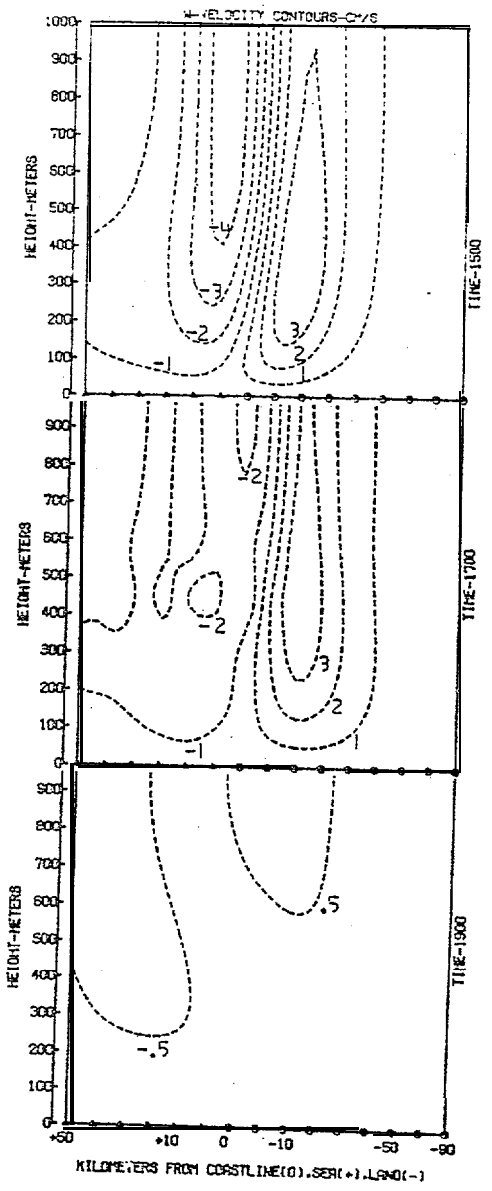

Fig. 49b. Model output of isotachs of ω' (cm/s) for a 5 m/s geostrophic wind from 220°T. Designations are the same as Figure 44. (Variable horizontal scale.)

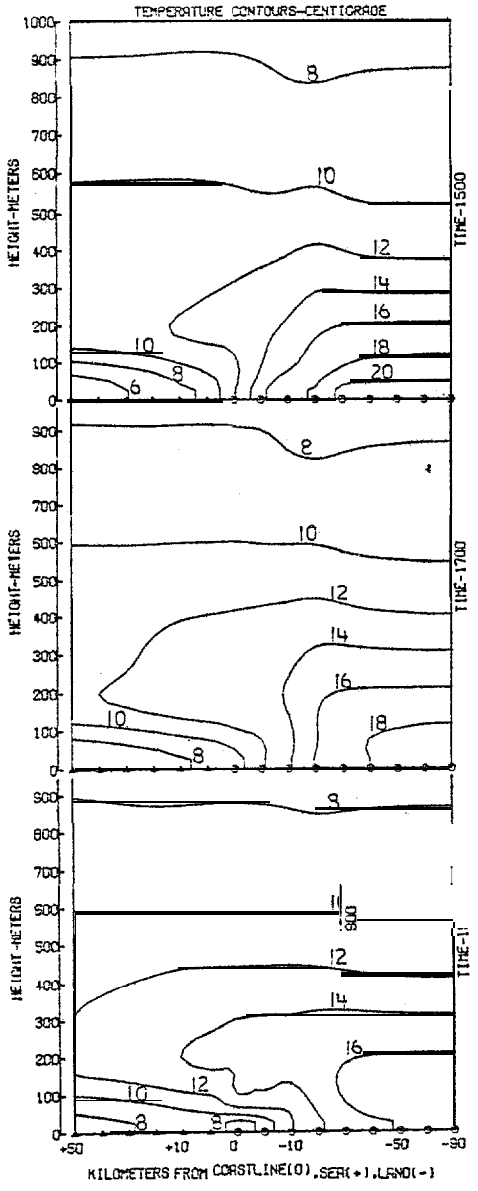

Fig. 50a. Model output of temperature contours (Co) for a 3 m/s geostrophic wind from 220°T. (Variable horizontal scale.)

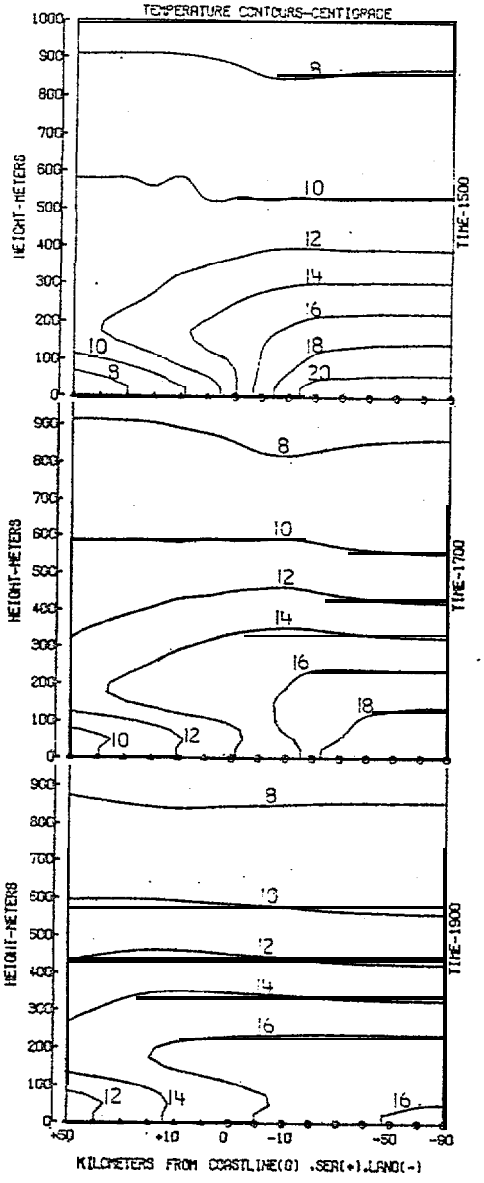

Fig. 50b. Model output of temperature contours (°C) for a 5 m/s geostrophic wind from 220°T. (Variable horizontal scale.)

Figures 46a and 46b depict the total u-w plane velocity vectors. The circulation pattern in both figures decays with time but unlike Case 2 progress inland is almost non-existent. Again, return flow aloft is predominantly due to the southerly geostrophic wind component. The surface flow in the 5 m/s case is from land to sea by 1900.

Isotachs of total u (Figures 47a and 47b) are shown, for 3 m/s and 5 m/s geostrophic winds, respectively, and the PBL heights are superimposed. Again, the boundary layer height over land increases and reaches 650 meters by 1700 while dropping within the surface-based inversion layer over water (both figures) as in Case 2. The isotach core due to the sea breeze and synoptic wind combination remains relatively stationary, with offshore dominance, for both the 3 m/s and 5 m/s large-scale wind inputs. In these cases little evidence of a sea breeze would would be seen inland beyond 10 km and from 10 km inland to the coast' extremely light or null surface winds would exist.

Figures 48a and 48b show that the isotach core of total v (maximum) remains relatively stationary and just offshore. The increased core strength (with time) represents augmented clockwise turning of the total wind vector (see Chapter V). This results in flow parallel to the "coast since the u component is small by 1900.

The w velocity contours (Figures 49a and 49b) show slightly stronger vertical circulation than Case 2. The inland penetration of the upward flow maximum is approximately 10 km. The opposing large-scale wind has effectively stalled the breeze advance.

The temperature contours ("C, Figures 50a and 50b) again show a surface-based inversion layer over water from 1500 to 1900 with the 12°

and 14° isotherm moving seaward with time due to horizontal temperature advection by the geostrophic wind.

The disturbance velocity V' (at 1500) is greater than Case 1 by 45% and 65% for the 3 m/s and 5 m/s goestrophic velocities, respectively.

4.4 Geostrophic Wind 090°T, at 3 m/s and 5 m/s (Case 4a and 4b), Velocity and Temperature Contours

Figures 51a and 51b show the total u-W plane velocity vectors. The circulation pattern for both figures shows reduced vertical motion which decays rapidly by 1900. The pattern center appears 10 km inland by 1500. These features are in contrast with Case 2 which has shown stronger vertical circulation and retarded inland advancement. Net horizontal flow aloft is again controlled by the shoreward component of the geostrophic wind.

Isotachs of total u (Figures 52a and 52b) are shown for 3 m/s and 5 m/s geostrophic winds, respectively, with the PBL heights superimposed. The lower level of the PBL over water is maintained but is extended 10 km inland by 1900 in both figures. The contours are similar for both geostrophic velocities with isotach cores appearing seaward (0-5 km, stationary) near the maximum land-sea temperature contrast and one inland (non-stationary, moving inland 30 km). The inland movement is augmented by a shoreward component (due to coastline orientation) of the geostrophic wind.

Figures 53a and 53b both show isotachs of total V ($V_L + V'$) with stationary cores offshore (5 km). An increased effect also appears 50 km inland by 1900. In this case the velocities over water do not show

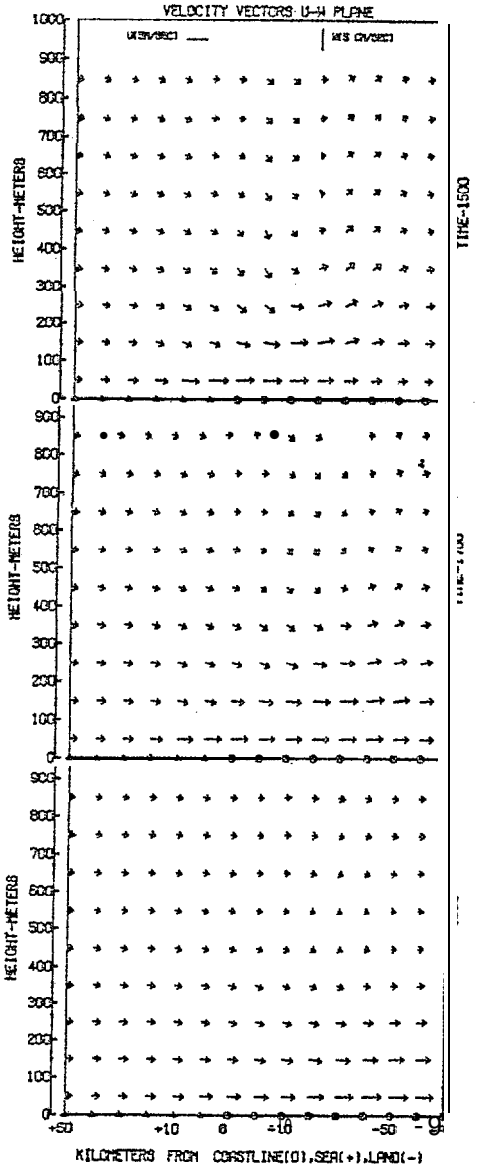

Fig. 51a. Model output of total u-w plane velocity vectors for a 3 m/s geostrophic wind from 090°T. Designations are the same as Figure 41. (Variable horizontal scale.)

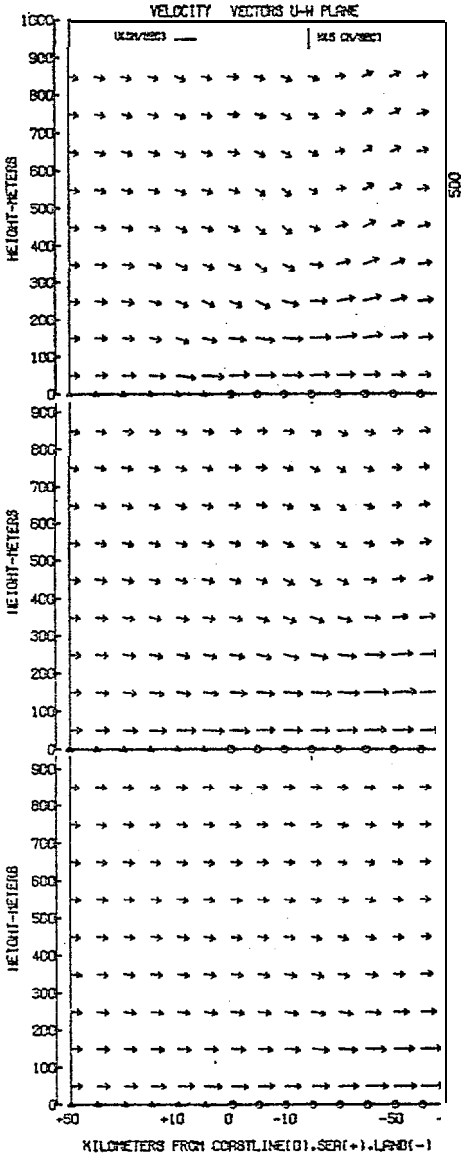

Fig. 51b . Model output of total u-w plane velocity vectors for a 5 m/s geostrophic wind from 090° T. Designations are the same as Figure 41. (Variable horizontal scale.)

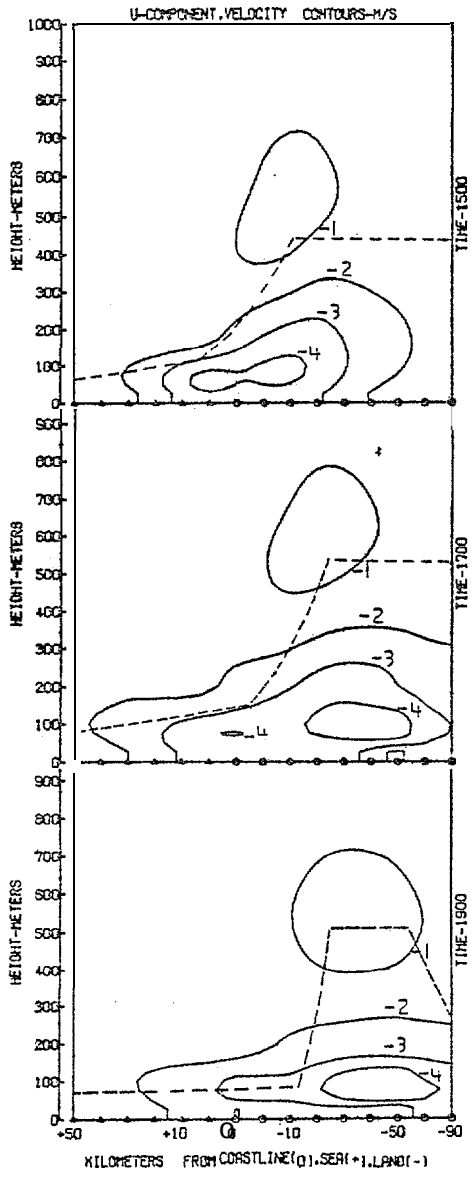

Fig. 52a. Model output of isotachs (m/s) of $U(U_L + U')$ for a 3 m/s geostrophic wind from 090°T. Designations are the same as Figure 42. (Variable horizontal scale.)

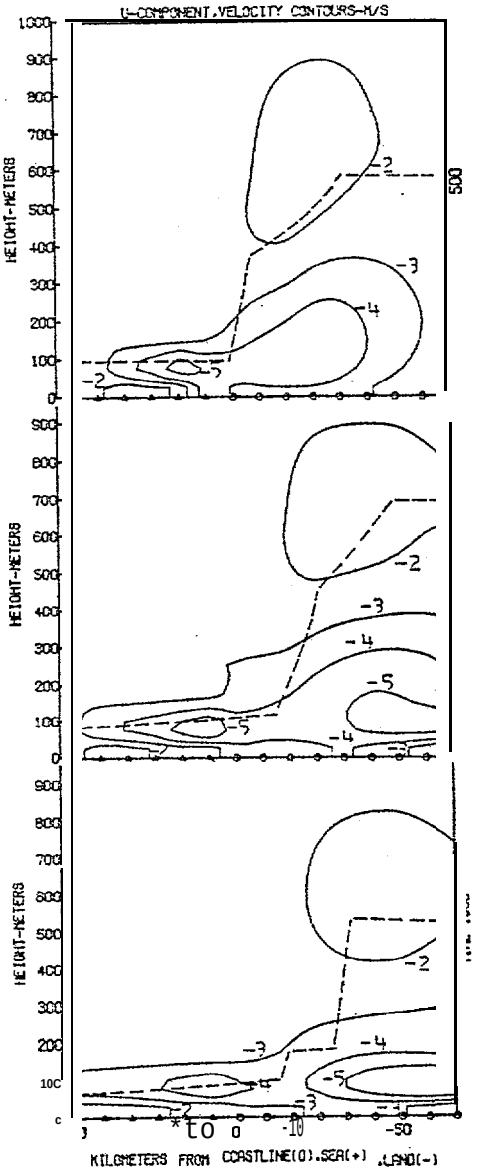

Fig. 52b. Model output of isotachs (m/s) of $U(U_L + U')$ for a 5 m/s geostrophic wind from 090° T. Designations are the same as Figure 42. (Variable horizontal scale.)

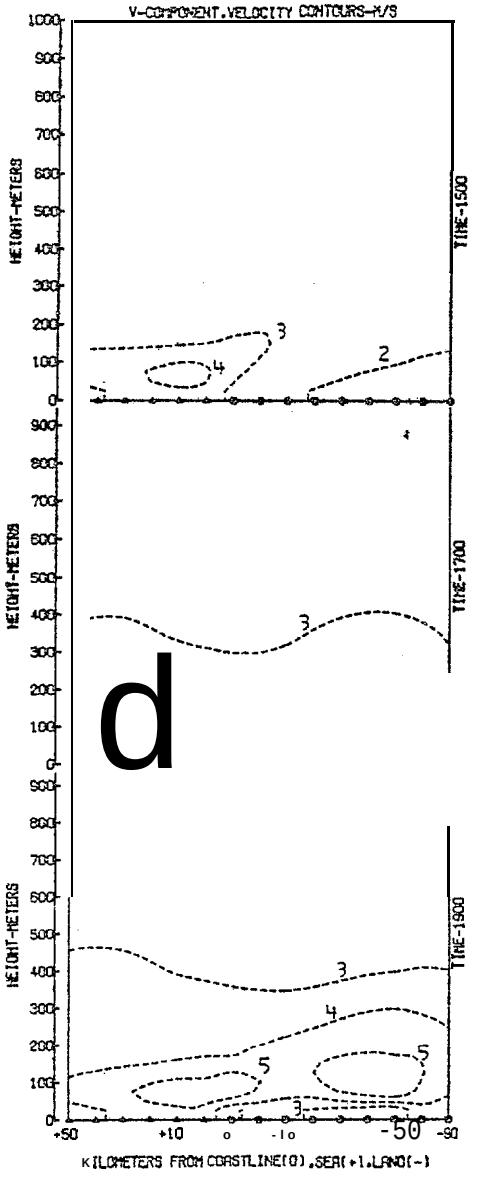

Fig. 53a. Model output of isotachs (m/s) of $V(V_L + V')$ fcr a 5 m/s geostrophic wind from 090° T. Designations are the same as Figure 43. (Variable horizontal scale.)

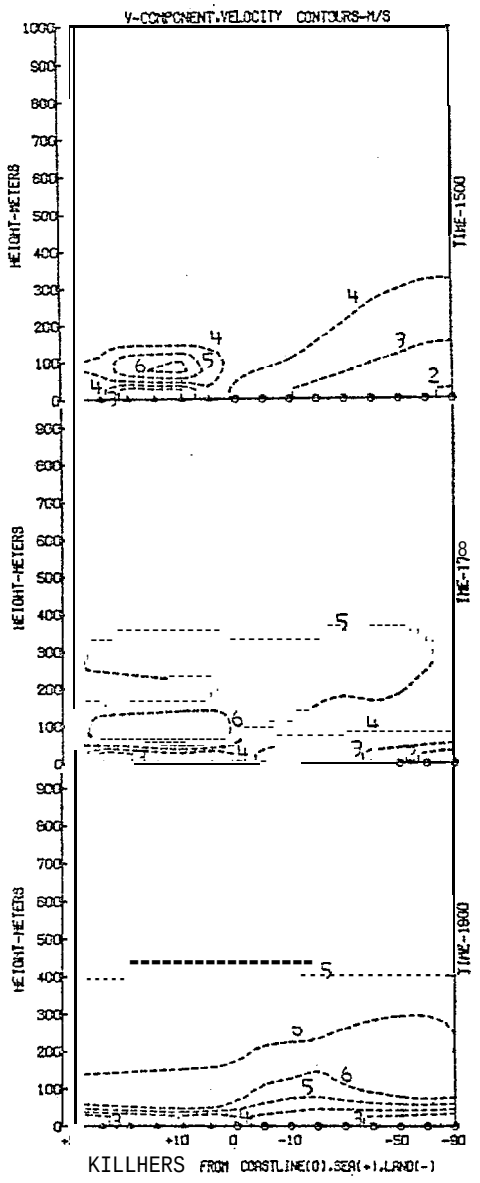

Fig. 53b. Model output of isotachs (m/s) of $V(V_L + V')$ for a 5 m/s geostrophic wind from 090° T. Designations are the same as Figure 44. (Variable horizontal scale.)

appreciable increases with time, which denotes retarded turning of the total surface wind vector (see Chapter "V).

The w velocity contours (Figures 54a and 54b) show weaker vertical circulation than Case 2 with inland penetration of the weak upward flow maximum near 50 km. A well-defined front probably does not exist and would be masked by the large-scale circulation. The shoreward geostrophic wind component has increased the inland movement of the weak circulation.

The temperature contours ("C, Figures 55a and 55b) show a surface-based inversion layer over water with a change from a super adiabatic lapse rate to an adiabatic lapse rate over land from 1500 to 1900. Horizontal temperature advection is responsible for the position of the 12° isotherm which moves inland with time.

The disturbance velocity V' is less than Case 1 by 30% and 50% for the 3 m/s and 5 m/s geostrophic velocity cases, respectively.

4.5 Geostrophic Wind 040°T, at 3 m/s and 5 m/s (Case 5a and 5b), Velocity and Temperature Contours

This is the opposite situation of Case 3 and is a direction similar to what the sea breeze surface wind would assume near maximum intensity on low synoptic wind days.

Figures 56a and 56b illustrate the total u-w plane velocity vectors. The sea breeze influenced circulation pattern is the weakest of all five cases and decays rapidly by 1900. Flow aloft is controlled by the northerly geostrophic wind component.

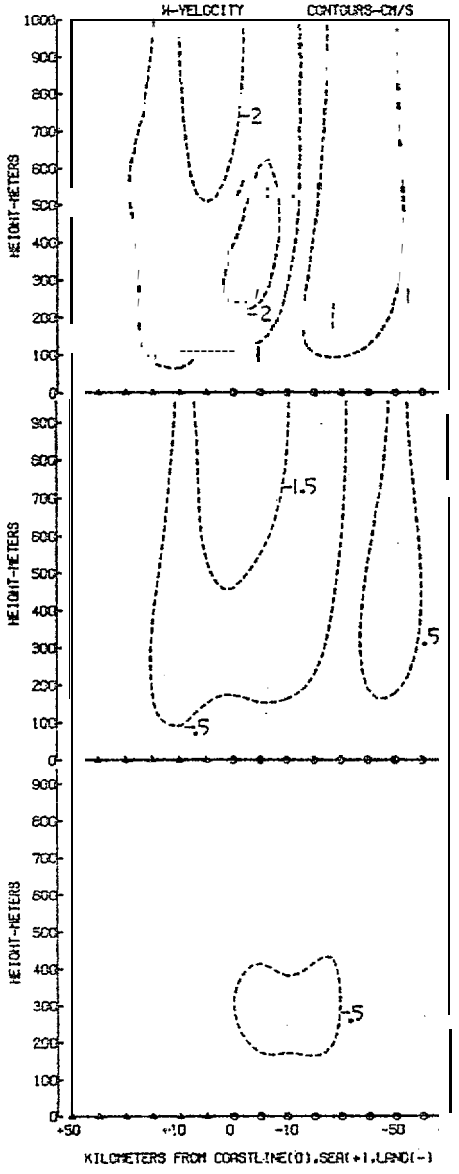

Fig. 54a. Model output of isotachs of w' (cm/s) for a 3 m/s geostrophic wind from 090°T. (Variable horizontal scale.)

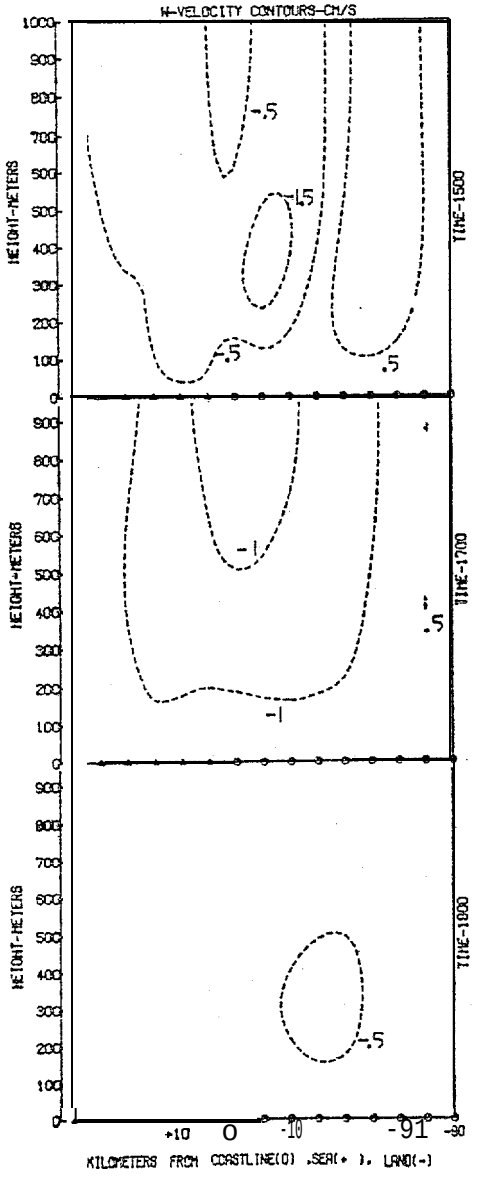

Fig. 54b. Model output of isotachs of w' (cm/s) for a 5 m/s geostrophic wind from 090°T. (Variable horizontal scale.)

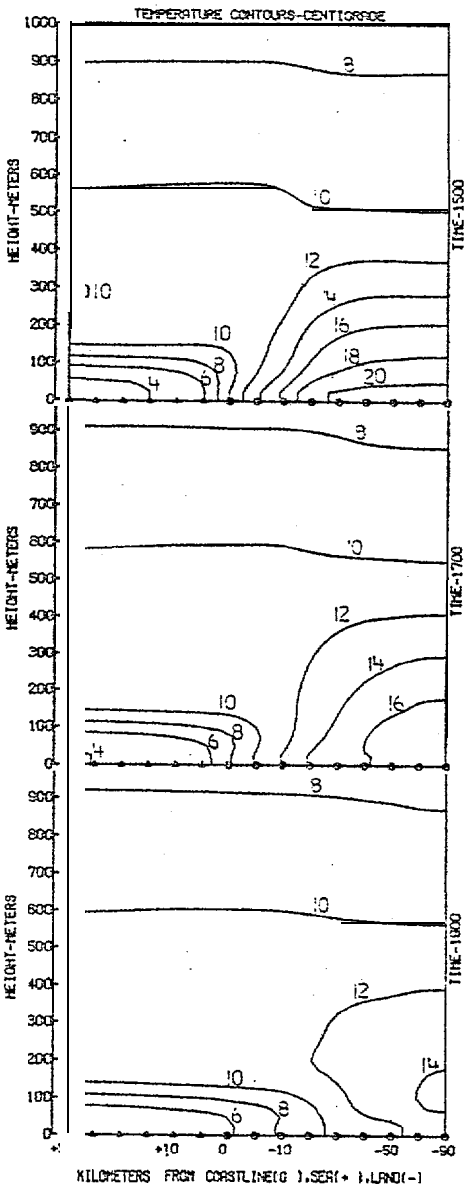

Fig. 55a. Model output of temperature contours (°C) for a 3 m/s geostrophic wind from 090°T. Designations are the same as Figure 44. (Variable horizontal scale.)

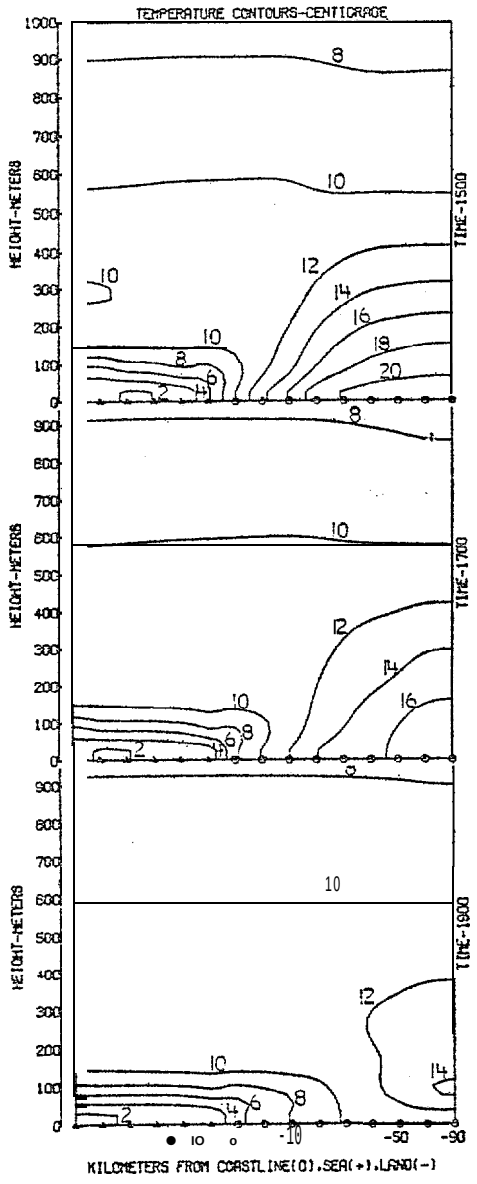

Fig. 55b. Model output of temperature contours (C°) for a 5 m/s geostrophic wind from 090°T. (Variable horizontal scale.)

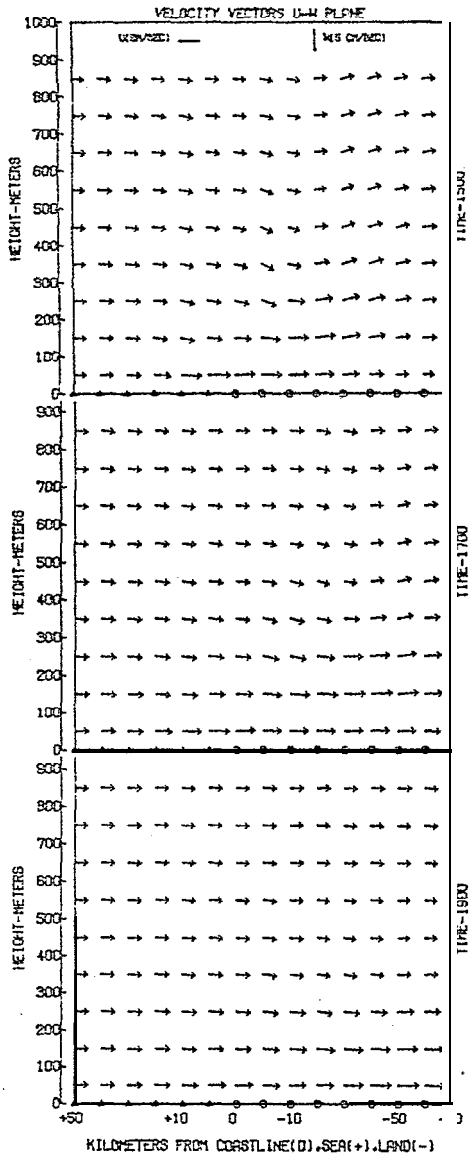

Fig. 56a. Model output of total u-w plane velocity vectors for a 3 m/s geostrophic wind from 040°T. Designations are the same as Figure 41. (Variable horizontal scale.)

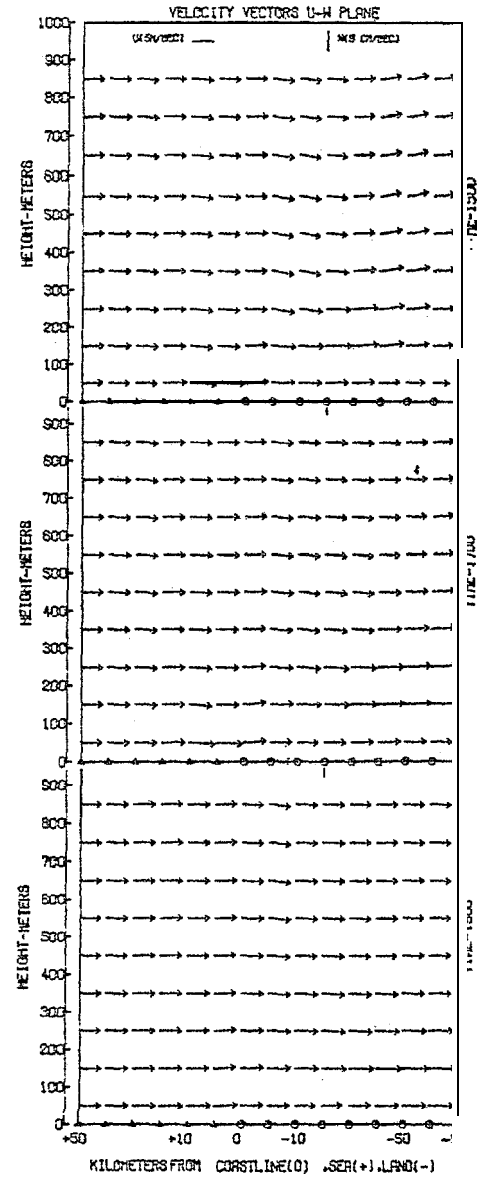

Fig. 56b. Model output of total u-w plane velocity vectors for a 5 m/s geostrophic wind from 040°T. Designations are the same as Figure 41. (Variable horizontal scale.)

Isotachs of total u (Figures 57a and 57b) are shown for 3 m/s and 5 m/s goestrophic winds. respectively, wiih PBL heights superimposed. Again. the boundary layer height is greater over land but the inversion influence appears farther inland due to low level advection of cold air. The appearance of isotach cores at 5–10 km seaward (stationary) and up to 50 km inland (moving) can be seen in both geostrophic wind cases. The inland movement is greater than Case 4 due to the larger northerly component of the geostrophic winds.

Figures 58a and 58b both show isotachs of total v. Stationary cores of V can be seen offshore in the 3 m/s and 5 m/s geostrophic wind case only, while a core appears in both large-scale wind cases by 1900 at 50 km inland. The at-sea clockwise turning of the surface wind vector is minimal from 1500 to 1900 since v remains relatively constant.

Figures 59a and 59b show limited vertical circulation of .5 cm/s or less. A measurable front would be hard to locate.

The temperature contours ("C, Figures 60a and 60b) show an inversion layer over water moving inland up to 10 km with a super adiabatic lapse rate at 1500 changing to a stable lapse rate by 1900 at distances greater than 20 km inland.

The disturbance velocity V′ is less than Case 1 by 100% and 300% for the 3 m/s and 5 m/s geostrophic velocity cases, respectively.

4.6 Surface Wind Vectors for Cases 2-5

Model generated surface wind vectors corresponding to Cases 2-5 above are shown in Figures 61-64 for geostrophic winds of (a) 3 m/s and (b) 5 m/s at"270°T, 220"T, 090°T and 040"T, respectively,

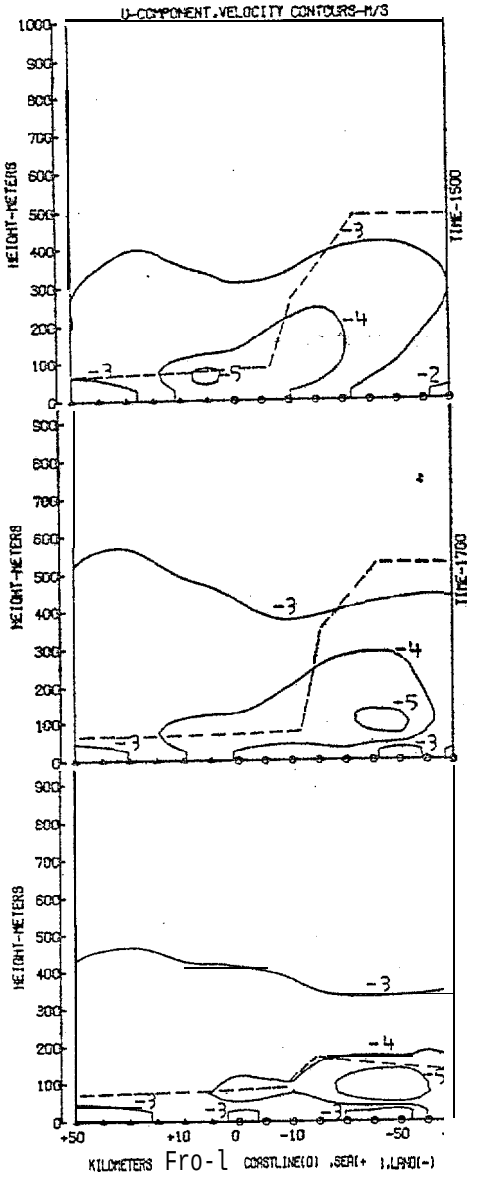

Fig. 57a. Model output of isotach (m/s) of $U(U_L + U')$ for ³'/ˢ geostrophic wind 'rem 040°T. Designations are the same as Figure 42. (Variable horizontal scale.)

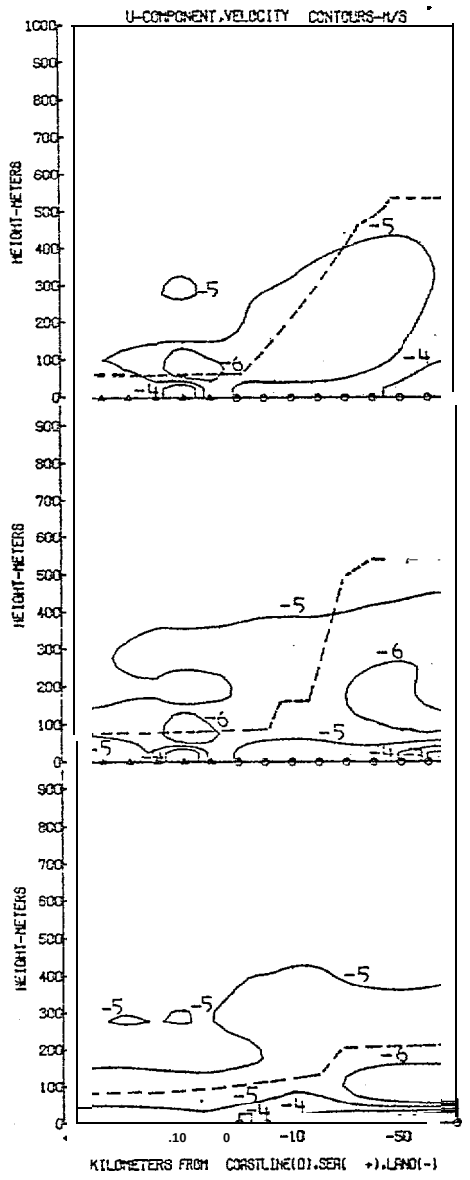

Fig. 57b. Model output of isotachs (m/s) Of $U(U_L + U')$ for a 5 m/s geostrophic wind from 040° T. Designations are the same as Figure 42. (Variable horizontal scale.)

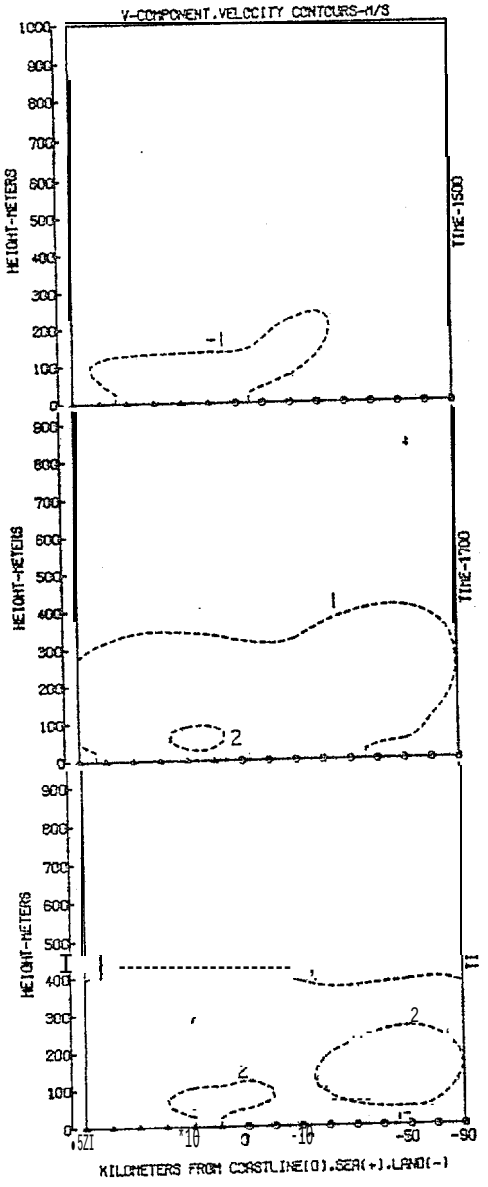

Fig. 58a. Model output of isotachs (m/s) of $V(V_L + V')$ *for a 3* m/s geostrophic wind from 040°T. Designations are the same as Figure *43.* (Variable horizontal scale.)

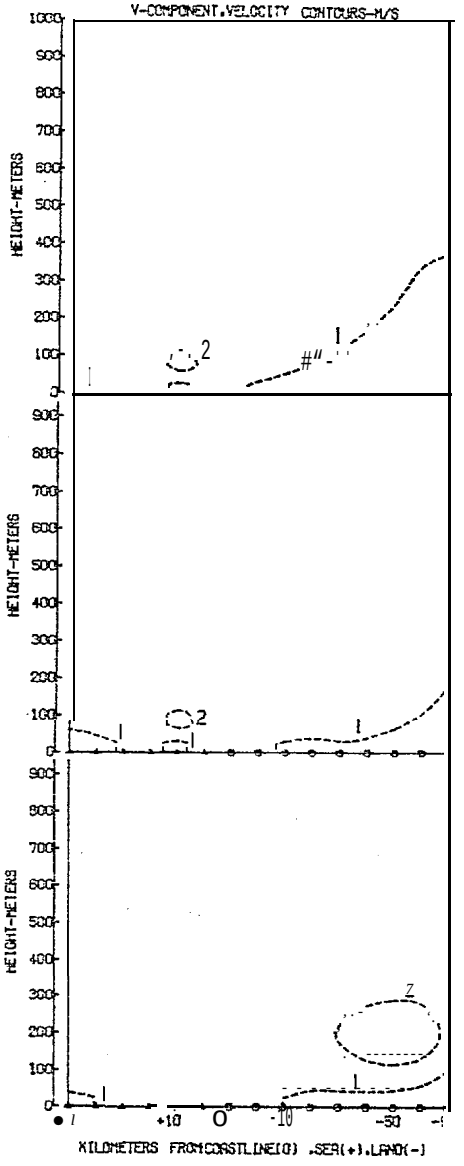

Fig. 58b. Model output of isotachs (m/s) of $V(V_L + V')$ for a 5 m/s geostrophic wind from 040°T. Designations are the same as Figure 43. (Variable horizontal scale.)

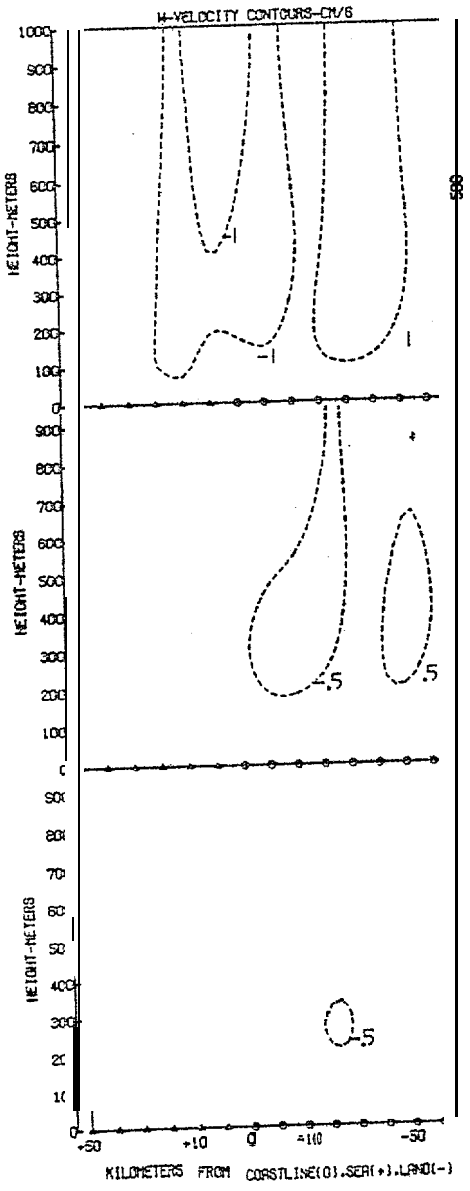

Fig. 59a. Model output of isotachs of w' (cm/s) for a 3 m/s geostrophic wind from 040° T. Designations are the same as Figure 44. (Variable horizontal scale.)

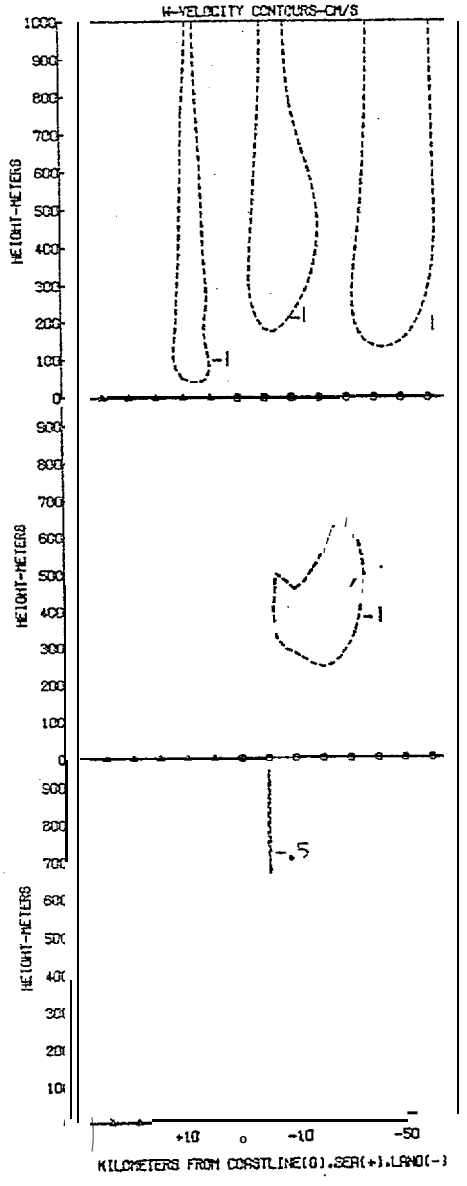

Fig. 59b. Model output of isotachs of v' (cm/s) for a 5 m/s geostrophic wind from 040°T. Designations are the same as Figure 44. (Variable horizontal scale.)

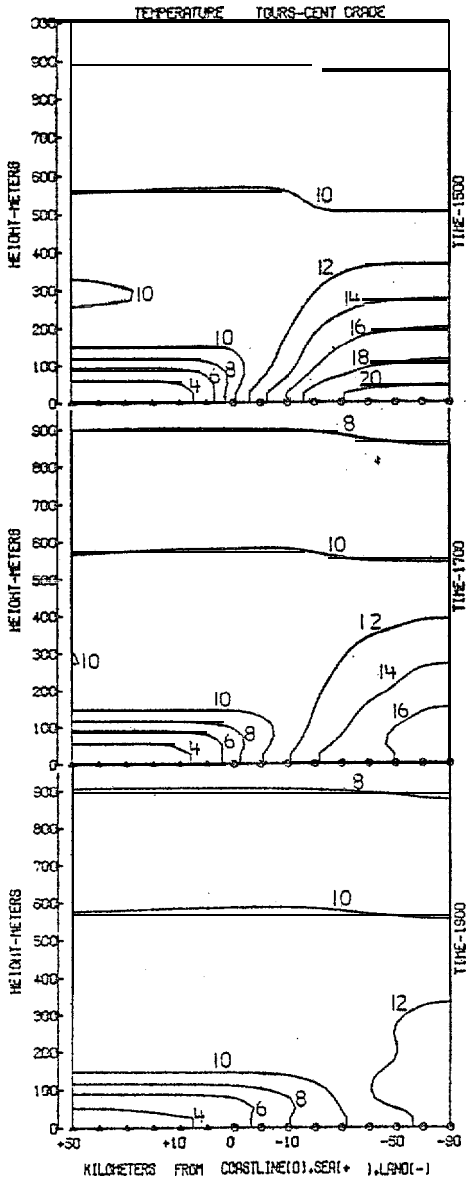

Fig. 60a. Model output of Temperature contours (°C) for a 3. m/s geostrophic wind from 040°T. (Variable horizontal scale.)

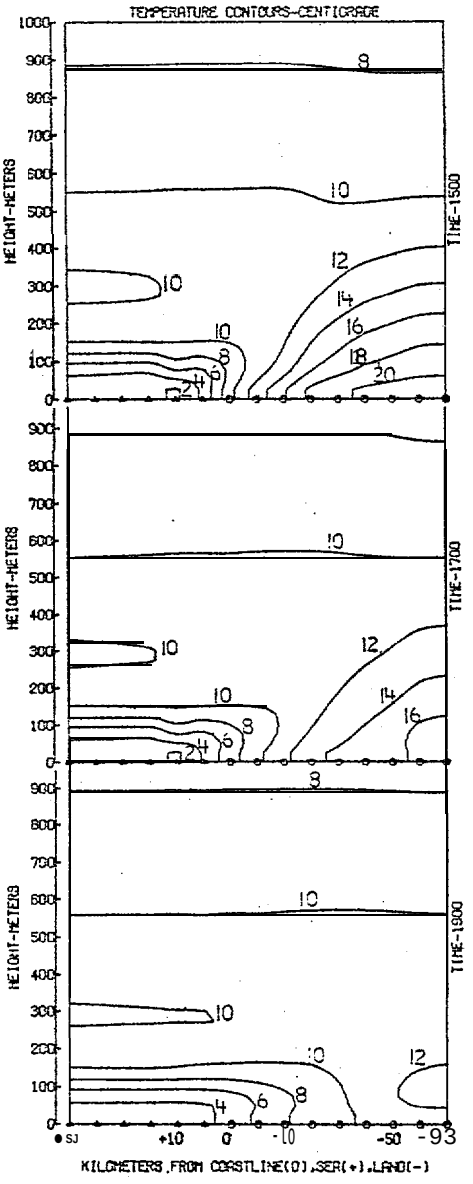

Fig. 60b. Model output of temperature contours (PC) for a 5 m/s geostrophic wind from 040°T. (Variable horizontal scale.)

a. Case 2.3 and 2b

The surface wind vectors (Figures 61a and 61b) exhibit clockwise turning at model positions ± 30 km from the coast. Limited effect can be seen at 50 km from the coast and 30 km inland (Figure 61b, $V_g = 5$ m/s). This type of turning is also seen in the real data from 7 August 1977 (Figure 30) and 19 August 1977 (Figure 34) when geostrophic winds were from 270° ± 10°T. On August 19, the breeze effect did not reach the 20 km inland station until later than 1500 while the model showed the breeze reaching the 30 km position by 1700 for the 3 m/s case.

b. Case 3a and 3b

The model surface wind vectors (.Figures 62a and 62b) exhibit clockwise turning from the coast to 30 km at sea where the sea breeze is stalled. Little effect is seen at 50 km offshore while inland 20 km a counterclockwise turning exists by 1700 when the sea breeze approaches and switches to clockwise turning afterward. August 17, 1976 (Figure 28) and August 15, 1977 (Figure 32) represent real sea breeze days when the geostrophic wind averaged 220°T. Counterclockwise turning can be seen from 1200 to 1500 as the sea breeze sets up 15 km inland then clockwise turning occurs afterward.

c. Case 4a and Case 4b

Minimal turning with time is seen in Figures 63a and 63b "for a 090°T geostrophic wind. The same thing can be seen in real data from 14 August 1977 (Figure 31) after 1800 when the geostrophic wind was from 090°T (see Chapter V). The surface wind vectors (model) "appear to have magnitudes slightly larger than the geostrophic winds aloft from the

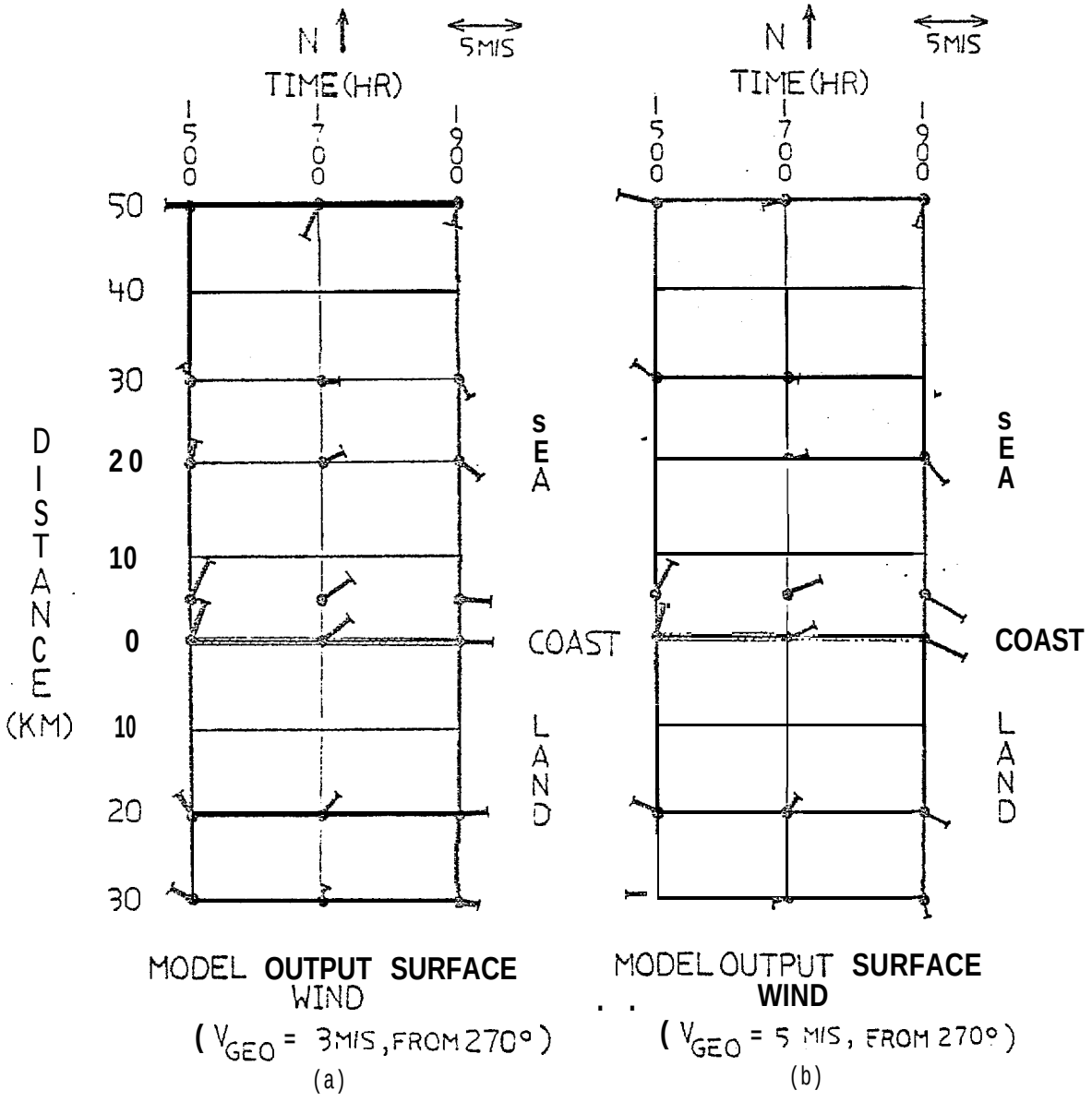

Fig. 61. Model output of Surface wind vectors for 1500, 1700 and 1900 with V_g (geostrophic wind) from 270°T at (a) 3 m/s and (b) 5 m/s.

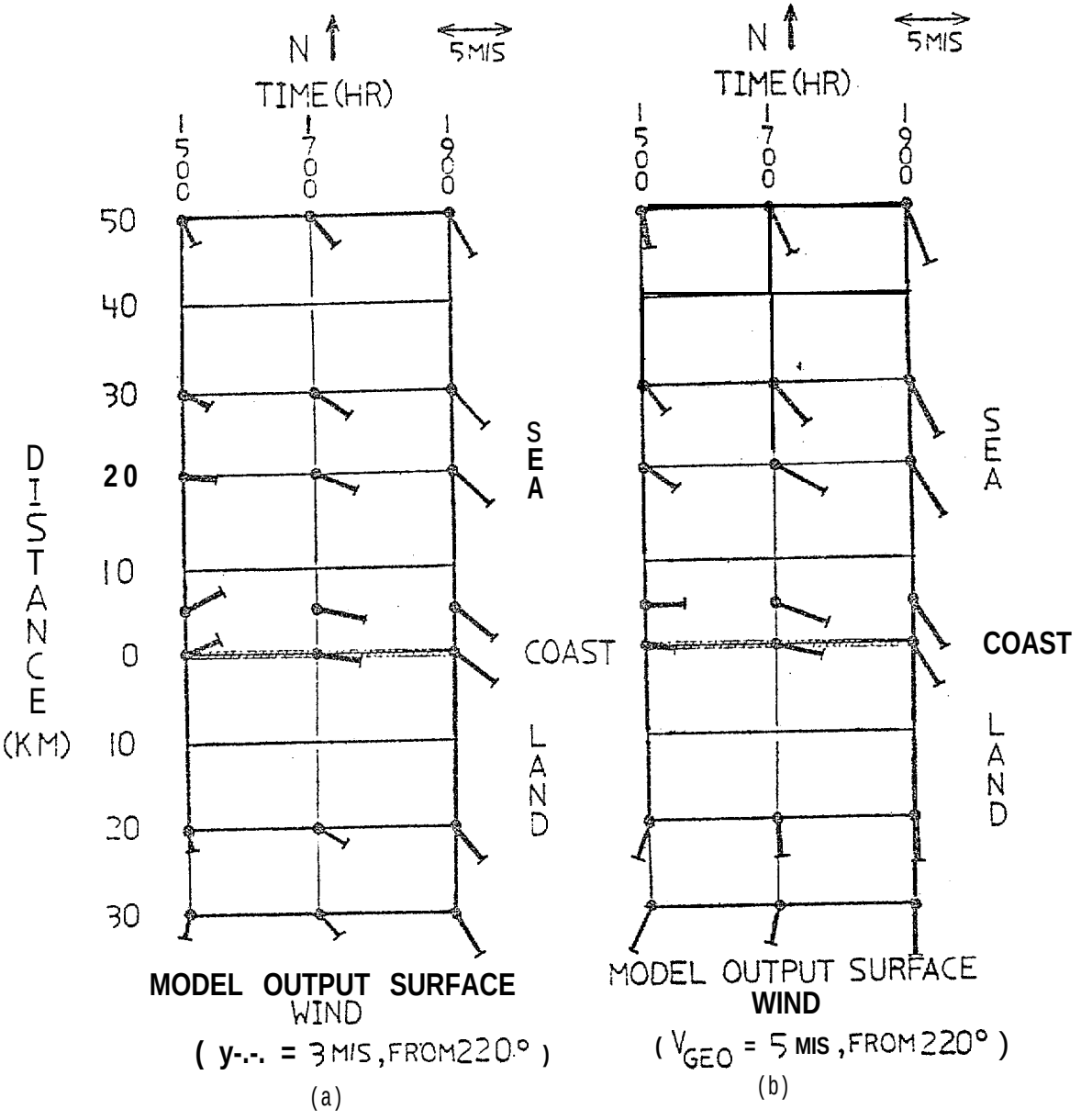

Fig. 62. Model output of surface wind vectors for 1500, 1700 and 1900 with V_g from 220°T at (a) 3 m/s and (b) 5 m/s.

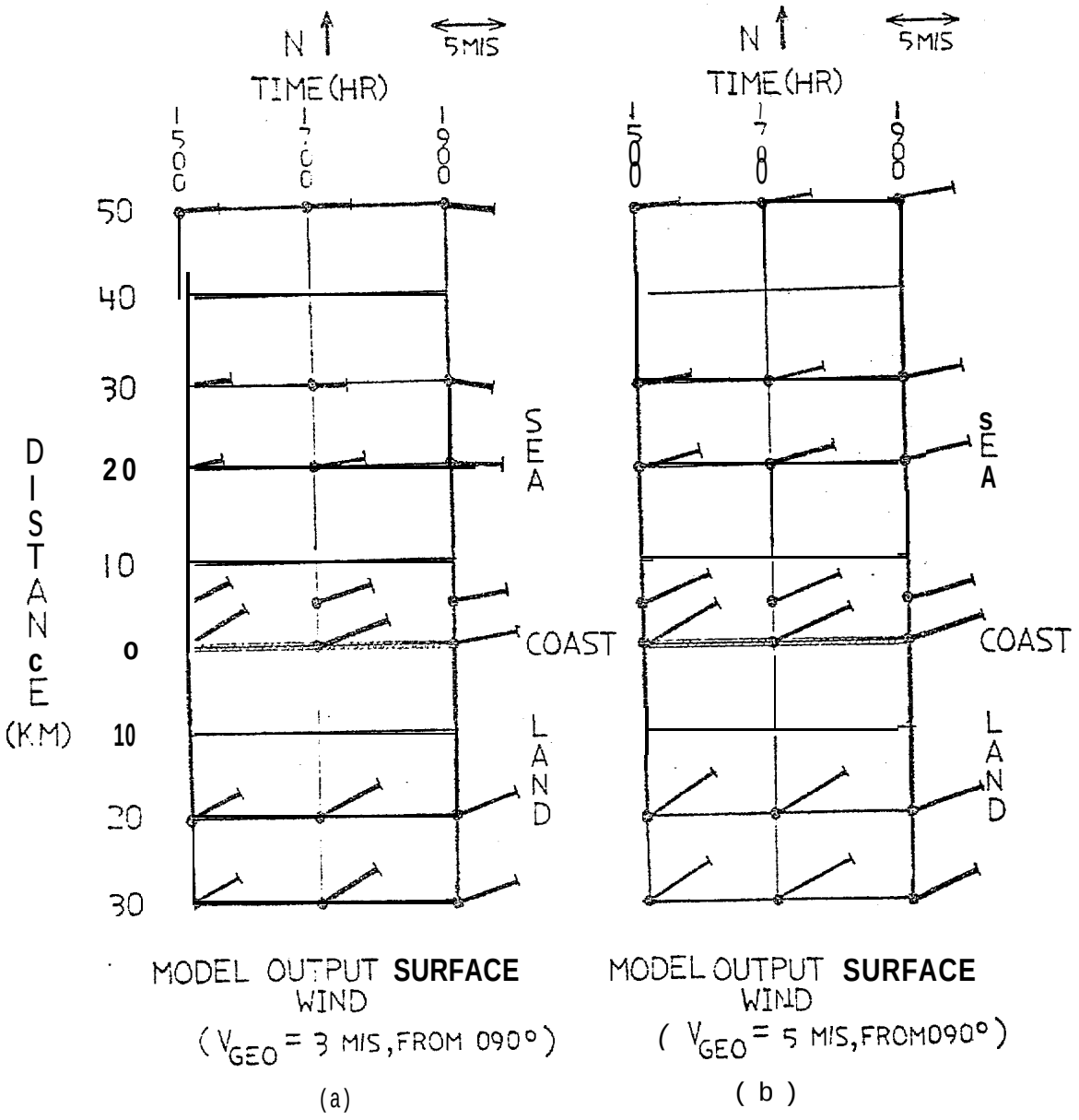

Fig. 63. Model output of surface wind vectors for 1500, 1700 and 1900 with V_g from 090°T at (a) 3 m/s and (b) 5 m/s.

5 km seaward (from the coast) to the inland stations.

d. Case 5a and Case 5b

The surface wind (model) manifestations (Figure 64) are similar to the 090°T output with little turning and slight increase in the surface velocity magnitudes from 5 km seaward of the coast to 30 km inland. These increases were exhibited in the isotach cores of u and v for the corresponding cases listed above (Section 4.5)..

4.7 Simulated Pilot Balloon Data for Cases 2-5 (5 km seaward of the coast}

Plots of wind velocity versus height corresponding to Cases .2-5 above are shown in Figures 65-6S for geostrophic winds of (a) 3m/s and (b) 5 m/s at 270°T, 220°T, 090°T and 040°T, respectively.

a. Case 2a and Case 2b

The wind speed (model) profiles (Figures 65a and 65b) show a velocity decrease at the inversion layer top (ILT) which is coincident with the layer of maximum wind direction change. The i500 profiles show a veering (clockwise turning with height) to 250 m. A clockwise turning with time (80° in 3.5 hours) is exhibited by the surface wind vector. Pilot balloon data indicating geostrophic winds from 270° On August 7, 1977 (Figure 13b) shows veering with height of 200° (up to 250 m) and August 19, 1977 (Figure 21) shows backing with height of 140°T (up to 250 m) which are comparable to the turning produced by the model. The real data also show surface clockwise turning with time (80° in 4 hours). Both the 3 m/s and 5 m/s geostrophic wind velocity cases (model) show a slight increase above their respective velocities (bowing out) in the

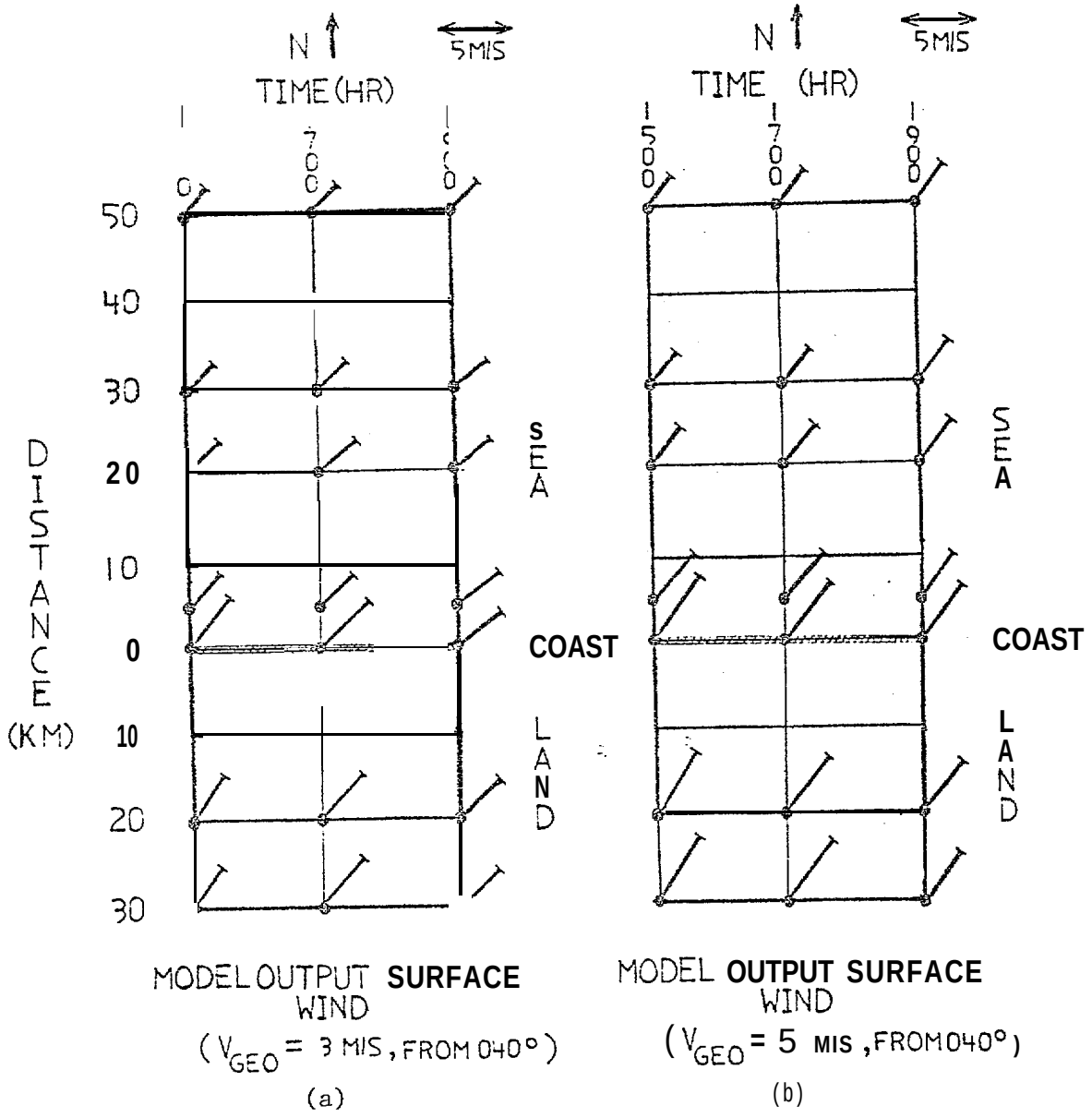

Fig. 64. Model output of surface wind vectors for 1500, 1700 and 1900 with V_g from 040°T at (a) 3 m/s and (b) 5 m/s.

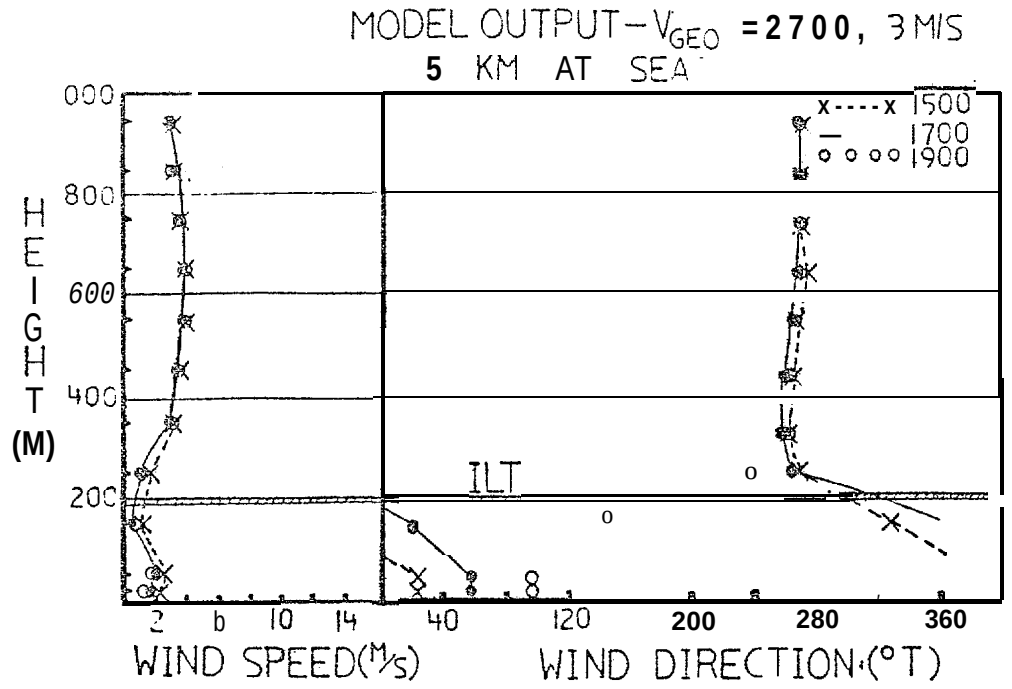

(a)

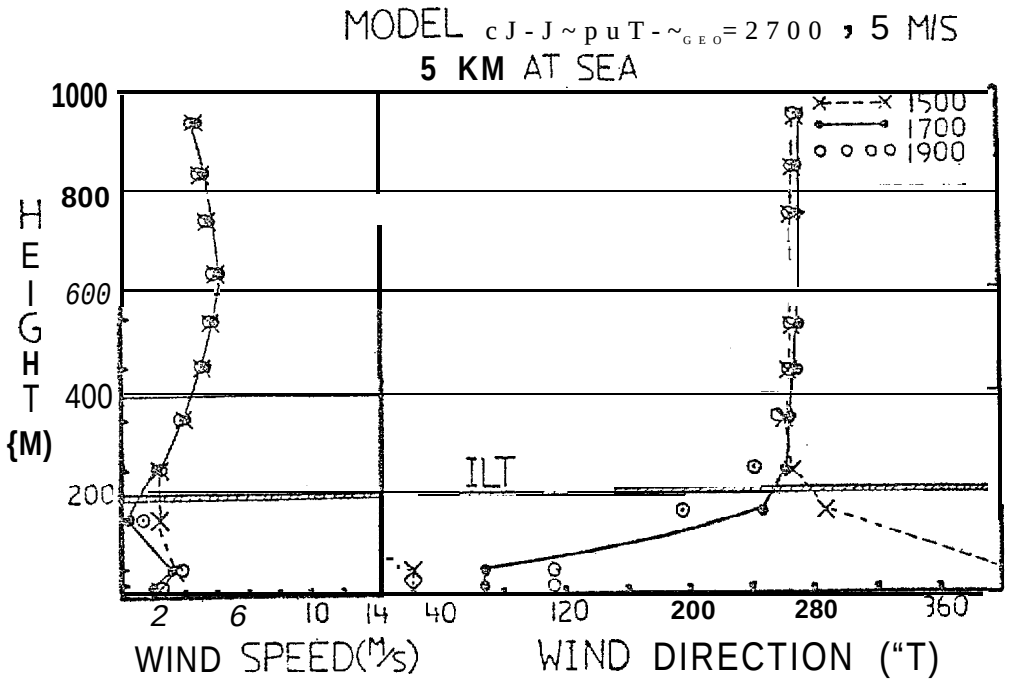

(b)

Fig. 65. Model output of wind speed and wind direction profiles, 5 km seaward from the coast, for 1500, 1700 and 1900 with V_g's of (a) 3 m/s and (b) 5 m/s (as shown) from 270°T.

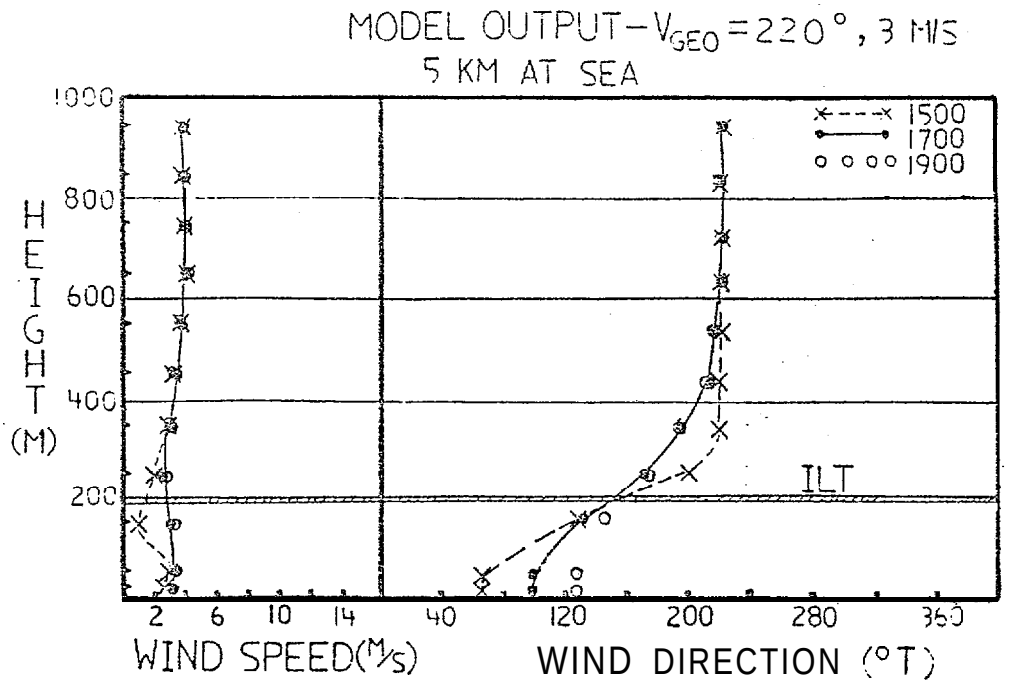

(a)

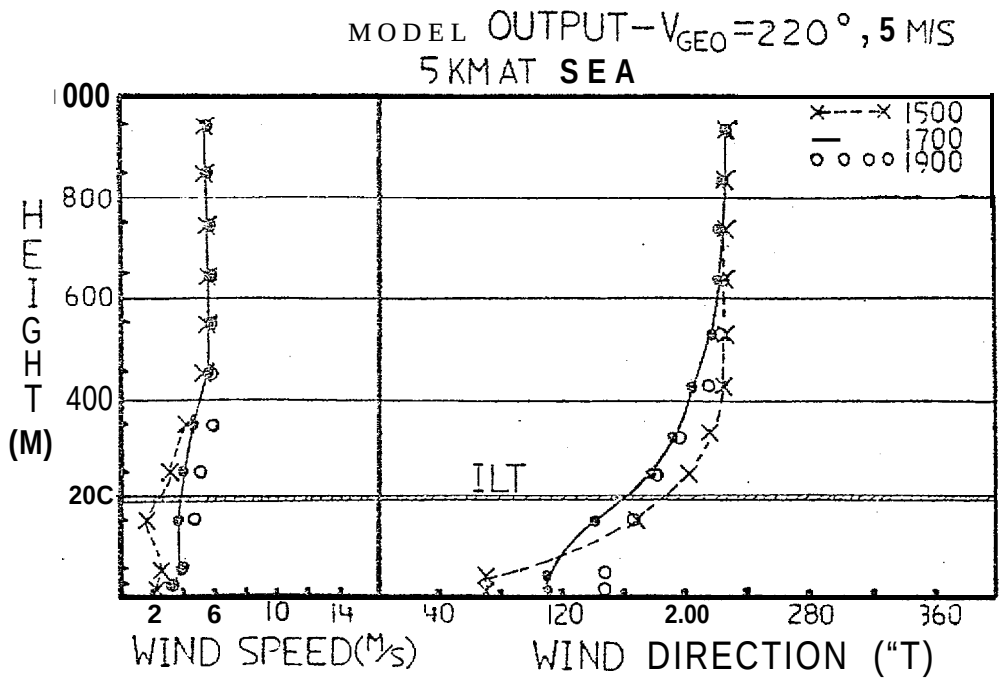

(b)

Fig. 66. Model output of wind speed and wind direction profiles, 5 km seaward from the coast, for 1500, 1700 and 1900 with V_g's of (a) 3 m/s and (b) 5 m/s (as shown) from 220°T.

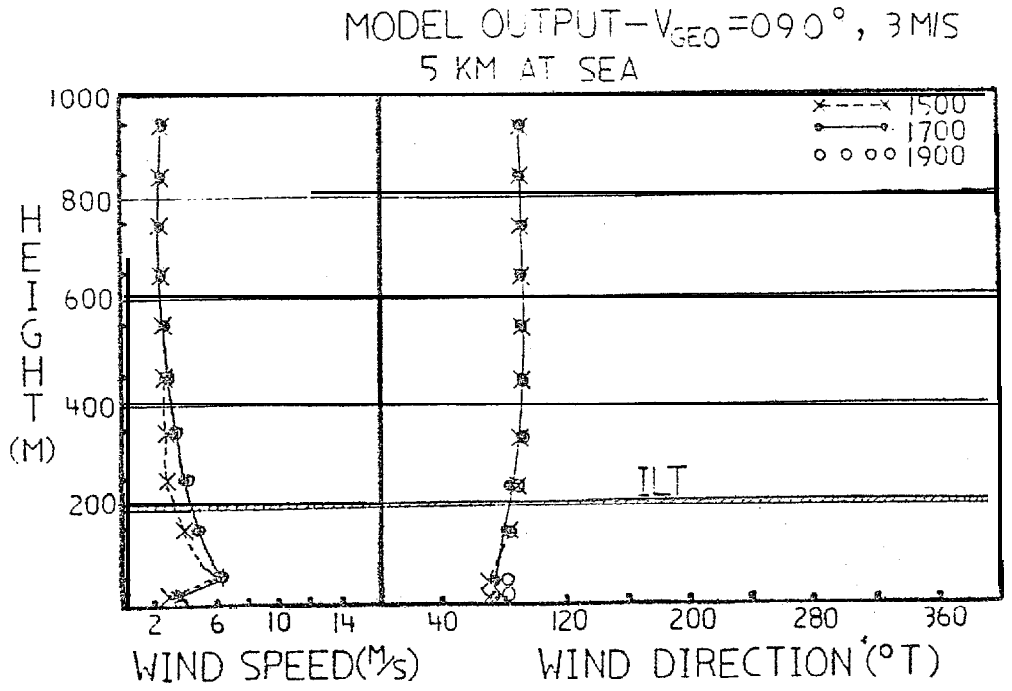

(a)

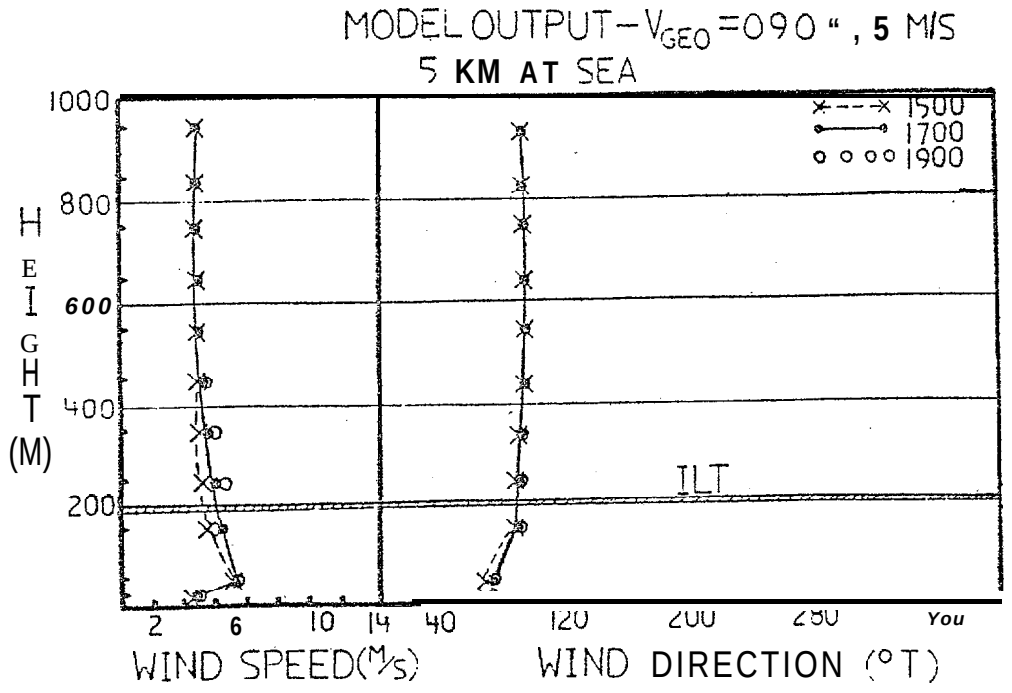

(b)

Fig. 67. Model output of wind speed and wind direction profiles, 5 km seaward from the coast, for 1500, 1700 and 1900 with V_g's of (a) 3 m/s and (b) 5 m/s from 090° T.

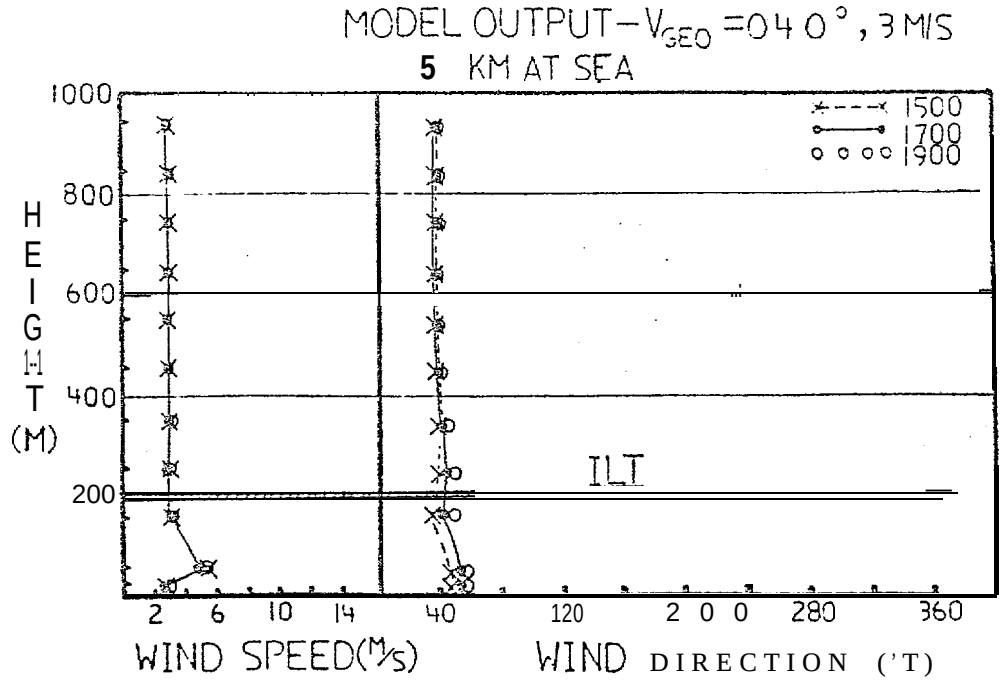

(a)

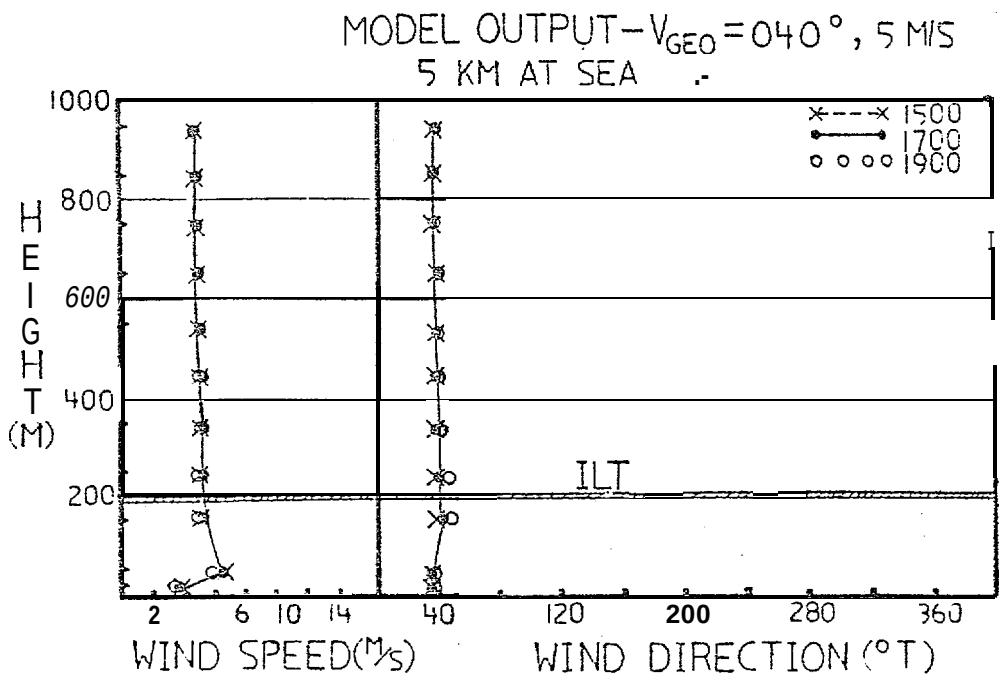

(b)

Fig. 68. Model output of wind speed and wind direction profiles, 5 km seaward from the coast, for 1500, 1700 and 1900 with V_g's of (a 3 m/s and (b) 5 m/s (as shown) from 040° T.

upper level winds From *400* m and *700* m. This is attributable to the coastline orientation and weak sea breeze return flow aloft (.5 m/s) adding to the geostrophic wind vector.

b. Case 2a and Case 3b

The wind speed (model) profiles (Figures 66a and 66b) also show a velocity decrease at the ILT which again is coincident with the layer of most wind directional change, Both model sets (3 m/s and 5 m/s output) show a veering up to 250 m which is comparable to real pilot balloon data from August 15, 1977 {Figure 17b). A *very* slight bowing out of the upper level winds (model) again can be attributed to the sea breeze return flow. The clockwise turning with time appears in the real data (70° in four hours) and the model (60° in four hours) at comparable rates.

c. Case 4a and Case 4b

The wind direction (model) profiles (Figures 67a and 67b) show a normal veering up to 250 m. The wind speed profiles denote the presence of a sea breeze by exhibiting a wind speed increase within the boundary layer (below the ILT) instead of a normal decrease in wind speed. This speed increase within the boundary layer is seen in real data from August 14, 1977 (Figure 15b) and August 17, 1977 (Figure 19b). A slight speed decrease in the upper level winds from 400 m to 800 m (bowing in), below that of the geostrophic speed, is' attributed to weak opposing return flow aloft generated by the seabreeze return circulation. The turning of the surface wind vector with time is negligible both in the model and from the real data for geostrophic winds from approximately 090°T.

d. Case 5a and Case 5b

The wind speed (model) profiles (Figures 68a and 68b) show a slight increase over the geostrophic winds aloft as in the 90°T cases above. The 3 m/s case shows a slight backing up to 250 m as the sea breeze effect influences the surface vector by turning it clockwise. The 5 m/s case indicates that the sea breeze is not strong enough to influence the surface direction (only the speed). There were no examples of real data with geostrophic wind directions similar to this case.

4.8 Synopsis of Chapter IV

Five cases of sea breeze circulation were modeled for various large-scale wind conditions. The zero geostrophic case was used as a basis for comparison with four cases of geostrophic winds from 270°T, 220°T, 090°T, and 040°T at 3 m/s and 5 m/s, respectively. Simulated surface wind vector turning and simulated pilot balloon data (5 km seaward from the coast) were examined for the four existing geostrophic wind cases. The latter model simulated vertical wind speed and direction profiles [at a distance 5 km seaward of the coast (Pingok Island)] compare favorably with the actual pilot balloon derived wind speed and direction data taken on Pingok Island for gesotrophic winds of 220°T (Figures 66 and 17b), 270°T (Figures 65 and 21b) and 090°T (Figures 67, 15b and 19b).

The model showed an average increase in the boundary layer height over land of 400 m (from an initial level of 200 m at 0300) by 1700 while the inversion layer top remained relatively stationary over water averaging 200 m. This output agreed with the radiosonde data from Pingok Island (August 1977) and the Deadhorse acoustic sounder data (August

1976, see Figure 35).

The stalling of the sea breeze front near the coast with augmentation of the sea breeze disturbance circulation, when the geostrophic wind had an offshore component, was exhibited by the model. Confirmation of this was seen in real data of surface wind velocity vectors where inland effects at 30 km never occurred or were minimal, while coastal surface winds were larger in magnitude and exhibited clockwise turning.

The model's surface wind vector rotation rates, pilot balloon simulations with backing and veering up the the inversion height, and the increase *in* wind speed within the boundary layer under a following geostrophic wind were all exhibited and matched in the real data.

This study has relied heavily on model output to fill in observational data gaps which are characteristic of most mesoscale studies. Data from beyond 20 km seaward or 20 km to 100 km inland are minimal and no vertical wind velocity or temperature soundings were obtained. Therefore, a detailed vertical sounding network seaward and landward from the coast does not exist to confirm the model output for Figures 33-41. This output, though mainly qualitative, does give theoretical evidence and reasons for the actual wind and temperature observations made at the 10 meter level and for the vertical sounding observations as seen in the pibal and radiosone data taken within 20 km of the coast (seaward and landward).

Model weaknesses are:

1. Lack of a theoretical scheme to represent the surface layer temperature and velocity profiles accurately under cases of extreme atmospheric stability such as during the early morning and late evening.

2. Using a relatively coarse horizontal grid (5 km minimum spacing) which limits the representation of the sea breeze front in the horizontal and vertical velocity fields.

3. Use of the incompressible form of the continuity equation to calculate w' which allows for the imposition of only one boundary condition ($w' = 0$ at the surface) and limits the accuracy of the w field as z increases.

4. Use of a tri-sinusoidal heating function to drive the model rather than a surface heat balance equation.

5. Lack of a procedure to adjust the height' of the surface layer as the boundary layer height changes.

6. Use of the approximation, that changes of the sea breeze velocity and temperature do not exist parallel to the coast.

V. THE PHYSICAL FACTORS WHICH CHARACTERIZE THE ARCTIC SEA BREEZE

5.1 *Zero* (0) Geostrophic Wind

The fact that the Coriolis parameter for 71°N is 37% greater than that for mid-latitudes and the fact that the summer sea breeze along the Alaskan arctic coast is not followed by a land breeze would result in a greater clockwise rotation of the breeze surface wind vector with time in only the 0° to 90° T quadrant for zero geostrophic wind conditions. Though an idealized case, this can be thought of as partial explanation for the persistence of winds from the northeast quadrant seen in August historical data taken near the experimental data site.

The sea breeze's initial driving mechanism depends on a horizontal pressure gradient force aloft in response to a surface horizontal temperature contrast. The arctic breeze initially faces a strong ground-based inversion which implies extreme stability and small eddy thermal diffusivity (K_h). This factor limits the vertical extent of the circulation to 1000 meters (depth of landward flow less than 400 meters) and the ω velocities (model) to less than 50% of those in mid-latitude models. This also implies that sea breeze fronts (if they exist at all) characterized by $+\omega$ maxima and large horizontal gradients of u, v, and θ will be *weaker* in the arctic. The initial conditions faced by the *arctic* breeze are similar to those encountered by mid-latitude land breezes. Pearson (1975) and Mak and Walsh (1976) maintain that given equal horizontal temperature gradients, land breeezes will still be

weaker than sea breezes due to stable stratification and small eddy diffusion coefficients.

In contrast to mid-latitude land breezes, the arctic sea breeze has a much larger sea-land temperature difference (12°C–14°C at the coast) which reaches 25°C at 30 km inland, and exists during a solar heating cycle, which partly compensates for the above mitigating factors.

The factors discussed in the 0 geostrophic case apply to the non-zero cases also. However, factors such as relative strength, rotation, rotation rate, frontal existence, and frontal advancement are largely functions of the degree of interaction with prevailing large-scale winds.

5.2 Intensity, Fronts and Frontal Advancement

Schmidt *(1947)* states that the sea breeze is most striking when moderate offshore motion of the geostrophic wind exists. Defant (1951) explained that offshore winds aid in mass transfer seaward and that particularly strong breezes occur on coasts with cold ocean currents nearby. The offshore winds retard the shoreward movement of the breeze and cause a cold front type system which Defant labels as "sea breezes of the second kind." Fisher (1960) found that early morning offshore winds advected warm air from land out over the ocean to start the sea breeze offshore instead of near the coast. Estoque(1961) also notes that when the large-scale wind is from land to sea, the sea breeze develops at sea and advances more slowly landward, reaching the coast much later in the afternoon. acting like a front with a characteristic wind shift. Estoque's model (1962) showed that the strongest vertical motions occur

in cases of no geostrophic wind, winds from 270°T and from 180°T {off-shore) . The weakest vertical motions occurred when geostrophic winds were from 0°T or 90°T. Again, this was a quantitative way of showing that the geostrophic wind field effects 'the development of the mesoscale pressure field by preventing excessive heating or cooling over the land, which in turn increases or decreases the breeze circulation.

This model demonstrates the above effects when the zero geostrophic wind (Section 4.1), 270°T geostrophic wind (Section 4.2) and the 220°T geostrophic wind (Section 4.3) sea breeze cases are compared. The 220°T case has the slowest frontal movement, farthest seaward net u_{max} core, largest magnitude of $\left|\frac{\partial u}{\partial x}\right|$ and $\left|\frac{\partial v}{\partial x}\right|$ (landward side of velocity cores) and the greatest land-sea thermal difference of the three mentioned sea breeze cases. The model cases of geostrophic winds with onshore components 090°T (Section 4.4) and 040°T (Section 4.5) show nothing resembling a front during the 1500 to 1900 time period, and show reduced temperature and velocity gradients.

The numerical method used in this study retained the non-linear advective terms which allowed for examination of the feedback effect of the wind field on itself and the effect of the flow on the temperature field. Fisher's model (1961) while also having this feature, did not use a time varying K (varied in vertical only). Therefore, the onset times of increased vertical circulation and maximum horizontal flow velocities are reduced due to application of a comparatively large eddy thermal diffusity in the more stable early morning hours. The evening effects on the land breeze casued by reduction of K and adecreasing boundary layer height would also not be exhibited (Fisher's model became

unstable after 1900 LT). Estoque's (1962) model looked at the same processes, but never combined the nonzero geostrophic cases with the inversion situation and never quantified the frontal advancement rates or vertical circulation strengths.

While a geostrophic wind with a *weak* offshore component has been seen to cause an increased sea breeze circulation (see Sections 4.2 and 4.3 and the above references), the resultant disturbance terms tend to reduce the large-scale wind influences. These nonlinear self-advective terms (sea breeze Eqs. 3.26, 3.27 and 3.28) act to prevent the net u_{max} core from being continually advected seaward in time by the geostrophic wind (see Section 4.3 and Walsh, 1974); diminish the magnitude of the $\left|\frac{\partial u}{\partial x}\right|$ and $\left|\frac{\partial v}{\partial x}\right|$ terms on the landward side of the disturbance core; reduce the vertical velocities (required by mass continuity), and decrease the the mal difference between land and sea. In the case of a geostrophic wind with an onshore component, the nonlinear self-advection terms (much reduced in magnitude), do not counteract but augment the large-scale wind effects and together they tend to suppress 'the sea breeze disturbance circulation (see Sections 4.4 and 4.5).

The August 7, 1977, data showed evidence (Figure 30) of stalling of the sea breeze "front" at sea until later than 1500 ADST, where the inshore stations began to be affected. The August 15, 1977, data (Figure *32)* is evidence of limited inland influence of the breeze. It should be noted that for the Beaufort Coast in the Study area, a 270°T geostrophic wind will have an offshore component relative to the coastline orientation. The example of sea breeze days shown in the data, for the most part, are those where the geostrophic wind has a seaward component.

The radiosonde data exhibit an intense inversion over the water during the sea breeze day. Adiabatic warming due to downward circulation will act to maintain a stable thermal stratification.

The model's increase with time of the depth of onshore flow from 0300 to 1500 agrees qualitatively with Fisher's observations (1960) and the August 1976 acoustic sounder data (Figure 35), since under weak geostrophic winds the return flow occurs above the PBL.

Walsh's (1974) study involving both a linear and nonlinear model that exhibited some of the characteristics mentioned above, was unable to handle a land-sea temperature difference greater than 9°C and utilized a constant K. His sea breeze occurrence criterion (see Chapter 1) was developed from the linear model with X = 10 m^2/sec and was based on the assumption that the maximum disturbance velocity will be found at the coastline. Unlike Walsh's model results, this model shows that the disturbance velocity increases when the opposing geostrophic wind is increased from 0 m/s to 3 m/s to 5 m/s (see Section 4.2 and 4.3). The net surface velocity near the coast still exhibits sea breeze effects. The model results (V_g = 5 m/s, Section 4.3) plus data from 15 August 1977 (Figure 17 and Figure 32) indicate that V_g may be as large as 6 m/s and still show a sea breeze inland. The sea breeze criterion of Walsh would limit V_G to 4.5 m/s or less for land-sea temperature difference of 14°C (at the coast). It is felt that criterion of Walsh underestimates the opposing V_g due to his use of a constant K linear model. Also, the sea breeze u_{max} core is displaced shoreward by the nonlinear self-advection effects in opposition to the V_G advection offshore and must result in a larger net velocity shoreward at the coast.

5.3 Rotation and Rotation Rates

The rotation of surface wind vectors under the influence of land and sea breezes has been shown by Haurwitz (1947) to be primarily due to Coriolis forces. In the case of a weak synoptic wind, a complete 360° turning of the surface wind vector can take place in a diurnal cycle. The surface winds on t'ne Beaufort Coast cannot exhibit 360° (under O synoptic wind conditions) turning, since the land remains warmer than the water during the short arctic night. For the study area, a wind direction from 25°T to 115°T would be the most predominant quadrant of influence due to the coastline orientation and the thermally induced mesoscale pressure gradient.

Observations by Defant (1951) and Neumann (1977) indicate that the rate of sea breeze turning is not uniform, The directional change from 1400 LST to 1700 LST during the breeze velocity maximum, is less than that between 0800 and 1100. while turning is more 'rapid between 2000 and 2300.

Neumann (1977) developed an expression for the rate of turning of a land-sea breeze. He used a coordinate system and notation similar to this model. Letting $\alpha \equiv \arctan \frac{v}{u}$ with α measured as the angle between the positive x-axis (north) and the wind, Neumann wrote 'he $\frac{\partial \alpha}{\partial t}$ in standard form and substituted Eqs. (3.19) and (3.20). Assuming that

$$u \frac{\partial}{\partial z}\left(K \frac{\partial v}{\partial z}\right) \simeq v \frac{\partial}{\partial z}\left(K \frac{\partial u}{\partial z}\right)$$

within the boundary layer,

$$\frac{\partial \alpha}{\partial t} = -f + \frac{1}{v^2}\left[\frac{v}{e}\frac{\partial P_m}{\partial x} + f(uu_g + vv_g)\right] - u\frac{\partial \alpha}{\partial x} - w\frac{\partial \alpha}{\partial z} \qquad \textbf{(5.01)}$$

where $P_m \equiv$ mesoscale pressure gradient

$u_g \equiv$ geostrophic component perpendicular to the coast

$v_g \equiv$ geostrophic component parallel to the coast

$f \equiv$ Coriolis parameter

$V^2 \equiv u^2 + v^2$

$u = u_g + u_m$, m denotes mesoscale

$v = v_g + v_m$, m denotes mesoscale

The second to last term is negligible except in the vicinity of a sea breeze front (Neumann and Mahrer, 1971) and the last term is usually negligible. For the Beaufort Coast, both model output and actual data show changes in α of 120° in 100 (vertical) meters (on days with offshore gradient winds), but $|w\ \partial\alpha/\partial z|$ is still one order of magnitude less than f for W velocities of .1 cm/sec (model) near the surface.

The following discussion of terms in Eq. (5.01) is adapted from Neuman (1977). Since $\frac{\partial\alpha}{\partial t}$ is an angular velocity representing a rotation about the local vertical. the terms on the right must be of the same form. The first term is a constant equal to twice the earth's rotation rate about the local vertical. Therefore, the other terms must be responsible for the variation in observed rotation rates. The next term is the mesoscale term and is the scalar form of the cross product of $\hat{i}\ (\rho V^2)^{-1}\left(\frac{\partial P_m}{\partial x}\right)$ and $\overline{V} \equiv \hat{i}u + \hat{j}v$ .where $\hat{i}$ and $\hat{j}$ are unit vectors in the x arid y directions. In a normal land-sea breeze situation its magnitude and direction vary diurnally. The' third term in Eq. (5.01) is large-scale and can be rewritten as

$$\frac{1}{\rho V^2}\left\{\frac{\partial P_L}{\partial x}v - \frac{\partial P_L}{\partial y}u\right\}$$

It is the scalar form of the cross product of the two horizontal vectors

[*J[WW-'EII'"'7

This term will vary in time even in the case of a constant large-scale pressure gradient,

For the case of $u_g = 0$, (5.01) cart be approximated by

$$\frac{\partial \alpha}{\partial t} = -f + \frac{v}{V^2 \rho}\left\{\frac{\partial P_m}{\partial x} + \frac{\partial P_L}{\partial x}\right\} \tag{5.02}$$

Using a coordinate system for the arctic coast (as in this-paper) the mesoscale pressure gradient which causes the sea breeze would always be +. For an easterly V_g, $\frac{\partial P_L}{\partial x}$ would be + to further reduce any clockwise turning. A westerly v_g would enhance the clockwise rotation rate since $\frac{\partial P_L}{\partial x}$ would be (-). This effect has been shown in the model in Chapter IV Sections 4.6 and 4.7 for a westerly v_g (Case 2), and an easterly v_g (Case 4). The actual data in Chapter II, Figures 21 and 13, show the westerly v_g case while Figure 15 shows the easterly v_g case. If the mesoscale pressure gradient is equal to and opposite the large-scale, the rotation rate is $-f$.

For $v_g = 0$, Eq. (5.01) can be written

$$\frac{\partial \alpha}{\partial t} = -f + \frac{1}{\rho V^2}\left\{v\frac{\partial P_m}{\partial x} - u\frac{\partial P_L}{\partial y}\right\} \tag{5.03}$$

For the arctic coast, the mesoscale term is +, as above. If u is (-) and $\frac{\partial P_L}{\partial y}$ is (-) [offshore geostrophic flow] the clockwise rotation is enhanced. If $\frac{\partial P_L}{\partial y}$ is (+) (onshore geostrophic flow) and u is (-), clockwise rotation is reduced further since the mesoscale term always *acts* to diminish clockwise rotation. This is seen in the model results for Chapter IV in Sections 4.6 [u_g offshore, Case 3: u_g onshore, Case 5]. The actual data show the rapid rotation in Figure 17b [u_g offshore, coastline orientation included].

The case v_g and u_g = 0 was tested against the model output only (5 km at sea), since it is a rare occurrence in nature. Eq. (5.01) would be rewritten as

$$\frac{\partial \alpha}{\partial t} = -f + \frac{1}{V^2}\left[\frac{u}{\rho}\frac{\partial P_m}{\partial x}\right] \tag{5.04}$$

Since the pressure gradient created by the sea-land termal contrast is (+) (negative $\frac{\partial P_m}{\partial x}$ doesn't exist along the Beaufort Coast in summer) and the resultant easterly V is (+), the mesoscale term is always +, which means that $\frac{\partial \alpha}{\partial t}$ will be smaller than $|f|$ or the sea breeze rotation will be decreased. Note: $\frac{\partial \alpha}{\partial t} = -f$ represents one complete clockwise rotation in 12.7 hours (the inertial period), or 280/hour. The model showed a surface wind clockwise rotation rate of 5.5°/hr *from 1000* to **1200**, while calculating $\frac{\partial \alpha}{\partial t}$ from model output (Eq.5.04) using $\frac{\partial P_m}{\partial x}$, v, and V^2 resulted in a rate of 7.4°/hr clockwise. For 1400-1600, the model showed a surface wind clockwise rotation rate of 2°/hr, versus 3.1°/hr clockwise from Eq. (5.04). The time period 1800-2000 had a model surface wind rotation rate of 5.5°/hr compared with 8.3°/hr from substituting

model output into Eq. (5.04). The model rotation rates and theoretical rotation rates from $\frac{\partial \alpha}{\partial t}$ are of the same order of magnitude and show similar changes at the same time of day. The model showed a total rotation at 5 km seaward from the coast of 67° clockwise (7°T at 1000 and 74°T at *0300* the following day) in 15 hours.

The 270"T, 5 m/s geostrophic case (model) exhibits a turning rate of 23.8°/hr clockwise versus 20.5°/hr clockwise, using the model output in the first three terms of Eq. (5.01). In this case u_g = 2.11 m/s and v_g = -4.53 m/s due to coastline orientation. Actual data taken 19 August 1977 (Figure 21b) shows an approximate surface turning of 22.8° clockwise, but is suspect since the upper level wind direction was not constant. In this case $u_g u$ and $V_g v$ are both (-), while $\frac{\partial P_m}{\partial x}$ is (+) as usual; therefore, the clockwise turning is augmented and approaches that of *-f.*

The 220"T, 5 m/s geostrophic case (with u_g = 4.83 m/s and v_g = -1.29 m/s due to coastline orientation) has turning in the model from 1500 to 1900 of 13.8°/hr clockwise. The $\frac{\partial \alpha}{\partial t}$ using model output in Eq. (5.01) First three terms) yields 8.1°/hr clockwise. Data from 15 August 1977 shows 12.5°/hr clockwise. Again the mesoscale term is (+) but the u term changes from (-) to (+) over four hours, so the large-scale term decreases and may become (+), which inhibits turning in the late afternoon. Reduced clockwise turning rates result.

The 090°T, 5 m/s geostrophic case (model) showed turning of 1.55°/hr clockwise from 1500 to 1900, while $\frac{\partial \alpha}{\partial t}$ using model output in Eq. (5.01) (first three terms) with v_g = -2 11 m/s and v_g = 4.33 m/s shows 1.75°/hr clockwise. The large-scale term in (5.01) was (-t-) and the mesoscale

term was (+), which caused the rotation to diminish rapid Ly. Actual data from Figures 15b and 19b show turning of approximately 5°/hr clockwise, but this is probably not a true sea breeze turning since wind speeds and directions above the boundary layer changed during the time period.

The 040°T cases are not covered since actual data with upper level winds from this direction were not obtained. The behavior would be similar to the 090 T case since u_g anti v_g would make the large-scale term (+).

5.4 Synopsis of Chapter V

Characteristics peculiar to the arctic sea breeze such as the 37% larger Coriolis force, quasi-permanent surface-based inversion over water, initial ground-based inversion overland [limits vertical extent of sea breeze and weakens fronts], absence of a land breeze [land-sea temperature difference is always +], large land-sea temperature difference [14°C at the coast and 25°C at a distance of 50 km inland] were discussed in relation to their resultant effects.

Characteristics of sea breezes in general due to interaction of the mesoscale and large-scale pressure gradients plus nonlinear self-advective effects on the temperature field and disturbance velocities were delineated. Asymmetry of the sea breeze velocity core ($\frac{\partial u}{\partial x}$ is greater on the landward side during offshore gradient winds), stalling of the sea breeze with possible frontal buildup, and temporal increase in height of landward flow have all been effectively modeled in this study.

Rotation and rotation rates of the surface sea breeze vectors were compared for model cases of 0 m/s, 270°T at 5 m/s, 220° at 5 m/s, and 090°T at 5 m/s geostrophic winds, with existing data (except for 0 m/s case), and an analytic expression for rotation rates derived by Neumann (1977). The rates were comparable in magnitude and trends "toward increasing or decreasing rotation rates.

Model evidence has shown that the sea breeze disturbance velocity increased (above that of 0 geostrophic winds) during offshore geostrophic wind' influence, enough to offset the prevailing wind at the surface. Actual data have shown that the sea breeze occurrence criterion of Walsh (1974) based on a linear constant K model, may underestimate the maximum offshore gradient wind allowable to eliminate a sea breeze.

VI. CONCLUSIONS AND RECOMMENDATIONS

The dominant physical factor causing the large atmospheric boundary layer turning of the wind (in space and time) on the Alaskan arctic coast is the sea breeze. The large diurnally varying land-sea thermal contrast, clockwise rotation of the surface wind vector, and surface wind flow in opposition to moderate offshore gradient flow are factors and evidence of this mesoscale phenomenon.

The inclusion of geostrophic winds in a nonlinear sea breeze model has successfully modeled the experimental pilot balloon data and surface wind vector turning. An additional interesting effect is that offshore geostrophic winds may lead to a stronger sea breeze disturbance velocity than possible with zero geostrophic flow. The resulting sea breeze will offset larger geostrophic seaward flows than previously thought possible on theoretical grounds. The model has shown this effect, and limited data agree. The method of imposition of this offshore gradient flow in the model and in nature may be critical since the actual data have shown the large-scale pressure gradient may not be constant in time (in the model: $\frac{\partial P_L}{\partial t}$ at, $\frac{\partial u_L}{\text{at}}$, $\frac{\partial v_L}{\text{at}}$, $\frac{\partial \theta_L}{\text{at}} = 0$) such as the case in Figure 17b where initial weak offshore synoptic winds (2 m/s) had built up to 6 m/s (220 T) in three hours without offsetting the surface sea breeze influence.

Further work with the model should include:

1. incorporating a heat balance equation to simulate surface heating rather than a sinusoidal temperature variation.

2. Choosing an optimum grid spacing with increased vertical resolution near the ground and increased horizontal resolution near the coast.
3. Utilizing a spatially varying large-scale temperature profile showing a decrease in static stability seaward, because the marine inversion is maintained in part by proximity of warm land air (model).
4. Adding a water vapor (mixing ratio) equation.

New sea breeze related experiments along the Alaskan arctic coast should include:

1. An attempt to determine the seaward extent of the sea breeze and its relation to surface currents and small ice flow movement.
2. Implementation of a more accurate surface pressure network comprised of buoys on the arctic ice pack and inland buoys (more than 100 km from the coast) to avoid sea breeze induced pressure variations.
3. Investigation of the sea breeze influence on coastal fogging.

REFERENCES

Anthes, R. A., The height of the planetary boundary layer and the production of circulation in a sea breeze model, *J. Atmos. Sci., 35, 1231-1239, 1.978.*

Berry, F. A., E. Bollay, and N. R. Beers, *Handbook of Meteorology*, McGraw-Hill, New York, 1068 pp., 1973.

Brewer, W. A., H. F. Diaz, A. S. Prechtel, H. W. Searby, and J. L. Wise, *Climatic Atlas of the Outer Continental Shelf Waters and Coastal Regions of Alaska*, NOAA, *NCC*, EDS, Asheville, North Carolina, 409 pp., 1977.

Brown, R. A., P. Maier, and T. Fox, Surface atmospheric fields and derived geostrophic winds, *AIDJEX Bulletin, 26*, 173-203, 1974.

Busch, N. E., On the mechanics of atmospheric turbulence, in *Workshop on Micrometeorology*, edited by D. A. Haugen, Amer. Meteorology Soc., Boston, Massachusetts, 1-27, 1973.

Businger, J. A., J. C. Wyngaard, Y. Izumi, and E. F. Bradley, Flux profile relationships in the atmospheric surface layer, *J. Atmos. Sci.*, 28, 181-189, 1971.

Carsey, F. D., Acoustic radar techniques in modeling and measurement of air stress over pack ice, *Final Report, NOAA Contract RW0000-8AA71880*, Boulder, Colorado, 30 pp., 1976.

Cotton, W. R., R. A. Pielke and P. T. Gannon, Numerical experiments on the influence of the mesoscale circulation on the cumulus scale. *J. Atmos. Sci.*, 33, 252-261, 1976.

Deardorff, J. W., Three-dimensional numerical modeling of the planetary boundary layer. In *Workshop on Micrometeorology*, edited by D. A. Haugen, Amer. Meteorology Soc., Boston, Massachusetts? 271-311, 1973.

Defant, F., Local winds, *Compendium of Meteorology*, Amer. Meteorology Sot., Boston, Massachusetts, 655-662, 1951.

Delage, Y., and P. A. Taylor, Numerical "studies of heat island circulations, *Boundary-Layer Meteor., 1, 201-226,* 1970.

DuFort, E. C., and S. P. Frankel, Stability conditions in the numerical treatment of parabolic differential equations, *Math. Tables Aids Comput., Vol. 7, 135-152, 1953.*

Dzerdzeevskii, B. L., Tsirkuliatsionnye skhemy v troposfere tsentral noi Arktiki, in *Izdatelstvo Akad. Nauk.* (English translation in *Sci. Report #3 under contract AF 19(122) - 228,* UCLA, 1945.

Estoque, M. A., A theoretical investigation of the sea breeze. *Quart. J. Roy. Meteor.* See., 87, 136-146, 1961.

Estoque, M. A., The sea breeze as a function of the prevailing synoptic situation. *J. Atmos. Sci., 19,* 244-250, 1962.

Estoque, M. A., A numerical model of the atmospheric boundary layer, *J. Geophys. Res., 68,* 1103-1113, 1963.

Estoque, M. A. Numerical modeling of the planetary boundary layer. In *Workshop on Microcmeteorology,* edited by D. A. Haugen, Amer. Meteor. Sot., Boston, Massachusetts, 217-270, 1973.

Fisher, E. L., An observational study of the sea breeze, *J. Meteor.,* 27, 645-660, 1960.

Fisher, E. L., A theoretical study of the sea breeze, *J. Meteor.,18,* 216-233, 1961.

Francis, P. E., The use of a multipoint filter as a dissipative mechanism in a numerical model of the general circulation of the atmosphere. *Quart. J. Roy. Meteor. Soc., 101, 567-582,* 1975.

Geisler, J. E., and F. P. Bretherton, The sea breeze forerunner, *J. Atmos. Sci.,* 26, 82-95, 1969.

Gonella, J., A rotary-component method for analysing meteorological and oceanographic vector time series, *Deep-Sea Res., 19,* 833-846, 1972.

Hall, F. F., J. G. Edinger, and W. D. Neff, Convective plumes in the planetary boundary layer, investigated with an acoustic echo sounder, *J. Appl. Meteor., 14, 513-523, 1975.*

Hart, R. L. F. R. George, L. S. VanLoon, B. B. Hicks, F. C. Kulhanek, The ANL 403 MHz radiosone system, *J. Appl. Meteor., 17., 235-238, 1978.*

Haurwitz., B., Comments on the sea-breeze circulation, *J. Meteor., 4,* 1-8, 1947.

Hawkins, J. D., A study of the mesoscale wind circulation in a land-sea breeze regime, *Bull. Amer. Meteor.* See., 58(12), 1294-1295, 1977.

Holmgren, B. L. Spears, C. Wilson, and C. Benson, Acoustic soundings of the Fairbanks temperature inversions. *Climate of the Arctic, conference* publication of the Geophysical Institute, Univ. of Alaska, Fairbanks, 293-305, 1974.

Holton, J. R., *An Introduction to Dynamic Meteorology*, Academic Press, New York, 319 pp., 1972.

Hufford, G.L., B.D. Thompson, and L.D. Farmer. Currents of the northeast Chukchi Sea, *Annual Report, RU 81 OCSEAP*, Arctic Project Office, Fairbanks, 1977.

Kozo, T.L., Coastal meteorology of the Alaskan arctic coast, OCS *Contract 03-5-022-672021, 1977.*

Kozo, T. L., Coastal meteorology of the Alaskan arctic *coast, OCS Contract 03-5-022-671011, 1978.*

Krishna, K., A numerical study of the diurnal variation of meteorological parameters in the planetary boundary layer, I. Diurnal variation of winds, *Monthly Weath. Rev., 96(5), 269-276, 1969.*

Krumbein, W. C., Trend surface analysis of contour-type maps with irregular control point spacing, *J. Geophys. Res., 64*, 823-834, 1959.

Kuo, H. L., The thermal interaction between the atmosphere and the earth and propagation of diurnal temperature waves, *J. Atmos. Sc., 25, 682-706, 1968.*

Mak, M. K., and J. E. Walsh, On the relative intensities of sea and land breezes, *J. Atmos. Sci., 33*, 242-251, 1976.

Martin, P., and M. Clarke, A test of barometric pressure and temperature measurements from ADRAMS buoys, *AIDJEX Bull., 40*, 61-81, *1978.*

Martin, P., and C. R. Gillespie, Arctic odyssey--five years of data buoys in AIDJEX, *AIDJEX Bull., 40, 7-11, 1978.*

Middleton, W. E. and .4. F. Spilhaus, *Meteorological Instruments*, University of Toronto Press, Toronto, 286 pp, 1953.

Moritz, R. E., On a possible sea breeze circulation near Barrow, Alaska, *Arctic Alp. Res., 9*, 427-431, 1977.

Moroz. W. J., A lake breeze on the eastern shore of Lake Michigan: observations and model, *J. Atmos. Sci.*, 24, 337-355, 1967.

Neumann, J., On the rotation rate of the direction of sea and land breezes, *J. Atmos. Sci.*, 34, 1914-1917, 1977.

Neumann, J., and Y. Mahrer, A theoretical study of the land and sea breeze circulation, *J. Atmos. Sci., 28*, 532-542.

Neumann, J., and Y. Mahrer, A theoretical study of the lake and land breezes of circular lakes, *Month. Weath. Rev., 103, 474-485, 1975.*

Nordlund, G., The sea breeze in south Finland according to a numerical model, *Finnish Met. Inst. Contr.*, *77*, 1-28, 1971.

O'Brian, J. J., and R. D. Pillsbury, Rotary wind spectra in a sea breeze regime, *J. Appl. Meteor.*, *1.3*, 820-825, 1974.

Paulson, C. A., The mathematical representation of wind speed and temperature profiles in the unstable atmospheric surface layer, *J. Appl. Meteor.*, *9*, *857-861, 1970.*

Reed, R. J., and B. A. Kunkel, The arctic circulation in summer, *J. Meteor.*, 17, 489-505, 1960.

Reynolds, R. M., An acoustic radar for studying low-level atmospheric phenomena. M.S. Thesis, Meteorology Dept., Univ. of Melbourne, Australia, 108 pp., 1970.

Rossi, V., Land und Seawind on den Finnischen Küsten. *Mitt. Met. Zentralans* Helsinki, *41*, 1-17, 1957.

Schmidt, F. H., An elementary theory of the land and< sea-breeze circulation, *J. Meteor.*, *4*, **9-15, 1947.**

Schroeder, M. J., M. A. Fosberg, O. P. Cramer, and A. O'Dell, Marine air invasion of the Pacific Coast: a problem analysis, *Bull. Amer. Meteor. Soc.*, 48(11), 802-808, 1967.

Shapiro, R., The use of linear filtering as a parametrization of atmospheric diffusion, *J. Atmos. Sci.*,*28*, 1971.

Shaposhnikova, M. I., V. N. Lykosov, and L. N. Gutman, *Nonstationary* nonlinear problem of a breeze in astably stratified atmosphere, *Izv. Acad. Sci.*, USSR, also in *Atmos. Ocean. Phys.*, *4, 79-89, 1968.*

Sheih, C. M., and W. J. Moroz, Mathematical modeling of lake breeze, *Atmos. Envir.*, *9, 575-586, 1975.*

Simpson, J. E., Sea-breeze fronts in Hampshire, *Weather*, 19, 208-220, 1964.

Simpson, J. E., D. A. Mansfield, and J. R. Milford, Inland penetration of sea-breeze fronts, *Quart. J. Roy. Met. Soc.*, *103*, 47-76, 1977.

Walsh, J. E., Sea breeze theory and applications, *J. Atmos. Sci.*, 31, 2012-2026, 1974.

Walsh, J. E.. Measurements of the temperature, wind and moisture distribution across the northern coast of Alaska, *Arctic Alp. Res.*, *9*, *175-182*, 1977.

Wyckoff, R. J., D. W. Beran, and F. F. Hall, A comparison of the low-level radiosonde and the acoustic echo sounder for monitoring

atmospheric stability, J. *Appl. Meteor.*, *12*, **1196-1204**, 1973.

Yoshino, M. M., *Climate in a Small Area*, University of Tokyo Press, Tokyo, Japan, 549 pp., 1975.

APPENDIX A

THE PREDICTION EQUATIONS IN FINITE-DIFFERENCE FORM

In the following equations for the model above the surface layer,

n = integer time step

i = integer grid point on the z-axis

j = integer grid point on the horizontal axis

Δx = grid interval on x-axis

Δz = grid interval on z-axis

Δt = time step

m = index with a value

1 for u, v, or $w > 0$

-1 for u, v, or $w < 0$

The x-axis and u velocity are perpendicular to the coast. The y-axis and v velocity are parallel to the coast. The z-axis and w velocity are in the usual vertical direction. Superscript L denotes the large-scale component of a variable and a prime (′) denotes the disturbance component of a variable. Terms without L or (′) are sums of the large-scale and disturbance components (i.e., $u = u^L + u'$).

The advective terms in (A1) through (A3) are written as unentered differences rather than centered to avoid numerical instabilities in a method used by Fisher (1961). The vertical diffusion term for equations (A1), (A2) and (A3) was developed by DeFort and Frankel (1953) and

results in a stable, explicit integration method (Estoque, 1963). The equation for the u' velocity, Eq. 3.26, is

$$\frac{u'_{n+1,i,j} - u'_{n-1,i,j}}{2\Delta t} = - u_{n,i,j} \left\{ \frac{u'_{n,i,j} - u'_{n,i,j-m}}{\Delta x} \right\} m$$

$$- w'_{n,i,j} \left\{ \frac{u'_{n,i,j} - u'_{n,i-m,j}}{\Delta z} \right\} m$$

$$\frac{RT_{n,i,j}}{P_{n,i,j}} \left\{ \frac{P'_{n,i,j+1} - P'_{n,i,j-1}}{2\Delta x} \right\} + f v'_{n,i,j} \tag{A1}$$

$$+ \left\{ \frac{K_{n,i+1,j} - K_{n,i-1,j}}{2\Delta z} \right\} \cdot \left\{ \frac{u_{n,i+1,j} - u_{n,i-1,j}}{2\Delta z} \right\}$$

$$+ K_{n,i,j} \left\{ \frac{u'_{n,i+1,j} + u'_{n,i-1,j} - u'_{n+1,i,j} - u'_{n-1,i,j}}{(\Delta z)^2} \right\}$$

The equation for the v' velocity (Eq. 3.27) with no variations in the y direction is

$$\frac{v'_{n+1,i,j} - v'_{n-1,i,j}}{2\Delta t} = - u_{n,i,j} \left\{ \frac{v'_{n,i,j} - v'_{n,i,j-m}}{\Delta x} \right\} m$$

$$- w'_{n,i,j} \left\{ \frac{v'_{n,i,j} - v'_{n,i-m,j}}{\Delta z} \right\} m - f u'_{n,i,j}$$

$$+ \left\{ \frac{K_{n,i+1,j} - K_{n,i-1,j}}{2\Delta z} \right\} \cdot \left\{ \frac{v_{n,i+1,j} - v_{n,i-1,j}}{2\Delta z} \right\} \tag{A2}$$

$$+ K_{n,i,j} \left\{ \frac{v'_{n,i+1,j} + v'_{n,i-1,j} - v'_{n+1,i,j} - v'_{n-1,i,j}}{(\Delta z)^2} \right\}$$

The equation for potential temperature (Eq. 3.29) θ' can be written

$$\frac{\theta'_{n+1,i,j} \quad \theta'_{n-1,i,j}}{2\Delta t} \cdot - u_{n,i,j} \left\{ \frac{\theta_{n,i,j} \quad - E_{n,i,j-m}}{Ax} \right\} m$$

$$- w'_{n,i,j} \left\{ \frac{\theta_{n,i,j} \quad \theta_{n,i-m,j}}{\Delta z} \right\} m \tag{A3}$$

$$+ \left\{ \frac{K_{n,i+1,j} \quad K_{n,i-1,j}}{2\Delta z} \right\} \cdot \left\{ \frac{\theta_{n,i+1,j} - \theta_{n,i-1,j}}{2\Delta z} \right\}$$

$$+ K_{n,i,j} \left\{ \frac{\theta_{n,i+1,j} + \theta_{n,i-1,j} - \theta_{n+1,i,j} - \theta_{n-1,j}}{(\Delta z)^2} \right\}$$

The equation for the vertical velocity (Eq. 3.30) is used to compute w' after every time step using the new u' velocities. The integration proceeds upward from the surface where $w' = 0$.

$$\frac{w'_{n,i+1,j} - w'_{n,i,j}}{\Delta z} = - \left\{ \left[\frac{\Delta u}{\Delta x} \right]_{n,i+1,j} + \left[\frac{\Delta u}{\Delta x} \right]_{n,i,j} \right\} \div 2$$

and (A4)

$$\left[\frac{\Delta u}{\Delta x} \right]_{n,i,j} = \frac{u'_{n,i,j+1} - u'_{n,i,j-1}}{2\Delta x}$$

The pressure equation (3.28) is used to compute p' after every time step.

$$\frac{P'_{n,i+1,j} - P'_{n,i,j}}{\Delta z} = - \frac{g}{R} \left\{ \frac{P^L_{n,i+\frac{1}{2},j} + P_{n,i+\frac{1}{2},j}}{T^L_{n,i+\frac{1}{2},j} + T_{n,i+\frac{1}{2},j}} - \frac{P^L_{n,i+\frac{1}{2},j}}{T^L_{n,i+\frac{1}{2},j}} \right\} \tag{A5}$$

where

$$P^{L}_{n,i+\frac{1}{2},j} \equiv \frac{P^{L}_{n,i+1,j} + P^{L}_{n,i,j}}{2}$$

$$P'_{n,i+\frac{1}{2},j} \equiv \frac{P'_{n,i+1,j} + P'_{n,i,j}}{2}$$

$$T^{L}_{n,i+\frac{1}{2},j} \equiv \frac{T^{L}_{n,i+1,j} + T^{L}_{n,i,j}}{2}$$

$$T'_{n,i+\frac{1}{2},j} \equiv \frac{T'_{n,i+1,j} + T'_{n,i,j}}{2}$$

The integration proceeds downward from the highest grid level where $p' = 0$.

APPENDIX B

DERIVATIONS OF THE u, θ, u_*, θ_*, AND $K(h)$ EQUATIONS FOR THE SURFACE LAYER

Case 1. Stable conditions (Ri number > 0)

$$\phi_m = \frac{k(z+z_0)}{u_*}\frac{\partial U}{\partial z} = 1 + 4.7\,\zeta \qquad \text{(dimensionless wind shear, Businger, et al., 1971)} \tag{B1}$$

where

$$\zeta = \frac{z}{L} = \frac{-kg\,\overline{w'\theta'}\,(z+z_0)}{\bar{\theta}\,u_*} \qquad \text{(dimensionless height)} \tag{B2}$$

therefore:

$$\frac{\partial U}{\partial z} = \frac{u_*}{k}\left\{\frac{1}{z+z_0} + \frac{4.7}{L}\right\} \tag{B3}$$

Integration with respect to z yields:

$$u = \frac{u_*}{k}\ln(z+z_0) + 4.7\,\zeta + C \tag{B4}$$

since $u = 0$ at $z = z_0$ (roughness length)

$$U = \frac{u_*}{k}\left\{\ln\left(\frac{z+z_0}{z_0}\right) + 4.7\,\zeta\right\} \tag{B5}$$

Similarly

$$\phi_h = \frac{k(z+z_0)}{\theta_*}\frac{\partial\theta}{\partial z} = .74 + 4.7\,\zeta \qquad \text{(dimensionless temperature gradient, Businger, et al., 1971)} \tag{B6}$$

therefore:

$$\frac{\partial\theta}{\partial z} = \frac{\theta_*}{k}\left\{.74\left(\frac{1}{z+z_0}\right) + \frac{4.7}{L}\right\} \tag{B7}$$

Integration with respect to z and noting $\theta = \theta_0$ at $z = z_0$ yields:

$$\theta = \frac{\theta_*}{k} \left\{ .74 \ln \left(\frac{z+z_0}{z_0}\right) + 4.7\ \zeta \right\} + \theta_0 \tag{B8}$$

Since we have assumed $K_h = K_m$, for Ri number > 0

$$\theta \simeq \frac{\theta_*}{k} \left\{ \ln \frac{z+z_0}{z_0} + 4.7\ \zeta \right\} + \theta_0 \tag{B9}$$

To calculate u_* and θ_*, continuity of vertical derivatives is assumed between the top of the surface layer, h, and the level immediately above [$(h+\Delta z)$ Estoque, 1963)1.

$$\left(\frac{\partial U}{\partial z}\right)_h = \frac{U(h+\Delta z) - U(h)}{\Delta z} \tag{B10}$$

with (B3) this implies

$$\frac{U(h+\Delta z) - U(h)}{\Delta z} = \frac{u_*}{k} \left\{ \frac{1}{(h+z_0)} + \frac{4.7}{L} \right\} \tag{B11}$$

using the differentiated form of (B9), a similar expression involving θ can be written,

$$\frac{\theta(h+\Delta z) - \theta(h)}{\Delta z} \cdot \frac{\theta_*}{k} \left\{ \frac{1}{(h+z_0)} + \frac{4.7}{L} \right\} \tag{B12}$$

With. (B5), (B11) can be rewritten

$$\frac{u(h+\Delta z)}{\Delta z} - \frac{u_*}{k} \left\{ \frac{\ln}{\Delta z} \left(\frac{h+z_0}{z_0}\right) + \frac{4.7\ h}{\Delta z\ L} \right\} = \frac{u_*}{k} \left\{ \frac{1}{(h+z_0)} + \frac{4.7}{L} \right\} \tag{B13}$$

now let $C \equiv \frac{1}{k} \ln \left(\frac{h+z_0}{z_0}\right)$, $A \equiv k\ (h+z_0)$

using (B9), (B12) is

$$\frac{\theta(h+\Delta z) - \theta_0}{\Delta z} - \theta_* \left\{ \frac{C}{\Delta z} + \frac{4.7\ h}{k\ \Delta z\ \mathrm{L}} \right\} = \theta_* \left\{ \frac{1}{A} + \frac{4.7}{k\,\mathrm{L}} \right\} \tag{B14}$$

From (B2)

$$\mathrm{L} = -\frac{u_*^3\ \bar{\theta}}{k\ g\ \overline{w'\theta'}} = +\frac{u_*^3\ \bar{\theta}}{k\ g\ \theta_* u_*}$$

where $\overline{w'\theta'}$ is replaced by $-\theta_* u_*$ (Busch, 1973). Therefore, (313) can be rewritten as

$$\frac{U(h+\Delta z)}{\Delta z} - \left\{ \frac{u_* C}{\Delta z} + \frac{4.7\ h\ \theta_* g}{\Delta z\ \bar{\theta}\ u_*} \right\} = \frac{u_*}{A} + \frac{4.7\ \theta_* g}{\bar{\theta}\ u_*} \tag{B15}$$

if $P \equiv \frac{4.7\ g}{\bar{\theta}}$

then (B14) can be rewritten as

$$\frac{\theta(h+\Delta z) - \theta_0}{z} - \theta_* \left\{ \frac{C}{\Delta z} + \frac{P}{\Delta z}\frac{\theta_* h}{u_*^2} \right\} = \frac{\theta_*}{A} + \frac{P\theta_*^2}{u_*^2} \tag{B16}$$

But (B15) can be rearranged to get θ_* in terms of u_* and known quant~-ties

$$\theta_* = \frac{-u_*^2 \left\{ \frac{\mathrm{L}}{A} + \frac{C}{\Delta z} \right\} + u_*^* \left\{ \frac{U(h+\Delta z)}{\Delta z} \right\}}{\left[\frac{Ph}{\Delta z} + P \right]} \tag{B17}$$

Substitution of (B17) into (B16) and rearranging terms gives:

$$u_* = U(h+\Delta z)\ A \left\{ \frac{1}{CA+\Delta z} - \frac{P[\theta(h+\Delta z) - \theta_0](h+\Delta z)}{(CA+\Delta z)\ U(h+\Delta z)^2} \right\}$$

or

$$u_* = \frac{U(h+\Delta z)\ k\ (h+z_0)}{\Delta z + (h+z_0)\ \ln\left[\frac{h+z_0}{z_0}\right]} \left\{ 1 - \frac{4.7\ g(h+\Delta z)[\theta(h+\Delta z) - \theta_0]}{(\theta)U(h+z_0)} \right\} \tag{B18}$$

Note: $U(h+\Delta z)$, $\theta(h+\Delta z)$ are values at level $h+\Delta z$.

The momentum flux for the surface layer at h can then be obtained since

$$K_m \frac{\partial U}{\partial z} \equiv u_*^2 \tag{B19}$$

To obtain θ_* substitute (B18) into (B17) and again after much algebra:

$$\theta_* = \frac{U_*[\theta(h+\Delta z) - \theta_0]}{U(h+\Delta z)} \tag{B20}$$

The sensible heat flux can then be calculated from:

$$K_h \frac{\partial \theta}{\partial z} \equiv u_* \theta_* \tag{B21}$$

where $K_h \approx K_m = K$.

To find *K(h)* where $K_m(h) = K_h(h) = K(h)$ use (B19) to obtain

$$K(h) = u_* \left\{ \frac{1}{k(h+z_0)} + \frac{4.7\, g\theta_*}{\bar{\theta}\, u_*^2} \right\}^{-1}$$

$$K(h) = u_* k(h+z_0) \left\{ 1 + \frac{4.7(h+z_0)}{L} \right\}^{-1} \tag{B22}$$

The final form of (B22) is obtained by dividing by $1/[k(h+z_0)]$ and using the expression for L above.

Case 2. Unstable conditions (Ri number < 0)

$$\phi_m = (1 - 15\ \mathrm{Ri})^{-1/4} \tag{B23}$$

$$\phi_h = .74(1 - 9\ \mathrm{Ri})^{-1/2} \tag{B24}$$

are from Businger et al. (1971). It must be noted that ζ and Ri are approximately equal for unstable conditions.

Therefore. .

$$\frac{\partial U}{\partial z} = \frac{u_*}{k} \frac{1}{(z+z_0)} \left\{ 1 - 15 \zeta \right\}^{-1/4} \tag{B25}$$

$$\frac{\partial \theta}{\partial z} = \frac{\theta_*}{k} \frac{(.74)}{(z+z_0)} \left\{ 1 - 9 \zeta \right\}^{-1/2} \tag{B26}$$

(B25) and (B26) can be integrated, resulting in the following expressions for u, and θ (Paulson, 1970).

$$U = \frac{u_*}{k} \left\{ \ln \frac{z+z_0}{z_0} - \psi_1 \right\} \tag{B27}$$

where

$$\psi_1 = 2 \ln[(1+x)/2] + \ln[(1+x^2)/2] - 2 \tan^{-1}(x) + \frac{\pi}{2}$$

and

$$x = \phi_m^{-1}$$

$$\theta = .74 \frac{\theta_*}{k} \left\{ \ln \frac{z+z_0}{z_0} - \psi_2 \right\} + \theta_0 \tag{B28}$$

where

$$\psi_2 = \ln[(1+y)/2], \; y = .74 \quad \phi_h^{-1}$$

and θ_0 is the temperature at $z = 0$.

Again, to calculate u_* and θ_*, continuity of vertical derivatives is assumed between the top of the surface layer, h, and the level immediately above $(h+\Delta z)$.

Using the definition of dimensionless wind shear and the stability parameter,

$$u_* = \frac{k(z+z_0)}{\phi_m\left(\frac{z}{L}\right)} \frac{\partial U}{\partial z} \tag{B29}$$

but

$$(z+z_0)\ \frac{\partial U}{\partial z} = \frac{\partial U}{\partial \ln(z+z_0)}$$

(B29) can be rewritten approximately in the layer from the surface to $h+\Delta z$ as

$$u_* = \frac{k\ \{U(h+\Delta z) - u_0\}}{\phi_m\left(\frac{z}{L}\right)\left\{\ln(h+\Delta z+z_0) - \ln z_0\right\}} \qquad u_0 = 0 \tag{B30}$$

where

$$\phi_m\left(\frac{z}{L}\right) \equiv \frac{1}{\left(\frac{h+\Delta z+z_0}{z_0}\right)}\int_0^{h+\Delta z+z_0} \phi_m\left(\frac{z}{L}\right)\partial z$$

by the mean value theorem of integral calculus, and since

$$\phi_m\left(\frac{h}{L}\right) \equiv \phi_m\left(\frac{h+\Delta z}{L}\right)$$

we have

$$u_* = \frac{k\ U(h+\Delta z)}{\ln\left(\frac{h+\Delta z+z_0}{z_0}\right)}\left\{\frac{h+\Delta z+z_0}{\Delta z\ \phi_m\left(\frac{h}{L}\right) + \int_0^{h+z_0} \phi_m\left(\frac{z}{L}\right)\partial z}\right\} \tag{B31}$$

To actually calculate u_* from the model which computes Ri from winds and temperatures at the ground and $h+\Delta z$ levels,

$$\frac{z}{L} \approx \frac{Ri}{h}\ z \quad \text{implying} \quad Ri = \zeta \quad \text{at level } h$$

was used by Krishna (1968). Using (B23) and the above approximation in (B31) (at $z = h$)

$$u_* = \frac{k\ U(h+\Delta z)(h+\Delta z+z_0)}{\ln\left(\frac{h+\Delta z+z_0}{z_0}\right)\left\{\Delta z(1-15\ Ri)^{-1/4} + \left(-\frac{4}{45}\ \frac{h}{Ri}\right)\left[(1-15\ Ri)^{3/4} - 1\right]\right\}} \tag{B32}$$

The momentum flux for the surface layer at h can be obtained from (B19)as before.

Using the dimensionless temperature gradient, the definition of the stability parameter ζ and previous mathematical operations,

$$\theta_* = \frac{k}{\phi_h\left(\frac{z}{L}\right)} \left\{\frac{\partial\theta}{\partial \ln(z+z_0)}\right\} \tag{B33}$$

(B33) can be rewritten approximately in the layer from the surface to $h+\Delta z$ as

$$\theta_* = \frac{k\{\theta(h+z) - \theta_0\}}{\ln\left(\frac{h+\Delta z+z_0}{z_0}\right) \bar{\phi}_h\left(\frac{z}{L}\right)} \tag{B34}$$

and finally applying the mean value theorem and

$$\phi_h\left(\frac{h}{L}\right) \approx \phi_h\left(\frac{h+\Delta z}{L}\right)$$

we have

$$\theta_* = \frac{k\ [\theta(h+\Delta z) - \theta_0]\ (h+\Delta z+z_0)}{\ln\left(\frac{h+\Delta z+z_0}{z_0}\right) \left\{ \Delta z\ \phi_h\left(\frac{h}{L}\right) + \int_0^h \phi_h\left(\frac{z}{L}\right) \partial z. \right\}} \tag{B35}$$

Now using (B24) and Ri = ζ at level h, the model calculates the Ri number to insert in the following expression

$$\theta_* = \frac{k\ [\theta(h+\Delta z) - \theta_0](h+\Delta z+z_0)}{\ln\left(\frac{h+\Delta z+z_0}{z_0}\right)\left\{\Delta z\left[.74(1-9\ \mathrm{Ri})^{-1/2}\right]+.74\left\{-\frac{2}{9}\frac{h}{\mathrm{Ri}}\left[(1-9\ \mathrm{Ri})^{1/2}-1\right]\right\}\right)} \tag{B36}$$

The sensible heat flux can be calculated from (B21) as before.

To find $K_m(h)$ the momentum flux, we rewrite (B19)

$$K_m(h) = \frac{u_*^2}{\left(\frac{\partial U}{\partial z}\right)_h} = k\, u_*(h+z_0)\left\{ 1 - 15\,\frac{h}{L} \right\}^{1/4} \tag{B37}$$

To find $K_h(h)$, the sensible heat flux, we rewrite (B21)

$$K_h(h) = \frac{u_*\,\theta_*}{\left(\frac{\partial \theta}{\partial z}\right)_h} = k\, u_*(h+z_0)(.74)\left\{ 1 - 9\,\frac{h}{L} \right\}^{1/2} \tag{B38}$$

VITA

THOMAS LESLIE KOZO

Born:	September 2, 1941: Allentown, Pennyslvania
Parents:	Lewis J. Kozo Mary T. Kozo
Wife:	Carolyn J. Kozo
Children:	Christopher and Justine
1959	Diploma, Bethlehem High School, Bethlehem, Pennsylvania
1963	B.S., Physics, Lafayette College, Easton, Pennsylvania
1964	U.S. Naval Marine Engineering Laboratory Underwater Acoustics, Annapolis, Maryland
1966	U.S. Naval Oceanographic Office, Geophysics, gravity surveying at sea. Suitland, Maryland
1967-1969	M.S., Physical Oceanography. Florida State University, Tallahassee, Florida
1970	U.S. Naval Oceanographic Office, Arctic Oceanography, Suitland, Maryland
1974-1979	Ph.D., Geophysics, University of Washington, Seattle, Washington

Appendix B

Evidence for Sea Breezes on the Alaskan Beaufort Sea Coast

EVIDENCE FOR SEA BREEZES ON THE ALASKAN BEAUFORT SEA COAST

Thomas L. Kozo

Polar Science Center, University of Washington, Seattle, Washington 98105

Abstract. Atmospheric environmental data collected in August 1976 and 1977 along the Beaufort Sea coast of Alaska exhibited both circumstantial and direct evidence of the existence of sea breezes at 70°N latitude. To estimate the total atmospheric boundary layer turning, a two-dimensional least squares technique was used to derive the three hourly gradient wind (above the atmospheric boundary layer) with data from surface pressure stations for simultaneous comparison to surface wind data. Results indicated the average turning of the wind from above the boundary layer to the surface was 120° on sea breeze days. Rotary spectra from time series data of surface winds measured at offshore and onshore sites have shown the horizontal extent of the sea breeze influence to include at least a 37 km zone centered on the coastline.

The sea breeze is largely responsible for the increased persistence of surface onshore (northeasterly and easterly) winds documented in August historical data for the Alaskan Beaufort Sea coast.

Introduction

The sea breeze is a mesoscale feature usually contained within the planetary boundary layer and is strongly influenced by eddy viscosity, surface roughness, and conduction processes. The intensity, duration, and extent of the sea breeze circulation are mainly determined by horizontal gradients in the amount of heat supplied by the earth's surface to the atmosphere (Defant, 1951). Its horizontal extent is large enough that the earth's rotation and the large scale atmospheric pressure gradient cannot be ignored (Walsh, 1974).

The data base for arctic sea breeze studies has been enhanced by the discovery and development of the Prudhoe Bay oil fields (mid-sixties). Since the nearshore ocean current flow along the Alaskan Beaufort Sea coast is primarily wind driven, a direct application to oil spill trajectories in lagoons and embayments exists.

The farthest north experimental sea breeze study in the literature was done by Rossi (1957) near Ilmala, Finland on the shores of the Baltic Sea (60°N). Nordlund (1971) did a theoretical study using Rossi's data.

Moritz (1977) after investigating historical data from Ft. Barrow, Alaska, discovered two significant facts. The first was the calculated geostrophic wind speeds in January were 40% greater than those calculated for July but the simultaneously observed surface wind speeds from both months were approximately the same. The second was that calculated geostrophic wind speeds and direction frequencies for July were similar for winds with east and west components, but measured surface east winds had greater magnitudes and frequency than west winds. He suggested that the surface temperature contrasts at Alaskats north coast produce an added pressure gradient component that is not recorded by the existing National Weather Service (NWS) synoptic observation network.

Walsh (1977) investigated the land-sea temperature contrast across the Alaskan north slope as a source of local thermal circulation. Unfortunately, his data was collected on days with synoptic winds unfavorable to sea breeze formation.

Experimental evidence has shown that the breeze dominated the surface wind direction at least 25% of the time during summer data collection periods along the Beaufort Sea coast.

The study area was contained within the latitudes 69"N - 74°N and longitudes 143°W - 157°W. In this way, buoys (1976 only) within the arctic ice pack, NWS stations at Barrow and Barter Island, Distant Early Warning (DEW) sites at Oliktok and Lonely (1976 only) and camps at Umiat and Happy Valley (1976 only) could be used as surface pressure data sources.

Figure 1 shows the positions of the pressure stations (P) (Weather Measure B211 microbarographs at all sites except Barter Island and Pt. Barrow) within the land-based grid for August 1976 and 1977. The primary study area (rectangle A) had surface wind (10 meter) stationa offshore on the Jones Islands (Pingok and Cottle), Cross Island and the McClure Islands (Narwhal) and onshore stations at Tolaktovut Point, Oliktok and Deadhorse. These coastal locations exist in an area where the summer tundra-ocean thermal contrast remains positive (land always warmer than water) despite 15°C drops in land temperature over the short arctic summer nights (Moritz, 1977). This unique feature of the Alaskan Beaufort Sea coast precludes a land breeze.

Data Analysis Discussion

The momentum equation for synoptic scale atmospheric flow is

$$\frac{\partial V}{\partial t} + \underset{\sim}{V} \cdot \nabla \underset{\sim}{V} + f(k \times V) + \frac{\nabla p}{\rho} = 0 \qquad (1)$$

The last two terms are generally dominant (geostrophic approximation) and yield the wind velocity in the free stream above the planetary boundary layer with flow parallel to the isobars.

It is not uncommon for the other terms to be important which can require a correction to the velocity calculated from the geostrophic approximation. The first term above becomes important during accelerating conditions such as frontal passages when large wind changes occur in less than five hours. The second term above can become significant when strong curvature of flow exists (radius of curvature of isobars less than

Copyright 1979 by the American Geophysical Union.

Paper number 9L1403.
0094-8276/79/009L-1403$01.00

00 km, where isobars are used to estimate air arcel trajectories).

Care must also be exercised when using easured surface atmospheric pressure gradients o determine the free stream flow. The calcu-ated free stream flow will be in error when the urface pressure gradient differs significantly rom that at the free stream level due to large tale horizontal quasi steady state temperature radients (thermal wind).

The first approximation to the geostrophic ind field was obtained from NWS twice-daily 0000 and 1200 GMT) surface pressure maps but ata from Barrow and Barter Island (520 km apart) re usually the only inputs within 500 km north nd south of the Alaskan Beaufort Sea coast. To ncrease the resolution beyond that of the exist-ng NWS pressure grid, the microbarograph network Figure 1) was used and extended to include two uoys in the polar ice pack. These data buoys epended on the Nimbus 6 satellite RAMS (Random ccess Measurement System) for tracking and data clay. These data provided the basic input to two-dimensional least squares fit (TDLSF) nu-erical technique for a cubic surface (Krumbein, 959) which produced a pressure map for the study rea and allowed for calculation of geostrophic elocities at field data sites where 10 meter inds were measured.

Figure 2 is a TDLSF plot on a sea breeze day. he 0000 GMT (Greenwich Mean Time) corresponds o 1500 ADST (Alaska Daylight Savings Time) on he previous day. The surface winds at the indi-ates stations are shown using standard NWS otation for the wind velocity arrows (—, hort flag ≡ 1.5 to 3.5 m/s; —, long flag ≡ to 6 m/s.

The calculated geostrophic wind for Cottle sland on August 16, 1976 (0000 GMT) was .93 m/s rom 188.5°T with a measured surface wind of .28 m/s from 90°T. The NWS chart (not shown) nd Figure 2 show a weak pressure gradient in the ottle Island area. The land-sea temperature ifference over 15 km (Prudhoe Airport to the east [P-c]) was 7.8°C.

The TDLSF technique applied for a cubic sur-ace was used for twice daily comparison with NWS urface pressure maps. To compare surface winds n Cottle Island (Jones Island chain) with the eostrophic winds on a 3-hourly basis the tech-ique was used to fit a plane surface to pressure ata from Deadhorse, Lonely, Umiat and one off here buoy (closest to coast). The time segment

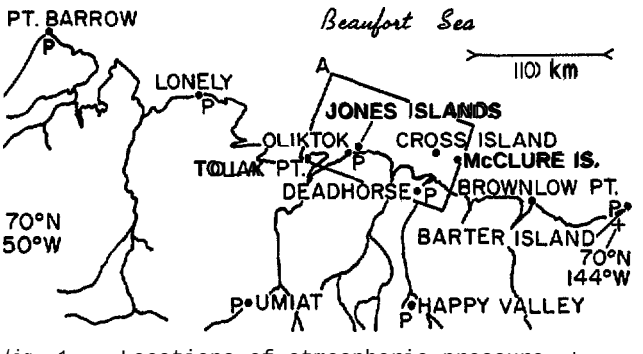

'ig. 1. Locations of atmospheric pressure sta-ions (P) within the land-based grid for 1976, .977 and 1978 and primary study area (A). (Alas-an Beaufort Sea Coast.)

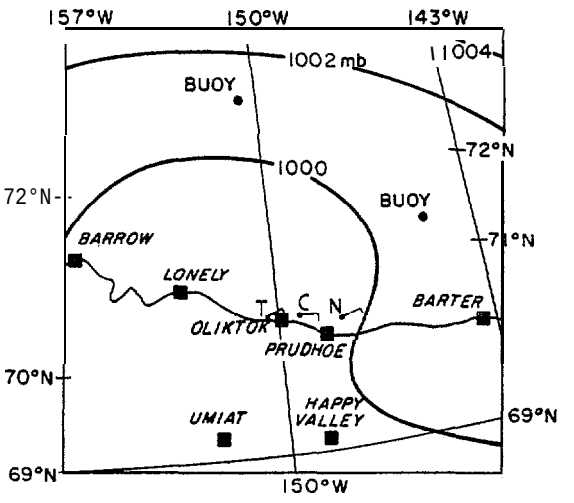

Fig. 2. Two-dimensional least squares fit (TDLSF) to surface pressure network on August 16, 1976 (0000 GMT). C, N, T represent actual sur-face wind measurements from Cottle Island, Narwhal Island and Tolaktovut Point, respectively. (Pressure contours - MB)

was from August 13 to 23 and August 30 to September 3, 1976.

The data (Figure 3) is presented with the geo-strophic wind direction (D_G, ordinate) plotted as a function of the surface wind direction (S_{10}, abscissa). The sea breeze influenced data points (*SB*) are contained within the dashed lines. The geostrophic winds within a 60″ band from 195° - 255° (SW quadrant) correspond to surface winds in a 60° band from 90° - 150° (SE quadrant). The sea breeze had offset weak geostrophic winds″ in the boundary layer to produce an average "turning" of 120″ CCW from the free stream level to the surface to increase the frequency of sur-face winds from the east. Planetary boundary layer turning, usually the result of a three-way balance between the Coriolis force, the large-scale pressure gradient force and the viscous force, should show winds shifted approxi-mately 20° counterclockwise (CCW) from their free stream direction to their 10-meter direction.

The surface wind velocity at the main experi-mental site in the Jones Islanda (Pingok Island) in August 1977 was obtained by a Climet cl-25 system with an accuracy of 1% for wind speed and ± 3° for wind direction. Surface wind velocities were recorded at other sites by Meteorology Research, Inc. remote mechanical weather stations (Model 1071). They were battery wound systems set for 30-day operations with a clock accuracy of ± 60 seconds per 24 hours.

Figure 4 for the Jones Islands (Cottle Island) was compiled by combining three Augusts of data from 1976 to 1978. This is a histogram of wind speed and direction with the top scales repre-senting direction (from) frequencies and indica-ted by bars. The bottom scales represent speed frequency and are indicated by printed numbers.

Allowing for synoptic effects Figure 3 above shows that a large percentage of the asymmetry in the wind direction data (Figure 4) must also be a thermally induced mesoscale effect (sea breeze).

Time series of surface wind data from coastal stations and islands were examined with a rotary

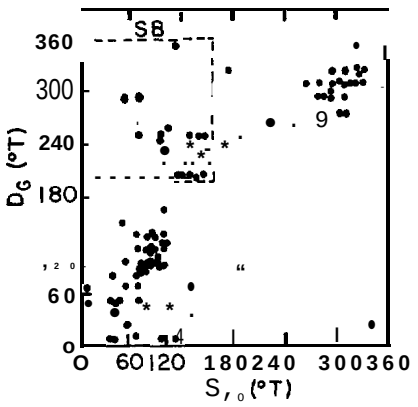

Fig. 3. Geostrophic wind direction (D_G) as a function of surface wind direction (S_{10}) in August 1976.

spectrum technique (Gonella, 1972). The variance for each frequency band is divided into clockwise (CW) rotating variance (negative frequency) and counterclockwise rotating variance (positive frequency). O'Brien and Pillsbury (1974) state that the rotary spectrum from time series of horizontal winds show the sea breeze to be a CW rotating wind oscillation and abaence of significant peaks at the 24-hour period in the CW part of the spectrum for at-sea buoys indicates absence of sea breeze ocean surface circulation,

Figure 5 is a semi-log plot of rotary spectra for August 1976 (Tolaktovut Point, coastal station) with 95% confidence limits (C) and bandwidths (B) indicated. The vertical axis has units of spectral density ([m^2/s^2]/c/3h]) with the horizontal axis in units of cycles/day. The significant peak occuring near -1 cycle/day (24-hour period) is the CW rotating contribution from the sea breeze. Peaks related to CW rotation in the Deadhorse and Narwhal spectra (not shown) are evidence of sea breeze influence in at least a 37 km band centered on the coastline.

A U. S. Coast Guard Icebreaker (*Glacier* WAGB-4) positioned approximately 64 km north of Pingok Island from 1200 to 1400 ADST on August 14, 1977 recorded surface winds averaging 170°T and 2.5 m/s while surface winds at Pingok Island were averaging 64"T and 4 m/s. This difference in

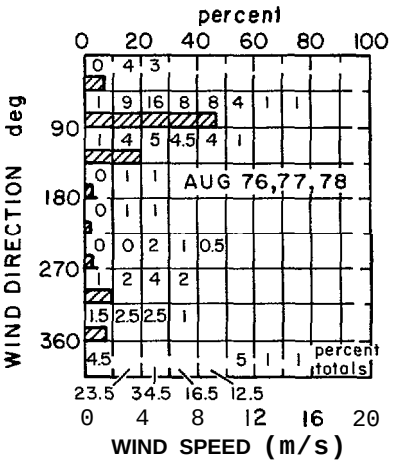

Fig. 4. Histogram of surface wind speed and direction for August 1976, 1977, and 1978 combined (from Cottle Island).

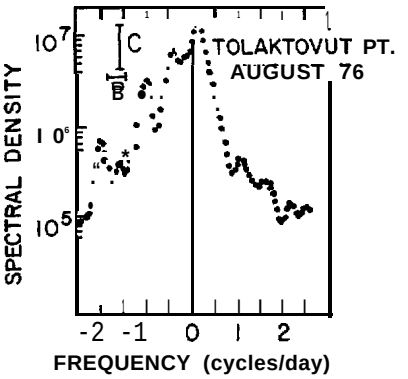

Fig. 5. Time series rotary spectra of surface wind velocity data for August 1976 collected from Tolaktovut Point.

surface wind direction shows the surface sea breeze influence to be less than 69 km from the coast.

Temporal rotation of the local surface wind vector with distance from the coast is presented for August 17, 1976 (Figure 6) with E ≡ Narwhal Island, C ≡ Tolaktovut Pt., D ≡ Cottle Island, A ≡ Deadhorse and B ≡ ARCO Airport. The calculated geostrophic wind was from 226.7°T at 3.2 m/s (1500 ADST). All sites had surface wind vectors that exhibited a CW ***rotation*** from 1500 (maximum sea breeze influence) to midnight while the 0900 to 1500 time period had generally CCW surface wind rotation. The computed geostrophic wind for midnight was 137°T and 2.2 m/s. The rotation of the computed geostrophic wind was CCW 110° from 1500 to midnight. The weak geostrophic winds had limited influence on the sea breeze rotation.

Two theodolites were used to track standard meteorological pilot balloons (August 1977, Pingok Island) at 20 end 30 second intervals. The balloon position data is converted to horizontal wind velocity versus height. An example is presented in Figure 7 for August 15, 1977. Radiosonde (battery powered expendable instrument that transmits radio signals during balloon borne accent) data (1526 and 1810 ADST) indicated the inversion layer top (ILT) to be at 200 meters with a temperature of 17°C and a 5.0" surface

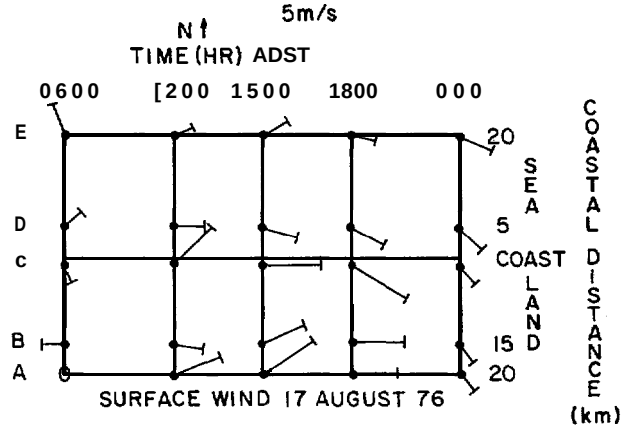

Fig. 6. Three hourly local surface wind vectors for designated stations on August 17, 1976. The calculated geostrophic wind was from 227"T at 3.2 m/s for 1500 ADST.

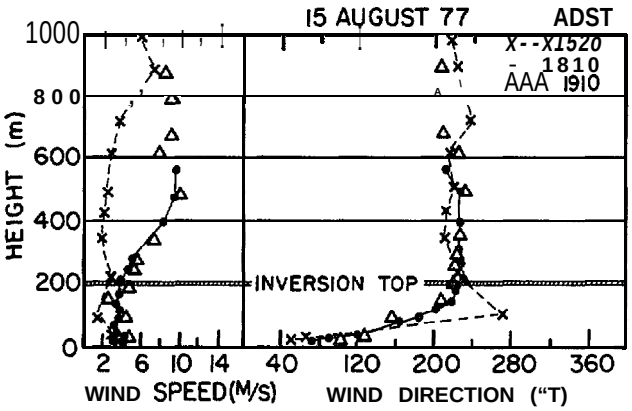

Fig. 7. Pilot balloon derived profiles of wind speed and wind direction from Pingok Island on August 15, 1977 for ADST times of 1524, 1810 and 1910.

temperature. The free stream wind remained constant at approximately 220°T for four hours during the balloon tracking. The 1524, 1810, and 1910 profiles show temporal CW rotation of the surface wind vector during times of sea breeze influence and all show large CW rotation of the wind vector with height (greater than 100° to the inversion layer top). The uPPer level winds at 1524 (sea breeze maximum) were weak, averaging 3 m/s and should have allowed for its development. The Prudhoe-Coast (P-C) temperature difference (1500 ADST) was 12.8°C.

Conclusions

The dominant physical factor causing the abnormal atmosphere boundary layer turning of the wind on the Alaskan Arctic coast is the sea breeze. The large diurnally varying land-sea thermal contrast, clockwise rotation of the surface wind vector, and surface wind flow in opposition to moderate offshore gradient flow are factors and evidence of this mesoscale phenomenon

Acknowledgments. This work was supported by Research Unit #519 Meteorology of the Alaskan Arctic Coast, a program carried out for NOAA/BLM Arctic Outer Continental Shelf Environmental Assessment Program.

References

Defant, F., Local Winds. Compendium of Meteorology. Amer. Meteor. Sot., Boston, Massachusetts, 655-662, 1951.

Gonella, J., A rotary-component method for analysing meteorological and oceanographic vector time series. Deep-Sea Res., 19, 833-846, 1972.

Krumbein, W. C., Trend surface analysis of contour-type maps with irregular control point spacing. J. Geophys. Res., 64, 823-834, 1959.

Moritz, R. E., On a possible sea breeze circulation near Barrow, Alaska. Arctic Alp. Res., 9, 427-431, 1977.

Nordlund, G., The sea breeze in south Finland according to a numerical model. Finnish Met. Inst. Contr., 77, 1-28, 1971.

O'Brien, J. J. and R. D. Pillsbury, Rotary wind spectra in a sea breeze regime. J. of App. Meteor., 13, 820-825, 1974.

Rossi, V., Land-und Seawind on den Finnischen Kusten. Mitt. Met. Zentralans, Helsinki, 41, 1-17, 1957.

Walsh, J. E., Sea breeze theory and applications. J. Atmos. Sci., 31, 2012-2026, 1974.

Walsh, J. E., Measurements of the temperature, wind and moisture distribution across the northern coast of Alaska. Arctic Alp. Res., 9, 175-182, 1977.

(Received September 5, 1979;
accepted September 27, 1979.)

Appendix C

Mountain Barrier Baroclincity Effects on Surface Winds Along the Alaskan Arctic Coast

MOUNTAIN BARRIER BAROCLINICITY EFFECTS ON SURFACE WINDS ALONG THE ALASKAN ARCTIC COAST

Thomas L. Kozo
Polar Science Center
University of Washington
Seattle, Washington 98195

February 1980

Abstract

The deployment of offshore pressure and position relaying buoys in February 1979 within the arctic ice pack has allowed for a more complete investigation of a wintertime mesoscale meteorological effect known as mountain barrier baroclinicity (MBB). Total atmospheric boundary layer turning was estimated by comparing computed three hourly gradient winds (above the boundary layer) with simultaneous surface winds at Barter Island, Alaska. This total turning compared with wind velocity versus height data obtained through rawinsonde launches at Barter Island. Results indicate that the average turning of the wind from above the boundary layer to the surface was 140° during periods of MBB influence. In addition the average difference between simultaneously measured surface winds at Barter Island and Pt. Barrow, Alaska (during MBB periods) was 140°, which cannot be explained by existing synoptic (large-scale) weather charts.

The evidence explains the wintertime abundance of west to southwest (W-SW) winds seen on historical monthly wind direction histograms from Barter Island (64 km north of the Brooks Range) while Pt. Barrow (300 km north of the Brooks Range) histograms for similar months show an east to northeast (E-NE) bias. Finally, the occurrences of the wintertime MBB effect and the summertime sea breeze effect have been related to the albedo of the arctic tundra surface.

Introduction

This wintertime phenomenon is responsible for 180 degree surface wind shifts along the Alaskan Arctic coast between Pt. Barrow and Barter island (a distance of less than 500 km) during moderate wind conditions. These shifts are not explained by National Weather Service (NWS) synoptic charts. The mechanism was described theoretically by Schwerdtfeger (1974) using arctic data from several stations north of the Brooks Range and more recently mentioned (1979) as an explanation for wind conditions on the east side of the Antarctic Peninsula.

both previous papers the data base was limited and the presentation was primarily in the form of compilation tables wi th wind direction percentages shown at various station locations. In no instance was simultaneity of measurements demonstrated at specific sites.

Schwerdtfeger (1974) states that a stable air mass moving toward a mountain range without heating from below induces baroclinicity by causing a downward tilting (away from the obstacle) of isobaric and isothermal surfaces, resulting in a mesoscale pressure gradient force away from the mountain barrier axis with a maximum value near the inversion layer top. This results in an effective thermal wind parallel to the mountain deflecting the low level flow to the left for barrier slopes in the northern hemisphere. In this case, for winds north of the Brooks Range, northeasterly flow near mountain slopes becomes directed toward the east (westerlies). It must be emphasized that the above effect is not due to orographic channeling or resultant pressure patterns during strong wind conditions (Dickey, 1961) caused by the "knob" of the Brooks Range.

A unique data set has been obtained through the implementation of the University of Washington, Polar Science Center's Arctic Basin Buoy (ABB) array (sponsored by the National Science Foundation) by mid-February 1979. These buoys, which were air dropped at various locations on the arctic ice pack, transmit pressure and position data to the TIROS-N satellite and use the ARGOS data collection and location system. Use of data from two of these offshore buoys with concomitant onshore station data has allowed the calculation of 3-hourly geostrophic winds through a two dimensional least squares fit (TDLSF) numerical fit technique (Kozo, 1979) for the north coast of Alaska. When this data was coupled to simultaneous rawinsonde (radio tracked meteorologically instrumented balloon) data from Barter Island, Alaska, a new look at a phenomenon which occurs at least 25% of the time in the winter months was made possible.

The horizontal extent of this phenomenon indicates that surface wind measurements in winter months for a coastal zone from Barter Island to Prudhoe Bay

may be poor indicators of the actual stress exerted on nearshore ice. Instead, the large scale (geostrophic) wind should be calculated farther out on the polar ice pack to determine the stress that will be transmitted to the ice closer to shore.

Data Analysis Discussion

Figure 1 is a section of a NWS synoptic chart for 11 March 1979 (1200 GMT) with the Brooks Range of Alaska cross hatched. F, L, G, H and S represent surface wind data locations at Pt. Barrow, Lonely, Prudhoe Bay, Barter Island (moving west to east along the Alaskan coast) and at a Russian ice station respectively. The surface winds are shown using standard NWS notation for the wind velocity arrows with the short flags denoting 1.5 - 3.5 m/s speeds. B_{13} and B_{14} represent the locations of the ABB array buoys which furnished surface pressure (accuracy ± 1.5 mb) out on the ice pack (no wind direction measurements are made at these locations). The pressure contours are in millibars (rob) and the numbers adjacent to the locations are surface pressures minus 1000 mb. For the stations shown, the NWS chart used data from S, F and H only to construct the contours depicted. The recorded surface winds at S and F and the measured surface pressure at B_{13} (1037.2 mb) are reasonable values for the offshore high pressure system (anti-cyclonic flow) shown. However, the winds at G and H (opposite to what the NWS pressure pattern indicate) and the measured surface pressure at B_{14} show that the analysis is inadequate. It should be noted that the actual pressure change from B_{13} to B_{14} was 15.3 mb (map contours indicate 8 mb) while the actual change from F to H (a comparable distance) is 5.6 mb. Simultaneous rawinsonde data (Figure 2) taken at Barter Island (H) shows a strong temperature inversion up to 400 m and approximately 150° of turning of the wind within the inversion layer. This demonstrates the existence of a pressure gradient force away from the Brooks Range axis since frictional turning of the wind will usually account for only 20-30 degrees of counter clockwise (CCW)

change from the upper free stream direction to the surface (10-meters). The computed geostrophic wind for this time using pressure data from buoys B_{13}, B_{14}, and Pt. Barrow was from 36°T at 15 m/s.

Figure 3 is a section of a NWS synoptic chart for 12 March 1979 (1200 GMT) with the same designations as Figure 1. Again, the recorded surface winds at S and F and the measured surface pressure at B_{13} (1036.1 mb) are reasonable values for the high pressure system shown. The lack of a wind arrow at G indicates 0 wind speed. This and the 180° surface wind reversal at H is not explained by the NWS chart analysis. The actual pressure change from B_{13} to B_{14} is 5.4 mb while the actual change from F to H (a comparable distance) is .2 mb. Simultaneous rawinsonde data (Figure 4) taken at Barter Island (H) shows an inversion layer up to 800 m and approximately 180° of turning of the wind within this layer. The computed geostrophic wind was from 68°T at 12 m/s at this time. The above figures are shown as further evidence for the existence of a pressure gradient component not recorded by the existing NWS synoptic observation network.

Figure 5 is a scattergram showing the 3-hourly surface wind direction at (H) Barter Island (ordinate) plotted as a function of the surface wind direction at (F) Pt. Barrow (abscissa) for the month of March 1979 (240 data points). Since Pt. Barrow is more than 300 km north of the Brooks Range, the surface wind should reflect a three-way balance between the Coriolis force, the large-scale pressure gradient force, and the viscous (friction) force and vary from the geostrophic wind direction by less than 30 degrees. The data points enclosed by the solid line represent simultaneous surface winds at Barter Island and Pt. Barrow with an average directional difference of 140 degrees..

To compare surface winds at Barter Island with geostrophic winds, a TDLSF numerical technique (Kozo, 1979) was applied to fit a plane surface to pressure data from B_{13}, B_{14} and pt. Barrow. It must be noted that Barter Island surface

pressure is "contaminated" by the mountain barrier baroclinicity effect and therefore not used in the computations. Figure 6 is a scattergram showing 3-hourly surface wind directions at Barter Island (ordinate) plotted as a function of the computed geostrophic wind (abscissa) for the month of March 1979. Figure 5 and Figure 6 are strikingly similar which is no surprise since surface winds at Pt. Barrow should be less than 30 degrees from the geostrophic winds for the same time periods. The data points enclosed by the solid line (Figure 6) now take on added significance as evidence for mountain barrier baroclinicity showing an average 140 degrees of turning from the geostrophic (free stream) wind level to the surface. This is the reason for the predominance of surface westerly winds seen in Barter Island wind direction histograms in the winter months (times of greater atmospheric stability) while histograms of wind direction for Pt. Barrow show a predominance of easterly winds (Brewer, et al., 1977).

Figure 7 was derived from historical compilations of monthly wind direction frequency histograms. It shows a plot of the percentage difference (A%) between occurrence of surface winds in the east to northeast (E-NE) quadrant and the west to southwest (W-SW) quadrant at Barter Island, Oliktok, and Lonely Distant Early Warning (DEW) stations (all on the Beaufort Sea coast of Alaska). Lonely, Oliktok (between Prudhoe Bay and Lonely), and Barter Island are approximately 275 km, 165 km and 64 km respectively from the foothills of the Brooks Range. Positive (A%) implies more E-NE winds than W-SW winds while negative (Δ%) implies more S-SW winds than E-NE winds. The months of October through April show a great disparity between Lonely (farthest from the mountains) and Barter Island (closest to the mountains). This again is evidence of eastward deflection of northeasterly winds due to mountain induced baroclinicity during the winter months when the atmospheric boundary layer has its greatest static stability.

In the months of May through August, when the sun is above the horizon for more than 20 hours (at these latitudes) and the land snow cover is depleted or completely gone, the land boundary layer becomes closer to neutral stability and

the three coastal stations become similar. They show an average of E-NE winds at 3 times the frequency of W-SW winds. The effect of the mountain range is minimized (except for orographic channeling) during this period and the meso-scale thermal effect of the coastline becomes a major influence' (Kozo, 1979) on the resultant surface winds in the coastal region.

Figure 8 isarecord of the average daily albedo over the arctic tundra near Pt. Barrow from March 25 to October 25, 1966 (Weaver, 1970). Albedo is tilt? ratio of reflected to incident shortwave radiation. The vertical dashed lines separate the four parts of the albedo regime as defined by Maykut <1973):

1. The winter stationary period occurs from mid-October to late May and is characterized by a completely snow covered tundra.
2. The spring transitional period occurs between late May and early June and shows a rapid drop in albedo from 75% to 10% over the tundra in 3-5 days.
3. The summer stationary period occurs from June to August and is characterized by disappearance of all snow and ice cover on land.
4. The autumn transition period occurs in September when the land surfaces freeze and become snow covered. It takes much longer to pass through this phase than in spring.

Year-to-year variations in climate will change the dates of the transition period but the general shape of the curve in Figure 8 will not be altered nor the magnitudes of albedo altered.

Figure 8 gives an additional explanation for the shape of the curves in Figure 7. The importance of a stable air mass moving toward a mountain range without heating from below is seen. The months (Figure 7) where Barter Island has a surface wind regime with a significant amount of W-SW winds (values approaching OA% or -A%) are part of the winter stationary period. The months (Figure 7) where Barter Island surface winds are similar to the other stations (large +Δ%) are part of the summer stationary period where air masses are heated from below on traversing the snowless tundra (decreasing the static stability). September

appears as a transition month on both Figure 7 and 8. May data is an apparent inconsistency but it is an average of twenty years of data (Figure 7) in a month where solar insolation has always reached 24 hours duration (May 11 at 71°N). In some years the tundra could be devoid of snow or completely covered by the last week of May. In any event temperature data from Barter Island rawinsondes "has shown that the atmospheric stability is greatly diminished by May.

Conclusions

Mountain Barrier Baroclinicity is a major physical process responsible for the wintertime abundance of coastal winds in the W-SW quadrant from Barter Island, Alaska to Prudhoe Bay along the Alaskan Arctic coast. It is a seasonal effect related to stability of the atmospheric boundary layer. The stability of the atmospheric boundary layer over land, in turn is affected by surface albedo which when high promotes a stable layer or when low (summer) establishes a more neutral boundary layer. Previous attempts at relating wintertime ice movement in coastal regions to actual surface winds must be reinvestigated in those locations within the MBB "shadow" of the Brooks Range.

Acknowledgments. This work was supported by Research Unit #519, Meteorology of the Alaskan Arctic Coast, a Program carried out for NOAA/BLM Arctic Outer Continental Shelf Environmental Assessment Program.

References

Brewer, W. A., H. F. Diaz, A. S. Prechtel, H. W. Searby and J. L. Wise, Climatic atlas of the outer continental shelf waters and coastal regions of Alaska, NOAA, NCC EDS, Asheville, North Carolina, 409 pp., 1977.

Dickey, W. W., A study of a topographic effect on wind in the arctic- J. of Meteor, 18, 790-803, 1961.

Kozo, T. L., Evidence for sea breezes on the Alaskan Beaufort Seacoast, Geophys. Res. Letters, G, 849-852, 1979.

Maykut, G. A. and P. E. Church, Radiation climate of Barrow, Alaska, 1962-66, J. of App. Meteor., 12, 620-628, 1973.

Schwerdtfeger, W., Mountain barrier effect on the flow of stable air north of the Brooks Range, in Proceedings of the 24th Alaskan Science Conference, pp. 204-208, Geophysical Institute, University of Alaska, Fairbanks, 1974.

Schwerdtfeger, W., Meteorological aspects of the drift of ice from the Weddell Sea toward the mid-latitude westerlies, J. Geophys. Res., 84, 6321-6328, 1979.

Weaver, D. F., Radiation regime over arctic tundra and lake, 1966. Sci. Rept., Dept. of Atmospheric Sciences, University of Washington, Seattle, 260 pp., 1970

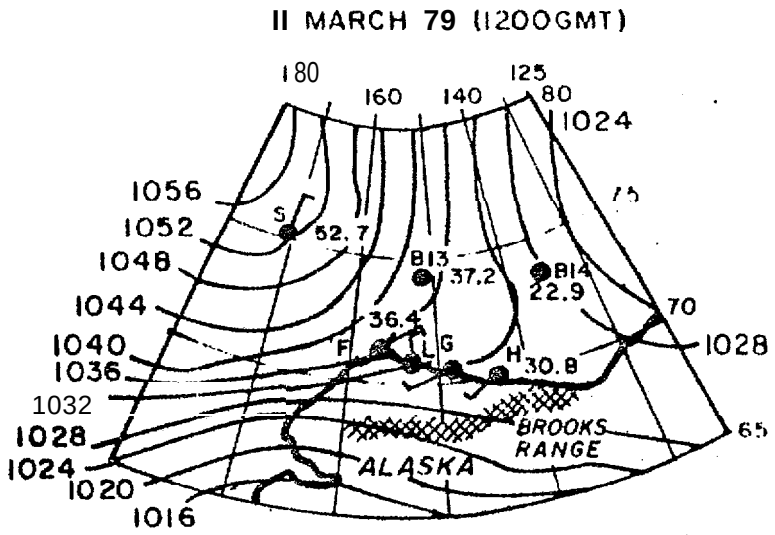

Fig. 1 Section of a NWS synoptic analysis chart for 11 March 1979 (1200 GMT) with the Brooks Range of Alaska cross-hatched. F, L, G, H and S represent surface wind data locations at Pt. Barrow, Lonely, Prudhoe Bay, Barter Island and a Russian ice station respectively. B_{13} and B_{14} are locations of two of the Arctic Basin Buoy array buoys used in this study. (Pressure contours-rob.) There were no wind measurements at B_{13} and B_{14}.

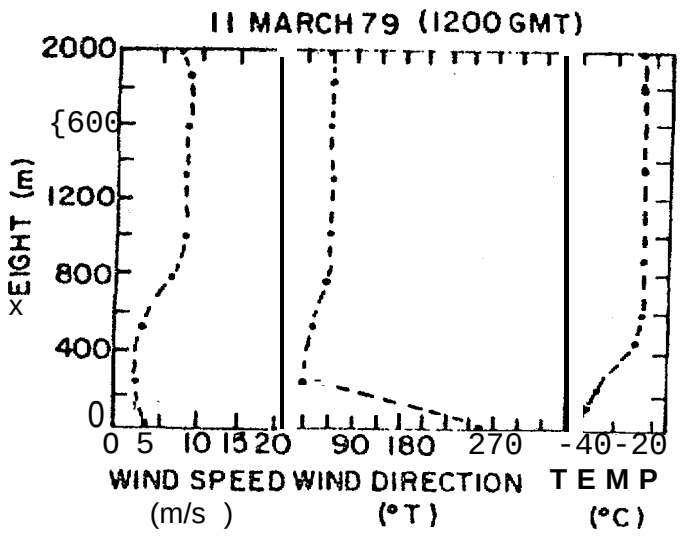

Fig. 2 Rawinsonde derived profiles of wind speed, wind direction and temperature taken at Barter Island, Alaska on 11 March 1979 (1200 GMT).

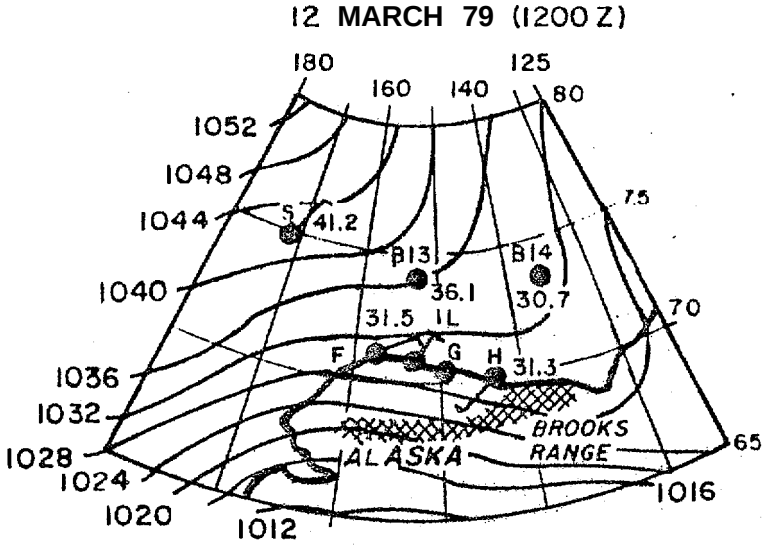

Fig. 3 Section of a NWS synoptic analysis chart for 12 March 1979 (1200 GMT) with the same designations as Figure 1.' Absence of a wind arrow at G indicates 0 winds.

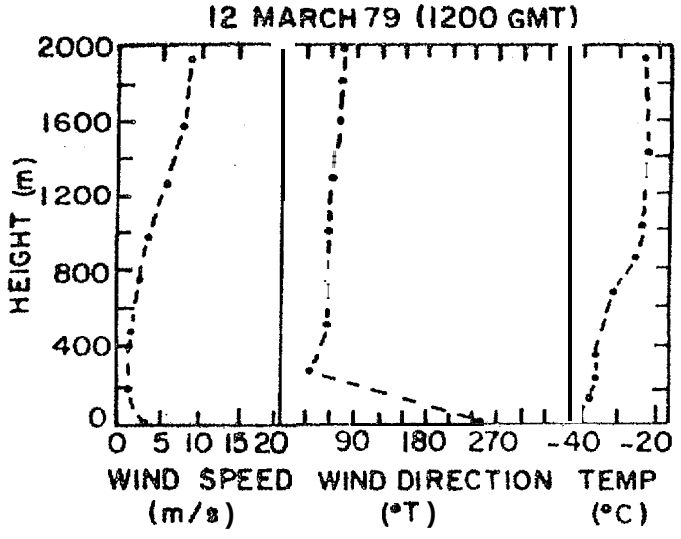

Fig. 4 Rawinsonde derived profiles of wind speed, wind direction and temperature taken at Barter Island, Alaska on 12 March 1979 (1200 GMT).

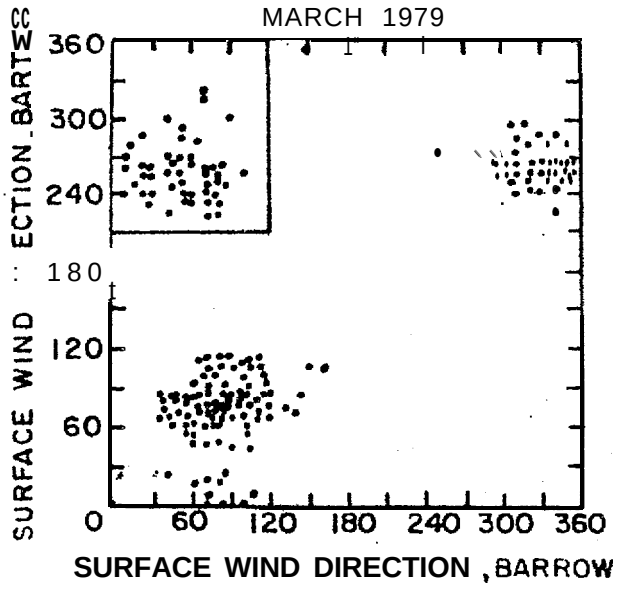

Fig. 5 Surface wind direction at Barter Island as a function of surface. wind direction at Pt. Barrow for March 1979.

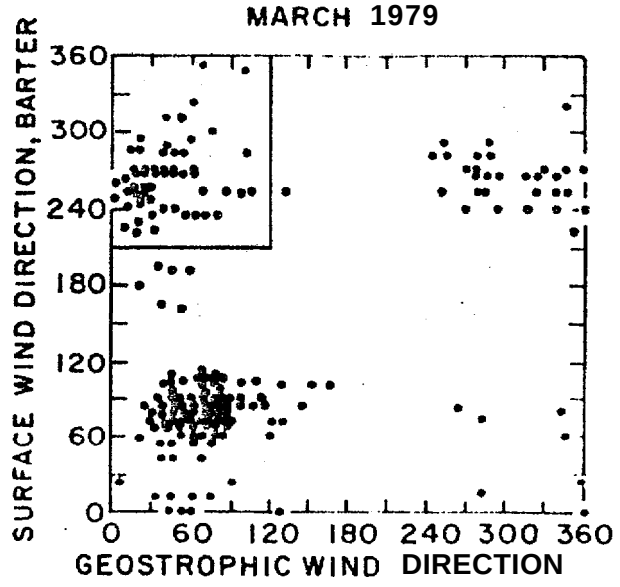

Fig. 6 Surface wind direction at Barter Island as a function of computed geostrophic wind direction for March 1979.

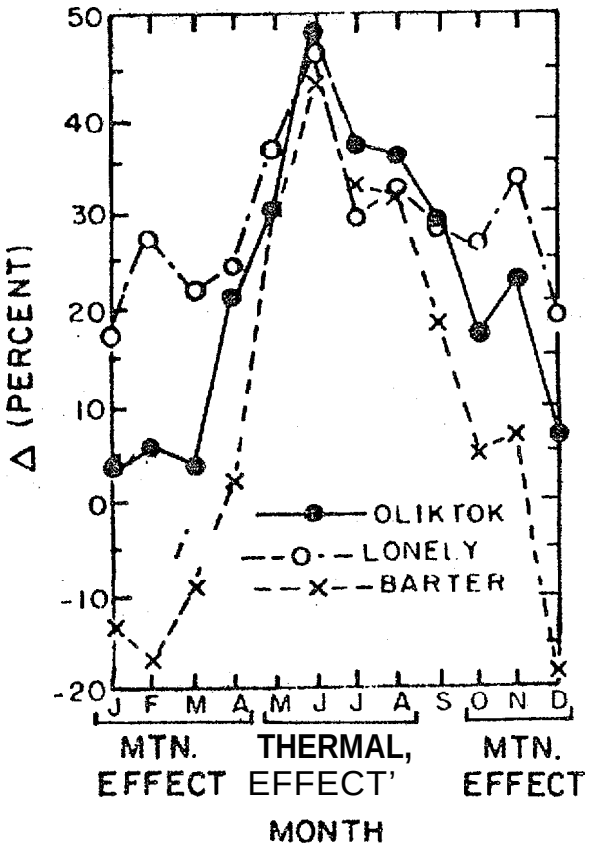

Fig. 7 Percentage difference (A%) between occurrence of surface winds in the E-NE quadrant and the W-SW quadrant for data locations at "Barter Island, Oliktok and Lonely, Alaska.

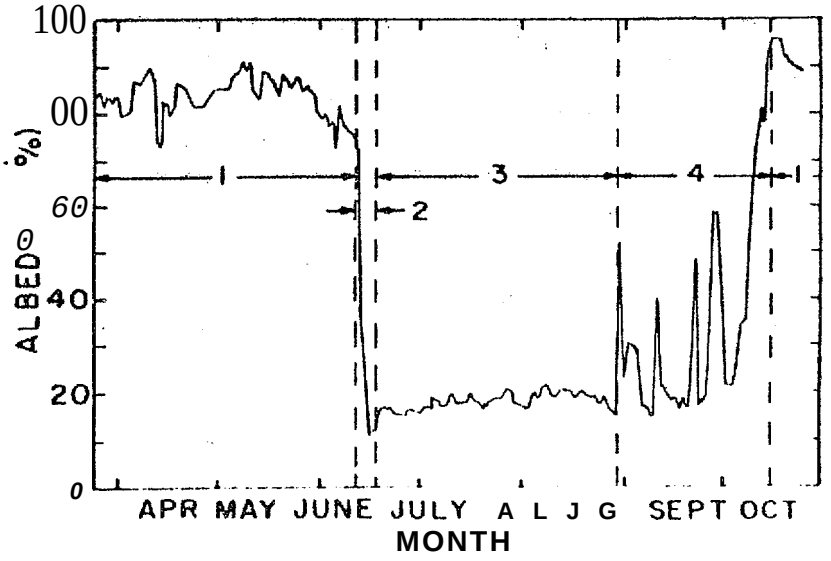

Fig. 8 Record of the average daily albedo over the arctic tundra near Pt. Barrow from March 25 to October, 1966 (Weaver, 1970).